THE UNIVERSITY OF CHICAGO

IDEALIZED MODELS OF ARCTIC SEA ICE MELT PONDS

A DISSERTATION SUBMITTED TO
THE FACULTY OF THE DIVISION OF THE PHYSICAL SCIENCES
IN CANDIDACY FOR THE DEGREE OF
DOCTOR OF PHILOSOPHY

DEPARTMENT OF THE GEOPHYSICAL SCIENCES

BY
PREDRAG POPOVIĆ

CHICAGO, ILLINOIS
MARCH 2020

"Eat, sleep, exercise, and don't worry."

– Dorian Abbot

TABLE OF CONTENTS

LIST OF FIGURES

LIST OF TABLES

ACKNOWLEDGMENTS

Thank you to Dorian Abbot and Mary Silber for being patient advisers and good friends. Thank you to BB Cael for being a colleague and a friend and for many discussions that inspired me to take the approach I did. Thank you also to Justin Finkel for great help with the last Chapter of this thesis. Thank you to members of my committee, Doug MacAyeal and Edwin Kite, for many useful comments and ideas. Thank you to Don Perovich for providing the images of melt ponds.

Thank you to my parents, Biljana and Dejan Popović and my grandparents, Istvan and Radmila Györfi and Nenad Popović. Thank you to all of my friends and especially to Branislav Kuzmanović and Miloš Pušić. Finally, a special thank you to my wife Milica Popović for persistent love and support.

We acknowledge a NASA Earth and Space Science Fellowship. This work was partially supported by the National Science Foundation under NSF award number 1623064 and under NSF award number 0940261, which is part of the Mathematics and Climate Research Network.

ABSTRACT

As Arctic sea ice starts to melt in the summer, melt ponds form on its surface and, in a matter of days, cover large portions of the ice. Due to their low reflectivity, melt ponds greatly accelerate ice melt. Despite their importance, they are poorly understood due the many processes that control their evolution, which operate on widely separated length-scales. In this thesis, we use idealized models of melt ponds with a goal to provide a fundamental understanding of their evolution.

First, we study the case of late-summer ponds that exist on highly permeable first-year sea ice. Assuming that ice is fully permeable, we show that pond coverage evolution can be approximately determined by solving two uncoupled ordinary differential equations (ODEs) in which the rate of change of pond coverage fraction is a function of itself, of the initial ice surface hypsographic curve, and of average melt rates of different regions of the ice. In this way, we show that it is possible to greatly reduce the complexity of pond evolution on permeable ice and to summarize all of the environmental conditions with only a few aggregate parameters.

Second, we show that melt pond geometry on both first and multi-year ice can be accurately captured by a simple geometric model where ponds are represented as voids that surround randomly sized and placed circles that represent snow dunes. There are only two model parameters: the characteristic circle radius and the pond coverage fraction. We set these parameters by matching two correlation functions, which determine the typical pond size and their connectedness, between the model and aerial photographs of melt ponds. With parameters calibrated in this way, we reproduce the previously-observed pond size distribution and fractal dimension as a function of pond size over the entire observational range of more than 6 orders of magnitude. Surprisingly, by further studying the correlation functions, we find that late-summer ponds are organized close to the critical percolation threshold. Moreover, we find that ponds from different years and documented at different

locations have very similar typical sizes.

Third, we explain the observation we made previously that the ponds are organized close to the percolation threshold. We show that, since ponds drain through large holes, the percolation threshold is an upper bound on pond coverage following pond drainage. Furthermore, because of the universality of systems close to the percolation threshold, we show that the pond fraction as a function of the number of open holes follows a universal curve. This curve governs pond evolution during and after pond drainage, which allows us to formulate an equation for pond coverage evolution that captures the dependence on physical properties of the ice and is supported by observations.

Finally, we generalize the void model we developed earlier and show that it accurately captures the pre-melt distribution of snow-depth. We find that the snow depth is distributed according to a Gamma distribution which can be fully characterized by the mean and the variance of snow depth. This allows us to derive an analytical formula for pond evolution during early summer when ice is impermeable.

By combining all of our results, we find that nearly the entire pond evolution since the onset of melt can be captured with computationally inexpensive analytical models that do not sacrifice accuracy and reveal relationships between pond evolution and measurable ice parameters that would not be captured using more complex models. These findings have significant potential to improve our parameterizations of sea ice albedo in large-scale climate models, thereby advancing our ability to predict the fate of Arctic sea ice.

This work was led, performed, and written by Predrag Popović under supervision of Dorian Abbot and Mary Silber.

CHAPTER 1

INTRODUCTION

Covering a vast area of nearly 15 million square kilometers in the far north, sea ice is a major component of the Arctic climate system (Perovich and Richter-Menge, 2009), part of the environment of one of the largest biomes on the Earth (Grebmeier et al., 1995), and a major obstacle for maritime trade between North America, Europe, and Asia. For these reasons, much effort has been put into predicting when the Arctic ocean will become ice-free in the summer due to the effects of man-made climate change (Serreze et al., 2007; Wang and Overland, 2009). This has proven to be an exceedingly difficult problem, as sea ice is controlled by processes that operate on scales ranging from less than a millimeter to hundreds of kilometers (Holland and Curry, 1999). As our best climate models can currently only have a resolution on the order of ten kilometers, many relevant smaller scale processes have to be parameterized, which relies on our physical understanding of them.

An important small-scale phenomenon that controls the rate of sea ice loss is the formation of meter-scale melt ponds on the ice surface during the summer months (Holland et al., 2012). Ponds form as the snow atop sea ice begins to melt. Unlike the surrounding bare ice that reflects the majority of sunlight, melt ponds absorb most of it thereby accelerating ice melt (Perovich, 1996). Pond evolution is highly non-linear and is controlled by the structure of the underlying ice.

Depending on ice permeability, pond evolution on first-year ice typically progresses in four stages (Landy et al., 2014; Polashenski et al., 2012). During the initial stage, fresh meltwater seeps into brine channels and pores within the ice. Because the ice interior is colder than the freezing point of fresh water, meltwater freezes and the ice becomes impermeable (Polashenski et al., 2017). During this period, usually called stage I of pond evolution, pond coverage grows quickly and within several days ponds can expand to cover a majority of the ice surface. As the ice warms, some of the pathways through the ice to the ocean

reopen. As above-freezing water pours through these newly opened channels, it melts them, expanding them into large holes. During this time, called stage II of pond evolution, ponds drain and pond coverage drops to its minimum. By the end of stage II, the ice becomes fully permeable, and the remaining ponds correspond to those regions of sea ice that are below sea level. While the ice is permeable (stage III of pond evolution), ponds remain at sea level and pond coverage grows slowly. This slow pond growth happens because ice thins, forcing more of the ice surface below sea level, and because ponds erode their side-walls by lateral melt. Finally, during stage IV, ponds either refreeze or the ice breaks up.

In addition to a complicated time-evolution, melt ponds also have a complex spatial structure. Previous studies have characterized some statistical properties of pond patterns. Perovich et al. (2002) showed that ponds follow a power law size distribution. Hohenegger et al. (2012) estimated the fractal dimension, D, of pond boundaries. They found that the fractal dimension transitions from $D \approx 1$ for small ponds to $D \approx 2$ for large ponds. All of these considerations highlight the complex nature of melt ponds.

Because the development of melt ponds is a multi-scale phenomenon, it is difficult to model. Most models of melt ponds so far have tried to capture as many details about physical processes as possible, while parameterizing those processes that cannot be captured due to resolution or computational constraints (Flocco and Feltham, 2007; Scott and Feltham, 2010; Skyllingstad et al., 2015; Taylor and Feltham, 2004). These models can accurately capture the large-scale distribution of melt ponds across the Arctic basin. However, the many assumptions these models make reduce their ability to provide a fundamental understanding and produce reliable predictions of melt ponds in a changing climate.

The goal of this thesis is to take an alternative approach to modeling melt ponds using reduced complexity models to provide a basic understanding of melt pond evolution. We will show that nearly the entire pond evolution as well as the pond geometry can be represented by simple models that sacrifice little accuracy, are highly computationally efficient, and make

clear the connections with measurable properties of ice. The thesis is organized as follows.

In Chapter 2, originally published as Popović and Abbot (2017), we consider the evolution of pond coverage fraction for stage III ponds, assuming that ice is fully permeable and hydrostatically balanced. Under these assumptions, the pond coverage fraction does not depend on the details of the topography, but is determined only by the fraction of the surface below the sea level. This fraction can be captured statistically by a quantile function of the surface height distribution (hypsographic curve) whose form stays approximately constant for different ice surfaces. We show that the effects of ice thinning, lateral melting, and ice topography on pond coverage evolution can be captured in a simple way under the permeability assumption. In particular, we find that pond evolution can be approximately calculated by solving two uncoupled ODEs whose form depends only on the initial hypsographic curve and four parameters that determine the average rates of pond bottom melting, bare ice melting, ice bottom melting, and lateral melting.

In Chapter 3, originally published as Popović et al. (2018), we explain the observations that the pond size distribution is approximately a power law and that the fractal dimension of the pond boundaries transitions from $D \approx 1$ to $D \approx 2$. We develop a simple geometric model where ponds are represented as voids that surround randomly sized and placed circles which represent snow dunes. The model has only two parameters, the typical circle size and the fraction of the surface covered by voids. We choose these two parameters by comparing two types of correlation functions, which measure typical pond size and pond connectedness, between the model and aerial photographs of melt ponds taken during two separate missions to the Arctic. We show that, after this calibration, the pond size distribution and the fractal dimension are reproduced highly accurately over the entire observational range of more than 6 orders of magnitude. Furthermore, by studying the correlation functions, we find two surprising observations: 1) ponds are organized close to the percolation threshold, and 2) ponds from different years and different locations have a very similar typical size.

In Chapter 4 (manuscript currently in review as Popović et al. (2019b)) we explain the observation we made in Chapter 3 that ponds seem to be organized close to the percolation threshold. We show that drainage through large holes during stage II necessarily constrains the ponds to exist below the percolation threshold. We develop a model where holes open at random locations and drain ponds that overlay a randomly generated topography. We show that above the percolation threshold, a single hole can drain vast portions of the surface, whereas below the threshold, new holes lead to minimal additional drainage. This model exhibits universality and is independent of details such as the underlying topography. This allows us to analytically derive a universal function that determines pond fraction as a function of the number of open holes. Using this function, and extending our model to include ice melting and maintaining hydrostatic balance, we find an analytical formula for pond coverage evolution during stage II that connects pond coverage evolution and the measurable properties of ice. Additionally assuming that there is no lateral melt and that ice was relatively flat at the beginning of the drainage stage, we show that a similar function can also be used to estimate pond evolution during stage III. We find that observations are consistent with all of our results.

In Chapter 5 (manuscript currently in review as Popović et al. (2019a)) we generalize the void model developed in Chapter 3 to a continuous surface by replacing circles with mounds of Gaussian shape. We then show that the pre-melt snow depth distribution determined from LiDAR measurements is closely matched by the height distribution of this synthetic topography and well-fit by a Gamma distribution. This means that the snow depth distribution can be fully characterized by only the mean and the variance of snow depth. It further allows us to formulate analytical equations for pond evolution during stage I. This shows that nearly the entire pond evolution can be accurately represented using simple models, thereby showing great potential for improving albedo parameterizations in future models of sea ice.

Finally, in Chapter 6, we summarize our results and conclude.

Some of the notation is inconsistent between different chapters. We chose to keep this notation in order to maintain consistency with the published papers. Each chapter will contain a table summarizing all of the variables used in that chapter.

1.1 Review of previous work

Most of the previous work on melt pond modeling involves models with many degrees of freedom that attempt to include as much realism as possible. Here we will review an example of such a model in some detail to give the reader a sense of the strengths and weaknesses of this approach.

As an example, we will consider the model of Scott and Feltham (2010). This model is a cellular automaton that updates, at each time-step, the ice, snow, and meltwater content of each grid-point. Here, grid-points represent 5m $\times$ 5m rectangular columns of ice, which can either be bare or covered with snow or meltwater. The model domain is a 200m$\times$200m square. Each column evolves thermodynamically independently of other columns and communicates with them via the transport of meltwater. To calculate the thermodynamic evolution of a column, it is further divided into 20 vertical grid-points. Then, a sophisticated heat transport model is used to calculate albedo, melt rates, and the snow saturation. This model includes mushy layer equations for sea ice, heat diffusion in snow, parameterization of turbulent heat flux in melt ponds, and a radiative transfer model. This allows for some realistic features to appear such as an ice crust on top of melt ponds that affects the albedo. Water that is generated by melting is drained vertically to the ocean and transported horizontally according to Darcy's law. Ice floes are kept in hydrostatic balance throughout the simulation. The model was initiated by randomly generating a bottom and a surface ice topography and a snow topography with the mean, standard deviation, and horizontal correlation length taken from field measurements and was forced by heat fluxes derived from meteorological

measurements.

The main advantage of this model is that it allowed for many of the observed features to emerge from first principles. For example, the model reproduced the observation that first-year ice had larger and shallower ponds than multi-year ice, it captured the timescale of pond coverage variation, and it captured the general trends in area-averaged albedo, although it somewhat overestimated the albedo relative to measurements. Moreover, including many physical processes allows one to perform sensitivity analyses to understand how each process affects pond evolution. A sophisticated model such as this one represents an idealized experiment of melt pond evolution.

By far, the main disadvantage of this model is its computational complexity. For example, the researchers report that simulating a 90-day pond evolution took over a week to complete. Tied to this computational complexity are the simplifying assumptions made in order to be able to complete the model runs in a reasonable amount of time. For example, the 5m horizontal resolution is relatively coarse since ponds exist on scales of several tens of meters, so a typical pond is only several grid-points wide. This coarse resolution requires some processes to be parameterized and it is not clear how well these parameterizations apply. An example of this is the fact that horizontal transport of water is modeled by Darcy's law with a fixed permeability, which neglects the possibility that water is transported by channels. In addition to such parameterizations, the realism of the model is eroded somewhat by the fact that some parameters are poorly constrained by measurements. For example, measurements show that the vertical permeability can vary by several orders of magnitude, while the horizontal permeability is very poorly constrained by measurements and, therefore, has to be guessed.

There are a number of examples of the similar flavor. As some examples we mention the models of Flocco and Feltham (2007); Lüthje et al. (2006); Scagliarini et al. (2018); Skyllingstad and Paulson (2007); Skyllingstad et al. (2009, 2015). Each of these models is

either a 2 or 3 dimensional representation of melt ponds evolving on an ice surface and each tries to incorporate as much realism as possible within the computational bounds. As melt pond evolution is a difficult real-world problem, each of these models has to sacrifice some processes, and each one does this based on the particular priorities and questions the model is trying to answer. In general, their strength is their sophistication and their weakness is their complexity.

CHAPTER 2

A SIMPLE MODEL FOR THE EVOLUTION OF MELT POND COVERAGE ON PERMEABLE ARCTIC SEA ICE[1]

2.1 Introduction

Over the past forty years, Arctic summer sea ice extent has reduced by 50 percent, making it one of the most sensitive indicators of man-made climate change (Perovich and Richter-Menge, 2009; Serreze and Stroeve, 2015; Stroeve et al., 2007). This rapid decrease is at least partially due to the ice-albedo feedback (Perovich et al., 2007; Screen and Simmonds, 2010; Zhang et al., 2008). Moreover, if the ice-albedo feedback is strong enough it could lead to instabilities and abrupt changes in ice coverage in the future (Abbot et al., 2011; Eisenman and Wettlaufer, 2009; Holland et al., 2006; North, 1984). The albedo of ice is significantly reduced by the presence of melt ponds on its surface (Eicken et al., 2004; Perovich and Polashenski, 2012; Yackel et al., 2000). Therefore, understanding the evolution of melt ponds is essential for understanding the ice-albedo feedback, and consequently, the evolution of Arctic sea ice cover in a warming world. This means that accurate melt pond parameterizations must be incorporated into Global Climate Models (GCMs) to improve their sea ice forecasts (Flocco et al., 2010; Holland et al., 2012; Pedersen et al., 2009). The main difficulties with including accurate melt pond parameterizations in large scale models are that pond evolution is nonlinear and that it is the result of a variety of different physical processes operating on a range of length and time scales. For these reasons, it is important to understand the mechanisms that drive the evolution of melt ponds.

Typically, the evolution of pond coverage on first-year ice proceeds in fairly consistent stages (Landy et al., 2014; Perovich et al., 2003; Polashenski et al., 2012; Webster et al.,

1. This chapter was originally published as Popović and Abbot (2017). It is nearly identical to the original apart from minor changes made mainly to fit the formatting requirements of the thesis and to respond to the comments made by the thesis committee.

2015). First the ponds grow quickly while the ice is impermeable. Next they drain quickly and pond coverage shrinks as the ice transitions from impermeable to permeable. Then the ponds grow slowly while the ice is permeable and pond water remains at sea level. Finally, the ponds either refreeze or the floe breaks up. The stage when ice is highly permeable is typically the longest, often longer than the first two stages combined. This stage is particularly suitable to model, since the ponds can be assumed to be at sea level and hydraulically connected to the ocean. On multiyear ice, ponds also experience a growth and a drainage stage, but often do not drain to sea level. On some occasions, however, ponds on multiyear ice can drain to sea level as well.

In this Chapter we will present a simple "0d" model for the evolution of melt pond coverage on sea ice floes. We will assume that ice is permeable, ponds are at sea level and hydraulically connected to the ocean, the whole ice floe is in hydrostatic balance, and different points on the ice surface may melt at different rates. The purpose of our model is: (1) to clarify the roles in the evolution of pond coverage played by energy fluxes, the ice thickness, bulk ice density, ice roughness, and initial pond coverage, (2) to provide a simple, yet accurate, way to estimate the pond coverage as a function of time, (3) to understand the behavior of melt ponds under general environmental conditions, and (4) to investigate different types of qualitative behavior that can arise from differential melting and maintaining hydrostatic balance.

Skyllingstad et al. (2009) also describe pond growth on permeable ice, but include only pond growth by lateral melt of pond walls. This contrasts with our model, which includes includes pond growth by vertical changes of the topography. Our models are different, but complementary, and we will draw parallels between our two models when discussing the possibility of lateral melt. Aside from Skyllingstad et al. (2009), previous melt pond modeling efforts include works by Taylor and Feltham (2004), Lüthje et al. (2006), Scott and Feltham (2010), and Flocco and Feltham (2007), who all created comprehensive models

that allowed for more realistic representations of physical processes such as heat and salt balance, and meltwater routing and drainage. The advantage of our model is its simplicity, which makes it possible to clarify the roles of each of the physical parameters involved.

This Chapter is organized in the following way. In section 2.2 we build a simple model for the evolution of pond coverage. In section 2.3, we compare the model to observations. In section 2.4 we discuss realistic values of physical parameters and solve the model numerically. In section 2.5 we assess the impacts of sea ice roughness and develop a simple parameterization to estimate mean pond coverage after a certain amount of time without solving the model. In section 2.6 we analyze the model analytically to gain a better understanding of the factors influencing pond evolution. In section 2.7 we discuss lateral melt and internal melt combined with effect of density variations. Finally in section 2.8 we summarize our results and conclude. In appendices A, B, C, and D we discuss some of the more technical aspects of our model.

2.2 Building the simple 0d model

In this section, we build the model for the evolution of melt pond coverage, and then solve it using realistic physical parameters. Before we proceed to build the quantitative model, we will first state the assumptions, and discuss the physical mechanisms driving pond evolution.

2.2.1 Assumptions of the model

Our model focuses on the stage of pond evolution when ice is highly permeable and all the meltwater created can be quickly removed to the ocean. The beginning of this stage can be identified as the point in time when the meltwater on the ice surface has drained to sea level, such that the remaining ponds correspond to places on the ice surface that are below sea level. We will assume that from this point on, the ponds are hydraulically connected with the ocean, and the only way for pond coverage to increase is for the points on the ice surface

which were above sea level to sink or melt below sea level. In reality, ponds can also grow through horizontal melting of their sidewalls. As some observations suggest that this type of growth is small at least on first year ice (Landy et al., 2014; Polashenski et al., 2012), we neglect it (see section 2.7.1 for further discussion). Furthermore, we will assume that all the melt occurs at the surface or the bottom of the ice. We thereby neglect the possibility of internal melt. We will also assume that ice has a uniform bulk density throughout the vertical column, and we discuss the effects of vertical non-uniformity in bulk density together with effects of internal melt in subsection 2.7.2. Finally, we will assume that the entire ice floe is in hydrostatic balance, rigid, and cannot tilt.

The main goal of our model is to determine the fraction of the ice surface above sea level that falls below sea level after some time. Therefore, we focus on the vertical displacements of points on the surface of the ice in response to melt. To this end, we define the ice topography, $s(\vec{r})$, as the elevation of the ice surface above sea level at the point $\vec{r}$, and we define melt ponds as those regions where $s(\vec{r}) < 0$. There are two main reasons why the topography might change in response to ice melt:

1. First, the topography at a point $\vec{r}$ at the surface changes when ice at that point melts (Fig. 2.1a). Here, the rate of change of topography at a point depends only on local characteristics of that particular point. For this reason, we will call this type of motion "local." Points on the surface that melt locally move "downwards," i.e. to lower elevations above sea level.

2. Second, in order to maintain hydrostatic balance, the entire ice surface can shift up or down in response to mass being removed above or below sea level. Since we are assuming that the entire ice floe is in hydrostatic balance, melting any region of ice moves the entire floe as a rigid body (Fig. 2.1b). For this reason, we will call this type of motion the "rigid body" motion. Melting above sea level induces an upward rigid body motion, whereas melting below sea level induces a downward rigid body motion.

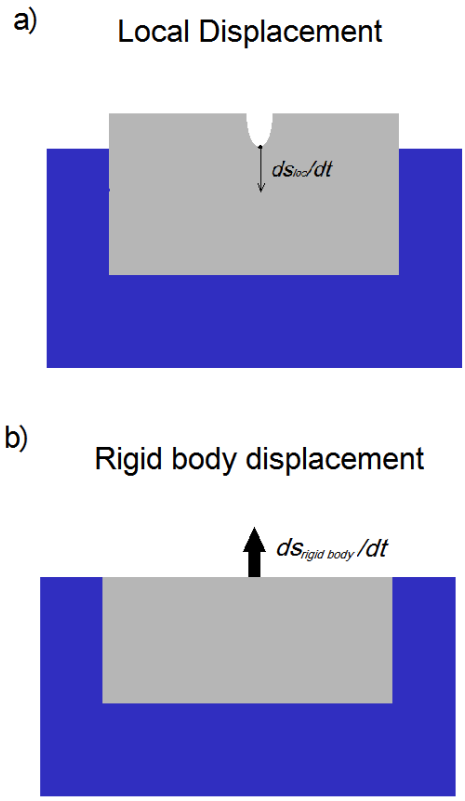

Figure 2.1: a) Local displacement represents the movement of a point on the ice surface as a result of ice melting at that particular point. It is a function only of local ice characteristics at that point. For both local and hydrostatic displacements the positive direction is defined as upwards. b) Rigid body displacement represents the motion of a floe as a whole in an effort to maintain hydrostatic balance because melting removes mass above or below sea level. Melting above sea level induces an upward motion of the floe, whereas melting below sea level induces a downward motion.

An ice floe is not a rigid body, but up to its flexural wavelength we can approximate it as such. As field studies did not record significant flexure of ice in the presence of melt ponds (Chris Polashenski, pers. comm.), the flexural wavelength is likely larger than the typical scale of melt ponds (roughly 10m), and the rigid body approximation is likely good.

At each point on the ice surface the change in elevation above sea level can be calculated as the sum of these two contributions.

In our model, ponds grow in two ways, "freeboard sinking" and "enhanced melting":

1. Freeboard sinking represents the average change in freeboard height (average height above sea level of bare ice). In this way the topography of ice above sea level remains unchanged. Freeboard sinking should not be confused with rigid body motion: the average freeboard height always decreases as a response to ice thinning, whereas the rigid body motion can point both upward and downward depending on whether mass is lost above or below sea level. Both rigid body motion and average local melting contribute to freeboard sinking.

2. Enhanced melting represents the change in the shape of the topography without changing its average height. Ponds can grow in this way if some regions melt faster than average. Therefore, a positive deviation in the local melt rate can grow ponds. Conversely, a negative deviation in the local melt rate can slow down or even reverse pond growth. Pond growth only occurs due to topography changes near sea level. Therefore, deviations from the mean melt rate for points high above the sea level do not influence pond evolution since these points are correlated with points close to sea level only through hydrostatic adjustment, which is determined by the average melt rates rather than the deviations from the average.

2.2.2 Equation for the evolution of topography

We now proceed to build the quantitative model of pond evolution. Following the above ideas, we divide the total rate of change of vertical position of the point $\vec{r}$ on the surface of the ice, $\frac{ds}{dt}(\vec{r})$, into a contribution from rigid body motion, $\frac{ds_{\text{rigid body}}}{dt}$, and a contribution from local melting, $\frac{ds_{\text{loc}}}{dt}(\vec{r})$,

$$\frac{ds}{dt}(\vec{r}) = \frac{ds_{\text{rigid body}}}{dt} + \frac{ds_{\text{loc}}}{dt}(\vec{r}) \ . \tag{2.1}$$

Ice above sea level must hydrostatically balance ice below sea level. We can write this

hydrostatic balance as

$$m_{\text{above s. l.}} = \frac{\rho_{\text{w}} - \rho_{\text{i}}}{\rho_{\text{i}}} m_{\text{below s. l.}} \ , \tag{2.2}$$

where $m_{\text{above s. l.}}$, and $m_{\text{below s. l.}}$ represent the mass of ice above and below sea level, and ρ_{w}, and ρ_{i} represent the densities of sea water and pure ice. Throughout the Chapter we use $\rho_{\text{w}} = 1025$ kg m^{-3} and $\rho_{\text{i}} = 916$ kg m^{-3}.

The mass above and below sea level can change either because the ice melts or because the floe moves as a rigid body, changing the proportion of ice above and below sea level. Therefore, differentiating Eq. (2.2) and splitting into melt and rigid body contributions, we find

$$dm^{\text{melt}}_{\text{above s. l.}} + dm^{\text{rigid body}}_{\text{above s. l.}} = \frac{\rho_{\text{w}} - \rho_{\text{i}}}{\rho_{\text{w}}} \left[dm^{\text{melt}}_{\text{below s. l.}} + dm^{\text{rigid body}}_{\text{below s. l.}} \right] \ , \tag{2.3}$$

where $dm^{\text{melt/rigid body}}_{\text{above/below s. l.}}$ represent changes in mass above and below sea level due to either ice melting or the entire floe floating up or down.

The mass melted above and below sea level after some time dt is

$$\begin{aligned} dm^{\text{melt}}_{\text{above s. l.}} &= -A_{\text{bi}} \frac{\overline{F}_{\text{bi}}}{l} dt \ , \\ dm^{\text{melt}}_{\text{below s. l.}} &= -A_{\text{mp}} \frac{\overline{F}_{\text{mp}}}{l} dt - A \frac{\overline{F}_{\text{bot}}}{l} dt \ , \end{aligned} \tag{2.4}$$

where $l = 334$ kJ kg^{-1} is the latent heat of melting, $\overline{F}_{\text{bi}}$ is the total energy flux used for melting bare ice averaged over all bare ice, $\overline{F}_{\text{mp}}$ is the total energy flux used for melting ponded ice averaged over ponded ice, $\overline{F}_{\text{bot}}$ is the total energy flux used for melting the ice bottom averaged over the ice bottom, A_{bi}, A_{mp}, and A are the area of bare ice, the area of melt ponds, and the area of the entire floe.

Since floating up or down does not change the total mass of the ice, mass changes above and below sea level due to rigid body motion are equal with an opposite sign, $dm^{\text{rigid body}}_{\text{above s. l.}} = -dm^{\text{rigid body}}_{\text{below s. l.}}$. We can express $dm^{\text{rigid body}}$ in terms of rigid body displacement of the floe

as

$$\begin{aligned} dm^{\text{rigid body}}_{\text{above s. l.}} &= \rho_b A_{\text{bi}} ds_{\text{rigid body}} \ , \\ dm^{\text{rigid body}}_{\text{below s. l.}} &= -\rho_b A_{\text{bi}} ds_{\text{rigid body}} \ , \end{aligned} \tag{2.5}$$

where ρ_b is the bulk ice density. This is the density of sea ice once all the brine has drained and is always less than ρ_i. We assume it to be uniform throughout the vertical ice column, but discuss the effects of vertical variations in ρ_b in section 2.7.2.

Substituting Eqs. (2.4) and (2.5) into Eq. (2.3), solving for $ds_{\text{rigid body}}$, and differentiating with respect to time, we find the rate of change of surface topography due to rigid body motion to be

$$\frac{ds_{\text{rigid body}}}{dt} = \left[\frac{\rho_{\text{i}}}{\rho_{\text{w}}}\frac{\overline{F}_{\text{bi}}}{l\rho_b}\right] - \left[\frac{\rho_{\text{w}}-\rho_{\text{i}}}{\rho_{\text{w}}}\frac{A_{\text{mp}}}{A_{bi}}\frac{\overline{F}_{\text{mp}}}{l\rho_b}\right] - \left[\frac{\rho_{\text{w}}-\rho_{\text{i}}}{\rho_{\text{w}}}\frac{A}{A_{\text{bi}}}\frac{\overline{F}_{\text{bot}}}{l\rho_b}\right] . \tag{2.6}$$

The three terms in large square brackets correspond to topography change due to bare ice melting, ponded ice melting, and ice bottom melting. Rigid body motion depends only on spatially averaged energy fluxes, which in turn depend on parameters such as the average insolation on the floe, the average albedo, and the average longwave, sensible, latent and bottom heat fluxes. If bare and ponded ice melt only from energy absorbed by the upper surface of the ice, the fluxes $\overline{F}_{\text{bi}}$, and $\overline{F}_{\text{mp}}$ can also be written in terms of albedo as:

$$\begin{aligned} \overline{F}_{\text{bi}} &= (1-\alpha_{\text{bi}})F_{\text{sol}} + F_{\text{r}} \ , \\ \overline{F}_{\text{mp}} &= (1-\alpha_{\text{mp}})F_{\text{sol}} + F_{\text{r}} \ , \end{aligned} \tag{2.7}$$

where α_{bi} and α_{mp} are the average albedos of bare and ponded ice, F_{sol} is the solar flux, and F_{r} is equal to the sum of net longwave, net sensible, and net latent heat fluxes. This parameterization neglects light transmission, and assumes that all of the energy is deposited in the surface. Much of the variation in albedo of ponded ice is due to the fact that the pond

bottom is partially transparent, and energy is deposited in the ocean instead of directly in the ice, from where it is eventually used to melt the ice bottom. However, this does not make much difference in our model since the energy deposited in the ocean is likely used for melting ice below sea level anyway.

Local displacement, $ds_{\rm loc}$, quantifies how much the ice surface topography changes as a result of local melt. We can determine the local melt rate from $F_{\rm surf}(\vec{r})$, the flux of energy used for melting the ice surface at a point $\vec{r}$

$$\frac{ds_{\rm loc}}{dt}(\vec{r}) = -\frac{F_{\rm surf}(\vec{r})}{l\rho_b} \ , \tag{2.8}$$

where the positive direction is defined as upwards. The local flux depends on parameters such as the local albedo, the local insolation, the local longwave, sensible and latent heat fluxes, and the angle between ice and incoming radiation at that point.

The flux $F_{\rm surf}(\vec{r})$ averaged over all the points on the surface of the ice above sea level equals $\overline{F}_{\rm bi}$

$$\langle F_{\rm surf}(\vec{r})\rangle = \overline{F}_{\rm bi} \ , \tag{2.9}$$

where $\langle ...\rangle$ represents averaging over all the points on bare ice. For this reason, we will parameterize the rate of local melting as

$$\frac{ds_{\rm loc}}{dt}(\vec{r}) = -k(\vec{r})\frac{\overline{F}_{\rm bi}}{l\rho_b} \ , \tag{2.10}$$

where $k(\vec{r})$ is a non-dimensional number that quantifies the deviation of the melt rate at the point $\vec{r}$ from the mean melt rate of the bare ice surface, which depends on the detailed conditions of ice and its environment. The parameter k could be either greater than or less than one. Here we will take k to be constant in time, but in reality it need not be. Finally, according to Eq. (2.1) we add Eq. (2.6) and Eq. (2.10) to get the equation for the evolution

of the bare ice topography. We express this in terms of melt pond fraction, $x \equiv \frac{A_{\mathrm{mp}}}{A}$

$$\begin{aligned}\frac{ds}{dt}(\vec{r}) = &-\left[(k(\vec{r})-1)\,\frac{\overline{F}_{\mathrm{bi}}}{l\rho_b}\right]- \\ &-\left[\frac{\rho_w-\rho_i}{\rho_w}\frac{1}{l\rho_b}\left(\overline{F}_{\mathrm{bi}}+\frac{x}{1-x}\overline{F}_{\mathrm{mp}}+\frac{1}{1-x}\overline{F}_{\mathrm{bot}}\right)\right]\ .\end{aligned} \tag{2.11}$$

Here, we split the equation into two terms, enclosed by the square brackets. The first term represents the local deviation from the average surface melt rate, which changes the general shape of the topography while preserving its average height above sea level. We identify this term with enhanced melting. The second term represents a global shift of the average elevation above sea level due to freeboard sinking.

In this way, the topographic evolution equation can be split into two terms: enhanced melting, and freeboard sinking:

$$\frac{ds}{dt} = \frac{ds_{\mathrm{em}}}{dt} + \frac{ds_{\mathrm{fs}}}{dt}\ , \tag{2.12}$$

where $\frac{ds_{\mathrm{em}}}{dt}$, and $\frac{ds_{\mathrm{fs}}}{dt}$ are contributions from enhanced melting, and freeboard sinking, and correspond to the first and second term of Eq. (2.11).

2.2.3 Model for the evolution of pond coverage

We now need to relate the vertical displacements near the sea level to the change in area of the melt ponds. To this end we define the hypsographic curve, $s(x_h)$, which relates the elevation above sea level, s, to the percent of ice surface below that elevation, x_h (Fig. 2.2). Such curves have been measured and reported on several occasions (e.g. Fig. 8 of Eicken et al. (2004), or Fig. 8 of Landy et al. (2014)). If the ice is highly permeable, the melt pond fraction, x, can be inferred from a hypsographic curve as the intersection of sea level with the curve. Since ponds are hydraulically connected with the ocean, the average freeboard height of bare ice, h, depends on the pond fraction. The average freeboard height, h, can be

expressed in terms of the ice thickness H and the pond fraction as

$$h = \frac{\rho_w - \rho_i}{\rho_w} \frac{H}{1-x} \ . \tag{2.13}$$

Here, the average freeboard height is defined as the elevation of the ice surface above sea level averaged over bare ice. For two ice floes of the same thickness, the one with higher pond coverage will also need to have a higher average freeboard in order to maintain hydrostatic balance.

The above sea level part of every measured hypsographic curve we tested can be fit relatively well with a tangent function (Fig. 2.2a, red line). We will assume that this fit holds for a wide range of different sea ice floes, and use it to initialize our model with different physical parameters. We give the exact form of this function in appendix A (Eq. 2.35). To get a hypsographic curve for a particular initial pond fraction, x_i, and ice thickness, H, we set it to zero at the initial pond coverage, $s(x_h = x_i) = 0$, and rescale it vertically to get a freeboard that hydrostatically balances the floe. The topography below sea level is not important for the evolution of pond coverage if the pond coverage grows, and we replace it with a straight line.

We show several curves for different initial ice thickness and initial pond coverage in Fig. 2.2b and Fig. 2.2c. We note that the initial pond fraction, x_i, corresponds to the pond fraction when ice first becomes permeable. Once we choose x_i and H, the tangent function Eq. (2.35) has only two unconstrained parameters, p_1 and p_2, that determine the exact shape of the curve. Knowing additional physical parameters, such as ice roughness, we can constrain additional parameters of this curve. Throughout this Chapter we will mostly use p_1 and p_2 that fit the measurements of the hypsographic curve made by Landy et al. (2014) for June 25th of 2011 or the measurements made during the SHEBA (Surface Heat Budget of the Arctic Ocean) mission (Uttal et al., 2002) along the topography profile "1" on July 10th 1998. However, when examining the effects of sea ice roughness, we will vary these

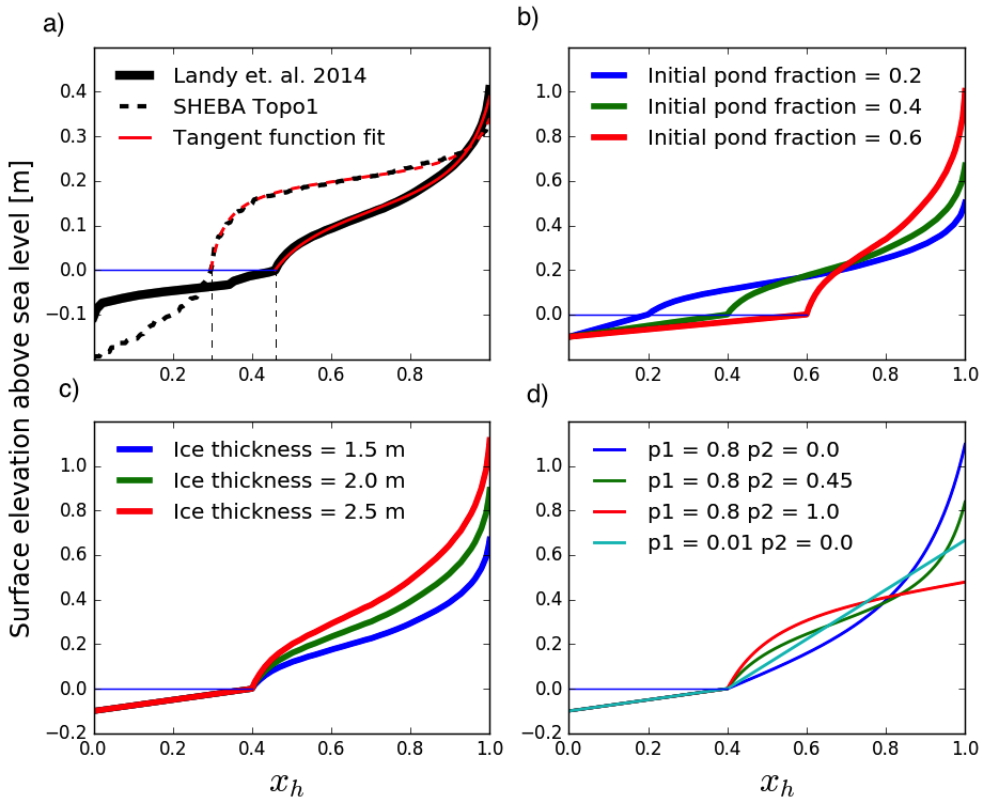

Figure 2.2: Hypsographic curves showing the percentage of the sea ice surface that is lower than a particular elevation. Pond coverage on highly permeable sea ice can be inferred from here as the intersection of sea level (horizontal blue line) with the hypsographic curve. a) A hypsographic curve measured by Landy et al. (2014) on June 25th of 2011 (solid black line), and a hypsographic curve measured during SHEBA along a 100m long "topography profile 1" on July 10th 1998 (black dashed line). The vertical dashed lines represent the pond coverage, assuming that ice is permeable. The red line represents a fit to the part of the hypsographic curve above sea level with a tangent function, Eq. (2.35). b) Adjusted hypsographic curves for different initial pond coverage, and the same ice thickness. c) Adjusted hypsographic curves for the same initial pond coverage and different ice thickness. d) Hypsographic curves for different shape parameters, p_1 and p_2, defined and discussed in appendix A, Eq. (2.35). Parameter p_1 controls the amount of curvature, while p_2 controls the position of the inflection point of the tangent function.

parameters to get curves of different shape. Several examples of hypsographic with different p_1 and p_2 are shown in Fig. 2.2d.

In the case of pure freeboard sinking the overall shape of the hypsographic curve does not change as the ice melts. Instead the whole curve is shifted following a displacement of $ds_{\rm fs}$ (Fig. 2.3a). We can calculate the resulting change in pond coverage as

$$\frac{dx}{dt} = \frac{dx_h}{ds}(x)\frac{ds_{\rm fs}}{dt} \ , \tag{2.14}$$

where $ds_{\rm fs}$ is the vertical displacement of the bare ice topography due to freeboard sinking (as determined by the second term in Eq. (2.11)), and $\frac{dx_h}{ds}(x)$ is the change in pond fraction for a vertical shift of the ice surface of $ds_{\rm fs}$ when the pond fraction is equal to x. It is equal to the reciprocal of the derivative of the hypsographic curve, $s(x_h)$, evaluated at $x_h = x$. Substituting $\frac{ds_{\rm fs}}{dt}$ from Eq. (2.11) we find

$$\frac{dx}{dt} = \frac{d\hat{x}_h}{d\hat{s}}(x)\Big[S_{\rm bi} + S_{\rm mp}\frac{\widehat{x}}{\widehat{1-x}} + S_{\rm bot}\frac{1}{\widehat{1-x}}\Big] \ , \tag{2.15}$$

where $\widehat{x} \equiv \frac{x}{x_i}$, and $\widehat{1-x} \equiv \frac{1-x}{1-x_i}$ are the pond and bare ice fractions normalized by the initial pond and bare ice fractions, $\frac{d\hat{x}_h}{d\hat{s}}(x) \equiv \frac{h}{1-x_i}\frac{dx_h}{ds}(x)$ is the non-dimensional slope of the hypsographic curve, and we have defined the strengths of pond growth by freeboard sinking due to melting bare, ponded, and ice bottom, $S_{\rm bi}$, $S_{\rm mp}$, and $S_{\rm bot}$ as

$$\begin{aligned} S_{\rm bi} &\equiv \frac{(1-x_i)^2\overline{F}_{\rm bi}}{Hl\rho_b} \ , \\ S_{\rm mp} &\equiv \frac{(1-x_i)x_i\overline{F}_{\rm mp}}{Hl\rho_b} \ , \\ S_{\rm bot} &\equiv \frac{(1-x_i)\overline{F}_{\rm bot}}{Hl\rho_b} \ . \end{aligned} \tag{2.16}$$

The non-dimensional factors $\widehat{x}$, $\widehat{1-x}$, and $\frac{d\hat{x}_h}{d\hat{s}}(x)$ are chosen to be of the order unity, so that $S_{\rm bi}$, $S_{\rm mp}$, and $S_{\rm bot}$ control the strengths of pond growth by melting bare ice, melting ponded

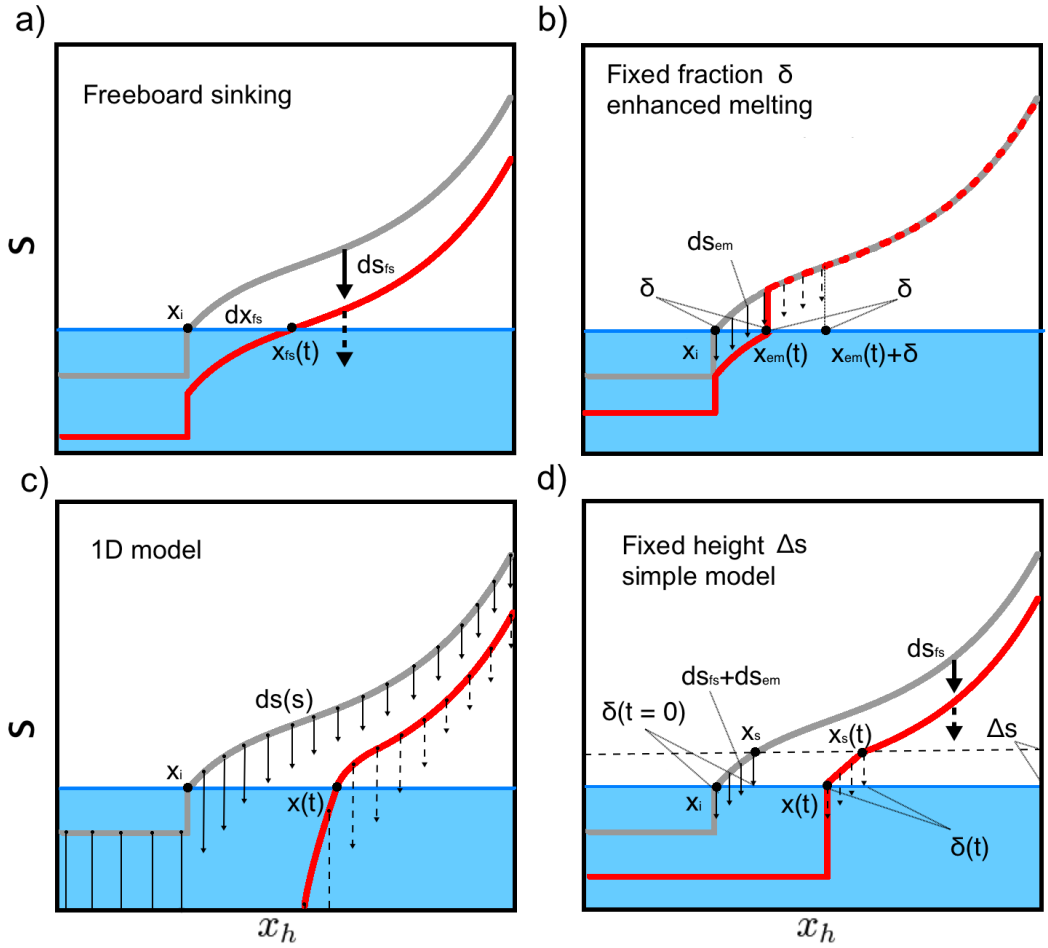

Figure 2.3: Explanation of different models of pond growth. Models evolve a hypsographic curve, $s(x_h)$, above sea level to find the pond coverage evolution. Evolution of the hypsographic curve below sea level is not relevant for pond growth and, apart from the 1d model, is not captured well in these models. a) Freeboard sinking shifts the entire hypsographic curve downward following a displacement of ds_{fs}. b) Enhanced melting acts on a constant ice fraction, δ, and there is no freeboard sinking. The hypsographic curve changes only between $x_h = x$ and $x_h = x + \delta$, and remains unchanged otherwise. After a time $\Delta t = \frac{s(x+\delta)}{ds_{\mathrm{em}}/dt}$ pond coverage grows by δ. The 0d model, Eq. (2.25), assumes that the total pond evolution is the sum of pond evolution due to such enhanced melting and freeboard sinking (panel a). c) The 1d model prescribes a melt rate at each point on the hypsographic curve as a function of height above sea level, $\frac{ds}{dt}(s)$. d) A simplified model that assumes both freeboard sinking and enhanced melting (appendix B). Enhanced melting occurs only below height Δs. After some time, the fraction of ice affected by enhanced melting, δ, becomes constant, meaning that a constant fraction model (panel b) and a constant height model are equivalent if δ and Δs are related appropriately.

ice, and melting ice bottom. The reciprocals of the strengths represent the timescales of the growth modes.

The set of parameters needed to describe pure freeboard sinking can be further reduced by rewriting Eq. (2.15) as

$$\frac{dx}{dt} = \frac{d\hat{x}_h}{d\hat{s}}(x)\Big[S_1 \frac{\widehat{x}}{\widehat{1-x}} + S_2 \frac{1}{\widehat{1-x}}\Big] , \tag{2.17}$$

where $S_1 \equiv S_{\rm mp} - x_i S_{\rm bi}/(1-x_i)$ and $S_1 \equiv S_{\rm bot} + S_{\rm bi}/(1-x_i)$ represent a minimal set of parameters needed to describe pure freeboard sinking. However, these parameters do not have a clear physical interpretation, and we will henceforth focus only on $S_{\rm bi}$, $S_{\rm mp}$, and $S_{\rm bot}$.

Next we need to consider the contribution from enhanced melting. Before doing so we need to make some assumptions about the nature of enhanced melt. There are multiple physical processes that can cause the melt rate to deviate from the mean. One process that stands out as being particularly important is albedo decrease due to ice wetting: ice close to sea level will likely be wet and therefore have a lower albedo compared to ice higher up. The deviation from the mean melt rate in this case depends primarily on the height above sea level. Another potential contribution to height-dependent enhanced melt may effectively come from random fluctuations in the melt rate around the average: ice near the sea level has a higher probability of falling below sea level due to random fluctuations than ice higher up. After falling below sea level, ice becomes ponded, melts faster, and is unable to return to its previous position. Other processes, such as lateral melt, may not depend on height above sea level, but for now we neglect this possibility (see section 2.7.1 for discussion).

Because of the processes described above, we will assume that the deviation from the mean melt rate, $k(\vec{r}) - 1$, depends only on height above sea level, s. In this scenario, we need to consider enhanced melting together with freeboard sinking, as freeboard sinking constantly supplies new ice to low elevations to be affected by enhanced melting. Effects of enhanced melting and freeboard sinking can be approximately separated if, instead of

height-dependence, enhanced melting is constrained to act on a fixed fraction of bare ice. In this case, a constant fraction of bare ice that would experience enhanced melting would evolve, at least approximately, independently of freeboard sinking.

Therefore, we will consider two cases of enhanced melting. Firstly, we will consider a height-dependent enhanced melting. In particular, we will assume that $k(0 < s < \Delta s) \equiv k$ and $k(s > \Delta s) \equiv 1$, where Δs is a height above which there is no enhanced melting and below which enhanced melting is constant $k > 1$. This is the case we ultimately wish to describe. We describe a potential model for pond growth under this assumption in appendix B and Fig. 2.3d. However, from a practical viewpoint, it is simpler to consider enhanced melting which acts upon a fixed fraction of bare ice. In this case, we will assume that $k(x < x_h < x + \delta) \equiv k$ and $k(x_h > x + \delta) \equiv 1$, where δ is a fraction of ice affected by enhanced melting (Fig. 2.3b). In appendix B, we show that, if δ is appropriately chosen, a height-dependent model and a fixed fraction model become equivalent. Therefore, we will first solve a model assuming a fixed δ and no freeboard sinking, and then relate it to a fixed Δs model by choosing the appropriate δ.

We note that the assumption that $k(\vec{r}) = 1$ high above the sea level and $k(\vec{r}) > 1$ near the sea level is strictly not true since averaged over all of bare ice $k(\vec{r})$ needs to equal one. However, it is approximately true if Δs or δ are small, such that the area where $k(\vec{r}) \neq 1$ is small compared to the total area of bare ice. Also, we have assumed $k(\vec{r}) = 1$ high above the sea level without loss of generality, since deviations from the mean melt rate high above the sea level are not important, as only ice close to sea level may become ponded.

Now we proceed to consider the case of "pure enhanced melting" that assumes a fixed fraction of the ice, δ, melts, and there is no freeboard sinking (Fig. 2.3b). If there is no topographic variation above sea level, and the entire ice floe above sea level has the same height, h, the pond coverage would grow by δ after a time $\Delta t = \frac{h}{ds_{\mathrm{em}}/dt}$, where ds_{em}/dt is the rate of change of topography due to enhanced melting as determined by the first term

of Eq. (2.11). Therefore, the pond growth rate in this case would be $\frac{\Delta x}{\Delta t} = \frac{\delta}{h}\frac{ds_{\rm em}}{dt}$. If there is non-negligible topography above sea level described by the hypsographic curve, the time Δt it takes for pond coverage to grow by δ, would be $\Delta t = \frac{s(x_h=x+\delta)}{ds_{\rm em}/dt}$. Here, $s(x_h = x + \delta)$ is the original hypsographic curve evaluated at $x_h = x + \delta$. We will assume this expression generally holds for enhanced melting. Thus, we arrive at the expression for pond growth due to pure enhanced melting with fixed δ

$$\frac{dx}{dt} = \frac{\delta}{s(x+\delta)}\frac{ds_{\rm em}}{dt} \ . \tag{2.18}$$

If δ is small compared to the variation in the hypsographic curve, we can substitute $s(x + \delta)$ with $s(x)$. This is only not justified near the beginning of the melt, when $s(x) \approx 0$. Substituting $\frac{ds_{\rm em}}{dt}$ from Eq. (2.11) we find

$$\frac{dx}{dt} = S_{\rm em}\frac{1}{\hat{s}(x+\delta)} \ , \tag{2.19}$$

where $\hat{s}(x) \equiv \frac{s(x)}{h}$ is the non-dimensional hypsographic curve, and the strength of the enhanced melting, $S_{\rm em}$, is defined as

$$S_{\rm em} \equiv \frac{\rho_{\rm w}}{\rho_{\rm w} - \rho_{\rm i}}\frac{(1-x_i)\delta(k-1)\overline{F}_{\rm bi}}{Hl\rho_b} \ . \tag{2.20}$$

Ultimately, however, our goal was to describe the height-dependent enhanced melting. In appendix B, we showed that such a model can be approximated with a fixed fraction model, if we appropriately relate δ and Δs. Here we simply state the result

$$\delta = \frac{\rho_{\rm w}}{\rho_{\rm w} - \rho_{\rm i}}\frac{2\Delta s(1-x_i)^2}{3H(1+\frac{ds_{\rm em}}{ds_{\rm fs}})} \ . \tag{2.21}$$

Here, $\frac{ds_{\rm em}}{ds_{\rm fs}}$ represents the ratio of the topographic rate of change due to enhanced melting

to freeboard sinking and is given by

$$\frac{ds_{\rm em}}{ds_{\rm fs}} = \frac{\rho_w}{\rho_w - \rho_i} \frac{|\overline{F}_{\rm bi}|(k-1)}{|\overline{F}_{\rm bi}| + \frac{x_i}{1-x_i}|\overline{F}_{\rm mp}| + \frac{1}{1-x_i}|\overline{F}_{\rm bot}|} \ , \tag{2.22}$$

where $|\overline{F}|$ are the representative values of energy fluxes, e.g. their time-averages. Therefore, the strength of height-dependent enhanced melting becomes

$$S_{\rm em} = \Big(\frac{\rho_{\rm w}}{\rho_{\rm w} - \rho_{\rm i}}\Big)^2 \frac{2\Delta s(1-x_i)^3(k-1)\overline{F}_{\rm bi}}{3H^2 l \rho_b (1 + \frac{ds_{\rm em}}{ds_{\rm fs}})} \ . \tag{2.23}$$

We have made a number of assumptions in deriving the expression for enhanced melting. Below we compare this model to a more complicated "1d" model and show that all these assumptions are justified. We also show that if the function describing the local melt rate, $k(s)$, has a non-trivial dependence on height above sea level, parameter $S_{\rm em}$ is better replaced with a parameter

$$\langle S_{\rm em} \rangle \equiv \Big(\frac{\rho_{\rm w}}{\rho_{\rm w} - \rho_{\rm i}}\Big)^2 \frac{2(1-x_i)^3\overline{F}_{\rm bi}}{3H^2 l \rho_b} \int_0^\infty \frac{k(s)-1}{1 + \frac{ds_{\rm em}}{ds_{\rm fs}}(s)} ds \tag{2.24}$$

In this way, we have separated the effects of freeboard sinking and enhanced melting. Finally, we will assume that contributions from freeboard sinking and enhanced melting can be added independently. Therefore, we solve Eq. (2.15) for pure freeboard sinking, and Eq. (2.19) for enhanced melting independently, and add them together to get the full evolution of pond coverage, $x(t)$:

$$x(t) = x_{\rm fs}(t) + x_{\rm em}(t) - x_i \ , \tag{2.25}$$

where $x_{\rm fs}(t)$, and $x_{\rm em}(t)$ are solutions to Eq. (2.15), and Eq. (2.19), both forced using the same parameters, and initialized with the same initial pond fraction x_i. This concludes the 0d model.

Equation (2.25) represents a sum of solutions to two simple ordinary differential equa-

tions, in which the rate of change of pond fraction depends on the pond fraction. Here, we have reduced the number of parameters from the original ten (H, x_i, ρ_b, $\overline{F}_{\rm bot}$, $F_{\rm sol}$, $F_{\rm r}$, $\alpha_{\rm bi}$, $\alpha_{\rm mp}$, k, and Δs) to four ($S_{\rm bi}$, $S_{\rm mp}$, $S_{\rm bot}$, and $S_{\rm em}$). The strengths of freeboard sinking, $S_{\rm bi}$, $S_{\rm mp}$, and $S_{\rm bot}$, depend only on the parameters that are available in GCM simulations, and are relatively easily measured in observational studies. The enhanced melting strength, $S_{\rm em}$, however, also depends on the difficult-to-measure parameters k and Δs that describe the melt rate near the sea level, and may also have contributions from processes that are not height dependent. Furthermore, as we discuss below, ice roughness can also play an important role in pond evolution. With reliable constraints on these parameters, our model would be a useful parameterization in GCMs for pond growth after ice becomes permeable.

2.2.4 Testing the model

In order to test the assumptions we made to simplify the model, we have developed a "1d" model in which we explicitly determine pond evolution when both freeboard sinking and enhanced melting are happening simultaneously. Apart from resolving the melt rates in one dimension, the underlying assumptions for the 1d model are essentially the same as for the simple model.

In the 1d model, we evolve the hypsographic curve by prescribing a melt rate, $ds_{\rm loc}$, to each point on the hypsographic curve depending on the height above sea level (Fig. 2.3c). The hypsographic curve high above sea level melts at a uniform rate, whereas the hypsographic curve slightly above sea level melts at an enhanced rate. Parts of the curve below sea level melt at a uniform rate determined by the flux used for melting ponded ice, $\overline{F}_{\rm mp}$. Finally, hydrostatic adjustment is calculated by finding the ice thickness directly at each time step, and placing the floe in hydrostatic balance. The evolution of pond coverage obtained from this model is shown in Fig. 2.4a. The comparison with the simple 0d model is excellent with a maximum deviation in pond coverage fraction of around 0.05. We note for

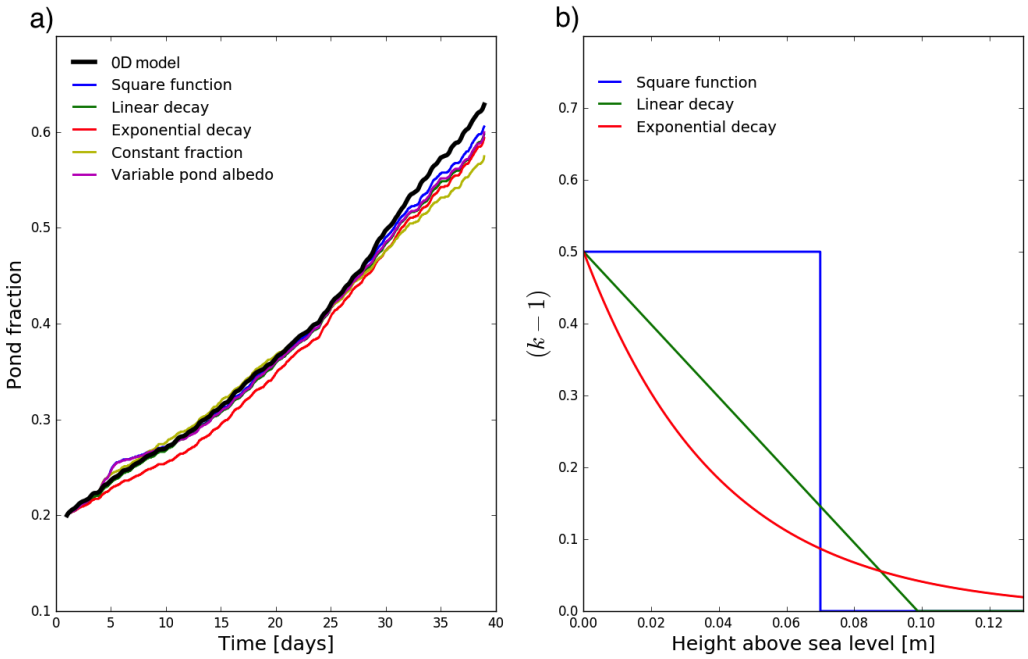

Figure 2.4: a) A comparison between pond evolution in the 0d model and the 1d model. The black curve represents the 0d model. The blue, green, and red curves represent the 1d model for different functions $k(s)$ shown in panel b). These different functions were chosen such that the integral parameter $\langle S_{\text{em}} \rangle$ (Eq. (2.24)) is the same as for the 0d model. The yellow curve represents the 1d model where enhanced melting acts on a constant fraction of bare ice, δ, chosen according to Eq. (2.21). The magenta curve represents the 1d model with pond albedo varying with depth. There is significant agreement between all of the curves, suggesting that the simplifications made in the simple model were justified. Since including variable pond albedo does not change the pond evolution significantly, this detail can be neglected when estimating the pond coverage on permeable ice. b) The blue, green, and red lines represent functions $k(s) - 1$ used to run the 1d model.

each parameter that enters the 0d model there exists a corresponding parameter that enters the 1d model, so the agreement between the 0d and the 1d model is achieved without any tuning.

The 1d model allows us some freedom to test the detailed assumptions of the 0d model. First, we can test how the functional form of $k(s)$ affects the pond evolution (Fig. 2.4b). The functions $k(s)$ were chosen such that they all have the same integral parameter $\langle S_{\mathrm{em}} \rangle$ defined in Eq. (2.24). Figure 2.4a shows that in each of these cases the evolution of pond coverage proceeds nearly identically. Second, we can test the difference between an assumption that enhanced melting acts below a constant height Δs and an assumption that enhanced melting acts on a constant fraction of ice, δ. The yellow line in Fig. 2.4a shows that if δ and Δs are chosen according to Eq. (2.21), both assumptions yield very similar results. Finally, we can test the effects of varying pond albedo. In reality pond albedo decreases as the ponds deepen. We assume a dependence of pond albedo on pond depth reported in Table VII of Morassutti and LeDrew (1996) for mean broadband albedo. The magenta line in Fig. 2.4a shows that allowing for pond albedo to vary has a negligible effect on pond evolution.

We should note that, when both freeboard sinking and enhanced melting occur simultaneously, the agreement between the 0d model and the 1d model becomes poor if the hypsographic curve is convex (e.g. Fig. 2.2d, blue curve), and the 0d model should be used with care. Happily, the measured hypsographic curves are mostly concave for pond coverage fractions at which pond evolution typically occurs, in which case the agreement between the two models is excellent.

2.3 A 0d model can approximate observations well using realistic parameters

In Fig. 2.5, we compare the results from our model to observations made on a 200m long albedo line during SHEBA (red line). An albedo line is a transect along which various

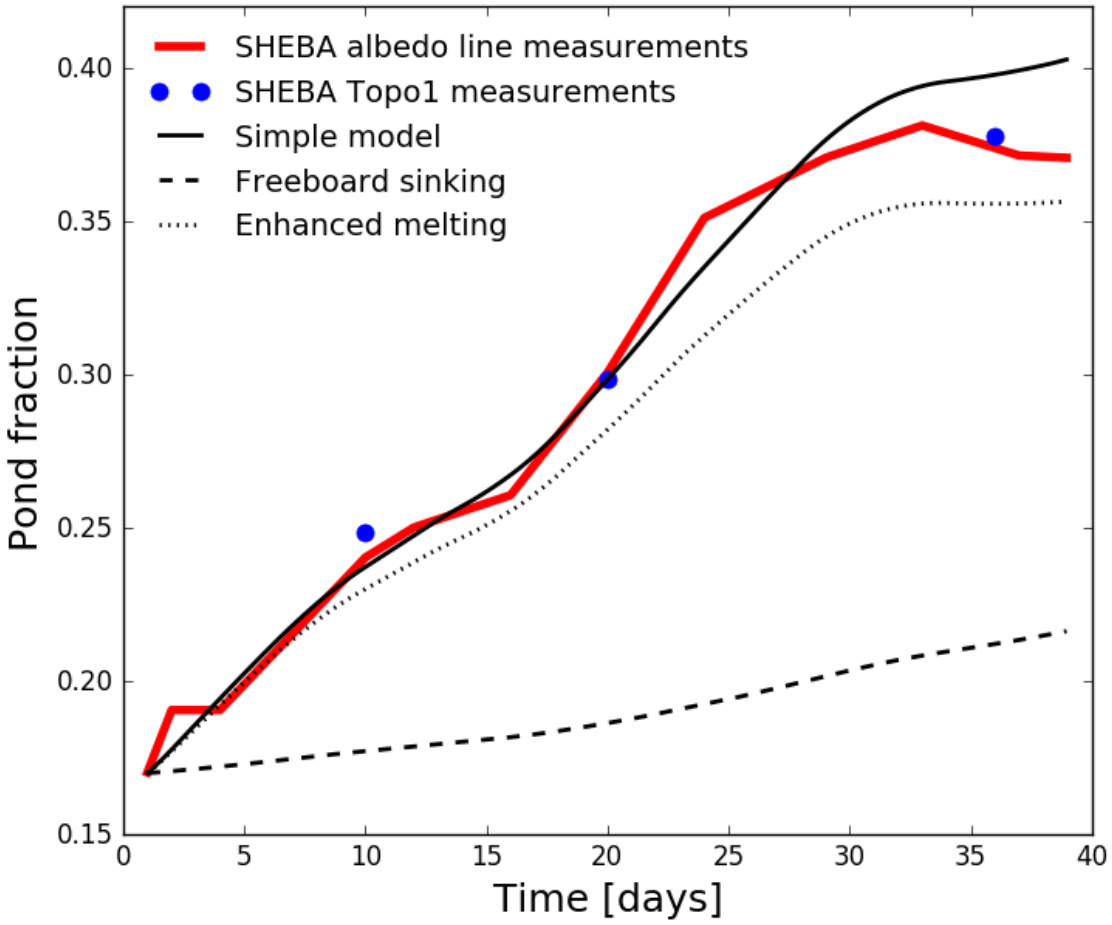

Figure 2.5: A comparison between measurements of pond fraction made during SHEBA along the albedo line (red line), along a topography profile (blue dots), and our model (black line). The blue dots have been shifted downward by 0.05 to make a more obvious comparison between albedo line and topography profile trends. The black dashed line is the contribution to our model from freeboard sinking and the black dotted line is the contribution from enhanced melting. Ponds grow almost entirely due to enhanced melting as a result of the steep topography of multiyear ice.

measurements including albedo are made in regular intervals of length. Ice along the albedo line was level multiyear ice, but the ponds drained to sea level after some time which makes them amenable to our model (Perovich et al., 2003). The pond coverage along the albedo line dropped to a minimum around the end of June. Therefore, we choose to model only the period after July 1st. In order to keep the albedo line pristine and not to interfere with the development of melt ponds, no holes were drilled through the ice along the albedo line in order to make ice thickness measurements. However, relatively close to the albedo line, topography measurements were made along a level multiyear ice profile roughly every ten days. After approximately July 10th, ponds along the topography profile also drained to sea level. We show the topography profile pond coverage in blue dots (we have artificially subtracted 0.05 from the pond coverage to facilitate comparison with the pond coverage along the albedo line). The pond coverage along the topography profile and along the albedo line follow roughly the same trend, suggesting that the physical parameters driving the pond evolution in the two places are likely similar. Based on the average freeboard height, we estimate the ice thickness on July 10th to be roughly 1.4m along the topography profile, meaning that on July 1st, ice thickness was around 1.6m. Therefore, we assume the same thickness for the ice along the albedo line, and use a hypsographic curve corresponding to the one measured along the topography profile on July 10th (Fig. 2.2a, dashed line). In order to run our model, we use the melt rates of bare ice, ponded ice, and ice bottom measured directly using ablation stakes during SHEBA (Perovich et al., 2003). We choose a realistic $\rho_b = 850$ kg m^{-3} (Timco and Frederking, 1996). We have no way of directly constraining the parameters Δs and k that control the strength of enhanced melting. Therefore, we treat S_{em} as a fitting parameter. Choosing $S_{\text{em}} = 0.22$ month^{-1} fits the observations well by eye. This value can be obtained using $\Delta s = 15$ cm and $k = 1.7$ which likely fall at the upper end of the range of reasonable values for these constants based on measurements of ice albedo as a function of height above sea level (see section 2.4 for details about this estimate). Such

a high value of S_{em} can possibly be explained by a significant contribution from lateral melting that is not height-dependent and, thus, does not enter our estimates of Δs and k based purely on albedo height-dependence.

The full black line in Fig. 2.5 represents a solution to the full Eq. (2.25). The agreement between model and observation is good, with a maximum discrepancy of 3% pond coverage at the end of the melt season. In particular, both the model and observed pond coverage grow by about 25% over a period of about 40 days after which the pond growth slows down. Even though we had some freedom to tune the model parameters, this comparison shows that our model is consistent with observations using realistic physical parameters. The dashed black line represents the contribution to pond growth due to freeboard sinking, whereas the dotted line corresponds to enhanced melting. Almost all pond growth in this case is due to enhanced melting. This is due to ice topography. On multiyear ice, meltwater typically collects in depressions formed by ponds in previous years. The topography created in this way is highly bimodal, and, after drainage, ponds typically have steep walls. Bare ice topography, on the other hand, is relatively smooth, preventing new pond formation. This is apparent in the hypsographic curve we used. Such a topography inhibits freeboard sinking, and pond coverage grows mostly by enhanced melting acting near the pond sidewalls, growing the existing ponds. In addition to height-dependent enhanced melting we introduced in the previous section, in this case there is likely a significant contribution from lateral melting as well. This contribution helps explain the high value of S_{em} we had to choose to get a close agreement between our model and observations. First year ice topography, on the other hand, permits ample pond growth through freeboard sinking. Observations suggest that on first year ice ponds grow primarily due to freeboard sinking (Landy et al., 2014; Polashenski et al., 2012).

2.4 Numerical solutions

We now solve Eq. (2.25) numerically to gain intuition about the behavior of our model. We use a set of realistic parameters we will henceforth refer to as the "default parameters."

For shortwave, longwave, latent, and sensible heat fluxes, we use values inferred by Skyllingstad et al. (2009) using hourly measurements from the SHEBA mission. We use the bottom heat flux inferred from measurements of ice bottom ablation during the SHEBA mission (Perovich et al., 2003). The albedo of bare ice can vary between 0.5 and 0.7 (Hanesiak et al., 2001), while the albedo of melt ponds can vary between 0.1 and 0.6, depending on pond depth and conditions of ice at the pond bottom (Morassutti and LeDrew, 1996; Perovich, 1996; Perovich et al., 1998). Here we prescribe a default bare ice albedo of 0.55, and a default pond albedo of 0.2. We use a realistic bulk ice density of $\rho_b = 850$ kg m^{-3} (Timco and Frederking, 1996). We use an initial ice thickness of 1.5 m, and use the first year ice topography measured by Landy et al. (2014) adjusted for the prescribed ice thickness and initial pond fraction (usually $x_i = 0.2$). We will assume enhanced melting is entirely due the albedo dependence on height above sea level. Some preliminary results based on field measurements of bare ice albedo on first year ice suggest that albedo changes from around 0.3 near sea level to around 0.55 at a height of around 10 cm above sea level, after which the correlation between albedo and surface elevation tapers off (Chris Polashenski, pers. comm.). Using such an albedo and the average values of shortwave, longwave, latent, and sensible heat fluxes, we can estimate the rate of melt as a function of height above sea level, $k(s) = \frac{\overline{F}(s)}{\overline{F}_{\text{bi}}}$. Using Eq. (2.24), we can then find the integral parameter $\langle S_{\text{em}} \rangle$. We choose $\Delta s = 6$ cm and $k = 1.7$ to correspond to the same integral parameter. We should note that there is significant scatter in the data, and measurements correspond to only one study. Therefore, this is a rough estimate of enhanced melting, but it is likely of the correct order of magnitude.

Figure 2.6a shows the solution to Eq. (2.25) for different initial conditions. We can

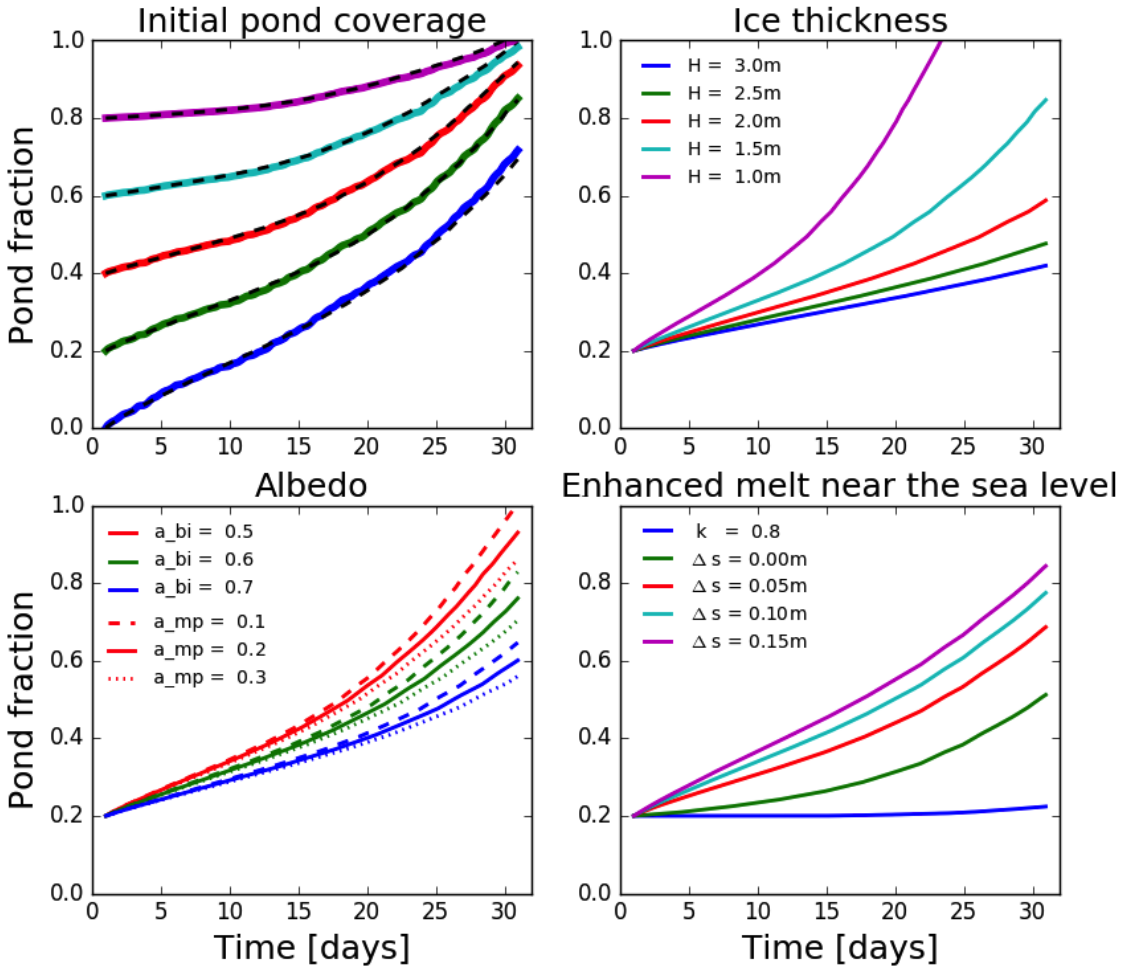

Figure 2.6: Numerical solutions to Eq. (2.25) with parameters varied around the defaults described in the text. a) Varying initial pond coverage. Solid lines represent solutions using full time-varying fluxes, while dashed lines represent solutions using time-averaged fluxes. The two solutions are very similar, so we subsequently use only the time-averaged fluxes. b) Varying ice thickness. Ponds grow slower on thicker floes. c) Varying pond and bare ice albedo. Different colors represent different bare ice albedos, and full, dotted, and dashed lines represent different pond albedos. A change in bare ice albedo has a much larger effect on pond fraction than the same change in pond albedo. d) Varying the Δs and k. For $k = 0.8$, the ponds shrink. However, pond evolution for $k < 1$ is not represented well in our model, so this curve serves only as an illustration.

see that ponds grow more rapidly when the initial pond coverage is lower, and the pond evolution curves cluster together as time progresses. This is because lower initial pond coverage corresponds to lower initial freeboard height, making the pond growth more rapid. The dashed line corresponds to the solution using the fluxes time-averaged over the 30 day run. The solutions using the averaged fluxes are very similar to the ones using time-varying fluxes, meaning that daily, and even monthly variations in the forcing have little effect on pond growth. This insensitivity to short time scale variations in the forcing means that pond coverage evolution may be faithfully represented in the large scale models, as it would not be affected by the coarse time scales of those models. Henceforth, we will use the time-averaged fluxes.

A larger ice thickness means a higher freeboard. For this reason, ponds grow more slowly on thicker ice. Because the pond growth rate is inversely proportional to ice thickness, pond coverage is more sensitive to variations in ice thickness when the ice is thin (Fig. 2.6b). In Fig. 2.6b we see that a 0.5 m difference in the initial ice thickness (between a floe 1.5m and a floe 2m thick) can mean a 20% difference in pond coverage at the end of the melt season.

Figure 2.6c shows the dependence of pond coverage on albedo. A variation of 0.1 in bare ice albedo has a much larger effect on pond evolution than the same change in pond albedo. The reason is that melting ponded ice only affects pond coverage through downward rigid body motion of the floe, whereas melting bare ice grows the ponds through both enhanced melting and freeboard sinking. Furthermore, when pond coverage is low, rigid body motion due to ponded ice melting is less efficient than that due to bare ice melting because it is proportional to melt pond fraction.

The parameters controlling the strength of enhanced melting are the least constrained parameters in our model. In Fig. 2.6d we show the dependence of pond evolution on the height below which enhanced melting is active, Δs. Exploring a range of realistic values for Δs, $0 < \Delta s < 15$ cm, we find that the pond fraction at the end of the melt season can vary by

about 30%. This difference would be larger if we chose a smaller ice thickness. The effects of changing k are relatively small, so long as k is large enough (not shown). For example, using current parameters, pond coverage evolution becomes fairly insensitive to k when $k > 1.5$. Smaller values of k, however, can significantly impact pond evolution. If k is enough smaller than 1, S_{em} can become negative, and the pond coverage can stop growing. In this case, ice near the sea level melts slowly enough such that an upward rigid body movement due to melting ice high above sea level pushes the ice near sea level upwards, preventing pond coverage growth. The evolution of such a pond coverage cannot be represented well in our model since the equation for enhanced melting becomes invalid in this case, and the blue curve in Fig. 2.6d serves therefore simply as an illustration.

2.5 Pond evolution is slower on smoother ice

The evolution of pond coverage in our model depends on the detailed shape of the hypsographic curve which is not captured by the strengths of freeboard sinking and enhanced melting. As we show below, pond coverage is sensitive to such details, and in particular to ice roughness. Below we will introduce the "effective strengths", S^*, which approximately capture the effects of roughness and allow us to estimate mean pond coverage after a period of time. Using effective strengths, we will demonstrate how multiyear ice topography suppresses pond growth by freeboard sinking, while first year ice topography permits it.

In the tangent function parameterization, Eq. (2.35), the exact shape of the hypsographic curve is determined by parameters p_1 and p_2. Here, we will not discuss these parameters individually, but will rather focus on often measured bare ice roughness, σ, defined as the standard deviation of surface elevation of ice above sea level:

$$\sigma \equiv \left(\frac{\int_{x_i}^{1} s^2(x_h) dx_h}{1 - x_i} - h^2 \right)^{\frac{1}{2}} . \tag{2.26}$$

We will use the non-dimensional form of bare ice roughness, defined as $\hat{\sigma} \equiv \frac{\sigma}{h}$. Typically, a concave hypsographic curve (e.g. Fig. 2.2d, red curve) will have a small $\hat{\sigma}$, whereas a convex hypsographic curve (e.g. Fig. 2.2d, blue curve) will have a high $\hat{\sigma}$.

During the permeable stage, all else equal, ponds will grow more rapidly on rougher ice, since a larger fraction of ice is close to sea level. This is not true on impermeable ice, as meltwater filling deep topographic lows on rough ice will cover a smaller area relative to the same amount of meltwater filling shallow topographic lows on smooth ice. For this reason, the initial pond coverage will likely be smaller on rougher ice due to a smaller pond coverage during the impermeable stage.

Figures 2.7 show the pond coverage evolution due to pure freeboard sinking (Fig. 2.7a) and pure enhanced melting (Fig. 2.7c) for hypsographic curves with different parameters p_1 and p_2 and all other parameters kept constant. For each choice of p_1 and p_2, we find the normalized bare ice roughness, $\hat{\sigma}$, represented by the color of the curves. Blue colors correspond to low roughness and red colors to high roughness. Pond evolution on measured topographies (Fig. 2.2a) is also shown. We can see that although roughness does not fully determine the pond evolution, it is a viable proxy for how pond coverage will evolve, with high roughness curves typically having a higher average pond coverage.

We wish to quantify the effect of roughness by its impact on the mean pond coverage. In particular, we hope to find the "effective strengths", $S^*(\hat{\sigma})$, which include the roughness effects and allow us to easily estimate the average pond coverage after some time t

$$\langle x(t) \rangle \approx \frac{1}{2} S^* t + x_i \ , \tag{2.27}$$

where $\langle x(t) \rangle \equiv \frac{\int_0^t x(t) dt}{t}$. Effective strengths are proportional to strengths of freeboard sinking and enhanced melting we derived in section 2.2.3. In general they themselves may depend on time, and are time-independent only if pond coverage evolution is linear, $x(t) = St + x_i$, in which case $S^* = S$, where S is either $S_{\text{fs}} \equiv (S_{\text{bi}} + S_{\text{mp}} + S_{\text{bot}})$ in the case of freeboard

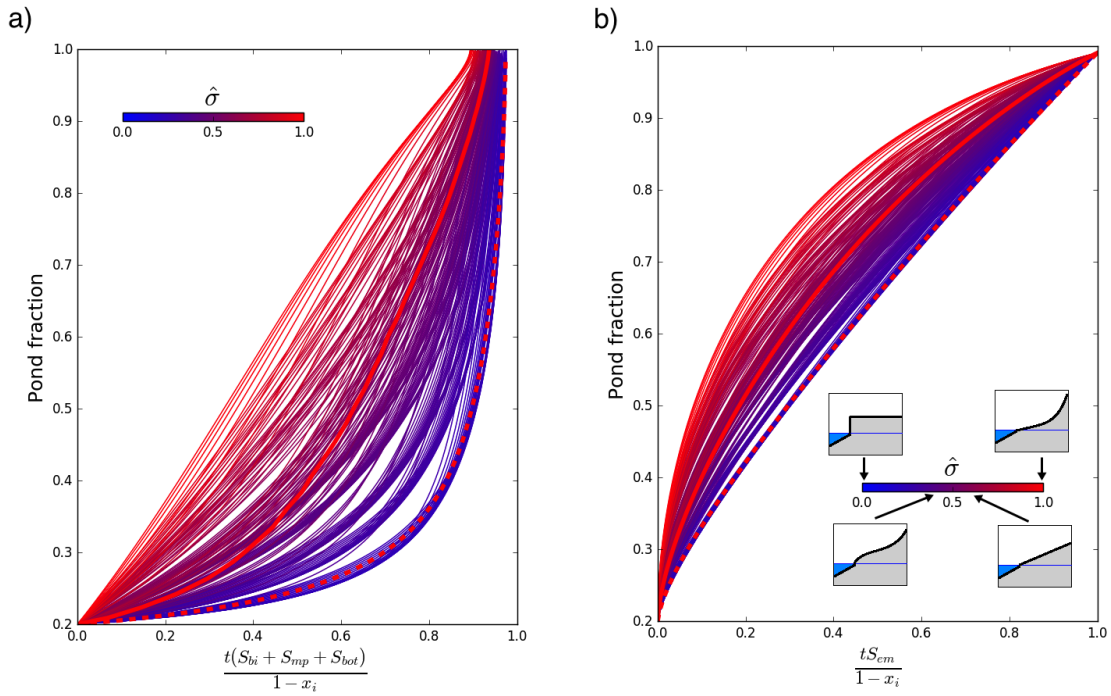

Figure 2.7: Exploring the effects of sea ice roughness. a) Pond evolution due to pure freeboard sinking for hypsographic curves with different shape parameters p_1 and p_2. The x-axis shows non-dimensional time $\hat{t} = \frac{t(S_{\text{bi}}+S_{\text{mp}}+S_{\text{bot}})}{1-x_i}$. Color represents normalized roughness, $\hat{\sigma}$, with blue colors corresponding to small $\hat{\sigma}$ and red colors corresponding to large $\hat{\sigma}$. Thick red solid line represents pond evolution on the measured first year ice hypsographic curve, and the thick red dashed line represents pond evolution on the measured multiyear ice hypsographic curve. All else equal, rougher ice has a larger pond fraction. b) Pond evolution due to pure enhanced melting for hypsographic curves with different shapes. The x-axis shows non-dimensional time $\hat{t} = \frac{tS_{\text{em}}}{1-x_i}$. Cartoon examples of hypsographic curves and their approximate positions along the $\hat{\sigma}$-axis are also shown.

sinking or S_{em} in case of enhanced melting.

In appendix C, we describe the procedure to estimate the effective strengths as functions of non-dimensional roughness and time. Here, we only state the result

$$\begin{aligned} S^*_{\mathrm{fs}} &\approx \left[1.3\hat{\sigma}^2\right]\left(S_{\mathrm{bi}} + S_{\mathrm{mp}} + S_{\mathrm{bot}}\right) \ , \\ S^*_{\mathrm{em}} &\approx \left[1 + \left(\frac{2}{\sqrt{\hat{t}_{\mathrm{em}}}} - \frac{3}{2}\right)\hat{\sigma}\right] S_{\mathrm{em}} \ , \end{aligned} \tag{2.28}$$

where S^*_{fs} is the effective strength of freeboard sinking, S^*_{em} is the effective strength of enhanced melting, and $\hat{t}_{\mathrm{em}} \equiv \frac{S_{\mathrm{em}} t}{1-x_i}$ is the non-dimensional time of pond evolution due to enhanced melting. The terms in square brackets represent the corrections due to roughness. If both freeboard sinking and enhanced melting occur simultaneously the total effective strength is the sum of these two, $S^* = S^*_{\mathrm{fs}} + S^*_{\mathrm{em}}$. Knowing the effective strengths, allows us estimate the mean pond coverage after a period of time without having to run the model.

Roughness has a different effect on freeboard sinking and enhanced melting. Freeboard sinking is roughly independent of time and proportional to the square of non-dimensional roughness. Therefore, it is very sensitive to variations in roughness: doubling the ice roughness roughly quadruples the mean pond coverage due to freeboard sinking after some time. Enhanced melting depends roughly linearly on roughness. However, as roughness tends to zero, the effective strength remains non-zero, $S^*_{\mathrm{em}}(\hat{\sigma} \to 0) \to S_{\mathrm{em}}$. Therefore, ponds on smooth ice grow primarily due to enhanced melting. Effective strength also depends on the non-dimensional time, $\hat{t}$, and is higher and more sensitive to variations in roughness early in the melt season.

Multiyear ice topography shown in Fig. 2.2a, dashed line, has $\hat{\sigma} \approx 0.25$ and is significantly smoother than first year ice topography shown in Fig. 2.2a, solid line, which has $\hat{\sigma} \approx 0.55$. From Eq. (2.28) it follows that freeboard sinking on multiyear ice is roughly 5 times less efficient in growing the ponds than on first year ice.

2.6 Analyzing the 0d model yields useful insight into factors influencing the pond evolution

Extracting the dependence of a desired property on physical parameters and understanding its scaling is the main strength of our model. These types of relationships would be difficult to obtain in a more complex model.

The parameters S^*_{bi}, S^*_{mp}, S^*_{bot}, and S^*_{em} control the mean rates of pond growth by melting different regions of ice. Roughly, they represent the amount of pond growth per unit time by freeboard sinking due to melting bare ice; freeboard sinking due to melting ponded ice; freeboard sinking due to melting ice bottom; and enhanced melting. Knowing these parameters allows us to estimate mean pond coverage after a period of time with significant accuracy without having to run any numerical models. Moreover, analyzing them can yield useful insight into the behavior of melt ponds under general circumstances.

We can estimate the change in magnitude of the strength of each of the growth modes when a physical parameters p changes by Δp as

$$\Delta S^*_i = \frac{\partial S^*_i}{\partial p} \Delta p \ , \tag{2.29}$$

where ΔS^*_i is the change in magnitude of the effective strength of the ith growth mode. This equation holds so long as the change in the physical parameter is not too large. A change in pond growth rate can then be estimated as $\Delta S^* = \sum_i \Delta S^*_i$. Then, using Eq. (2.27), we can roughly estimate a change in mean pond fraction, $\Delta\langle x\rangle$, after some time, Δt, following a change in physical parameter, p, as $\Delta\langle x\rangle \approx \frac{1}{2}\Delta S^* \Delta t$. This provides a means to estimate changes in mean pond coverage under different environmental conditions.

2.6.1 Ponds are more sensitive to changes in bare ice albedo than changes in pond albedo

We will illustrate the use of effective strengths using an example where we vary the ice and pond albedos. If the bare ice albedo changes by $\Delta\alpha_{\rm bi}$, the change in growth rate would be roughly

$$\Delta S^* = -\left[S^*_{\rm bi} + \frac{\frac{\rho_w-\rho_i}{\rho_w}(ds_{\rm em}/ds_{\rm fs})^2 + (k-1)}{(1+\frac{ds_{\rm em}}{ds_{\rm fs}})(k-1)} S^*_{\rm em}\right] \frac{F_{\rm sol}}{\overline{F}_{\rm bi}} \Delta\alpha_{\rm bi} \approx -0.9 \frac{1}{\rm month} \Delta\alpha_{\rm bi} \ . \quad (2.30)$$

On the other hand, if the melt pond albedo changes by $\Delta\alpha_{\rm mp}$, the change in growth rate would be roughly

$$\Delta S^* = -\left[S^*_{\rm mp} + \frac{(\rho_w-\rho_i)x_i(ds_{\rm em}/ds_{\rm fs})^2\overline{F}_{\rm mp}}{\rho_w(1+\frac{ds_{\rm em}}{ds_{\rm fs}})(k-1)(1-x_i)\overline{F}_{\rm bi}} S^*_{\rm em}\right] \frac{F_{\rm sol}}{\overline{F}_{\rm mp}} \Delta\alpha_{\rm mp} \approx -0.2 \frac{1}{\rm month} \Delta\alpha_{\rm mp} \ . \quad (2.31)$$

It follows from these estimates that after a month the mean pond fraction would differ by roughly 4.5% for a bare ice albedo difference of 0.1, and by around 1% for a pond albedo difference of 0.1. Therefore, variation in pond albedo affects pond evolution roughly five times less than variation in bare ice albedo. This explains our observation from Fig. 2.6c that pond evolution is much more sensitive to variations in bare ice albedo than to variations in pond albedo. In this way, we also extract the dependence of sensitivity on physical parameters. A major difference between the two sensitivities is their dependence on the initial pond coverage: the sensitivity to pond albedo is proportional to x_i, whereas the sensitivity to bare ice albedo is proportional to $1 - x_i$. In the above example we used $x_i = 0.2$, which explains most of the large difference between the two sensitivities. If the pond coverage were higher, variations in the pond albedo could become more important than variations in bare ice albedo. For example, assuming no enhanced melting, the sensitivity to pond albedo would become greater than the sensitivity to bare ice albedo at 50% pond coverage.

2.6.2 Under global warming, pond feedback could lead to significant ice thinning

We now use the effective strengths to roughly estimate the impact of global warming on the pond coverage. At high latitudes, feedbacks due to changes in albedo, the atmospheric lapse rate, and clouds can amplify the forcing due to global warming (Holland and Bitz, 2003). For this reason forcing at high latitudes is generally larger than direct radiative forcing due to an increase in CO_2 concentration. In a global warming scenario, the pond growth rate would increase because the ice melts faster, but also because ice at the beginning of the melt would be thinner. We can emulate a global warming scenario by increasing the flux F_r by a certain amount, ΔF_r, and by assuming that the initial ice thickness decreases by $\Delta H \equiv \frac{\partial H}{\partial F_r}\Delta F_r$, where $\frac{\partial H}{\partial F_r}$ is the ice thinning per 1 Wm^{-2} of warming. Therefore, we split the change in pond growth rate due to global warming, ΔS^*, into a contribution from direct forcing, ΔS^*_F, and a contribution from ice thinning, ΔS^*_H. Using the above formalism, we find

$$\begin{aligned}
\Delta S^*_F \equiv \sum_i \frac{\partial S^*_i}{\partial F_r}\Delta F_r &= \left[\frac{S^*_{\mathrm{bi}}}{\overline{F}_{\mathrm{bi}}} + \frac{S^*_{\mathrm{mp}}}{\overline{F}_{\mathrm{mp}}} + \frac{\frac{\rho_w-\rho_i}{\rho_w}(ds_{\mathrm{em}}/ds_{\mathrm{fs}})^2 + (k-1)(1-x_i)}{(1+\frac{ds_{\mathrm{em}}}{ds_{\mathrm{fs}}})(k-1)(1-x_i)}\frac{S^*_{\mathrm{em}}}{\overline{F}_{\mathrm{bi}}}\right]\Delta F_r \\
&\approx \frac{0.5\%}{\mathrm{W/m^2 \times month}}\Delta F_r \ , \\
\Delta S^*_H \equiv \sum_i \frac{\partial S^*_i}{\partial H}\frac{\partial H}{\partial F_r}\Delta F_r &= -\big(S^*_{\mathrm{bi}} + S^*_{\mathrm{mp}} + S^*_{\mathrm{bot}} + 2S^*_{\mathrm{em}}\big)\frac{1}{H}\frac{\partial H}{\partial F_r}\Delta F_r \\
&\approx \frac{1.9\%}{\mathrm{W/m^2 \times month}}\Delta F_r \ , \\
\Delta S^* \equiv \Delta S^*_F + \Delta S^*_H &\approx \frac{2.4\%}{\mathrm{W/m^2 \times month}}\Delta F_r \ .
\end{aligned} \tag{2.32}$$

The numbers in Eq. (2.32) were obtained using the default values of the parameters, and $\frac{\partial H}{\partial F_r} = -0.05\ \mathrm{m}^3\ \mathrm{W}^{-1}$ roughly estimated using the Eisenman and Wettlaufer (2009) model.

This means that global warming would increase mean pond coverage by roughly 1.2% per 1 Wm^{-2} of warming after a month's growth. Nearly half of this increase in the mean pond coverage comes from an increase in the strength of enhanced melting due to ice thinning. Simulating a 30 day melt numerically using our model predicts an increase in mean pond coverage with forcing at a rate of 1.5% per 1 Wm^{-2} of warming for small forcing ($\Delta F_r \approx 0$), which confirms the approximate validity of our linearization. For larger forcing, the sensitivity of pond coverage to forcing increases because the ice thins. Our linearized estimate, Eq. (2.32), also gives the dependence of the sensitivity on physical parameters. In a likely scenario where the forcing is around 10 Wm^{-2}, our estimate predicts that after a month mean pond coverage would increase by around 15%, which corresponds to around 12 cm of ice thinning solely due to the pond feedback. Ice thinning after a month directly due to forcing would be only around 9 cm, meaning that the pond feedback must be taken into account to understand ice thinning under global warming. Increased forcing could also lead to changes in initial pond coverage, changes in ice roughness or changes in Δs or k. We ignored these feedbacks, as we have no way of reliably estimating $\frac{\partial p}{\partial F_r}$ for these parameters.

2.6.3 Different growth modes yield different pond evolution

Each of the four growth modes has different effects on the pond coverage. We will now look in detail at each of the growth modes, their effect on the pond evolution, and their scaling with physical parameters. Figure 2.8 shows the dependence of growth rate on pond fraction and solutions to Eq. (2.25) when only one of the strengths is non-zero, assuming a first year ice topography. Figure 2.9 shows the evolution of pond coverage distribution when only one of the strengths is non-zero.

All modes of growth depend in the same way on the bulk ice density, ρ_b. Each of the strengths is inversely proportional to ρ_b, meaning that ponds grow faster on ice with a lower bulk density. The effect is, however, modest: within a reasonable range of 916 kg m^{-3} >

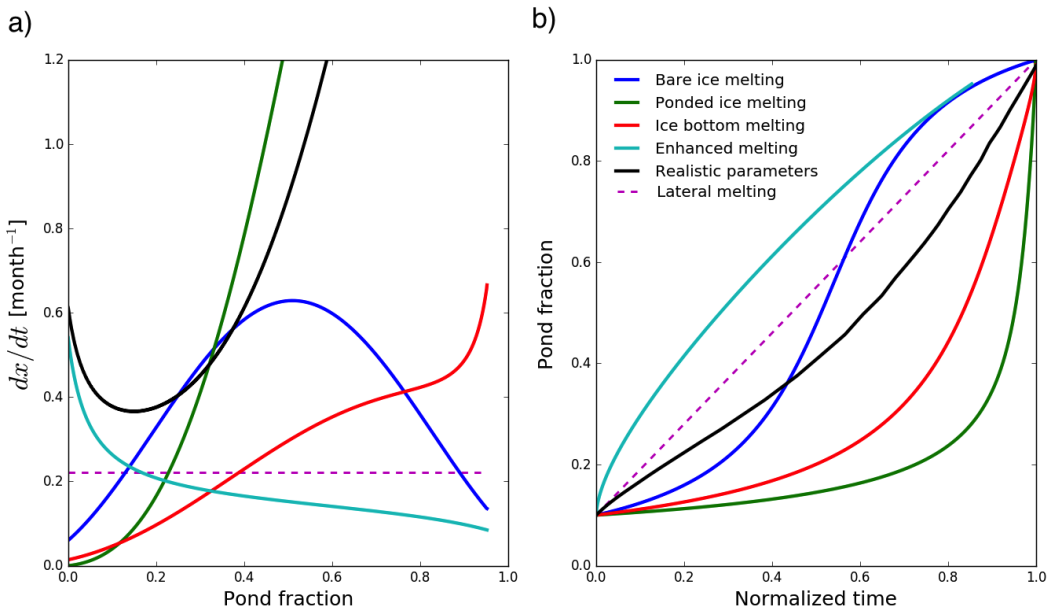

Figure 2.8: a) Dependence of growth rate on pond coverage for different modes of pond growth. The y-axis shows the growth rate, $\frac{dx}{dt}$, for each of the growth modes calculated using the default parameters and $x_i = 0$. Pond growth rate for bare ice melting (blue line) first increases up to a certain pond coverage and then decreases. Ponded ice melting (green line) increases with pond coverage from $\frac{dx}{dt} = 0$ at $x = 0$ to very high values at high pond coverage. The ice bottom melting rate (red line) gradually increases with pond coverage. The vertical enhanced melting rate (cyan line) decreases with pond coverage. The black line represents a realistic combination of the four growth modes, and shows that pond growth is dominated by enhanced melting early in the season, and by freeboard sinking late in the season. The dashed magenta line represents lateral melting estimated using parameters described in section 2.7.1. b) Solutions to Eq. (2.25) when only one of the growth modes is active. The x-axis shows the normalized time, where 0 corresponds to the beginning of the melt and 1 to entire floe being flooded.

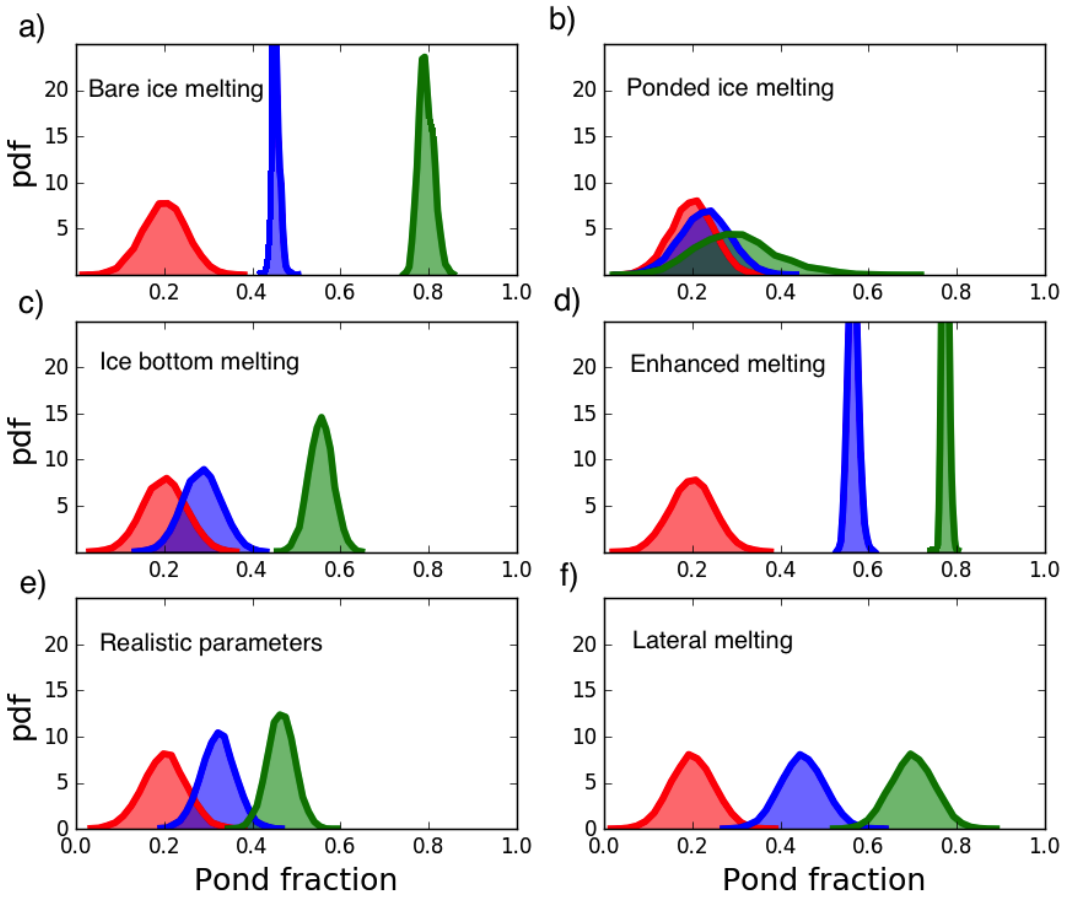

Figure 2.9: In this figure we have evolved an ensemble of 10^5 floes with varying initial pond coverage according to Eq. (2.25) when only one of the growth modes is active. Red curves represent the initial pond fraction distribution, blue curves represent the pond fraction distribution after a time, t, while the green curves represent the pond fraction distribution after $2t$. A time used in panel a is $t = \frac{1}{2}\frac{1-x_i}{S_{\rm bi}}$, in panel b it is $t = \frac{1}{6}\frac{1-x_i}{S_{\rm mp}}$, and in panels c through f it is $t = \frac{1}{4}\frac{1-x_i}{S}$, where x_i is the mean pond fraction of the initial distribution and S is an appropriate strength. We show how different growth modes have different effects on the pond fraction distribution. a) Bare ice melting first narrows the distribution, and then widens it. b) Ponded ice melting widens the distribution. c) Bottom ice melting narrows the distribution, while the mean of the distribution increases at an increasing rate. d) Enhanced melting narrows the distribution, while the mean of the distribution increases at a decreasing rate. e) Using realistic parameters, the pond distribution slowly narrows and accelerates. f) Due to lateral melting, pond coverage distribution does not change width, and the growth is linear.

$\rho_b > 750$ kg m^{-3}, pond growth rate can vary by at most 20%.

We will first discuss freeboard sinking. Common to all modes of freeboard sinking is the dependence on ice thickness. Each freeboard sinking growth mode is inversely proportional to the ice thickness, $S^*_{\text{fs}} \propto \frac{1}{H}$, meaning that, all else equal, ponds grow proportionally slower on thicker ice.

Although ice roughness may have a different effect on each of the individual modes of freeboard sinking, for simplicity we will assume that they are all affected by roughness in the same way, as parameterized in Eq. (2.28). In that case, each of these strengths is roughly proportional to the square of the non-dimensional ice roughness, $S^*_{\text{fs}} \propto \hat{\sigma}^2$, meaning that pond growth due to freeboard sinking is suppressed on smooth ice.

We will now focus on individual components of freeboard sinking. The parameter S^*_{bi} controls pond growth by freeboard sinking due to melting bare ice. On first year ice, owing to the shape of the hypsographic curve, the pond growth rate by bare ice melting increases up to a certain pond coverage and decreases afterwards (Fig. 2.8, blue line). S^*_{bi} is proportional to the flux $\overline{F}_{\text{bi}}$, and depends on the initial pond coverage as $S^*_{\text{bi}} \propto (1 - x_i)^2$. The quadratic dependence on initial bare ice fraction means that ponds on floes with less initial pond coverage grow faster. It also means that floes that start off less ponded can at some point become more ponded than floes that start off more heavily ponded. We can see this in Fig. 2.9a, where the pond coverage distribution narrows up to a certain point, after which it starts to widen again because floes with lower x_i overtake the floes with higher x_i. Using the default values of physical parameters of $\overline{F}_{\text{bi}} = 85$ Wm^{-2}, $H = 1.5$ m, $x_i = 0.2$, and $\hat{\sigma} = 0.55$, we get $S^*_{\text{bi}} \approx 0.13$ month^{-1}.

The parameter S^*_{mp} controls pond growth by freeboard sinking due to melting ponded ice. The pond growth rate increases with pond fraction from 0 at $x = 0$ to very high values at high pond coverage, and can be the dominant mode of pond growth if the pond coverage is high enough (Fig. 2.8, green line). For this reason, giving a representative number to

pond growth rate, such as S_{mp}, is only meaningful if the melt season is short enough such that pond coverage during that period does not change substantially. The dependence on initial pond coverage is $S^*_{\mathrm{mp}} \propto x_i(1 - x_i)$. For this reason the pond coverage distribution widens over time when S^*_{mp} is dominant (Fig. 2.9b). Using $\overline{F}_{\mathrm{mp}} = 171$ Wm^{-2} and other parameters the same as above, we get $S^*_{\mathrm{mp}} \approx 0.07$ month^{-1}. Although in this case, melting ponded ice affects pond evolution less than bare ice melting, it can become stronger if the pond coverage is higher. For example, S^*_{mp} and S^*_{bi} are roughly the same at $x = 0.35$, while at $x = 0.5$, S^*_{mp} is roughly twice as large as S^*_{bi}.

The parameter S^*_{bot} controls pond growth by freeboard sinking due to melting of the ice bottom. The pond growth rate due to bottom melting increases with increasing melt pond fraction, although more gradually than in the ponded ice melting case (Fig. 2.8, red line). Since the growth rate is proportional to the bare ice fraction, $S^*_{\mathrm{bot}} \propto (1 - x_i)$, the pond coverage distribution gets concentrated over time (Fig. 2.9c). Using $\overline{F}_{\mathrm{bot}} = 20$ Wm^{-2} and other parameters the same as above, we get $S^*_{\mathrm{bot}} \approx 0.04$ month^{-1}. The contribution from ice bottom melting becomes larger than the contribution from bare ice melting only at high x.

Now, we will turn to enhanced melting. The parameter S^*_{em} controls pond growth by enhanced melting, and is the least constrained in our model due to the many poorly-constrained physical processes that potentially contribute to it. Here we will only consider enhanced melting due to height-dependent processes (Eq. (2.23)) and leave lateral melting for the discussion (subsection 2.7.1).

Because the growth rate by enhanced melting is inversely proportional to the hypsographic curve, pond growth by enhanced melting is very fast at the beginning of the melt, and decelerates afterwards (Fig. 2.8, cyan line). The enhanced melting strength is inversely proportional to the square of the ice thickness, $S^*_{\mathrm{em}} \propto \frac{1}{H^2}$, meaning that it is significantly more sensitive to variations in thickness than freeboard sinking. On the other hand it is sig-

nificantly less sensitive to variations in ice roughness, Eq. (2.28). Even on perfectly smooth ice, $\hat{\sigma} = 0$, ponds will grow due to enhanced melting. In that case, however, lateral melt, rather than height-dependent enhanced melting may dominate.

The strength of enhanced melting is proportional to the height below which enhanced melting is operational, $S^*_{\mathrm{em}} \propto \Delta s$. If we take ice wetting as a physical example, this means that enhanced melting is sensitive to microphysical processes that determine how high above sea level the ice will be wet. The dependence on the parameter k depends on its magnitude. It appears in S^*_{em} in the term $\frac{k-1}{ds_{\mathrm{em}}/ds_{\mathrm{fs}}+1}$. The term $ds_{\mathrm{em}}/ds_{\mathrm{fs}}$ is proportional to $k-1$. Therefore, if $ds_{\mathrm{em}}/ds_{\mathrm{fs}} \ll 1$, enhanced melting is proportional to $k-1$. On the other hand, if $ds_{\mathrm{em}}/ds_{\mathrm{fs}} \gg 1$, enhanced melting becomes independent of k. Using default parameters, we find this transition happens at around $k \approx 1.2$. In the example of ice wetting, this means that enhanced melting is sensitive to albedo variations near sea level when ice near sea level has a similar albedo to the rest of the floe. On the other hand, if the albedo near sea level is significantly lower than the average, pond growth is insensitive to variations in properties of ice near sea level.

Enhanced melting is proportional to the cube of the bare ice fraction, $S^*_{\mathrm{em}} \propto (1-x_i)^3$, making it very sensitive to variations in initial pond coverage. For this reason, the pond coverage distribution gets quickly concentrated (Fig. 2.9d), and it is possible for initially less ponded floes to overtake initially more ponded floes. If we assume ice wetting is the only physical process responsible for enhanced melting, we can place a rough estimate on S^*_{sm}. Taking $k = 1.7$, $\Delta s = 0.06$ m, and $t = 30$ days, we get for default parameters $S^*_{\mathrm{em}} \approx 0.31$ month^{-1}. This suggests that the contribution to mean pond coverage from enhanced melting is slightly larger than the contribution from freeboard sinking after 30 days of melt.

The black line in Fig. 2.8 shows the total pond evolution using the default physical parameters. The pond growth rate when both freeboard sinking and enhanced melting occur

is not simply a sum of the growth rates of the four modes since the equations for freeboard sinking and enhanced melting are solved separate of each other. Therefore, the dependence of growth rate on pond coverage (Fig. 2.8a, black line) was obtained by finding the derivative of the pond evolution curve. The pond growth rate first decreases with pond fraction indicating that enhanced melting dominates early in the season and then increases indicating that freeboard sinking dominates later in the season. The pond coverage distribution using realistic parameters narrows with time (Fig. 2.9e). Since each growth mode affects the pond coverage distribution in a distinct way, fitting both the evolution of the mean and the standard deviation of the pond coverage distribution in observational data could add constraints on the relevant strengths. Using the above values of strengths, we find that after a month of growth bare ice melting contributes to roughly 25% of mean pond coverage, ponded ice melting contributes to around 13%, ice bottom melting contributes to around 7%, and enhanced melting contributes to roughly 55%.

2.7 Discussion

2.7.1 Lateral melting of pond walls by pond water

In our model, we focused on vertical changes in topography, and neglected pond growth by lateral melting of pond sidewalls by pond water. We will now briefly discuss this second possibility.

This type of melt was the main focus of Skyllingstad et al. (2009), who carefully calculated the lateral melt rates of pond sidewalls by pond water. The red line in Fig. 2.10 shows their results. The rate of change of pond fraction due to a lateral melt flux $\overline{F}_{\text{lat}}$ is

$$\frac{dx_{\text{lat}}}{dt} = \frac{P}{A}\frac{\overline{F}_{\text{lat}}}{l\rho_b} \ , \tag{2.33}$$

where P is the total perimeter of the ponds and A is the area of the floe. If $\overline{F}_{\text{lat}}$ is constant

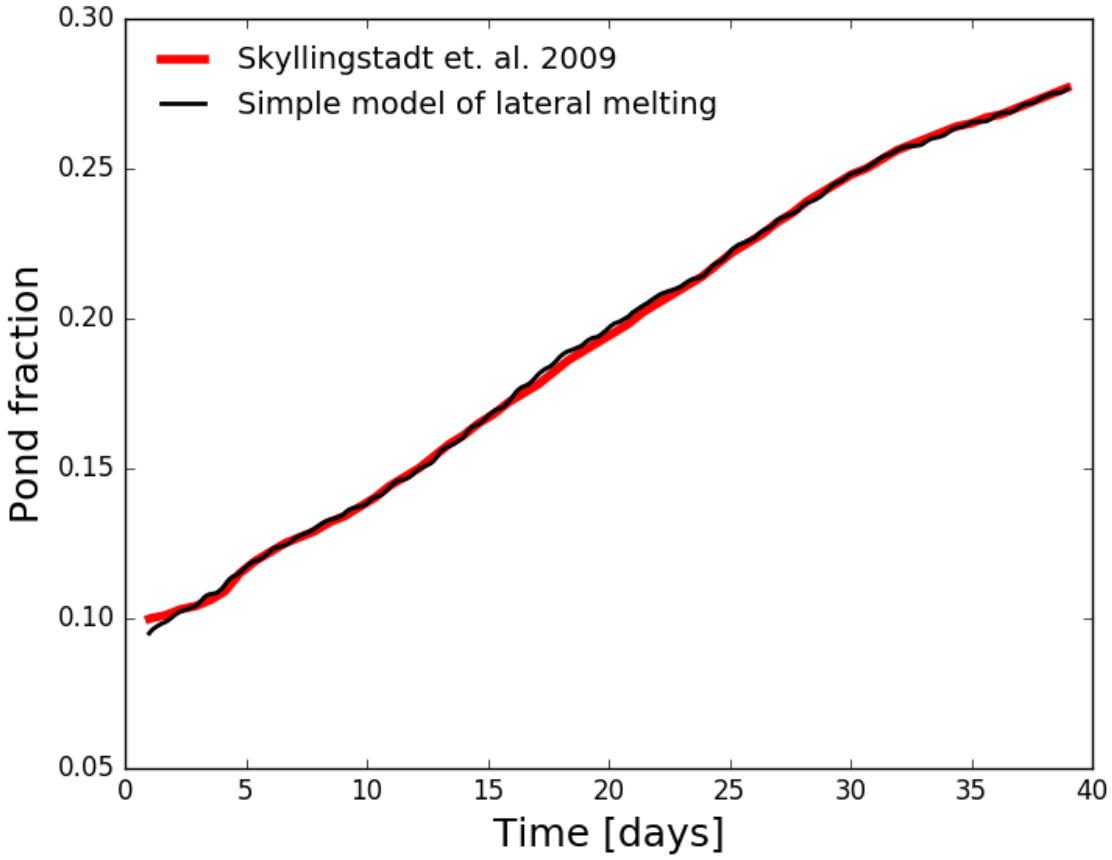

Figure 2.10: The red curve is the results of Skyllingstad et al. (2009). The black curve is the solution to Eq. (2.33) with $\overline{F}_{\text{lat}} = K_{\text{lat}}\overline{F}_{\text{mp}}$. The pond albedo and the shortwave, longwave, sensible, and latent heat fluxes used to find $\overline{F}_{\text{mp}}$ are the same as used in Skyllingstad et al. (2009) and $K_{\text{lat}} = 1.5$. A nearly perfect agreement between the two curves suggests that a single non-dimensional constant, K_{lat}, is enough to describe pond growth by lateral melting, and the complicated physics of lateral melting are important only in determining the value of K_{lat}.

and the dependence of P on pond fraction is weak, pond growth is linear, which explains the roughly linear pond coverage evolution in Skyllingstad et al. (2009). In Fig. 2.10, black line, we solve Eq. (2.33) assuming a lateral melt flux proportional to the ponded ice melting flux, $\overline{F}_{\rm lat} = K_{\rm lat}\overline{F}_{\rm mp}$, where $K_{\rm lat}$ is a constant. We use the same energy fluxes used by Skyllingstad et al. (2009), and estimate $\frac{P}{A} \approx 0.1$ m^{-1} from the aerial photographs taken during SHEBA. A nearly perfect match is obtained with $K_{\rm lat} = 1.5$ with pond coverage deviation of less than 1%. Therefore, a single constant that relates the rate of melt of ponded ice to the rate of melt of pond walls, $K_{\rm lat}$, is enough to capture the effects of lateral melting on pond growth, at least as parameterized in Skyllingstad et al. (2009). This suggests that the complicated physics of lateral melting can, to a large extent, be ignored. More work would, however, be needed to determine to what degree $K_{\rm lat}$ varies under different circumstances.

If we ignore the topographic variation above sea level, pond growth due to enhanced melting also becomes linear (Eq. (2.19)). Therefore, lateral melting can approximately be considered a contribution to enhanced melting, $S_{\rm em}$, although it scales differently with physical parameters than the height-dependent enhanced melting, Eq. (2.23). It is important to note that in this model lateral melt does not depend on ice thickness, H, or on initial pond coverage, x_i, although, in reality, it may depend on these to some degree. For this reason, the pond coverage distribution width does not change in time, while the mean increases linearly (Fig. 2.9f).

It is not simple to understand the contribution of lateral melting to pond growth when both lateral and vertical melting occur simultaneously. Each point along the pond boundary can either expand by lateral melting or by vertical melting, but not by both. This is because when a point along the pond boundary melts laterally, it creates a completely vertical slope at that point. Therefore a small vertical shift will not grow the ponds, and a large vertical shift will outgrow the lateral expansion. Therefore, if pond growth due to vertical melting

is strong, the contribution from lateral melting will be small. This is consistent with observations of Polashenski et al. (2012) and Landy et al. (2014) who found that on first year ice the contribution from lateral melting is small. On the other hand, steep topography on level multiyear ice inhibits pond expansion through vertical motion and could lead to lateral melting being the dominant mode of growth. This is consistent with our findings of a large contribution from enhanced melting to pond growth on multiyear ice during SHEBA (Fig. 2.5).

2.7.2 Effects of density variations and internal melt

So far, we have assumed that all the melt occurs either on the top or the bottom surface of the ice. However, some of the melt can happen internally, in the bulk of the ice. Internal melt occurs when trapped brine pockets with high salt content expand and dilute in order to reach a thermodynamic equilibrium with the surrounding ice. This phenomenon has been reported to occur both above and below sea level. Internal melt leads to a reduction in bulk ice density, ρ_b, which in turn affects pond evolution. Accounting for internal melt correctly can be quite challenging as it requires detailed knowledge of the vertical structure of internal melt and bulk density. Nevertheless, we find that although the effects of internal melt and density variation may be significant when considered individually, if considered together, they are likely small.

If internal melt is uniform throughout the vertical ice column, the only effect is a gradual reduction in ρ_b over the course of the melt season, slightly increasing the pond growth rate. If, on the other hand, internal melt has a vertical structure, it will create a vertically non-uniform bulk ice density which can have more complicated effects on pond evolution. Variations in bulk density and internal melt affect pond evolution in the following ways: 1) mass transported across sea level due to rigid body movement depends on the bulk density at sea level, 2) the volume of ice removed by local melt depends on the bulk ice density at

the surface, 3) freeboard height depends on average bulk densities above and below sea level, and 4) internal melt induces rigid body motion by melting mass above and below sea level, without changing the ice surface. We outline the procedure to include these effects in the pond evolution model in appendix D. The resulting equation for pond coverage evolution has the same form as Eq. (2.25), with only the strengths modified. Here, we only qualitatively discuss our findings. Pond evolution is most sensitive to

1. The difference between the internal melt rate above and below sea level, $\overline{e}_{\text{asl}} - \overline{e}_{\text{bsl}}$, creating a rigid body motion. Here, $\overline{e}_{\text{asl/bsl}}$ is the energy density used for internal melting, averaged over all ice above or below sea level. More internal melt above (below) the sea level will create an upward (downward) rigid body motion of the floe, slowing down (speeding up) pond growth.

2. The difference between the bulk ice density at the surface and the bulk ice density at sea level, $\rho_b(h) - \rho_b(0)$, changing the ratio of topographic change due to local melt to rigid body motion. Using default parameters, rigid body motion is upwards, slowing down pond growth. Therefore, a lower (higher) bulk ice density at the surface relative to sea level increases (decreases) the rate of local melt relative to rigid body motion, speeding up (slowing down) pond growth.

If considered as independent processes, vertical variations in bulk ice density and internal melt can significantly alter the rate of pond growth. For example, assuming $\rho_b(0) = 850$ kg m^{-3}, $\rho_b(h) = 750$ kg m^{-3}, and no internal melt, leads to a roughly 60% increase in the pond growth rate. However, these processes depend on each other and have the opposite effects on pond evolution. For example a high rate of internal melt above sea level, slowing down pond growth, will lower the bulk ice density above sea level, speeding up pond growth.

Density and internal melt can be related via a differential equation, $\frac{\partial \rho_b(z)}{\partial t} = -\frac{e(z)}{l} - \frac{\partial \rho_b(z)}{\partial z}\frac{ds_{\text{rigid body}}}{dt}$, where z is a vertical coordinate within the ice column. Assuming vertically uniform rates of internal melt above and below sea level, an approximate long-time solution to

this equation yields a vertically uniform bulk density below sea level, and a linearly decreasing bulk density above sea level. This also defines a long-time relationship between the vertical profiles of internal melt and bulk ice density, $\overline{e}_{\text{asl}} - \overline{e}_{\text{bsl}} = \frac{l}{h}\frac{ds_{\text{rigid body}}}{dt}(\rho_b(0) - \rho_b(h))$. Using densities from the example in the paragraph above, and the rate of internal melt obtained in this way, leads to a roughly 10% increase in pond growth rate, significantly less than 60% we found when considering only the effects of vertical density structure.

Thus, after a time long enough for the ice density profile to reach a steady-state with respect to the internal melt, the effects of vertically non-uniform internal melt and density always significantly compensate each other as illustrated in the example above. For this reason, we believe that including a vertical structure of density or internal melt in the simple model of pond evolution model is most likely unnecessary for the purpose of making a first-order estimate of pond coverage growth rate.

2.7.3 Under certain conditions, ponds can stop growing

Here, we will entertain the possibility of pond growth by vertical motion of the topography stopping entirely for a period of time. This is an example of a possible transient effect of internal melting, which, although interesting, seems unlikely.

If there is enough mass removed above sea level to induce an upward rigid body motion that is able to compensate for the effects of local melting near the sea level, points near the sea level would move upwards, $\frac{ds}{dt} > 0$, and pond growth would stop. This could, for example, occur if there is strong internal melting above sea level. After a time, however, high internal melt above sea level would lower the bulk ice density at the surface thereby increasing the rate of local melt, and reinitializing pond growth.

We will use an equation for $\frac{ds}{dt}$ that includes the effects of vertically non-uniform internal melt and bulk ice density we derive in appendix D, Eq.(2.42). Requiring that $\frac{ds}{dt}(x) > 0$ for

any x, we find the condition for pond growth stopping as

$$k < \frac{\rho_b(h)}{\rho_b(0)} \frac{\rho_\mathrm{i}}{\rho_\mathrm{w}} \left(1 + \frac{h}{\overline{F}_\mathrm{bi}} \left(\overline{e}_\mathrm{asl} - \overline{e}_\mathrm{bsl} \frac{\overline{\rho}_\mathrm{asl}}{\overline{\rho}_\mathrm{bsl}}\right)\right) - \frac{\rho_\mathrm{w} - \rho_\mathrm{i}}{\rho_\mathrm{w}} \frac{\overline{F}_\mathrm{bot}}{\overline{F}_\mathrm{bi}} \ , \tag{2.34}$$

where $\overline{\rho}_\mathrm{asl/bsl}$ is the average bulk density above and below sea level. Using the values of internal melt and bulk densities from the previous chapter and taking $\frac{\overline{\rho}_\mathrm{asl}}{\overline{\rho}_\mathrm{bsl}} \approx 1$, we find that in order for ponds to stop growing, k has to be less than 0.85. This is unlikely as ice near the sea level likely melts faster than ice higher up. Nevertheless, if internal melt has not had enough time to adjust densities above and below sea level, it is possible that pond growth could be stopped for a time by the action of internal melt above sea level. For example, assuming the same internal melt as in the previous example but a uniform bulk ice density ($\rho_b(h) = \rho_b(0)$), pond growth would be stopped at $k = 1$. In this case it is likely that growth by lateral melt would take over, as Eq. (2.34) ensures only that pond growth by vertical motions is prevented.

2.8 Conclusions

We presented a simple analytical model for melt pond evolution on permeable Arctic sea ice. The model is represented by two ordinary differential equations in which the rate of change of pond coverage depends on pond coverage. The model is governed by four parameters, S_bi, S_mp, S_bot, and S_em, that control the rate of pond growth by bare ice melting, ponded ice melting, ice bottom melting, and enhanced melting. Using this model we are able to reproduce observations well.

Our main finding is that we can estimate the mean pond coverage as a function of time without running the model by using "effective strengths:" S^*_bi, S^*_mp, S^*_bot, and S^*_em. Here all the physical parameters combine in a known way which permits understanding of the behavior of pond coverage under general conditions. The most important conclusions we

draw from analyzing the effective strengths are:

1. Ponds grow slower on smoother ice, with freeboard sinking roughly proportional to the square of the bare ice roughness and enhanced melting increasing roughly linearly with roughness.

2. Ponds respond to both freeboard sinking and enhanced melting on first year ice and almost entirely to enhanced melting on multiyear ice.

3. The pond growth rate is more sensitive to changes in bare sea ice albedo than changes in pond albedo unless the ice is already mostly covered in ponds.

4. Under a global warming scenario, the pond feedback could lead to a reduction in annual minimum ice thickness of the same order of magnitude as the thickness reduction due to direct forcing.

5. The dependence of ice albedo on height above sea level is likely a significant control on pond evolution on multiyear ice, so that ignoring it, thereby neglecting enhanced melting, could lead to an order of magnitude decrease in the pond growth rate on multiyear ice.

6. The pond coverage distribution over an ensemble of floes likely narrows over time.

7. Pond evolution is insensitive to small time scale variations in the forcing.

8. If freeboard sinking is suppressed by topography, lateral melting likely plays an important role, making it a significant factor on multiyear ice.

9. The complicated physics of lateral melting can be summarized by a single non-dimensional constant K_{lat} that relates the lateral melt flux to the flux used for melting the pond bottom.

10. The vertical structure of density and internal melt can likely be ignored for the purpose of making a first-order estimate of pond coverage growth rate.

As melt pond coverage is one of the key controls on summer Arctic sea ice albedo, some representation of it in GCMs is necessary for predicting the future of sea ice and its impact on global climate. With the exception of enhanced melting, our model depends only on parameters that are either available in large scale models or that can be reasonably estimated. Therefore, if stricter constraints can be placed on the strength of enhanced melting, our model may present an accurate and computationally low-cost representation of sea level melt ponds that could be used in GCMs. A major limitation of our model is our lack of complete understanding of enhanced melting. Thus, to improve it, further field studies about melt processes near the pond boundaries, such as lateral melting or the melting due to a lower ice albedo near the pond boundaries, are needed. Moreover, processes that determine ice topography at the beginning of stage III should also be addressed. We discuss this somewhat in Chapter 4.

2.9 Appendix A

A good fit to measured hypsographic curves is a tangent function (Fig. 2.2):

$$\begin{aligned} s(x_h) &= a\Big[\tan\Big(\frac{\pi}{2m}p_1\big((x_h - x_i) - p_2(1-x_i)\big)\Big) + \tan\Big(\frac{\pi}{2m}p_1p_2(1-x_i)\Big)\Big] \\ m &\equiv \max\Big(p_2(1-x_i), (1-x_i) - p_2(1-x_i)\Big) \end{aligned} \tag{2.35}$$

Although this function has a cumbersome form, the parameters involved have a clear interpretation. The requirement that the initial pond fraction is at $x_h = x_i$ is automatically satisfied as this is a zero of the function Eq. (2.35). The parameter a is determined by the requirement of hydrostatic balance, $\langle s(x_h)\rangle = h$. Therefore, after specifying the initial pond fraction, x_i, and the initial ice thickness H, the only two unconstrained parameters are p_1 and p_2. Parameter $0 < p_1 < 1$ determines the level of "variability" of the curve: if p_1 is close to 0, $s(x_h)$ is roughly linear, whereas if p_1 is close to 1, $s(x_h)$ is highly curved. Parameter p_2 determines the position of the inflection point of the tangent function relative to x_i. Therefore $p_2 < 0$ means that the inflection point is to the left of x_i, and $s(x_h)$ is fully convex. For $p_2 > 1$, the inflection point is to the right of $x_h = 1$, and $s(x_h)$ is fully concave. If $0 < p_2 < 1$, $s(x_h)$ transitions from concave to convex at $x_h = x_i + p_2(1-x_i)$. We note that the non-dimensional bare ice roughness, $\hat{\sigma}$, for a hypsographic curve defined in this way does not depend on ice thickness or initial pond coverage, but only on parameters p_1 and p_2. For the hypsographic curve measured by Landy et al. (2014) for June 25th of 2011, the values of the shape parameters are $p_1 \approx 0.8$ and $p_2 \approx 0.4$, whereas for the hypsographic curve measured during SHEBA (Fig 2.2a, dashed line) the parameters are $p_1 \approx 0.9$ and $p_2 \approx 0.5$.

2.10 Appendix B

In order to make a connection between a model where a constant fraction of bare ice, δ, is affected by enhanced melting, and a model where ice below a fixed elevation, Δs, is affected,

we need to estimate how δ scales with Δs. It is important to make this connection since several physical mechanisms that significantly affect the melt rate depend on the elevation of ice above sea level. To do this, we will use an alternative model where we assume both freeboard sinking and enhanced melting occur simultaneously, and enhanced melting only affects ice below Δs (Fig. 2.3d). We define x_s to be the fraction of ice below Δs, x to be the fraction of the ice below sea level, and $\delta \equiv x_s - x$ to be the difference between the two. x_s evolves only due to freeboard sinking, whereas x evolves due to both freeboard sinking and enhanced melting. The equations for the evolution of x_s and x are

$$\begin{aligned} \frac{dx_s}{dt} &= \frac{dx_h}{ds}|_{x_s} \frac{ds_{\text{fs}}}{dt} \\ \frac{dx}{dt} &= \frac{dx}{ds}\left[\frac{ds_{\text{fs}}}{dt} + \frac{ds_{\text{em}}}{dt}\right] . \end{aligned} \tag{2.36}$$

Here, $\frac{ds_{\text{fs}}}{dt}$ and $\frac{ds_{\text{em}}}{dt}$ are determined by Eq. (2.11). Since freeboard sinking does not change the shape of the topography and x_s evolves only due to freeboard sinking, $\frac{dx_h}{ds}|_{x_s}$ is simply the inverse slope of the original hypsographic curve evaluated at x_s. On the other hand, the hypsographic curve near sea level is affected by enhanced melting, and therefore changes shape over time. For this reason, $\frac{dx}{ds}$, which relates the change in pond fraction, dx, to the vertical change in the hypsographic curve at sea level, ds, changes with time. Nevertheless, if Δs is small enough, we can approximate the hypsographic curve between x and x_s to be a straight line, meaning that $\frac{dx}{ds} \approx \frac{x_s - x}{\Delta s} = \frac{\delta}{\Delta s}$. This approximation closes our alternative model. This model provides a similar level of agreement with the 1d model as the 0d model Eq. (2.25), but is more complicated to analyze. For this reason, we focus on Eq. (2.25) to analyze pond evolution, and use Eq. (2.36) only in what follows. We note that if the hypsographic curve is convex, Eq. (2.36) agrees better with the 1d model than Eq. (2.25). This configuration is, however, unrealistic.

Using $\frac{dx}{ds} = \frac{\delta}{\Delta s}$, and subtracting $\frac{dx}{dt}$ from $\frac{dx_s}{dt}$ in Eq. (2.36), we get an equation for

evolution of δ:

$$\frac{d\delta}{dt} = \frac{dx_h}{ds}|_{(x+\delta)} \frac{ds_{\rm fs}}{dt} - \frac{\delta}{\Delta s}\Big[\frac{ds_{\rm fs}}{dt} + \frac{ds_{\rm em}}{dt}\Big] \ . \tag{2.37}$$

Since $\frac{ds_{\rm fs}}{dt} + \frac{ds_{\rm em}}{dt}$ is larger than $\frac{ds_{\rm fs}}{dt}$, δ decreases until it reaches a constant value after some time. Therefore, a constant Δs model and a constant δ model become equivalent after some time. Therefore, finding the value of δ for which $\frac{d\delta}{dt} = 0$, represents a natural way to relate the two models.

The values of $\frac{ds_{\rm fs}}{dt}$, $\frac{ds_{\rm em}}{dt}$, and $\frac{dx_h}{ds}|_{(x+\delta)}$ themselves depend on pond fraction, x (Eq. (2.11)). Furthermore, $\frac{ds_{\rm fs}}{dt}$ and $\frac{ds_{\rm em}}{dt}$ depend on the energy fluxes used for melting the ice, which may fluctuate in time. For these reasons, δ is never fully constant. To deal with this this, we estimate the magnitudes of $\frac{ds_{\rm fs}}{dt}$, $\frac{ds_{\rm em}}{dt}$, and $\frac{dx_h}{ds}|_{(x+\delta)}$ by substituting $x \to x_i$, $\frac{dx_h}{ds}|_{(x+\delta)} \to \frac{1-x_i}{h}$, and energy fluxes, $\overline{F}$, with their representative values, $|\overline{F}|$, e.g. their time-averages. We then find the magnitude of δ as

$$\delta = C\frac{\rho_{\rm w}}{\rho_{\rm w} - \rho_{\rm i}} \frac{\Delta s(1-x_i)^2}{H} \frac{1}{\frac{ds_{\rm em}}{ds_{\rm fs}} + 1} \ , \tag{2.38}$$

where C is a non-dimensional number that does not depend on physical parameters, there to compensate for the crude approximations of using only the initial pond fraction and the average slope of the hypsographic curve. Comparing to 1d model, we find $C \approx \frac{2}{3}$. The term $\frac{ds_{\rm em}}{ds_{\rm fs}}$ is the ratio of magnitudes of $\frac{ds_{\rm em}}{dt}$ and $\frac{ds_{\rm fs}}{dt}$, and is given by

$$\frac{ds_{\rm em}}{ds_{\rm fs}} = \frac{\rho_w}{\rho_w - \rho_i} \frac{|\overline{F}_{\rm bi}|(k-1)}{|\overline{F}_{\rm bi}| + \frac{x_i}{1-x_i}|\overline{F}_{\rm mp}| + \frac{1}{1-x_i}|\overline{F}_{\rm bot}|} \ . \tag{2.39}$$

Using δ defined in this way in the 0d model, Eq. (2.25), provides excellent agreement with Eq. (2.36) and the 1d model run with constant Δs. We note that this agreement is reached in the long-time limit, and for times shorter than roughly $\frac{\Delta s}{(ds_{\rm em}/dt + ds_{\rm fs}/dt)}$ some disagreement can persist. Although the magnitude of the disagreement depends on the shape of the

hypsographic curve, it is typically not very large, and the 0d model provides a reasonable estimate of pond evolution even for short times.

2.11 Appendix C

Here we describe the procedure we used to estimate the effective strengths, Eq. (2.28). We write the effective strengths as

$$S^* = f(\hat{\sigma}, \hat{t})S \ , \tag{2.40}$$

where $f(\hat{\sigma}, \hat{t})$ is a non-dimensional function of non-dimensional roughness $\hat{\sigma}$ and non-dimensional time $\hat{t} \equiv \frac{St}{1-x_i}$, and S is either $S_{\rm fs} \equiv (S_{\rm bi} + S_{\rm mp} + S_{\rm bot})$ in the case of freeboard sinking or $S_{\rm em}$ in case of enhanced melting. The non-dimensional time, $\hat{t}$, defined in the above way measures how far the melt season has progressed, with $\hat{t} = 0$ corresponding to the beginning of pond growth and $\hat{t} = 1$ roughly corresponding to the end of pond growth with entire floe flooded. The function $f(\hat{\sigma}, \hat{t})$ measures how much the mean pond coverage deviates from a mean coverage of linearly evolving ponds. For a linear pond evolution, $x(t) = St + x_i$, the function $f(\hat{\sigma}, \hat{t}) = 1$.

We separately consider freeboard sinking and enhanced melting. For all the curves in Figs. 2.7a and b, we find $f(\hat{\sigma}, \hat{t})$ at several different times $\hat{t}$ as $f(\hat{\sigma}, \hat{t}) = 2\frac{\langle x(t)\rangle - x_i}{St}$. We show the results in Figs. 2.11a and b, where f are plotted as functions of roughness and different colors correspond to different times $\hat{t}$. For any given time, the scatter comes from the fact that the hypsographic curve is not fully determined by roughness.

In the case of freeboard sinking, $f_{\rm fs}$ does not depend much on $\hat{t}$. A quadratic $f_{\rm fs}(\hat{\sigma}, \hat{t}) = c\hat{\sigma}^2$ fits the scatter data well. Based on best fit estimates, we find $c \approx 1.3$ (Fig. 2.11a, red dashed line).

In the case of enhanced melting, $f_{\rm em}$ depends strongly on time $\hat{t}$. We choose to parameterize $f_{\rm em}$ with a linear function of the form $f_{\rm em}(\hat{\sigma}, \hat{t}) = 1 + c(\hat{t})\hat{\sigma}$. We can approximate

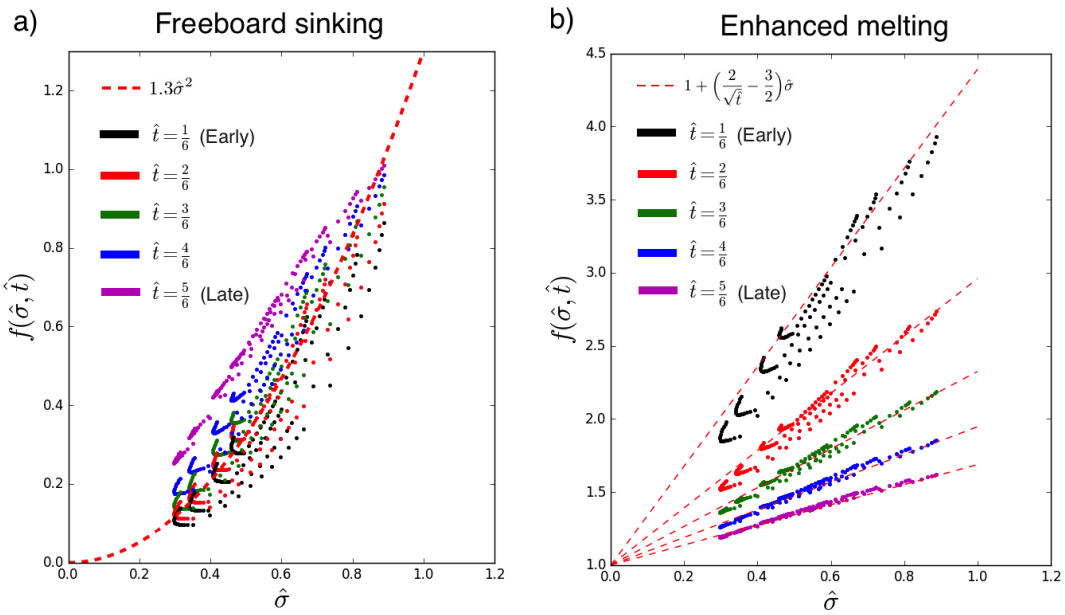

Figure 2.11: Determining the effective strengths, $S^* \equiv f(\hat{\sigma},\hat{t})S$. Points represent estimates of the correction $f(\hat{\sigma},\hat{t})$ for each of the curves in Fig. 2.7 evaluated at different times $\hat{t} \equiv \frac{St}{1-x_i}$. The function $f(\hat{\sigma},\hat{t})$ is evaluated as $f(\hat{\sigma},\hat{t}) \equiv 2(\langle x(t)\rangle - x_i)/(St)$. Different colors correspond to different times with black corresponding to early in the season and magenta to late in the season. Non-dimensional roughness, $\hat{\sigma}$, is shown on the x-axis. a) $f_{\text{fs}}(\hat{\sigma},\hat{t})$ evaluated for the freeboard sinking curves in Fig. 2.7a. There is no obvious dependence on $\hat{t}$. Freeboard sinking becomes completely suppressed as roughness tends to zero. The dashed red line represents the fit to these estimates of the form $f_{\text{fs}}(\hat{\sigma},\hat{t}) = a\hat{\sigma}^2$. b) $f_{\text{em}}(\hat{\sigma},\hat{t})$ evaluated for the enhanced melting curves in Fig. 2.7b. There is a clear dependence on $\hat{t}$. Enhanced melting proceeds even as roughness tends to zero. Red dashed lines are fits to these data of the form $f_{\text{em}}(\hat{\sigma},\hat{t}) = 1 + c(\hat{t})\hat{\sigma}$, where $c(\hat{t}) \equiv \frac{2}{\sqrt{\hat{t}}} - \frac{3}{2}$.

$c(\hat{t})$ by exactly solving the equation for enhanced melting, Eq. (2.19), for a linear hypsographic curve, $s(x_h) \propto (x_h - x_i)$. Finding the roughness and $\langle x(t) \rangle$ in this case, we find $c(\hat{t}) \approx \left(\frac{2}{\sqrt{\hat{t}}} - \frac{3}{2}\right)$. Red dashed lines in Fig. 2.7d show f_{em} parameterized in this way.

2.12 Appendix D

Here, we outline the procedure to include the effects of vertically non-uniform internal melt and bulk ice density. We assume that the bulk ice density, ρ_b, and the energy density used for melting the ice internally, e, have a vertical structure, $\rho_b(z)$ and $e(z)$, where z is positive upwards, $z = 0$ corresponds to sea level, and $z = h$ corresponds to ice surface.

Mass transported across sea level depends on the bulk density at the sea level, the rate of local melting depends on the bulk ice density at the surface, and the freeboard height depends on the average densities above and below sea level, $\overline{\rho}_{\text{asl/bsl}}$. Internal melt above and below sea level creates a rigid body motion. This is summarized as

$$
\begin{aligned}
dm^{\text{rigid body}} &= \rho_b(0) A_{\text{bi}} ds_{\text{rigid body}} \ , \\
dm^{\text{melt}}_{\text{above s. l.}} &= -A_{\text{bi}} \frac{\overline{F}_{\text{bi}}}{l} dt - A_{\text{bi}} h \frac{\overline{e}_{\text{asl}}}{l} dt \ , \\
dm^{\text{melt}}_{\text{below s. l.}} &= -A_{\text{mp}} \frac{\overline{F}_{\text{mp}}}{l} dt - A \frac{\overline{F}_{\text{bot}}}{l} dt - A H_d \frac{\overline{e}_{\text{bsl}}}{l} dt \ , \\
h &= \frac{\rho_w - \rho_i}{\rho_w} \frac{H}{1-x} \frac{1}{1 - \Delta\rho_b \frac{\rho_i}{\rho_w}} \ , \\
\frac{ds_{\text{loc}}}{dt}(\vec{r}) &= -k(\vec{r}) \frac{\overline{F}_{\text{bi}}}{l \rho_b(h)} \ ,
\end{aligned}
\tag{2.41}
$$

where H_d is the ice draft depth defined as the volume of ice below sea level divided by the area of the ice floe, $\overline{e}_{\text{asl/bsl}}$ is the energy density used for internal melting averaged over all ice above or below sea level, and $\Delta\rho_b \equiv \frac{\overline{\rho}_{\text{bsl}} - \overline{\rho}_{\text{asl}}}{\overline{\rho}_{\text{bsl}}}$ is the relative difference in mean bulk density above and below sea level.

With these changes, we can find the equation for pond coverage evolution straightfor-

wardly, by repeating all of the steps from section 2.2. We first derive the equation for the vertical motion of points near the sea level

$$\frac{ds}{dt} = -\left[(k-1)\frac{\overline{F}_{\rm bi}}{l\rho_b(h)}\right] - \\ -\left[\frac{1}{l\rho_b(0)}\left(\overline{F}_{\rm bi}(\frac{\rho_b(0)}{\rho_b(h)} - \frac{\rho_i}{\rho_w}) + \frac{(\rho_{\rm w}-\rho_{\rm i})x}{\rho_{\rm w}(1-x)}\overline{F}_{\rm mp} + \frac{\rho_{\rm w}-\rho_{\rm i}}{\rho_{\rm w}(1-x)}\overline{F}_{\rm bot} + \frac{\rho_i}{\rho_w}h\overline{e}_{\rm bsl}(\Delta e - \Delta\rho_b)\right)\right] , \tag{2.42}$$

where $\Delta e \equiv \frac{\overline{e}_{\rm bsl}-\overline{e}_{\rm asl}}{\overline{e}_{\rm bsl}}$ is the relative difference in average energy density used for internal melting below and above sea level. The two terms in square brackets correspond to enhanced melting and freeboard sinking. Then we repeat the procedure to relate Eq. (2.42) to the change in pond coverage. The resulting equation has the same form as Eq. (2.25), with only the strengths modified

$$\begin{aligned} S_{\rm int} &= \frac{(1-x_i)\frac{\rho_i}{\rho_w}\overline{e}_{\rm bsl}(\Delta e - \Delta\rho_b)}{l\rho_b(0)} , \\ S_{\rm bi} &= \frac{(1-x_i)^2(1-\Delta\rho_b\frac{\rho_i}{\rho_w})(1+\frac{\rho_w(\rho_b(0)-\rho_b(h))}{\rho_b(h)(\rho_w-\rho_i)})}{Hl\rho_b(0)}\overline{F}_{\rm bi} , \\ S_{\rm mp} &= \frac{(1-x_i)x_i(1-\Delta\rho_b\frac{\rho_i}{\rho_w})}{Hl\rho_b(0)}\overline{F}_{\rm mp} , \\ S_{\rm bot} &= \frac{(1-x_i)(1-\Delta\rho_b\frac{\rho_i}{\rho_w})}{Hl\rho_b(0)}\overline{F}_{\rm bot} , \\ S_{\rm em} &= \Big(\frac{\rho_{\rm w}}{\rho_{\rm w}-\rho_{\rm i}}\Big)^2\frac{2\Delta s(1-x_i)^3(k-1)(1-\Delta\rho_b\frac{\rho_i}{\rho_w})^2}{3H^2l\rho_b(0)(1+\frac{ds_{\rm em}}{ds_{\rm fs}})}\overline{F}_{\rm bi} . \end{aligned} \tag{2.43}$$

Here, the strength of internal melting, $S_{\rm int}$ should be included in the equation for freeboard sinking. The term $\frac{ds_{\rm em}}{ds_{\rm fs}}$ is given by the ratio of the two terms in Eq. 2.42. The equation for pond growth, Eq. (2.25), using the above strengths, Eq. (2.43), should also be supplemented

with an equation for evolution of bulk density

$$\frac{\partial \rho_b(z)}{\partial t} = -\frac{e(z)}{l} - \frac{\partial \rho_b(z)}{\partial z}\frac{ds_{\text{rigid body}}}{dt} \ . \tag{2.44}$$

Table 2.1: A table of parameters used in this Chapter

Parameter	Meaning
t, $\hat{t}$	Time and non-dimensional time, $\hat{t} = \frac{St}{1-x_i}$.
$s(\vec{r})$	Surface elevation above sea level at point $\vec{r}$.
$s(x_h)$, $\widehat{s}(x_h)$, $\frac{d\widehat{s}}{d\widehat{x}_h}$	Hypsographic curve, non-dimensional hypsographic curve, $\widehat{s}(x_h) = \frac{s(x_h)}{h}$, and its non-dimensional derivative, $\frac{d\widehat{s}}{d\widehat{x}_h} = \frac{1-x_i}{h}\frac{ds}{dx_h}$.
$ds_{\text{rigid body}}$, $ds_{\text{loc}}(\vec{r})$	Change in surface elevation due to rigid body motion and due to local melting at point $\vec{r}$.
ds_{fs}, ds_{em}, $ds_{\text{em}}/ds_{\text{fs}}$	Change in surface elevation due to freeboard sinking, due to enhanced melting, and the magnitude of their ratio.
$dm^{\text{melt/rigid body}}_{\text{above/below s. l.}}$	Change in mass above and below sea level due to ice melting or rigid body motion.
x, $\widehat{x}$, $\widehat{1-x}$	Pond fraction, normalized pond fraction $\widehat{x} = \frac{x}{x_i}$, and normalized bare ice fraction, $\widehat{1-x} = \frac{1-x}{1-x_i}$
x_i	Initial pond fraction.
x_h	Fraction of ice below an elevation given by the hypsographic curve.
x_s	Fraction of ice below Δs.
$x_{\text{fs}}(t)$, $x_{\text{em}}(t)$, $x_{\text{lat}}(t)$	Pond coverage evolution due to freeboard sinking, enhanced melting, and lateral melting.
A, A_{bi}, A_{mp}	Areas of the floe, bare ice, and melt ponds
P	Total perimeter of the ponds.
ρ_w, ρ_i, ρ_b	Densities of salt water, pure ice, and bulk ice once all the brine has drained.
l	Latent heat of melting.
H, h	Initial thickness of the ice and average initial freeboard height.
σ, $\hat{\sigma}$	Bare ice roughness and non-dimensional bare ice roughness, $\hat{\sigma} = \frac{\sigma}{h}$.
p_1, p_2	Shape parameters of the hypsographic curve that control the "amount of variability" of the curve and the location of the inflection point.
$k(\vec{r})$	Ratio of the melt rate at point $\vec{r}$ to the average rate of bare ice melting.
Δs	Height above sea level below which there is enhanced melting.
δ	Fraction of the ice affected by enhanced melting.
α_{bi}, α_{mp}	Albedos of bare ice and melt ponds.
F_{sol}, F_{r}	Solar energy flux and the sum of longwave, latent, and sensible heat fluxes.
$\overline{F}_{\text{bi}}$, $\overline{F}_{\text{mp}}$, $\overline{F}_{\text{bot}}$, $\overline{F}_{\text{lat}}$	Fluxes of energy used for melting bare ice, ponded ice, ice bottom, and lateral melting averaged over bare ice, ponded ice, ice bottom, and the pond perimeter.
$\lvert\overline{F}\rvert$	Representative values of fluxes, e.g. their time-averages.
K_{lat}	Constant relating the flux of energy used for melting ponded ice to the flux of energy used for lateral melting.
S_{bi}, S_{mp}, S_{bot}, S_{em}	Strengths of bare ice melting, ponded ice melting, ice bottom melting, and enhanced melting.
S^*_{bi}, S^*_{mp}, S^*_{bot}, S^*_{em}	Effective strengths of bare ice melting, ponded ice melting, ice bottom melting, and enhanced melting, that take into account the effects of bare ice roughness.
S^*_{fs}	Effective strength of freeboard sinking, $S^*_{\text{fs}} = S^*_{\text{bi}} + S^*_{\text{mp}} + S^*_{\text{bot}}$.
S^*	Total effective strength, $S^* = S^*_{\text{bi}} + S^*_{\text{mp}} + S^*_{\text{bot}} + S^*_{\text{em}}$.

CHAPTER 3

SIMPLE RULES GOVERN THE PATTERNS OF ARCTIC SEA ICE MELT PONDS[1]

3.1 Introduction

Arctic sea ice plays a major role in Arctic climate (Perovich and Richter-Menge, 2009), ecology (Grebmeier et al., 1995), and economy. Sea ice's recent rapid decline is a hallmark of climate change (Serreze et al., 2007) that global climate models have systematically underestimated (Stroeve et al., 2007). This is believed to be largely due to small-scale processes that cannot be captured accurately by large-scale models (Holland and Curry, 1999). One such process is the formation of melt ponds on the ice surface during the summer (Holland et al., 2012). Melt ponds absorb significantly more sunlight than the surrounding ice, making ponded ice melt faster, creating a positive feedback (Morassutti and LeDrew, 1996; Perovich, 1996). The central importance of melt ponds was demonstrated by Schröder et al. (2014), who showed that the September sea ice minimum extent can be accurately predicted solely based on spring melt pond fraction. Current models of melt ponds include comprehensive representations of many physical processes and are capable of reproducing Arctic-scale spatial distributions of pond coverage (Flocco and Feltham, 2007; Lüthje et al., 2006; Skyllingstad et al., 2009; Taylor and Feltham, 2004). However, their complexity and numerous assumptions reduce their ability to provide a fundamental understanding of pond evolution, and call into question their applicability in a changing climate.

Ponds typically evolve through several stages that are controlled by ice permeability (Landy et al., 2014; Polashenski et al., 2012). Early in the season (typically late spring and early summer), ice is impermeable so that melt ponds can exist above sea level and cover a

1. This chapter was originally published as Popović et al. (2018). It is nearly identical to the original apart from minor changes made mainly to fit the formatting requirements of the thesis and to respond to the comments made by the thesis committee.

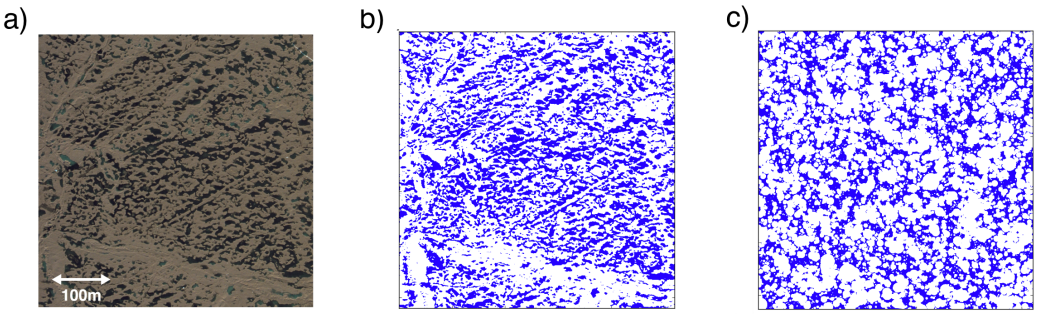

Figure 3.1: a) A photograph of melt ponds taken on August 7, 1998 during the SHEBA mission. b) A binarized version of the same image. c) A void model with a typical circle radius of $r_0 = 1.8$ m, and a coverage fraction of $\rho = 0.31$.

large portion of the ice. Later in the season, as ice permeability increases, the ponds drain to the ocean so that remaining ponds correspond to regions of sea ice that are below sea level. After drainage, ponds have a typical length-scale of several meters, likely determined by the scale of winter snow dunes (Petrich et al., 2012), and are often connected by channels that form during drainage. This post-drainage stage is typically the longest part of melt pond evolution. An aerial photograph of drained melt ponds is shown in Figure 3.1a.

Melt pond geometry has been shown to control the strength of lateral melting of ice by pond water (Skyllingstad and Paulson, 2007), to impact the pattern of floe breakup (Arntsen et al., 2015), and to set the landscape of available light for the organisms living beneath the ice (Frey et al., 2011). Several critical observations have previously been made about pond geometry. Hohenegger et al. (2012) showed that the fractal dimension, D, of late-summer melt ponds, which characterizes their area-perimeter relationship ($P \propto A^{D/2}$), transitions from $D \approx 1$ for small ponds to $D \approx 2$ for large ponds. The size (area) distribution of melt ponds has also been shown to be a power law (Perovich et al., 2002). Several models reproduce these observations. For example, Bowen et al. (2017) qualitatively reproduced the fractal transition by representing ponds as an intersection of a flat plane with a certain type of randomly generated surface. Ma et al. (2014) showed that both the power law size distribution and the fractal transition are captured by ponds represented as spin-clusters

in a random-field Ising model. However, neither of these works attempted to explain the origin of this behavior or the reason for its ubiquity, nor has made detailed comparison with observations. In this Chapter we will explain both the observation of fractal transition and of power-law size distribution using a simple geometric model without invoking any assumptions about the dynamics that govern the melt pond evolution, and will confirm the model's validity by comparing it in detail with observations from two different missions.

3.2 The void model

Our model is a representation of post-drainage melt ponds. It consists of randomly placing circles of varying size on a plane and allowing them to overlap. The area covered by circles in our model represents ice, while melt ponds are represented by the voids left between the circles (Figure 3.1c). Similar models are sometimes used to study transport properties in inhomogeneous materials, and are known as "Swiss cheese" models (Halperin et al., 1985). Physically, the circles can be thought of as regions where snow dunes used to be in the winter, and melt ponds fill in the space around them. Circle centers are placed with equal probability throughout the domain. Individual circles have radii, r, randomly drawn from an exponential probability distribution $p(r) = \frac{1}{r_0} e^{-r/r_0}$, where r_0 is the mean circle radius and defines the physical scale for the model. We chose this probability distribution mainly due to its simple form, but all of our main conclusions are robust to using other distributions (see Supplementary section 3.S4). After choosing r_0, the model is fully specified by choosing the fraction of the surface covered by voids, ρ. To compare our model with melt pond data, we analyzed hundreds of photographs of sea ice taken during helicopter flights on multiple dates during the SHEBA (Surface heat budget of the Arctic Ocean) (Uttal et al., 2002) mission of 1998 and the HOTRAX (Healy-Oden Trans-Arctic Expedition) (Darby et al., 2005) mission of 2005, and separated them into ice and pond categories using a machine learning algorithm (Figures 3.1a and b, Supplementary section 3.S1). In order to facilitate

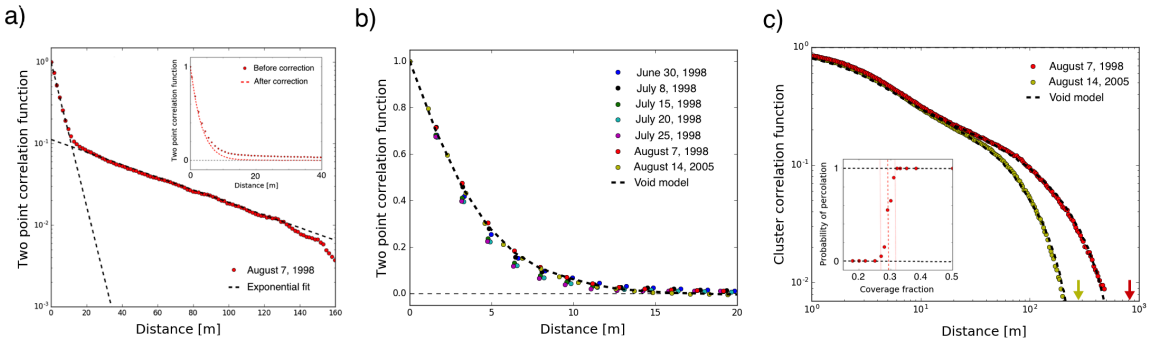

Figure 3.2: a) An example of the two-point correlation function, $C(l)$, for melt ponds shown on a semi-log plot. Dashed black lines represent fits to a small length scale exponential and a large length scale exponential. The inset shows $C(l)$ before and after a fit to the large length scale exponential has been subtracted. b) A comparison between the two-point correlation function for ponds from 1998 and 2005 (circles), and the void model (dashed line). Ponds on all dates show a similar scale matched by the void model using $r_0 = 1.8$ m. c) A comparison between the cluster correlation function, $g(l)$, for August 7, 1998 (red circles), August 14, 2005 (yellow circles), and the void model using the same r_0 as in panel b (black dashed lines). Both model lines use $\rho = 0.31$, and the difference between them is due only to differing simulated image sizes. The image size for 1998 is indicated by a red arrow and the image size for 2005 is indicated by a yellow arrow. The fact that the exponential cutoff is set by the image size indicates that the ponds are roughly at the percolation threshold. The inset shows an independent estimation of the percolation threshold. Red points show the probability of finding a spanning cluster in the void model implemented on a grid the same size and resolution as the SHEBA images. The probability of finding a spanning cluster increases from 0 to 1 between $\rho = 0.28$ and $\rho = 0.31$.

comparison with pond images, we implemented the void model on a grid with the same resolution and size as the pond images.

3.3 Calibrating the model parameters

We begin the comparison by choosing the model parameters, r_0 and ρ. To this end, we define two functions - the two-point correlation function, $C(l)$, and a cluster correlation function, $g(l)$, and compare them for pond images and the model. A two-point correlation function measures the probability that two points separated by a distance l are both located on *some* pond, while a cluster correlation function measures the probability that they are

both located on *the same* pond. We first estimate r_0 using $C(l)$, because we can define it to be largely insensitive to changes in ρ (see below). Once we have calibrated r_0 by matching $C(l)$, we can choose ρ using $g(l)$.

For two points, $\mathbf{x}$ and $\mathbf{y}$, separated by a distance l, the two-point correlation function can be defined as:

$$C(l) = \frac{\langle z(\mathbf{x})z(\mathbf{y})\rangle - \rho^2}{\rho(1-\rho)} \ , \tag{3.1}$$

where $z(\mathbf{x}) = 1$ if a point $\mathbf{x}$ is located on a pond, and $z(\mathbf{x}) = 0$ otherwise, and $\langle ... \rangle$ represents averaging over different points and over different images. Subtracting ρ^2 and dividing by $\rho(1-\rho)$ constrains $C(l)$ to vary between 1 and 0, and makes it insensitive to changes in ρ (see Supplementary section 3.S2). The two-point correlation function determines a typical length scale of variability in melt pond coverage.

Plotting $C(l)$ for melt ponds on a semi-log plot reveals that it is approximately a sum of two exponentials (Figure 3.2a). Therefore, there are two characteristic length scales in melt pond images - a small length scale comparable to the size of individual ponds and a large length scale that is comparable to the size of the image. The large length scale corresponds to variability of pond fraction due to large-scale ice features such as ridges or rafted ice floes. To focus on melt pond features, we have removed the contribution to $C(l)$ from large scale ice features by subtracting a fit to an exponential of $C(l)$ for $l > 25$ m. We varied this threshold, but found little difference in the results. After subtracting the fit, we normalized the remainder so that $C(0) = 1$ (inset of Figure 3.2a). We show the resulting functions for all of the available dates and compare them to the void model in Figure 3.2b. Ponds of all dates show similar $C(l)$ dropping by a factor of e after roughly 3.3m. We found that this is well reproduced by the void model using $r_0 = 1.8$ m (see Supplementary section 3.S2). The fact that the void model reproduces the shape of the two-point correlation function suggests that our assumption of randomly placing the circles is reasonable.

Next, we determine ρ. With this parameter, we wish to capture the pond geometric

features such as the pond size distribution and the fractal dimension, rather than simply the pond coverage. For this reason, we do not set ρ equal to the pond coverage fraction of melt pond images, but instead we use the cluster correlation function to determine ρ. Essentially, the cluster correlation function, $g(l)$, measures the probability that two points separated by a distance l belong to the same finite pond. However, there are some technical subtleties in how we define $g(l)$, and we give a precise definition in Supplementary section 3.S2.

In the model, in the limit of infinite domain size, there exists a well-defined coverage fraction, ρ_c, the "percolation threshold," above which infinite clusters exist, and below which there is a maximum cluster size. The cluster correlation function in the void model sensitively depends on the deviation of the pond fraction from this percolation threshold, $|\rho - \rho_c|$ (see Supplementary section 3.S2). Below and above the percolation threshold, the cluster correlation function is greater than zero up to a certain distance, after which it exponentially decreases. As the coverage fraction approaches the percolation threshold, this cutoff length grows, and sufficiently close to the threshold, it is set by the image size. The location of the exponential cutoff quantifies the typical size of the largest finite connected pond cluster. We discuss the functional form of $g(l)$ in detail in Supplementary section 3.S6.

Narrow connections between ponds are often missed by the image processing algorithm so that for many dates $g(l)$ depends on the artificial threshold parameter used in the machine learning algorithm to separate ice from ponds (see Supplementary section 3.S1, for details). The only dates after pond drainage for which $g(l)$ is stable against changes in this threshold are August 7 of 1998 and August 14 of 2005. In Figure 3.2c, we compare the cluster correlation function for the void model and data on those dates. Remarkably, the pond clusters for both dates appear to be organized very near the percolation threshold, as indicated by the fact that the length scale of exponential cutoff in $g(l)$ is set by the image size. In Figure 3.2c we use $\rho = 0.31$ to match the pond data, and the difference between $g(l)$ for the ponds from 1998 and ponds from 2005 is solely due to a different image size. In fact, using any ρ

from a range $0.28 < \rho < 0.31$ provides an equally good fit to the data, which indicates that within this entire range the size of the largest pond is determined by the image size. We note that in real pond images, there exist large-scale features such as ridges, cracks, or ice floes that may also limit the size of the largest connected pond. However, since these features are often of size that exceeds the image size as evidenced by the large length scale comparable to image size derived from $C(l)$, the exponential cutoff in $g(l)$ for real images is likely still determined by the size of the image.

To independently confirm that ponds are well-described by the void model near the percolation threshold, we ran the void model, 50 times at multiple values of ρ, and found the probability of forming a cluster that spans at least one dimension of the image (inset of Figure 3.2c). We found that this probability increases from 0 to 1 between $\rho = 0.28$ and $\rho = 0.31$, which closely matches the range of coverage fractions that fit the pond $g(l)$. We note that although we chose ρ to match the cluster structure between the model and the data, the value we found agrees reasonably well with the pond coverage fraction on those dates ($30\% \pm 5\%$ on August 7 of 1998, and around $40\% \pm 5\%$ on August 14 of 2005). We discuss the relationship between the pond coverage fraction and pond geometry in detail in Supplementary section 3.S6.

It is remarkable that the properties of ponds from 1998 and 2005, which likely developed under very different environmental conditions, are so similar: the correlation functions for both years are well-fit by the void model using the same r_0 and ρ. This is particularly surprising since sea ice during the 1998 mission had a large proportion of multiyear ice, whereas ice during the 2005 mission was predominantly first-year ice.

3.4 Fractal dimension and size distribution in model and data

Having chosen r_0 and ρ, we can proceed to explain the observations of pond fractal dimension and size distribution. Following Hohenegger et al. Hohenegger et al. (2012), we define

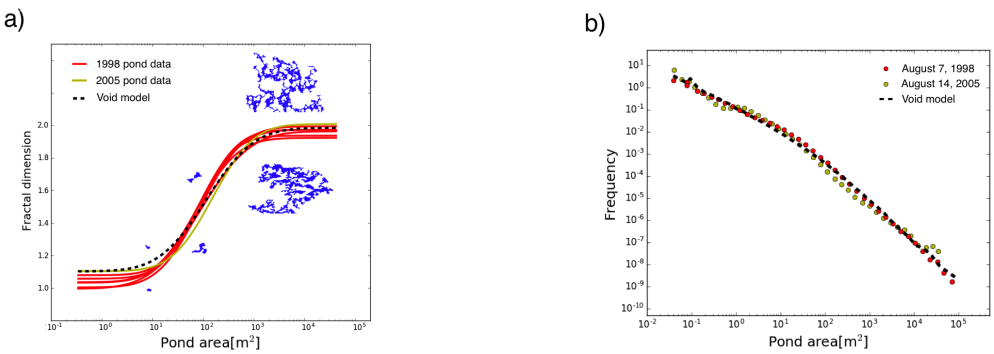

Figure 3.3: a) A comparison between the fractal dimension of pond boundaries for different dates after pond drainage from 1998 (red curves), 2005 (yellow curve), and the void model with r_0 and ρ the same as in Fig 2 (black dashed curve). Examples of ponds (below the curve) and voids (above the curve) of various sizes are also shown. b) Size distribution for ponds on August 7, 1998 (red dots), ponds on August 14, 2005 (yellow dots), and the void model (black dashed line).

the fractal dimension of the pond boundary as the exponent that relates the area and the perimeter of the pond, $P \propto A^{D/2}$. The fractal dimension can vary between the fundamental limits of $D = 1$ for regular shapes such as circles to $D = 2$ for space-filling or linear shapes. We find D as a function of A by fitting a curve to the area-perimeter data. We explain the details of this fitting procedure in the Supplementary section 3.S3.

In Figure 3.3a we find D as a function of A for pond data on all dates from the summer of 1998 after pond drainage (red curves) and 2005 (yellow curve). Our results are consistent with Hohenegger et al. (2012), with the pond fractal dimension transitioning from $D \approx 1$ to $D \approx 2$ at $A_c \approx 100$ m^2, and a transition range spanning roughly 2 orders of magnitude. Without any tuning other than choosing r_0 and ρ using the correlation functions, the void model is able to match the observed transition in pond fractal dimension nearly perfectly (Figure 3.3a, black dashed curve).

In the Supplementary section 3.S7, we give an argument that a transition from $D < 2$ to $D \approx 2$ is a generic consequence of individual objects connecting and, therefore, cannot be used as strong support for any particular physical model of melt ponds. On the other hand, matching the fractal transition scale and the transition range are non-trivial, and cannot

be reproduced by an arbitrary model of randomly connecting objects (see Supplementary section 3.S9). At small sizes, the void model predicts a dimension slightly larger than 1, likely corresponding to the fact that small voids are not necessarily simple smooth shapes. It is possible that small-scale physical processes in real ponds, such as erosion of pond walls, are responsible for smoothing small ponds into more circular shapes with $D \approx 1$.

Finally, we compare the pond size distribution with the void model in Figure 3.3b. Again as a result of sensitivity to the threshold parameter in the machine learning algorithm, we only use pond data for August 7th of 1998 and August 14th of 2005. At scales larger than roughly 10 m^2 the pond size distribution follows an approximate power law, in agreement with previous findings. The power law behavior is particularly clear for ponds from 1998, and the power law exponent (approximately 1.8) is slightly larger than previously found (Perovich et al., 2002). Using the same r_0 and ρ as before, the void model reproduces the pond size distribution over the entire range of observations, more than 6 orders of magnitude. This matching is highly robust: the void model matches the pond size distribution even at the smallest scales regardless of details such as the circle radius distribution or the shape of the objects placed randomly (see Supplementary section 3.S4).

3.5 Conclusions

We have shown that a simple model of voids surrounding overlapping circles captures key geometric patterns of Arctic melt ponds with high fidelity and robustness, with only two parameters that can be chosen naturally by comparing the model and the data. Our model is purely geometric, and can therefore be used as a benchmark against which to test any physical model. This work shows that much of melt pond geometry can be understood simply by assuming that melt ponds are placed randomly and have a typical size. Even though many models will reproduce the same universal features, our model is special in that it captures quantitative details of melt pond geometry beyond what an arbitrary model of

connecting objects is capable of doing. Our work raises two critical questions about melt pond physics that must be answered. First, why does the pond scale appear to be so robust for ponds evolving under differing environmental conditions, and, second, why do ponds seem to be organized near the percolation threshold? The answer to the second question is particularly interesting, as points to self-organized critical behavior in melt ponds, and suggests that the pond coverage fraction is more constrained than previously thought. We address this question in Chapter 4. Answering these questions may yield deeper insight into melt pond physics and allow for a better representation of this important process in global climate models.

3.6 Supplementary Information

3.S1 Image analysis

We used airborne photographs taken during the SHEBA mission of 1998 and the HOTRAX mission of 2005 (Figure 3.3a). During SHEBA, sea ice was regularly photographed from a helicopter, and the SHEBA photographs are available on eight dates spanning the entire melt season of 1998. Six of those eight dates were after pond drainage. Helicopter photographs from the HOTRAX mission that have unfrozen ponds on unbroken ice floes are only available for August 14th of 2005. SHEBA images have dimensions of 819 m by 1228 m, with a resolution of roughly 0.2 m per pixel. HOTRAX images have dimensions of 427 m by 284 m, with a resolution of 0.14 m per pixel and are higher quality than SHEBA images. For each available date, we only used images that have few cracks in the ice and little crushed ice that might be mistaken for melt ponds by the image classifying algorithm. We also manually removed the regions of open ocean before running the algorithm. Finally, we separated ice from ponds using an open access machine learning software "ilastik" (http://ilastik.org/). For most dates we analyzed more than 10^5 individual ponds.

We trained the machine learning algorithm "ilastik" using information from images about color, intensity, color gradient, and texture, which are available as options in the software's user interface. The output of the algorithm is a probability matrix characterizing the likelihood that each pixel is ice or pond. To identify ponds, we chose a threshold probability, p_t (usually 0.5), and classified each pixel as a melt pond if the algorithm found it to have a higher probability than p_t. To make sure melt pond features we wish to describe are robust, we varied the threshold probability. We found that some characteristics of binarized images depend on p_t. For example, pond coverage fraction varies by as much as 10% between $p_t = 0.1$ and $p_t = 0.9$. For this reason, in the main text and the remainder of the Supplementary Material, when referring to the mean pond coverage fraction on particular dates, we also give a range of coverage fractions that can be obtained by changing p_t. Furthermore, we found that for many dates the cluster correlation function, $g(l)$, and the pond size distribution are sensitive to this parameter. Therefore, we only considered $g(l)$ and the pond size distribution on dates for which ponds could be clearly distinguished so that these statistics were insensitive to changes in p_t. This was true only for June 22 and August 7 of 1998 and August 14 of 2005. As June 22 is before complete pond drainage, in the main text we report $g(l)$ and the pond size distribution only for August 7 of 1998 and August 14 of 2005. This sensitivity of $g(l)$ and the size distribution to p_t is likely due to the fact that these statistics rely on accurately identifying the narrow connections between the ponds. Images from 2005 were high enough quality, and August 7 of 1998 had ponds that were dark enough to be easily distinguished from ice. However, we acknowledge the possibility that the perceived similarity in the cluster correlation function for the two dates may be due to this early selection bias.

The size of melt ponds can be accurately estimated by summing all the areas of individual pixels within a pond. Estimating the pond perimeter is slightly more challenging (Figure 3.S1). Summing the lengths of all pixel edges on the pond boundary gives an inaccurate

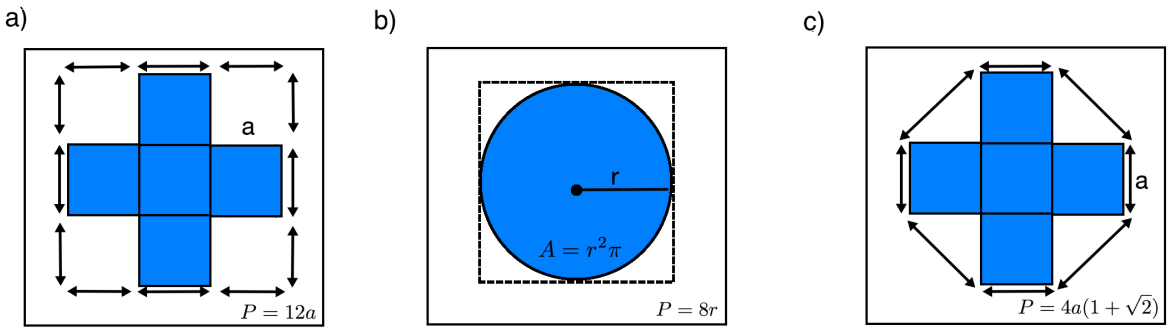

Figure 3.S1: A diagram explaining how we find the perimeter. a) Blue squares represent individual pond pixels. The perimeter is estimated as the sum of all boundary pixel edges. b) Finding the perimeter of a circle as in panel a), we inaccurately estimate it to be the perimeter of a square surrounding the circle. Estimating the perimeter in this way is equally inaccurate regardless of how fine the image resolution is. c) The problem is partially corrected if we take into account the relative positions of the nearest neighbor boundary pixels. If two nearest neighbor pixels are located diagonally, we add the distance between them to the total perimeter.

estimate of the perimeter, because pixels are located on a grid, and cannot take into account the curvature of the boundary. For example, if we try to estimate the perimeter of a circle by summing the lengths of all pixel edges on its boundary, we will get the perimeter of a square enclosing that circle (Figure 3.S1b). We partially correct for this by considering the nearest neighbor pixels on the boundary: if the nearest neighbors are positioned diagonally, we add a distance between them to the total perimeter (Figure 3.S1c). Even with this correction, there is still a small systematic error in the estimate. This, however, did not affect our estimates of the pond statistics: different methods used for finding the perimeter simply introduced a constant bias in the perimeter of the ponds, and therefore did not change our estimates of the fractal dimension. Some objects in nature (a notable example is the coast of Britain (Mandelbrot, 1967)) suffer from a fundamental difficulty in determining the perimeter, because the length of the perimeter depends on the length of the measuring stick. In our case this is not a problem, because small ponds are regular shapes ($D_1 \approx 1$) and we can resolve them easily in our images.

3.S2 Correlation functions

In this section, we will first give a precise definition of the cluster correlation function, $g(l)$, and then we will explore how the two correlation functions, $C(l)$ and $g(l)$, depend on the model parameters r_0 and ρ.

We define the cluster correlation function, $g(l)$, as the probability that two points separated by a distance l belong to the same non-spanning pond given that one of the points is already located on a non-spanning pond. For both model and data, "spanning ponds" are those ponds that span at least one dimension of the image. In order to obtain a good fit to the data, it is necessary to exclude spanning clusters from the computation of $g(l)$. This is reasonable since in the pond images, ponds are constrained by large scale features, such as floe edges or ridges, which make the void model inapplicable above a certain pond size (see also Supplementary section 3.S5). In the void model, above the percolation threshold, there is typically one spanning pond, while in the pond images spanning ponds typically do not exist.

We found the parameters r_0 and ρ approximately by running the model at multiple values of of these parameters, and among these runs choosing the one for which the two-point correlation function, $C(l)$, and the cluster correlation function, $g(l)$, best agree with the correlation functions of ponds. Because r_0 is the only length scale in the model (apart from the image size), all of the characteristic lengths must scale with r_0. In Figs. 3.S2a and c, we show how $C(l)$ and $g(l)$ depend on r_0. We can see that the decay rate of $C(l)$ for the model is proportional to r_0, and the model and data agree well for $r_0 = 1.8$m. At small l, $g(l)$ is also scaled by r_0, but at large l, it is insensitive to changes in r_0 because the cutoff length is set by the image size. In Fig. 3.S2b and d, we show how $C(l)$ and $g(l)$ vary with ρ at fixed r_0. The two-point correlation function is largely insensitive to changes in ρ: $C(l)$ decreases slightly with decreasing ρ, but this effect only becomes noticeable at low coverage fraction, $\rho \approx 0.1$, beyond the range of coverage fractions we are considering in this

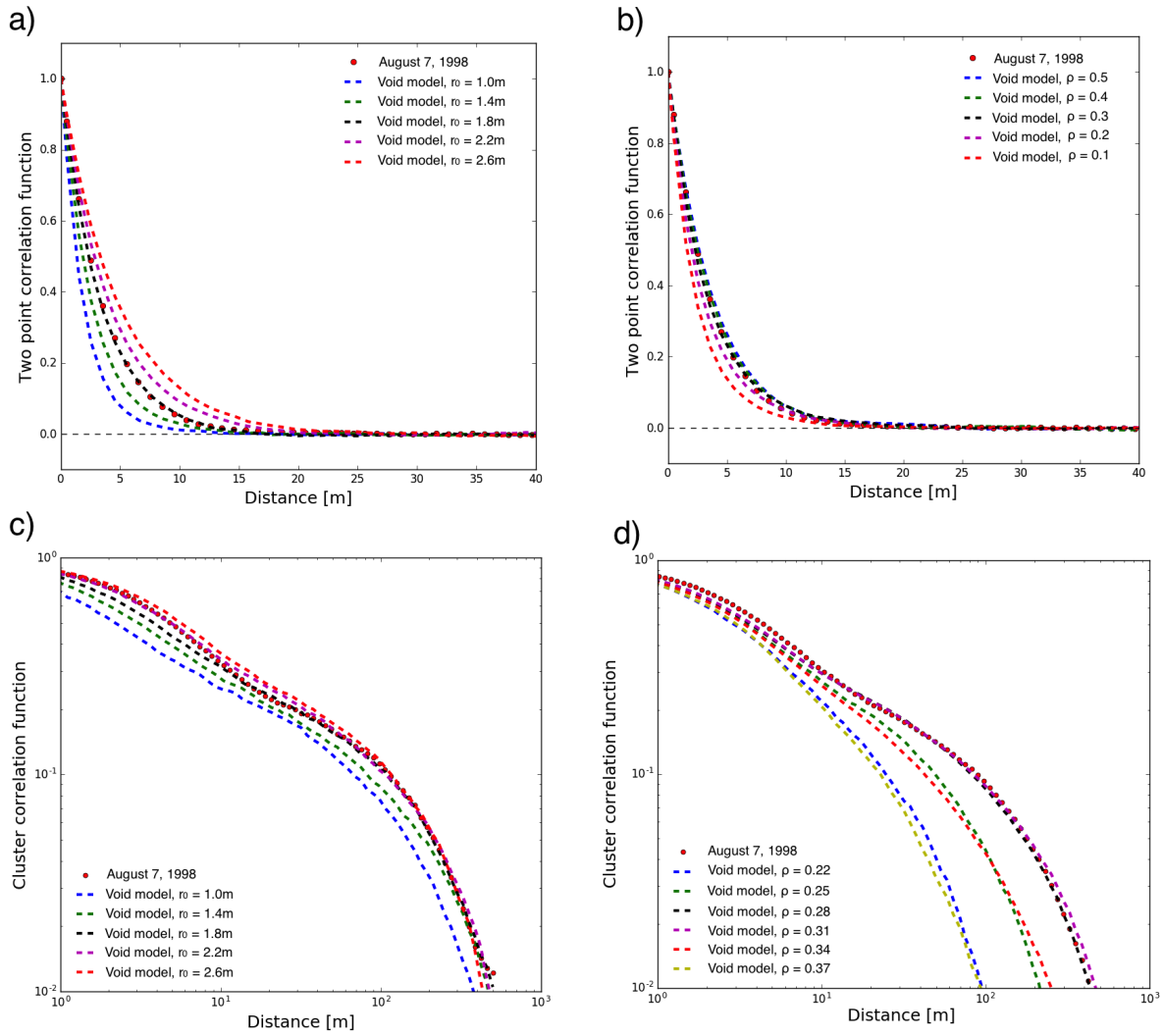

Figure 3.S2: Dependence of correlation functions on model parameters r_0 and ρ. In each plot, red dots represent data for August 7th,1998. a) Two-point correlation function for different values of r_0 at $\rho = 0.3$. b) Two-point correlation function for different values of ρ at $r_0 = 1.8$m. c) Cluster correlation function for different values of r_0 at $\rho = 0.3$. d) Cluster correlation function for different values of ρ at $r_0 = 1.8$m.

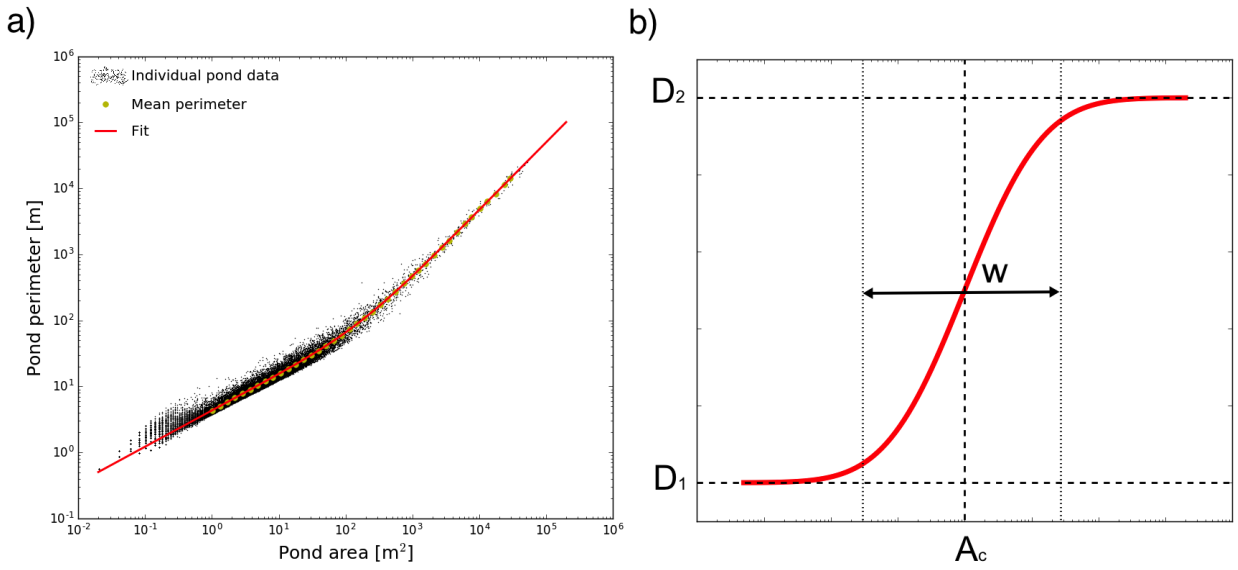

Figure 3.S3: An explanation for the fitting procedure to determine the fractal dimension curve. a) The black dots represent area and perimeter of individual ponds. The yellow dots represent a moving average of the perimeter. The red line is a fit of the mean area-perimeter data to a function $f(\log(A))$ defined in Eq. (3.S2). b) Fractal dimension, D, as a function of size, determined as a derivative of the red line in panel a with respect to $\log A$. Fitting parameters defined in Eq. 3.S1 are also shown.

Chapter. On the other hand, $g(l)$ depends sensitively on ρ. The cutoff length of the cluster correlation function reaches its maximum close to the percolation threshold ($\rho \approx 0.3$), and decreases sharply when ρ deviates from this threshold. Because we excluded the spanning clusters from calculations of $g(l)$, the cluster correlation function has the same shape both above and below the percolation threshold.

3.S3 Estimating the fractal dimension

The fractal dimension may be obtained from the derivative of the pond perimeter with respect to pond area in log-log space, $D = 2\frac{d\log P}{d\log A}$. In order to estimate the fractal dimension, we first find the moving average of the perimeter of all the ponds that fall into a certain log-area bin, $\langle P\rangle$, as a function of $\log A$. A log-area bin of width Δ centered on A is defined as a range from A/Δ to $A\Delta$. Log-binning defines a set of points $(\log A, \log\langle P\rangle)$. Direct differencing of

these data gives noisy results. Instead, we first fit a function to the $(\log A, \log \langle P \rangle)$ points, and then take its derivative. Anticipating that the fractal dimension will change from a low to a high value, we choose to represent it with an error function of log-area

$$D(A) = \frac{D_2 - D_1}{2} \text{ erf } \log \left(A/A_c\right)^{1/w} + \frac{D_2 + D_1}{2} \ , \tag{3.S1}$$

where D_1, D_2, $\log A_c$, and w are fitting parameters and represent the lower fractal dimension, the upper fractal dimension, the center of the fractal transition in log-area, and the width of the fractal transition. Assuming this form of $D(A)$, the fitting function is given by the integral of Eq. 3.S1 (Figure 3.S3a):

$$f(x) = \frac{D_2 - D_1}{4} \left((x - \log A_c) \text{ erf } \frac{x - \log A_c}{w} + \frac{w}{\sqrt{\pi}} e^{-\frac{(x - \log A_c)^2}{w^2}} + \frac{D_2 + D_1}{D_2 - D_1} x \right) + C \ , \tag{3.S2}$$

where C is a constant of integration, which we regard as another fitting parameter. The fractal dimension is then found as

$$D = 2 \frac{df(\log(A))}{d \log A} \ , \tag{3.S3}$$

and is given by Eq. 3.S1 (Figure 3.S3b). We found that this method of estimating D is in good agreement with other similar methods, such as fitting a function to directly differenced data or smoothing out the directly differenced data. Log-binning the data before any additional processing was important for two reasons: 1) it smooths the data, and 2) it assigns equal weights to large and small ponds during fitting. This latter property is especially important since there are several orders of magnitude more small ponds than large ponds, and a fit to data that was not log-binned would be determined nearly entirely by small ponds.

3.S4 Robustness of the void model

The void model reproduced the pond data highly robustly, regardless of details such as the distribution of circle radii, $p(r)$, or the exact shape of the objects placed. In addition to an exponential distribution of circle radii, we tested the model using other distributions, such as Gaussian, Rayleigh, and Gamma distributions, and found that the correlation functions, fractal dimension, and size distribution are insensitive to these details. Even in the limit of no variation in the circle radius, all of the characteristics can be reasonably well reproduced, although the agreement with the data is affected somewhat. Real melt ponds are often strongly anisotropic (compare Figures 3.1b and c). We tested the effect of anisotropy in our model by placing randomly sized ellipses with a fixed ratio of semi-major to semi-minor axis instead of circles. The ellipses had a preferred orientation and we changed the degree to which they align with this preferred orientation. None of these changes altered the main conclusions of our model: matching the correlation functions led to matching fractal dimension curves and size distributions for the broad range of ellipse parameters used in the simulations. Some quantities were slightly affected. For example anisotropy decreased the value of the percolation threshold by several percent.

In addition to the void model, we also explored its negative: a model where ponds are represented by overlapping circles. The circle model can also reproduce most of the observations, but the results are less robust and quantitatively less accurate. For example, matching the two correlation functions does not reproduce the center of the fractal transition. It is possible to remedy this by placing ellipses instead of circles or changing the circle radii distribution, but in this case the range of the transition is affected by the ratio of the semi-major to semi-minor axis if we place ellipses, or the particular form of the circle radii distribution. The circle model also suffers other drawbacks compared to the void model: it reproduces the pond size distribution over only 4, rather than more than 6, orders of magnitude and only for large ponds, it does not match the cluster correlation function

as well, and it matches the observations at a ρ significantly higher than the actual pond coverage (actual pond coverage fractions for August 7th of 1998 and August 14th of 2005 were 0.3 ± 0.05 and 0.4 ± 0.05, close to the void model $\rho \approx 0.3$, and significantly less than the circle model $\rho \approx 0.7$). The fact that the circle model captures the pond size distribution only for large ponds is due to the fact that beyond the typical circle size, the shape of the connecting clusters is roughly independent of the detailed shape of the connecting objects. Therefore, the fact that the void model captures the measured pond size distribution over the entire observational range suggests that it captures the essential elements of melt pond geometry even at the small scale. For all of the reasons above, we believe the void model is a better description of melt ponds than the circle model.

The exponent of 1.8 we found for the pond size distribution is slightly less than 2.05, which is predicted for the universality class of percolation models. This is likely due to finite size effects, as the image size is less than two orders of magnitude larger than the length scale determined by the two point correlation function. To support this hypothesis, we ran a "site percolation" model for different lattice sizes. In this model, each grid point on a lattice is occupied with a certain probability, and two occupied nearest neighbor sites are considered connected. We found that the cluster size distribution of site percolation on a 100x100 lattice decays with an exponent close to 1.8, while the exponent approaches 2.05 for large lattices.

3.S5 Limitations of the void model

When calibrating the circle scale using the two-point correlation function, we had to remove a long length-scale exponential from the correlation function. This indicates a limitation of our model: it is unable to represent pond variability on an arbitrarily large scale, because in real ice there exist large features, such as ridges, cracks, or floe edges, that are not represented in the model. One result of this limitation is that the void model predicts infinite ponds,

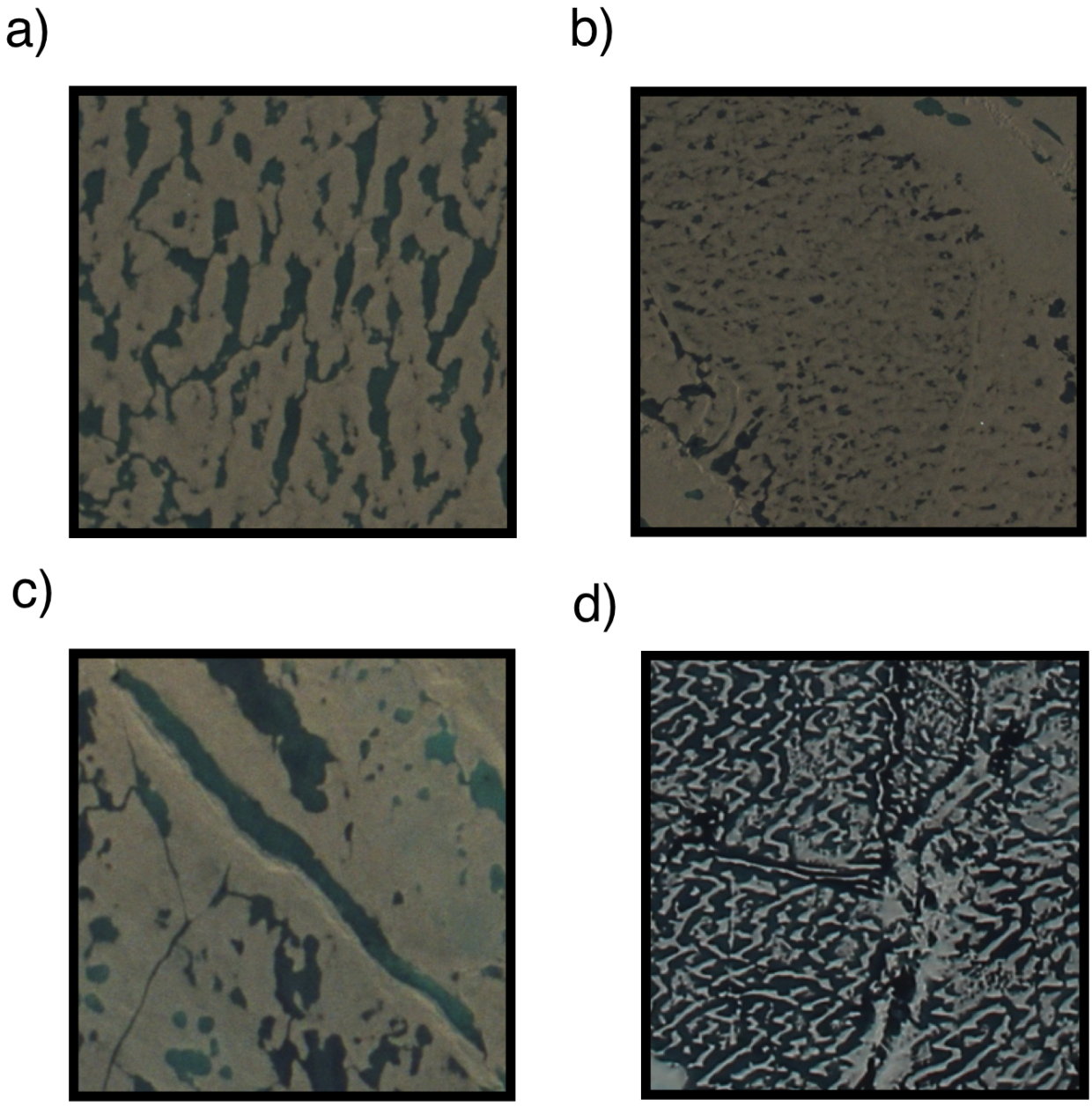

Figure 3.S4: Examples of melt ponds that appear to violate the assumption of random placement. a) "Banded" melt ponds with clear spacings between melt pond bands. b) A low pond coverage region of the ice with small melt ponds that seem to be located non-randomly. c) A long melt pond located along a ridge. d) "Tiger stripe" melt ponds with clear ordering.

which are unrealistic, and which we had to remove from the analysis in order to obtain a good match between the model and the data (see the definition of the cluster correlation function in section 3.S2). The limit of applicability of our model can be estimated from the long length exponential of the two-point correlation function to be several hundred meters.

One of the key assumptions of our model is the random placement of circles on a plane; however, real melt ponds sometimes violate this assumption. Examples of ponds that are not randomly placed are shown in Figure 3.S4. The fact that our model is able to reproduce pond statistics suggests that these types of ponds were not very prevalent in our data. However, it may happen that under different conditions, non-random ponds might become significant.

3.S6 Relationship between pond geometry and coverage fraction

The parameter ρ in the void model controls both the connectedness of the voids and the void coverage fraction. A priori, there is no reason to believe that such a link between coverage fraction and geometry exists in real melt ponds. For example, ponds may be connected by narrow channels, thereby increasing the typical pond size while leaving the coverage fraction virtually unchanged. On the other hand, pond growth by lateral melting would likely increase the coverage fraction without changing the connections between ponds much. In section 3.3, we chose ρ in the void model such that it reproduces the geometry of melt ponds, and did not consider the pond coverage fraction and whether it is related to geometry. For this reason, in this section we will show that this relationship also exists in real melt ponds. To avoid confusion, in this section we will call ρ^m the coverage fraction in the model, and ρ^p the pond coverage fraction.

The key to understanding pond connectedness is the cluster correlation function, $g(l)$. We can guess the functional form of $g(l)$ for the void model solely from considering its asymptotics. Properties of $g(l)$ to note are:

1. At small separation, l, two points located on a pond will most likely belong to the

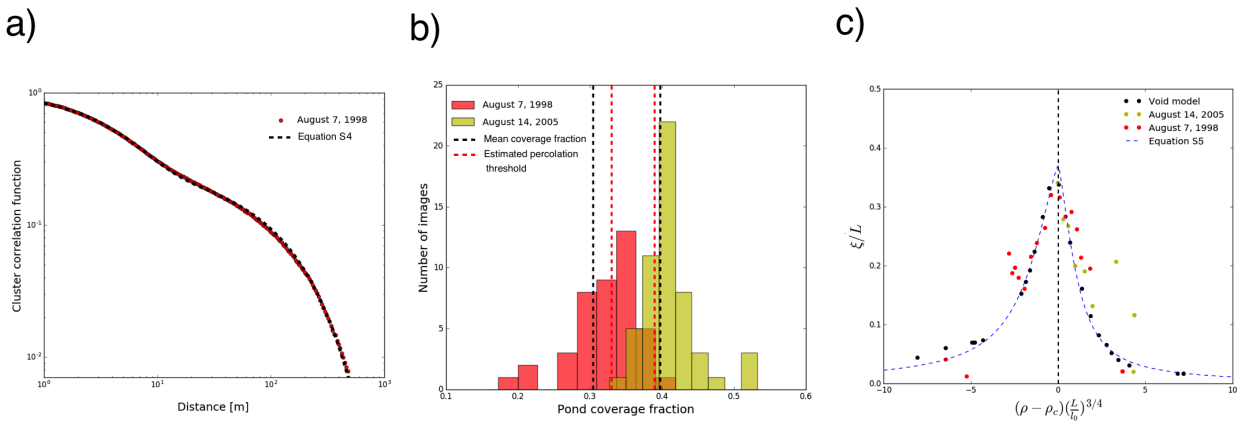

Figure 3.S5: a) A fit of Eq. 3.S4 (black dashed line) to the cluster correlation function of ponds on August 7, 1998 (red dots). We set ρ equal to the mean pond coverage on August 7, and we treat l_0 and ξ as fitting parameters. b) Number of images that fall into each bin of pond coverage fraction for August 7, 1998 (red bars) and August 14, 1998 (yellow bars). Vertical black dashed lines represent mean coverage fraction on the two dates, while the vertical red dashed lines represent the estimated coverage fraction of the percolation threshold for each date. All of the pond coverage fractions were estimated using the machine learning threshold $p_t = 0.5$. c) Estimated correlation length scaled by the image size, ξ/L, as a function of the appropriately scaled distance from the percolation threshold, $(\rho-\rho_c)(L/l_0)^{3/4}$, for the void model (black dots), August 7, 1998 (red dots) and August 14, 2005 (yellow dots). Values for the percolation threshold used were 0.3 for the void model, 0.33 for 1998 ponds, and 0.39 for 2005 ponds. Also shown is Eq. 3.S5 (blue dashed line), consistent with theoretical considerations.

same pond. So, $g(l)$ should be the same as the two-point correlation function up to normalization by the coverage fraction. Therefore, $g(l) \approx (e^{-l/l_0}(1-\rho)+\rho)$ for $l \ll l_0$, where e^{-l/l_0} is the two-point correlation function for randomly placed objects.

2. At separations on the order of or larger than the correlation length, ξ, $g(l)$ should decay to zero exponentially. So, $g(l) \approx e^{-l/\xi}$ for $l > \xi$.

3. At intermediate separations, $l_0 \ll l \ll \xi$, percolation theory predicts a power law decay with a universal exponent, $g(l) \propto l^{-5/24}$ (Aharony and Stauffer, 2003; Essam, 1980).

A function consistent with these asymptotics is:

$$g(l) = \left(e^{-l/l_0}(1-\rho)+\rho\right)\left(\frac{l_0+l}{l_0}\right)^{-5/24} e^{-l/\xi} \ . \tag{3.S4}$$

In Figure 3.S5a, we show that this equation and $g(l)$ for ponds on August 7th, 1998 agree nearly perfectly. Equally good fits can be obtained for 2005 ponds and for the void model.

The link between coverage fraction and geometry in the void model is reflected in the fact that the correlation length, ξ, that measures the size of the largest voids, is a function of the coverage fraction, ρ^m. Near the percolation threshold, ρ_c, percolation theory predicts this dependence to be of the form $\xi = \xi_\infty f\left(\frac{L}{\xi_\infty}\right)$ (Aharony and Stauffer, 2003; Essam, 1980; Goldenfeld, 1992), where L is the image size, ξ_∞ is the correlation length on an infinite image, and $f(x)$ is a universal function that scales as $f(x) \propto x$ for $x \to 0$, and $f(x) \to 1$ for $x \to \infty$. The correlation length on an infinite image, ξ_∞, is given by $\xi_\infty = A_\pm l_0 |\rho^m - \rho_c|^{-4/3}$ (Aharony and Stauffer, 2003; Essam, 1980), where $\pm$ stands for $\rho^m > \rho_c$ and $\rho^m < \rho_c$, and $A_\pm$ are non-dimensional numbers with $A_-/A_+ = 2$ (Delfino et al., 2010). To obtain the correct units, the correlation length must be proportional to the fundamental length scale, l_0, that can be estimated from a fit to Eq. 3.S4. A non-dimensional correlation length,

$\hat{\xi} \equiv \xi/L$, consistent with these asymptotics is

$$\hat{\xi} = \hat{\xi}_\infty \left(1 - e^{-\frac{B}{\hat{\xi}_\infty}}\right) , \tag{3.S5}$$

where B is a non-dimensional number, and $\hat{\xi}_\infty = \xi_\infty/L$. Here, we wish to test whether there is such a relationship between pond coverage, ρ^p, and the correlation length in real melt pond images.

In Figure 3.S5b, we show the distribution of pond coverage fraction for images taken on August 7th, 1998 and August 14th, 2005, estimated using the threshold $p_t = 0.5$, used by the machine learning algorithm to identify the melt ponds. We can use the fact that there is substantial spread around the mean pond coverage to test the relationship between ξ and ρ^p. We split the entire range of pond fractions into bins and find $g(l)$ only for images with ρ^p that falls into a certain bin. We then use Eq. 3.S4 to fit $g(l)$ for each of the coverage bins. When fitting, we set the parameter $\rho = \rho^p$, and treat l_0 and ξ as fitting parameters. We also perform the same procedure to the void model with different ρ^m.

In Figure 3.S5c, we compare the model, the data, and Eq. 3.S5. The void model conforms to Eq. 3.S5 except sufficiently far from the percolation threshold where the theoretical prediction for ξ_∞ is no longer valid. Melt ponds on both August 7th, 1998, and August 14th, 2005 also seem to follow the same trend. These data indicate that the pond coverage fraction controls the pond geometry in a similar way as in the void model. However, we cannot simply relate ρ^m in the void model to the pond coverage fraction, because the values of the percolation threshold differ between the two dates and the model. To obtain a match in Figure 3.S5c, we used $\rho_c = 0.3$ for the void model, $\rho_c = 0.33$ for 1998 ponds, and $\rho_c = 0.39$ for 2005 ponds. In Figure 3.S5b we indicated these values and compared them to the mean pond coverage fraction. For both dates, the percolation threshold used in Figure 3.S5c is very close to the mean coverage fraction, indicating again that the ponds are organized near the percolation threshold.

Mean pond coverage fraction, and its effect on sea ice albedo, is often the main quantity of interest in the large scale models. Here we showed that the mean ρ^p is very close to the percolation threshold, meaning that ρ^p may be more constrained than previously thought. Understanding what physically sets the percolation threshold may be crucial to understanding the evolution of melt ponds and representing them in large scale models.

3.S7 A fractal transition is a general consequence of connecting objects

The void model is not the only model able to produce a transition in fractal dimension from $D < 2$ to $D = 2$. As described above, its negative, a model of overlapping circles, produces a transition from $D = 1$ to $D = 2$. Many other models, such as a model of random topography (Bowen et al., 2017) or the Ising model (Ma et al., 2014), also reproduce the same feature. Here we give a qualitative argument for why this is a general feature of connecting objects.

To understand why the transition happens in the void model, we will first show that voids may be seen as a collection of connecting objects of a typical size, and then we will argue that for such systems the upper fractal dimension should be $D \approx 2$. We will neglect the variation in the circle size, but a similar argument applies even in the presence of this variation.

If all the circles have the same size, the void model may be mapped onto a random network of nodes and bonds in the following simple way (Kerstein, 1983). We first segment the entire plane into regions, such that all of the points within a given region are closest to one of the circle centers (Figure 3.S6a). The regions obtained in this way are polygons (known as the Voronoi polygons), and the procedure of segmenting the plane is known as the Voronoi tessellation. Boundaries of these polygons define a network of nodes (the corners of the polygons) and bonds (sides of the polygons). We consider two nodes to be connected if a bond between them does not pass through any of the circles (Figure 3.S6b). It was shown (Kerstein, 1983) that if the circles have a constant radius, nodes that are connected

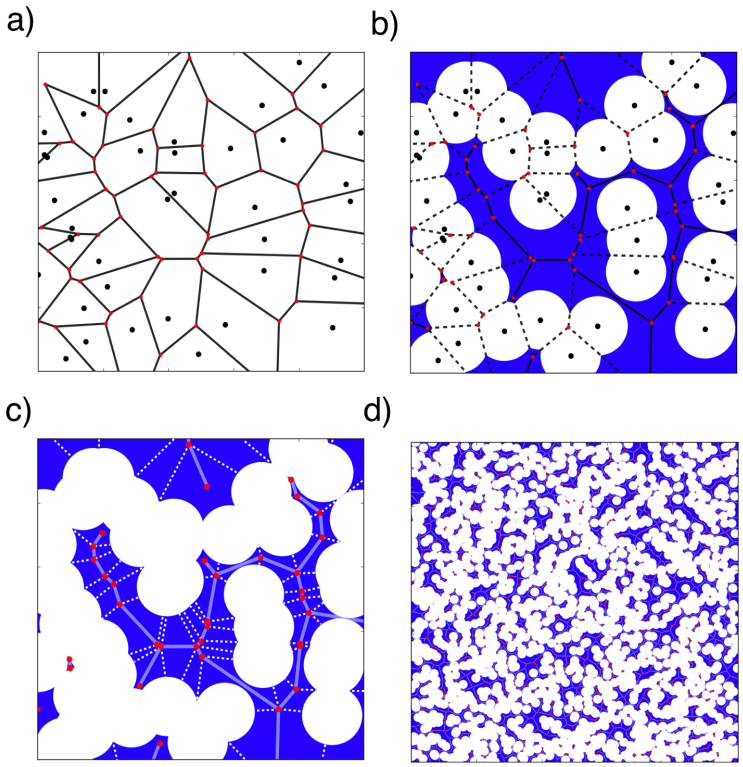

Figure 3.S6: a) Circle centers are placed randomly on a plane (black dots). We segment the plane into regions, each region being a set of points closest to a circle center. These regions are polygons and define a natural "grid" for the void model. Sides of the polygons are bonds of the grid (black lines), and corners of the polygons are nodes of the grid (red dots). b) Bonds are removed if they pass through a circle. Removed bonds are shown as black dashed lines. The remaining bonds (solid black lines) all lie within voids and connected bonds correspond to connected voids. c) Each void can be partitioned into a sum of contributions from bonds. We can do this in the following way. Every node (red dots) is associated with three circle centers and, correspondingly, three bonds (solid pale blue lines). If all three of these bonds belong to a void, we draw three lines from a node towards its corresponding circle centers. If two bonds belong to a void, but one intersects a circle, we draw two lines from a node - one along the missing bond and one towards a circle center not associated with the missing bond. Finally, if a node only has one bond that belongs to a void, we draw no lines. Lines drawn in this way (white dashed lines) segment a void in a unique way, with each segment associated with only one bond. Contributions to area and perimeter segments vary significantly, but have a typical scale. d) For large enough voids, variability in area and perimeter of segments associated with each bond tends to average out, making both the total area and perimeter proportional to the number of bonds in a void.

are located within connected voids. This establishes a mapping from the void model to the network. We can then segment each void into pieces and assign each piece to a bond of the network (Figure 3.S6c). In this way, each bond carries some fraction of the total area and perimeter of the void. Although there is significant variation in how much area and perimeter each individual bond contributes, there is a typical scale above which bond contributions generally do not exist. Therefore, we can imagine that for large enough voids, these variations will average out and each bond will contribute some average amount to the total area and perimeter of the void (Figure 3.S6d). Variation in the area and perimeter of such large voids will be mainly due to differing numbers of bonds, rather than variation in contributions from individual bonds. Therefore, both the area and perimeter of the void will be proportional to N, the number of bonds in a void, $P \propto N$ and $A \propto N$, implying $P \propto A$ and a dimension of $D = 2$. For small voids consisting of just a single bond, area and perimeter will vary due to variation in exact placement of the surrounding circles, and will therefore have a dimension generally less than 2. The beginning of the fractal transition will occur roughly at an area where a two-bond void is as likely as a single-bond void of the same size. The fractal transition will end at a scale where there are enough bonds so that variations due to individual bonds become negligible.

3.S8 Ponds before drainage

We have excluded ponds before drainage from our analysis. This is partly because we do not have reliable data on them: there are only two dates during the SHEBA mission that show ponding before complete drainage, June 15 and June 22. June 15 is the very beginning of the melt season showing only minor pond coverage, while on June 22 only some of the ponds were undrained, making the data inconclusive. We identified June 22 as partially drained by the fact that certain parts of the ice had a low pond coverage while other, often nearby, parts of the ice had a high pond coverage. Nevertheless, we can proceed to calculate the

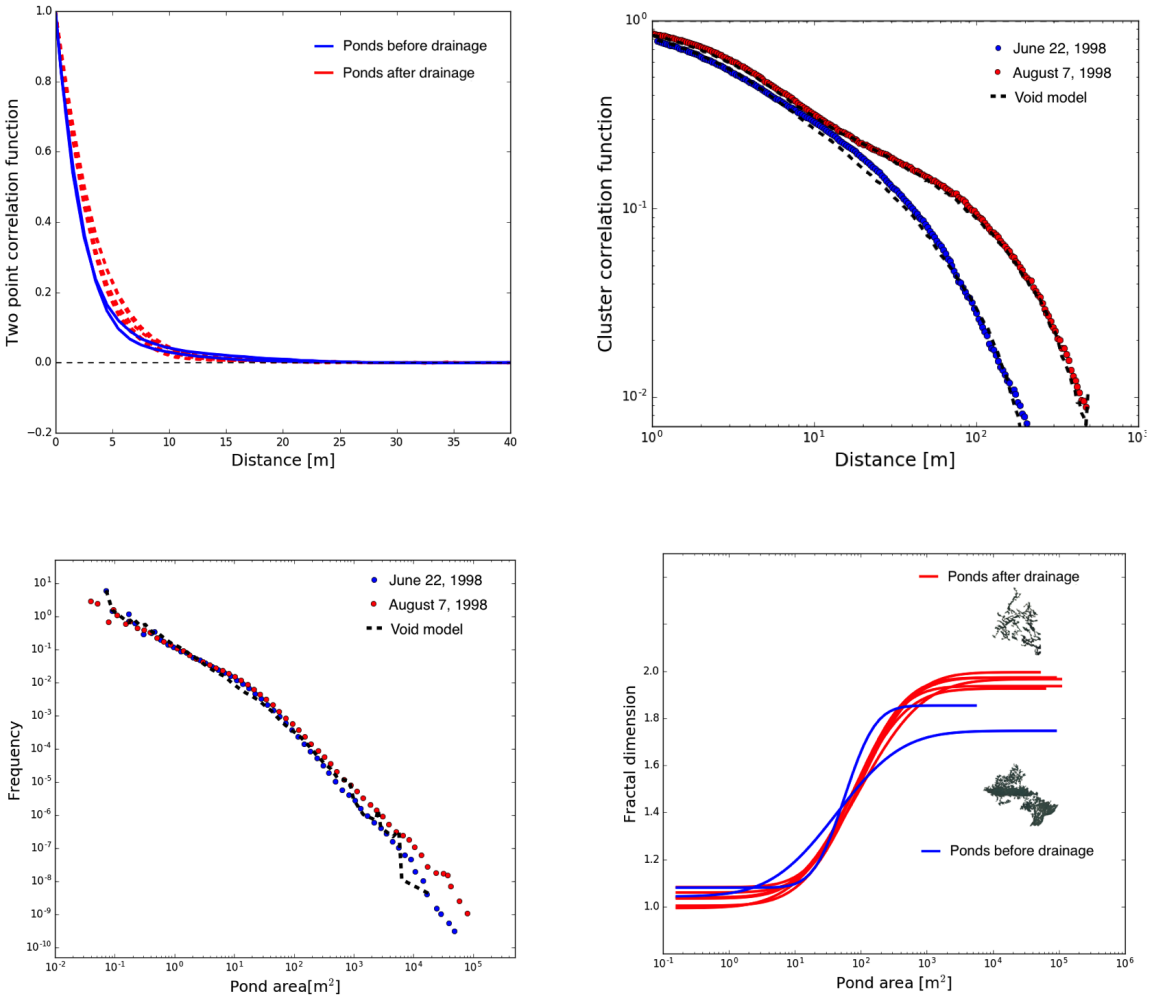

Figure 3.S7: Geometric statistics of ponds before drainage: a) A comparison between a two-point correlation function for ponds before drainage (blue lines) and ponds after drainage (red dashed lines). b) A comparison between a cluster correlation function for June 22 (blue circles), August 7 (red circles), and a void model (black dashed lines). c) Pond size distribution for June 22 (blue circles), August 7 (red circles), and a void model (black dashed line). d) Fractal dimension curves for ponds before drainage (blue lines) and after drainage (red lines). Lines end at the maximum pond size found at that date. Examples of a drained and undrained pond are also shown.

geometric properties for these dates as well. The two point correlation function shows that both of these dates have roughly the same scale as ponds after drainage, consistent with pre-melt snow dunes setting the pond scale (Figure 3.S7a). The cluster correlation function and the pond size distribution for ponds on June 15th depend on the threshold parameter, p_t, used by the machine learning algorithm to classify the melt ponds, described in section 3.S1. For this reason, these quantities can only be reliably calculated for June 22 (Figures 3.S7b and 3.S7c). Both the correlation function and the size distribution for June 22nd can be fit using $\rho = 0.35$, slightly higher than for August 7, and above the percolation threshold. Finally, we find the fractal dimension, D, as a function of pond size (Figure 3.S7d). We do this for both June 15 and June 22, although results for June 15 are inconclusive since there are not many large ponds, so the estimate for the upper fractal dimension has a large error. The upper fractal dimension for both pre-drainage dates is below $D = 2$, in contradiction with the void model. This suggests a qualitative change in the pond morphology before and after drainage. Because of this mismatch and a lack of reliable data, we chose not to apply the void model to pre-drainage ponds.

3.S9 Many models of melt pond geometry

Many models other than the void model are capable of reproducing the geometric features we studied in this Chapter. These models include a model of overlapping circles, a model of random topography (Bowen et al., 2017), and several models with coarsening dynamics such as the quenched Ising model (Ma et al., 2014; Sicilia et al., 2007). We show examples of large melt ponds derived from these models in Figure 3.S8. All of these models share a common key feature - they represent melt ponds as objects of a typical scale connecting randomly. Any model with such a feature should be able to reproduce the correlation functions, the fractal transition and the size distribution of melt ponds. As we commented in section 3.S4, the basic reason for this is that at scales larger than the typical size of the connecting

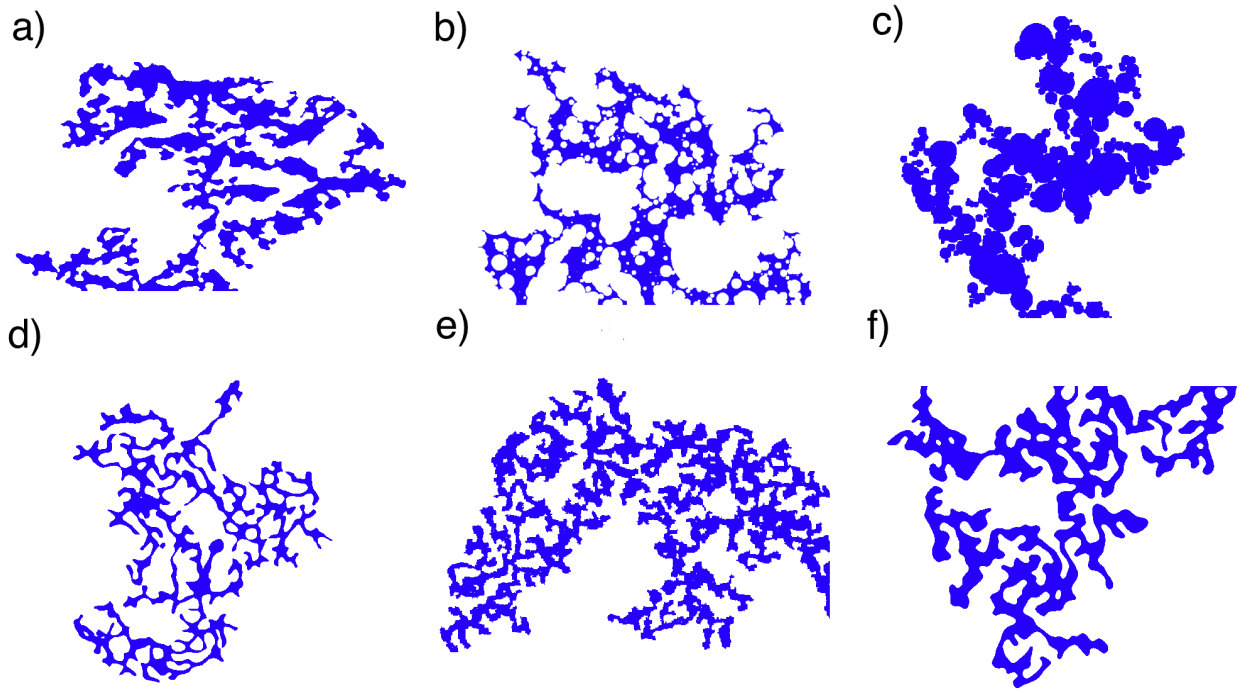

Figure 3.S8: Examples of large ponds in different models. a) A real melt pond. b) A void model. c) A circle model. d) A random topography model. e) A quenched Ising model. f) A model of coarsening due to repeated dilations of a binary image with random initial conditions.

objects, the shape of the clusters is largely independent of the shape of the objects. These models, however, cannot necessarily reproduce all of these pond geometric properties without separately tuning parameters each time. For example, in the complement of the void model, a model of overlapping circles, matching the correlation functions does not yield a correct scale for the fractal transition. The void model is special in that it can robustly match so many pond features with only two parameters that can be independently determined from the data. Moreover, the fact that the void model can reproduce the pond size distribution over the entire observational range suggests that it robustly captures the essence of pond geometry even at the small scale.

CHAPTER 4

CRITICAL PERCOLATION THRESHOLD RESTRICTS LATE-SUMMER ARCTIC SEA ICE MELT POND COVERAGE[1]

4.1 Introduction

Arctic sea ice covers a vast area of nearly 15 million square kilometers at its peak annual extent. It sculpts the Arctic environment, supports its ecosystem, and presents a significant obstacle to trade (Perovich and Richter-Menge, 2009). In recent years, sea ice has been rapidly disappearing at a rate underestimated by most climate models (Stroeve et al., 2007). These climate models cannot resolve processes on scales smaller than tens of kilometers, and the disagreement with observations is largely attributed to such unresolved processes (Holland and Curry, 1999). A notable example of a small-scale process contributing to the uncertainty of the large-scale predictions is meter-sized melt ponds that form on the ice surface during summer (Fig. 4.1a). Melt ponds absorb roughly twice as much solar radiation as surrounding bare ice, which significantly accelerates ice melt (Perovich, 1996). Several works have shown the crucial role ponds play in predicting the state of sea ice (Holland et al., 2012; Schröder et al., 2014). Currently, the most common tactic for modeling melt ponds is to try to represent as many of the physical processes that contribute to pond evolution as realistically and as comprehensively as possible (Flocco and Feltham, 2007; Lüthje et al., 2006; Skyllingstad et al., 2009, 2015). Although such models capture many properties of melt pond evolution, it is unclear how assumptions and details of these complex models might change in a warmer climate. This suggests an opportunity for modeling based on universal properties of sea ice that will likely remain unchanged in a warmer climate.

1. This chapter corresponds to Popović et al. (2019b) that, at the time of writing, was under review in JGR: Oceans. It is nearly identical to the manuscript submitted to JGR: Oceans apart from minor changes made mainly to fit the formatting requirements of the thesis and to respond to the comments made by the thesis committee.

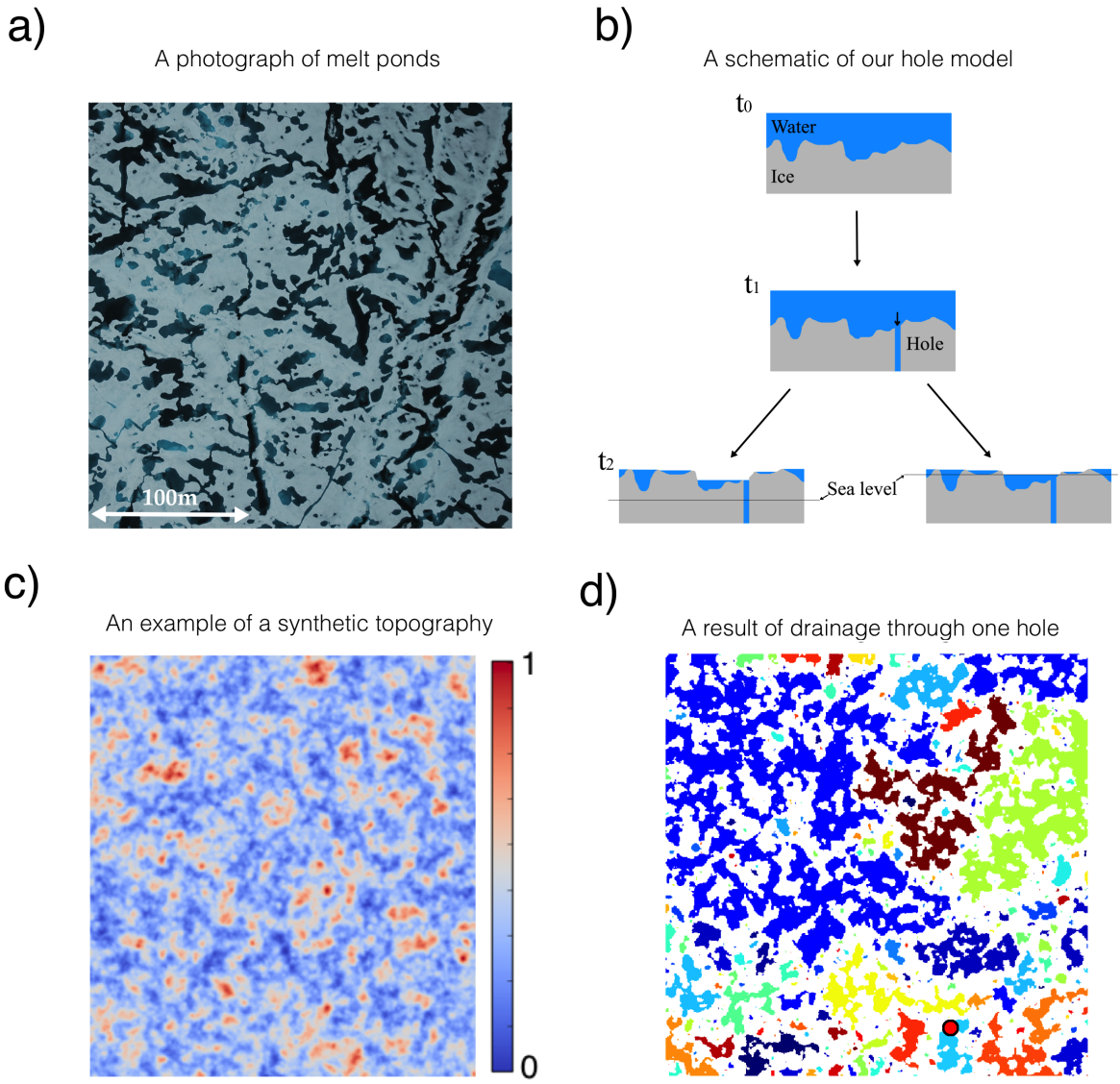

Figure 4.1: a) A photograph of melt ponds taken during the 2005 HOTRAX (Healy-Oden Trans-Arctic Expedition) (Darby et al., 2005) mission. b) A sketch of the hole drainage model. The model begins with an ice surface, a large fraction of which is flooded. A hole opens at a random location on the ice and starts draining the ponds that are connected to it. As the drainage progresses, some regions of the ice become disconnected from the hole and can no longer drain through it. Drainage stops when either the hole is exposed to the atmosphere or when the water level of the pond connected to the hole reaches sea level. c) An example of randomly generated "snow dune" topography. Red colors stand for topographic highs while blue colors stand for topographic lows. The upper bound on the scale bar, here set to 1, is arbitrary. This panel is taken from Chapter 5. d) Ponds after drainage on the topography in panel c) through the hole marked with a red dot. Different colors correspond to distinct ponds.

Melt ponds develop in several stages that depend on the microstructure of the underlying ice (Landy et al., 2014; Polashenski et al., 2017, 2012). As sea ice forms from freezing salty water, brine pockets and channels fill the ice interior (Cole and Shapiro, 1998; Golden et al., 2007; Perovich and Gow, 1996). When the summer melt season begins, fresh water from melting snow penetrates into the cold ice interior through these brine structures, freezes, and thereby plugs the pathways connecting the ice surface to the ocean. The lack of pathways to the ocean allows water to collect in ponds at the top of the ice (Polashenski et al., 2017). Since the ice is relatively flat, ponds grow rapidly during this time, and sometimes end up covering the majority of the ice surface at their peak. This rapid growth stage is usually known as "stage I" of pond evolution. Later, as ice warms, some of the frozen freshwater plugs melt, once again opening the pathways to the ocean and draining the ponds. As relatively warm pond water flows through these channels, it can expand them into large holes that can drain very large areas in a matter of hours (Polashenski et al., 2012). More such holes open with time, and, over the course of several days, pond coverage falls to its minimum. The period during which ponds that are above sea level drain to reduce their hydraulic head is known as "stage II" of pond evolution. Afterwards, the remaining ponds correspond to those regions of ice surface that are below sea level. From this point, pond coverage slowly grows as the ice thins and more of the ice surface falls below sea level. This is known as "stage III" of pond evolution. Observations show that during stage II, meltwater is mainly drained through large holes, while during stage III it is mostly drained through microscopic pathways in the ice (Polashenski et al., 2012).

In Chapter 3, we analyzed photographs of melt ponds and showed that the post-drainage melt pond geometry can be accurately described by a purely geometrical model where ponds are represented as voids that surround randomly sized and placed circles, which can be loosely interpreted as snow dunes. Surprisingly, we found that in order to match various statistics derived from images of late-summer ponds, the fraction of the surface covered by voids had to

be tuned to a special value: the percolation threshold. The concept of a percolation threshold coverage fraction, p_c, was developed in physics and applied to modeling diverse phenomena ranging from electrical transport in disordered media to turbulence (Isichenko, 1992). In the idealized setting of an infinite plane covered randomly by objects that can overlap to form larger clusters, the percolation threshold is the coverage fraction below which only finite connected clusters can exist and above which an infinite cluster that spans the domain forms. Exactly at p_c, connected clusters of all sizes exist, and the system becomes scale-invariant. Close to this threshold, percolation models exhibit *universality* (Goldenfeld, 1992) which means that much of the system behavior does not depend on details such as, for example, the shape of connecting objects. Generally speaking, universality is often observed near the critical point of continuous phase transitions. Thus, for example, universality allows both the magnetic phase transition and the phase transition of fluids near the critical point to be accurately described by the idealized Ising model (Goldenfeld, 1992; Nishimori and Ortiz, 2010).

Our observation that late-summer ponds seem to be organized close to the percolation threshold presents a puzzle and suggests that there is a mechanism driving the ponds to this threshold. Here, we show that drainage through large holes can account for this observation. Specifically, we develop an idealized model of pond drainage through large holes to show how this mechanism drives melt pond evolution to lie below the percolation threshold. We then use this model to formulate a pond fraction evolution equation that reveals the connections between the pond evolution and measurable physical parameters. Even though our hole drainage model explicitly represents the drainage stage (stage II), we show that it can also be used to understand elements of pond evolution during stage III. By clarifying the relation of pond coverage to the percolation threshold, we place melt pond formation within the broader context of critical phenomena and phase transitions.

Our approach to modeling melt ponds here is very different from using a typical pond-

resolving model. Such models solve pond and ice evolution on a grid, often in 3 dimensions, parameterizing the sub-grid scale processes that cannot be explicitly resolved. For example, in a recent attempt, Skyllingstad et al. (2015) solved a 3d model of pond evolution coupled with ice thermal evolution, assuming that ponds drain through the bulk of the ice, and allowing the possibility for an impermeable ice layer to form. Their model physics allowed for all stages of pond evolution to emerge naturally as the ice permeability evolves, but, to match the measured pond evolution, the ice permeability had to be tuned several orders of magnitude below the typically observed values. In this Chapter, for the first time, we explicitly model pond drainage through large holes and, as a result, we are able to match the observations using realistic physical parameters. Moreover, we use an explicitly solvable model that exhibits universality, which makes it numerically inexpensive and easily interpreted.

This Chapter is organized as follows: First we formulate a model of drainage through large holes. Next, we use this model to explain why the ponds organize around the percolation threshold. After this, we show that the drainage process is in fact universal. In the two following sections, we use universality to formulate an equation for pond coverage evolution that approximately solves the hole model. Next, we show that our results are consistent with observations. Then, we discuss the dependence of pond coverage evolution on physical parameters and the challenges of pond modeling and, finally, we conclude with a summary of our results. All of the parameters used in the Chapter are summarized in a table in appendix 4.10. We summarize technical details required to reproduce the results of this Chapter in the Supporting Information (SI).

4.2 The hole model

To investigate pond drainage through macroscopic holes, we created a simple model of pond drainage, sketched in Fig. 4.1b and explained in detail in SI section 4.S1. We discuss the physics of hole formation later, in section 4.5. To mimic the conditions at the end of stage

I of pond evolution, we start with a random synthetic two-dimensional ice surface, a large fraction of which is covered by water. We are assuming that variations in ice topography are initially much smaller than freeboard height (mean height above sea level), such that no regions of the ice are initially below sea level. Such a configuration is consistent with conditions on undeformed first-year ice. The ice topography can change over the course of the melt season, as preferential melting of ponded ice alters the topography. A hole opens at a random location on the ice surface and drains water from all of the ponds it is connected to. As drainage through this hole progresses, some parts of the surface can become disconnected from the hole and can no longer drain through it. Drainage stops when either the hole is exposed to the atmosphere or when the pond connected to the hole reaches sea level. As water is lost from the ice surface, the ice floats up to maintain hydrostatic balance. Hydrostatic balance depends on ice thickness, which can decrease over time. Since ponded ice melts faster than bare ice, we evolve the topography by preferentially melting ponded regions. We are assuming that this melt occurs much slower than drainage through a hole. We are also assuming that the topography only changes due to albedo differences between bare and ponded ice so that channels that connect ponds cannot form as the ponds drain. Later, more holes open on the ice surface and the process continues until all the ponds are at sea level.

In practice, we implemented our model on a square grid, typically 500×500 grid points in size, with boundaries that we regard as rigid walls over which ponds cannot spill. We initiated the model by randomly generating a topography according to one of the schemes described in SI section 4.S3 and setting an initial water level, typically so that 100% of the surface is water-covered. During each simulation run, we tracked the ice height above sea level and the water level at each grid point as well as a global variable, θ, loosely interpreted as ice temperature. θ increases at a fixed rate and determines where the holes open - to each grid point, we assign a critical value, θ_0, drawn independently from a normal distribution,

so that a hole opens at that grid point when $\theta > \theta_0$. Ice thickness, which controls the height of the freeboard, decreases at a constant rate $\mathrm{d}H/\mathrm{d}t$, which we take to be an independent model parameter, separate from the surface melt rate. We consider both simulations with $\mathrm{d}H/\mathrm{d}t = 0$ and with $|\mathrm{d}H/\mathrm{d}t| > 0$. We simulate pond and ice evolution iteratively - 1) first, we update θ to find grid points where the new holes open, 2) then we drain the ponds through these holes by incrementally decreasing the water level, at each step updating the ponds connected to the holes until either the holes emerge above the pond surface or ponds fall to sea level, 3) next, we update the surface topography by preferentially melting ponded regions, and 4) finally, we update ice thickness and impose hydrostatic balance. We repeat these steps until θ is high enough so that all grid points have a hole in them. We describe this model in more detail and carefully consider all of the model assumptions in SI sections 4.S1 and 4.S2. Code for this model is available at `https://github.com/PedjaPopovic/hole-model`.

Ice topography determines how the ponds will drain. As we will show, the effects of topography on pond coverage can be summarized with only a few parameters. Importantly, though, for our analysis to apply, ice topography has to be well-described by a single length scale, l_0, defined, for example, as the autocorrelation length. In the case of melt ponds, l_0 would be determined by the typical size of snow dunes. By only considering single-scaled topographies, we are restricting our analysis to flat regions of the ice away from large-scale features such as the ridges. As we mentioned in the introduction, an especially important property of the surface is its percolation threshold, p_c. We estimate p_c for a given topography as the coverage fraction at which a connected "pond" that spans the domain first appears as we incrementally raise the "water level" (a horizontal plane that cuts through the topography, see SI section 4.S3 for details). Motivated by the void model described in Chapter 3 where ponds surround circular "snow dunes," in Chapter 5 we developed a "snow dune" model of the ice topography generated by summing randomly placed mounds of Gaussian form, each with a randomly chosen horizontal scale and a height proportional to that scale. There,

we showed that this topography reproduces the statistical properties of the pre-melt snow surface highly accurately. An example of this surface is shown in Fig. 4.1c and a typical configuration of ponds after drainage through one hole on this surface is shown in Fig. 4.1d. However, our analysis applies to any random surface with a single characteristic scale, and we also show the results for other topography types. We discuss all of these topographies in SI section 4.S3.

4.3 The origin of the percolation threshold in melt ponds

Figure 4.2a shows the pond coverage fraction, p, as a function of the number of open holes, N, in the hole model if we assume ice does not melt. Figure 4.2a provides insight into the mechanism for pond coverage being organized close to the percolation threshold, p_c. Specifically, we can see that the first several holes drain the entire ice surface from $p = 1$ to $p \approx p_c$, while it takes on the order of 10^5 more holes to drain the rest of the surface. In these simulations, the total number of pixels was $N_0 \approx 2.5 \times 10^5$, so to fully drain the surface, a hole needed to exist on nearly every pixel. This resembles the opening of microscopic pathways in real ice, and explains why the transition from stage II to stage III is also marked with a transition from drainage through large holes to drainage through microscopic pathways. This result was robust - we ran multiple simulations on three kinds of topographies and in each case the first several holes were able to drain ponds to below p_c, while the remainder of the drainage curves were robust against the randomness in our model.

We can now understand why the initial drainage is so abrupt and leads to pond coverage close to the percolation threshold. If pond coverage is above the threshold, then a large fraction of the surface is connected and a single hole can drain a vast area. On the other hand, if pond coverage is below the threshold, then ponds become disconnected and holes can drain ponds only incrementally. To explain why ponds remain close to the percolation threshold as more holes open, we need to include the fact that ponded ice melts faster than

bare ice. In this case, the topographic variations that determine the pond patterns amplify over time, so that percolation pond patterns can be preserved if ponded ice melts sufficiently fast compared to bare ice.

The percolation threshold is a statistical property of the ice surface. As such, it does not depend on many of the details of the topography. Importantly, it does not typically depend on dimensional properties such as the mean height or roughness (standard deviation), but rather on generic statistical properties of the surface (Weinrib, 1982). For example, any surface that has a height distribution with a point of symmetry (e.g., a Gaussian), will have $p_c = 0.5$ (Zallen and Scher, 1971). Non-symmetric surfaces have a p_c that deviates from 0.5, but our experiments on non-symmetric "snow dune" and Rayleigh topographies suggest that these deviations are typically not very large (see SI section 4.S3). This means that the percolation threshold for real ice can likely be accurately estimated using an appropriate statistical model of ice topography. We note that if channels that connect ponds form in a significant number as the ponds drain, statistical properties of the topography may change over the course of pond drainage, thereby lowering the value of the percolation threshold.

4.4 Universality of drainage through holes

The curves for drainage on different topographies shown in Fig. 4.2a all appear different. However, by rescaling p and N, we can collapse these curves onto a single universal curve (Fig. 4.2b). The appropriate rescaling is

$$p \rightarrow \Pi \equiv \frac{p}{p_c} \tag{4.1}$$

$$N \rightarrow \eta \equiv cN\frac{l_0^2}{L^2}\ , \tag{4.2}$$

where L is the size of the domain and c is a non-dimensional number of order unity that, like p_c, depends on the type of the topography but not on its dimensional properties such

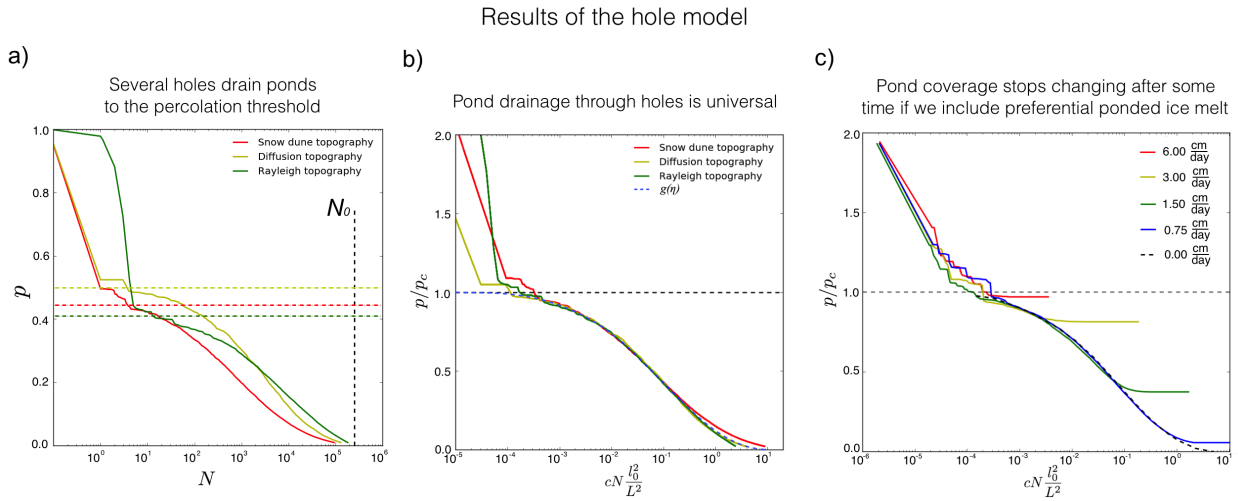

Figure 4.2: a) Semi-log plot of pond coverage fraction as a function of the number of open holes for three different topography types and no ice melt. Percolation thresholds for each of the three topographies are shown as horizontal dashed lines. The vertical dashed line marks the total number of pixels in these simulations. The simulations start at $N = 0$ and $p = 1$ which cannot be shown due to the logarithmic scale, so, for visual clarity, we artificially place the origin at $N = 0.1$. b) A plot of rescaled pond coverage, $\Pi \equiv p/p_c$, as a function of rescaled number of holes, $\eta \equiv cNl_0^2/L^2$ for the three surfaces in panel a. The horizontal dashed line marks the percolation threshold, $\Pi = 1$. Following initial drainage above the percolation threshold, all three curves fall approximately on a universal function, $g(\eta)$, marked with a dashed blue line. c) Rescaled pond coverage, Π, as a function of rescaled number of holes, η, now with preferential ponded ice melt, for different rates of ponded ice melt relative to bare ice melt, $\mathrm{d}h_{\mathrm{diff}}/\mathrm{d}t$. Ice thinning rate is kept at 0, i.e., $\mathrm{d}H/\mathrm{d}t = 0$. The horizontal dashed line has the same meaning as in panel b.

as mean height or roughness. Below we show that c can be defined using a theoretical curve that arises from the general percolation theory. A factor L^2/l_0^2 in the parameter η is approximately the number of ponds of size l_0 within the domain of size L. Therefore, the parameter η represents, approximately, the number of open holes per pond of size l_0. As we can see in Fig. 4.2b, the surface is significantly drained when η is of the order one, meaning that it takes about one hole per pond to drain the surface. After this rescaling, drainage on all surfaces follows a universal law

$$\Pi = g(\eta) \ . \tag{4.3}$$

Pond coverage in our model falls on this universal curve after the first several holes have drained the ponds to the percolation threshold. For a general discussion on universality see Goldenfeld (1992).

The universality of the curve $g(\eta)$ is a consequence of the universality of the percolation model near p_c. In SI section 4.S6, we use this fact to motivate the form of $g(\eta)$. In particular, we define a correlation function for ponds, $G(l)$, as the probability that two randomly chosen points on the surface, separated by a distance l, are both located on the same pond. With this definition, the integral of $G(l)$ is proportional to the fraction of the surface connected to a randomly located hole, and, so, can be related to an average decrease in pond coverage per hole. The universality of pond drainage then arises from the fact that, close to the percolation threshold, $G(l)$ has the same form for all models within the percolation universality class. In SI section 4.S6, we use this line of reasoning to show that g is approximately a solution to an ordinary differential equation

$$\frac{\mathrm{d}g}{\mathrm{d}\eta} = -g^2(1-g)^{-19/18} \ . \tag{4.4}$$

This reasoning only holds near p_c, so, when Π deviates significantly from 1, the universality breaks down, which we can see in the hole model with the slight deviation among the curves

at low pond coverage in Fig. 4.2b. We use Eq. 4.4 to specify the constant c in the parameter η. We chose c so that the simulated curves $\Pi = g(\eta)$ best correspond to Eq. 4.4. All tested topographies yielded a similar scaling factor, c, so this constant had only a small effect in our simulations (see SI section 4.S3).

Since $g(\eta)$ does not depend on model details, a solution for one model will apply to all models within the same universality class. Therefore, it is likely that solving for g using Eq. 4.4 will apply well to real sea ice, so long as real ice topography does not qualitatively differ from our synthetic surfaces. This is supported by the results of Chapter 5, where we showed that pre-melt ice topography on undeformed ice is very accurately described by the synthetic "snow dune" surface we considered here. We note, however, that if ice topography changes significantly during drainage, e.g. due to the formation of channels that connect ponds, real ice may fall out of the percolation universality class, so more study is needed to ensure that our results apply to real ice. As a final remark, we note that the function $g(\eta)$ may in fact describe diverse physical phenomena, some of which may be seemingly very different from pond drainage on sea ice.

Identifying the function $g(\eta)$ is a central result of this Chapter. In the rest of the Chapter we will be concerned with using this function to understand pond evolution and its connection to measurable parameters.

4.5 Pond evolution during stage II

So far, we have neglected the preferential melt of ponded ice. In this section, we will include this effect and we will derive an equation for pond coverage time-evolution, $p(t)$, during pond drainage. Figure 4.2c shows rescaled pond coverage as a function of the rescaled number of holes for different rates of ponded ice melt relative to bare ice melt, $\frac{\mathrm{d}h_{\mathrm{diff}}}{\mathrm{d}t} \equiv |\frac{\mathrm{d}h_{\mathrm{pi}}}{\mathrm{d}t}| - |\frac{\mathrm{d}h_{\mathrm{bi}}}{\mathrm{d}t}|$, where $\frac{\mathrm{d}h_{\mathrm{pi}}}{\mathrm{d}t}$ and $\frac{\mathrm{d}h_{\mathrm{bi}}}{\mathrm{d}t}$ are ponded and bare ice melt rates and $|...|$ is the absolute value. We are still neglecting the thinning of the ice, assuming that $\frac{\mathrm{d}H}{\mathrm{d}t} = 0$. We can see that, in this

case, pond coverage still follows the same curve $p = p_c g(\eta)$ up to a point, $p = p_{\min}$, when it stops changing as more holes open. As we hinted at before, the greater $\frac{\mathrm{d}h_{\mathrm{diff}}}{\mathrm{d}t}$ is, the higher this pond coverage will be, and, if $\frac{\mathrm{d}h_{\mathrm{diff}}}{\mathrm{d}t}$ is large enough, the pond coverage will get pinned to the percolation threshold.

The pond coverage eventually stops changing because, after a certain amount of time, the base of the ponds melts below sea level so that new holes that open cannot drain the ponds fully. In this way, the pond patterns become "memorized." This happens when ice melts through the thickness of the post-drainage freeboard, h. We can express h and $\frac{\mathrm{d}h_{\mathrm{diff}}}{\mathrm{d}t}$ in terms of physical parameters to find the time, T_{m}, to memorize the pond patterns

$$h = \frac{\rho_w - \rho_i}{\rho_w} \frac{H}{1 - p_{\min}} \ , \tag{4.5}$$

$$\frac{\mathrm{d}h_{\mathrm{diff}}}{\mathrm{d}t} = \frac{\Delta\alpha F_{\mathrm{sol}}}{l_m} \ , \tag{4.6}$$

$$T_{\mathrm{m}} \approx \frac{h}{\mathrm{d}h_{\mathrm{diff}}/\mathrm{d}t} = \frac{l_m}{\Delta\alpha F_{\mathrm{sol}}} \frac{\rho_w - \rho_i}{\rho_w} \frac{H}{1 - p_{\min}} \ , \tag{4.7}$$

where H is the post-drainage ice thickness, $p_{\min}$ is the post-drainage pond coverage, F_{sol} is the solar radiation flux, $\Delta\alpha$ is the albedo difference between ponded and bare ice, l_m is the latent heat of melting in Jm^{-3}, and ρ_w and ρ_i are the densities of water and ice. Equation 4.5 comes from hydrostatic balance of the ice floe, taking into account the fact that after drainage, only the non-ponded ice that covers a fraction $1 - p_{\min}$ of the total area is above sea level and can balance the buoyancy of the submerged ice. Equation 4.6 follows from the assumption that bare and ponded ice melt differently only due to their albedo difference.

Based on the above, if we know the number of holes that have opened by time t, we can estimate the pond coverage evolution, as $p(t) \approx p_c g(\eta(t))$ for $t < T_{\mathrm{m}}$ and $p(t) = p_{\min} \equiv p_c g(\eta(T_{\mathrm{m}}))$ for $t > T_{\mathrm{m}}$. To do this, we must model the hole opening dynamics in some way. The formation of holes depends on ice microphysics, and is not very well understood. For this reason, we will first describe the hole opening process in a general way, making few

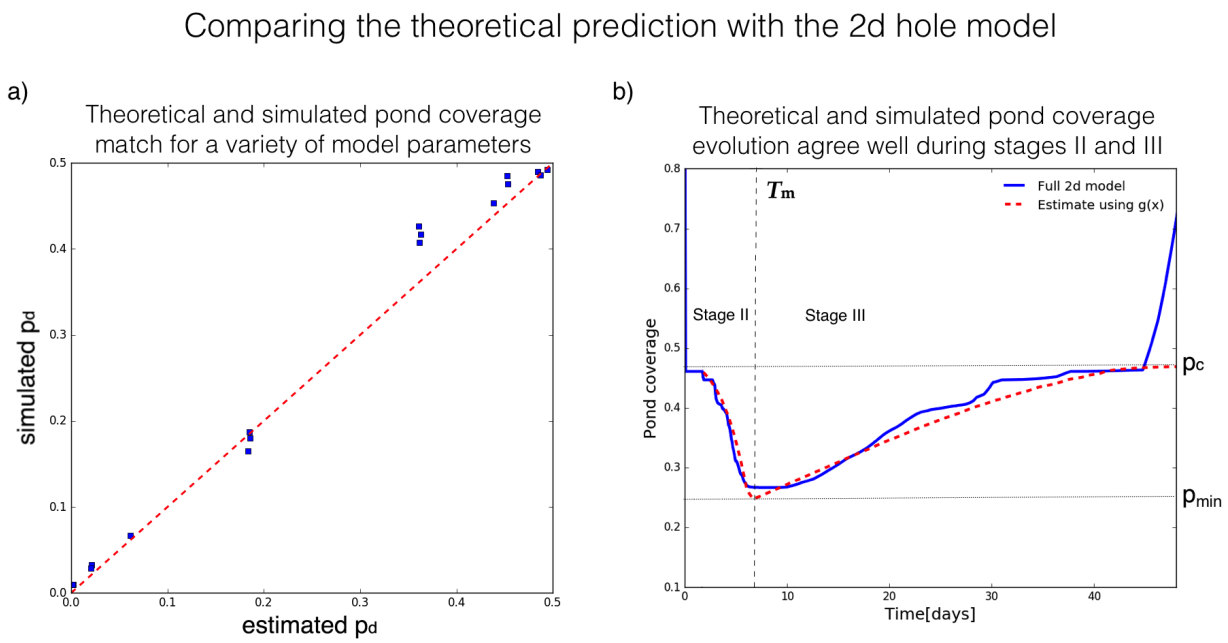

Figure 4.3: a) Post-drainage pond coverage, $p_{\min}$, found using our full 2d model against the coverage estimated using Eq. 4.13. Each point is a separate simulation with different rates of ponded ice melt and hole opening timescales. The red dashed line marks the 1:1 ratio. b) Pond coverage evolution using the full 2d model (blue line) and estimated using Eqs. 4.12 and 4.14 (red dashed line). Time of memorization, T_{m}, percolation threshold, p_c, and the post-drainage pond coverage, $p_{\min}$, are marked with dashed and dotted black lines. Times earlier than T_{m} correspond to stage II of pond evolution, while later times correspond to stage III.

assumptions. Afterwards, we will test concrete assumptions within this framework to make estimates of the pond coverage evolution.

Holes form mainly as enlarged brine channels (Polashenski et al., 2012). Such brine channels are tubes, roughly a centimeter in diameter, that run through the entire thickness of the ice (Cole and Shapiro, 1998). Not all brine channels span the entire depth of the ice (Lake and Lewis, 1970), so, likely, only some can become enlarged into holes. Polashenski et al. (2012) showed that, depending on the channel radius, ice temperature, salinity, and other bulk properties, a channel can either close or enlarge when meltwater flows through it. In the beginning all the channels are closed, but as the ice warms, some of them start to open. Polashenski et al. (2017) suggested that as the ice temperature passes through a

particular threshold, some channels begin to open, while above a certain temperature nearly all channels become open.

Based on the above, we choose to model the evolution of the number of holes as

$$N(t) = N_0 F\left(\tfrac{t-t_0}{T_\mathrm{h}}\right) , \tag{4.8}$$

$$t_0 \sim -T_\mathrm{h} F^{-1}(\tfrac{1}{N_0}) , \tag{4.9}$$

where N_0 is the total number of brine channels that can possibly become holes, F is the fraction of those channels that become holes by time t, and can be seen as a cumulative distribution of some underlying probability density function f, and T_h and t_0 are the width and the center of this distribution. The parameter t_0 can be interpreted as the time between when the first hole opens and when a fraction of holes, $F(0)$, open. Equation 4.9 then follows by noting that time $t = 0$ corresponds to the opening of the first hole, so that $N(t = 0) = 1$. This relationship is approximate because the timing of opening the first hole is intrinsically stochastic. So, each independent model run will have a slightly different t_0 even if all large-scale parameters are the same (see SI section 4.S9). Nevertheless Eq. 4.9 shows that, to first order, t_0 is not an independent parameter. Currently, we are only assuming that the distribution F has a well-defined width, controlled by a unique hole opening timescale, T_h. Thus, we are assuming that a significant fraction of holes open within time T_h, and that within several T_h almost all of the brine channels open. From Eq. 4.8, we can see that under these relatively broad assumptions, ice microphysics contributes to pond evolution by changing the hole timescale, T_h, number of channels, N_0, and the distribution F.

The hole opening timescale, T_h, depends on specific mechanisms that control the formation of holes and is, therefore, more difficult to relate to measurable parameters than the memorization timescale (Eq. 4.7). Polashenski et al. (2017) suggested that a significant fraction of holes open up when the ice interior warms by some amount $\Delta\theta \sim 1^\circ$C beyond the temperature at which the first hole opens. This suggests a way to relate T_h to physical

parameters in a way that is consistent with observations, but we note that a better understanding of hole formation physics is needed to make this estimate more realistic. Therefore, we estimate

$$T_{\mathrm{h}} \approx \frac{\Delta\theta}{\mathrm{d}\theta/\mathrm{d}t} \ , \tag{4.10}$$

$$\frac{\mathrm{d}\theta}{\mathrm{d}t} \approx \frac{\theta_0^2}{\rho_i \gamma S}\left(c^* k \frac{\theta_0}{H^2} + (1-\alpha_p) F_{\mathrm{sol}} \kappa e^{-\kappa z^*}\right) \ , \tag{4.11}$$

where $\mathrm{d}\theta/\mathrm{d}t$ is the warming rate of the ice interior, S is the ice salinity, θ_0 is a reference temperature in degrees Celsius at which the holes tend to start opening, γ is a constant that relates the ice heat capacity to the salinity, k is the thermal conductivity of the ice, α_p is the albedo of ponded ice, κ is the extinction coefficient from Beer's law, z^* is the depth within the ice at which we are estimating the warming rate, and c^* is a constant that accounts for the shape of the vertical temperature profile. Equation 4.11 is an order-of-magnitude estimate of the ice warming rate in terms of measurable parameters that we derive in SI section 4.S7 following Bitz and Lipscomb (1999). We note, however, that T_{h} can change by a factor of several by changing the under-constrained properties such as the depth at which the freshwater plugs form or the reference temperature, θ_0.

With a model for hole opening, we can estimate the pond evolution, $p(t)$, and pond coverage after drainage, p_{min}, by combining Eqs. 4.3 and 4.8

$$p(t) \approx p_c g \left(c N_0 \frac{l_0^2}{L^2} F\left(\frac{t-t_0}{T_{\mathrm{h}}}\right)\right) \ , \quad t < T_{\mathrm{m}} \tag{4.12}$$

$$p(t) \approx p_{\mathrm{min}} \equiv p(T_{\mathrm{m}}) \ , \qquad t > T_{\mathrm{m}} \ . \tag{4.13}$$

These equations can be solved once we assume a concrete distribution F. As a default, we used a cumulative normal distribution F throughout this Chapter. In SI section 4.S9, we explored other distributions and showed that, due to the fact that N_0 is very large, pond evolution only depends on the tail of F. Since T_{m} depends on p_{min} through Eq. 4.7, Eqs.

4.7 and 4.13 have to be solved simultaneously for $p_{\min}$ and T_{m}. To test the above relations, we compared $p_{\min}$ found using Eq. 4.13 against our full 2d hole model (see SI section 4.S4 for details). Figure 4.3a shows that the simulations and the estimates agree well, confirming that the above equations do in fact approximately solve the full hole model. In SI section 4.S8, we use Eqs. 4.7 and 4.9 - 4.13 to explore how the pond coverage depends on physical parameters.

4.6 Pond evolution during stage III

We have shown that the universal function $g(\eta)$ can be used to solve our hole model, providing a formula for pond coverage evolution during stage II. In our model so far, we have neglected ice thinning, and so were unable to explicitly model stage III of pond evolution. Here we will extend our analysis to this stage as well. We will show that the same function $g(\eta)$ also governs the evolution of pond coverage during stage III under certain assumptions.

We start by explaining the relationship between pond behavior during stage II and stage III (see Fig. 4.4). To this end, we have to make several assumptions. In particular, we will assume that ponds are approximately level during stage II, that bare ice melts at a spatially uniform rate, that pond coverage only decreases during stage II and only increases during stage III, and that there is no lateral melt during stage III. If ponds during stage II are approximately level, ice at the pond boundaries has approximately the same height, and is thus, approximately, a level-set of the ice topography. As the ponds drain and the water level decreases during stage II, ice at the pond boundaries quickly becomes pond-free and, assuming that bare ice melts at a spatially uniform rate, remains approximately level for the remainder of stage II. During stage III, ponds are drained to sea level nearly completely, so pond boundaries are again level-sets of the ice topography and the pond coverage is equal to the fraction of the ice surface below sea level. If there is no lateral melting of pond walls, pond growth during stage III is entirely due to ice thinning and consequent freeboard

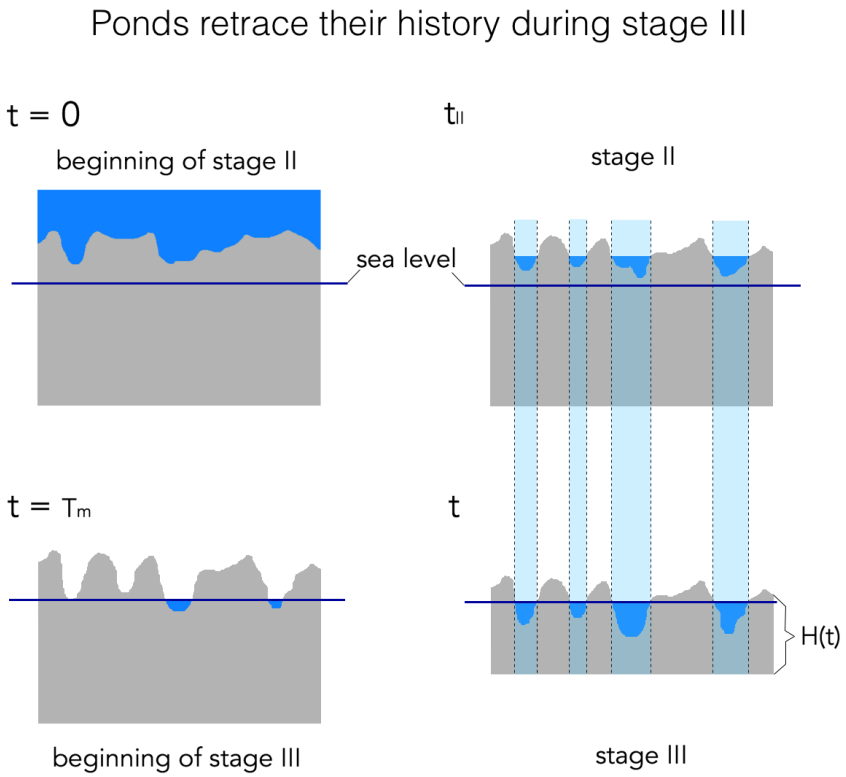

Figure 4.4: A schematic of pond evolution under the assumptions stated in section 4.6. Stage II begins at time $t = 0$, with a high pond coverage and ice surface above sea level. At a time t_{II} during stage II, water level decreases and pond coverage evolves according to Eq. 4.12. We assume that the ponds are approximately level so their boundaries define a level-set of the topography. Ponded ice may melt in a complicated way, but we assume that bare ice melts spatially uniformly, so the topography left in the wake of the decreasing water level remains unchanged. When ponds reach sea level, stage II ends and stage III begins. During stage III, ponds are defined by the intersection of sea level and the ice topography, and are thus also level-sets of the topography. The above-sea-level topography at the beginning of stage III determines pond evolution during stage III if there is no lateral melt of pond walls. As the ice thins, sea level intersects this topography at different levels. Since this topography has not changed since the last time it was ponded during stage II, there exists a time t during stage III for which the horizontal distribution of ponds is the same as it was at a time t_{II} during stage II. In this sense, ponds retrace their history. For visual clarity, we have not shown ice thinning during stage II, but it is assumed that ice thins throughout its evolution.

sinking, which leads to more of the ice surface falling below sea level. Thus, the above-sea-level topography, which consists only of bare ice, does not change until it is submerged. This means that pond coverage at any time during stage III is uniquely determined by the above-sea-level topography at the beginning of stage III, which is unchanged since it was last ponded during stage II, and the current ice thickness, $H(t)$, which determines the freeboard height. Therein lies the connection between stage II and stage III ponds - both are approximately level-sets of the same topography created in the wake of decreasing water level during stage II. In this sense ponds during stage III approximately retrace their history - for every water level during stage II there exists a corresponding ice thickness during stage III so that ponds are approximately the same. Using this idea, we can estimate the pond evolution during stage III.

In order for ponds to retrace their history, the assumptions we stated at the beginning of the previous paragraph have to hold. These assumptions are likely satisfied in reality, at least approximately. In our hole model, ponds are certainly not exactly level during stage II, since this would prevent them from becoming disconnected. Nevertheless, this assumption likely holds well enough so that ponds approximately retrace their history, as we show below by directly simulating stages II and III in our model. Note that we only had to assume that bare ice melts spatially uniformly, and made no assumptions about ponded ice - whichever way the ponded ice melts, the topography set during stage II will be re-submerged during stage III, and ponds will retrace their history. However, a spatially non-uniform melt rate of ponded ice may affect the mapping between stage II and stage III ponds, so, to construct this mapping explicitly, below we will consider only the case where ponded ice does melt uniformly in both time and space.

Now, we can proceed to explicitly relate stage II and stage III pond coverage. Consider a time t_{II} since the beginning of stage II at which the pond coverage is $p_{\mathrm{II}}(t_{\mathrm{II}})$. If the ice is flat compared to freeboard thickness at the beginning of stage II and ponded ice melts

uniformly, the depth of topographic depressions created by preferential ponded ice melting by time t_{II} is approximately $\delta h(t_{\mathrm{II}}) \approx \frac{\mathrm{d}h_{\mathrm{diff}}}{\mathrm{d}t} t_{\mathrm{II}}$. Thus, ice that was ponded at t_{II} will have carved depressions of at least δh by the beginning of stage III. On the other hand, since pond coverage only decreases during stage II, any non-ponded location at t_{II} will have carved depressions less than δh deep by the beginning of stage III. During stage III, depressions of depth δh will be below sea level when the freeboard height, h, is less than δh. So, if the ponds retrace their history, we can use the relationship $h(t) = \delta h(t_{\mathrm{II}})$, to find the time t_{II} at which the pond coverage was the same as it is at time t during stage III. Thus, we find $t_{\mathrm{II}}(t) \approx \frac{h(t)}{\mathrm{d}h_{\mathrm{diff}}/\mathrm{d}t}$.

Note that t_{II} has the same form as the memorization timescale, T_{m}, given by Eq. 4.7 - both are a ratio of a freeboard thickness, h, and a differential melt rate, $\mathrm{d}h_{\mathrm{diff}}/\mathrm{d}t$, the only difference being that Eq. 4.7 is estimated using h at the end of stage II and t_{II} is estimated using h at some time, t, during stage III. So, we can use $T_m(t)$ calculated by Eq. 4.7 using the values for ice thickness and pond coverage at time t, and define $t_{\mathrm{II}}(t) = T_{\mathrm{m}}(t)$. We thus relate stage II and III pond coverage as $p(t) = p_{\mathrm{II}}(T_{\mathrm{m}}(t))$. Therefore, using Eq. 4.12, the pond evolution during stage III can be approximately captured as

$$p(t) \approx p_c g\left(cN_0 \frac{l_0^2}{L^2} F\left(\frac{T_{\mathrm{m}}(t) - t_0}{T_h}\right)\right) , \tag{4.14}$$

$$T_{\mathrm{m}}(t) \approx \frac{h(t)}{\mathrm{d}h_{\mathrm{diff}}/\mathrm{d}t} = \frac{l_m}{\Delta \alpha F_{\mathrm{sol}}} \frac{\rho_w - \rho_i}{\rho_w} \frac{H(t)}{1 - p(t)} . \tag{4.15}$$

This equation is applicable after complete pond drainage to sea level. In SI section 4.S4, we note that the transition between stage II to stage III can be approximated as the time at which $p(t)$ estimated using Eq. 4.14 exceeds $p(t)$ estimated using Eq. 4.12 (i.e., when $t > T_{\mathrm{m}}(t)$). After choosing F, Eqs. 4.12 and 4.14 together describe the pond evolution after the beginning of pond drainage below the percolation threshold.

We test these equations against our full 2d hole model that includes ice thinning and assumes a constant thinning rate, $\mathrm{d}H/\mathrm{d}t$, in Fig. 4.3b (see SI section 4.S4 for more details).

We can see that the two agree well most of the time, suggesting that our assumption about ponds retracing their history is justified in our model. Since $g \leq 1$, Eqs. 4.12 and 4.14 predict that p_c is an upper bound on pond coverage during stages II and III. This is approximately obeyed in the full hole model where the pond coverage during stage II quickly falls below the percolation threshold after the first several holes, and where the ice quickly floods during stage III after pond coverage reaches p_c. The rapid flooding after the pond coverage reaches p_c during stage III in the model is due to the fact that we assumed the ice was very flat at the beginning of stage II. In reality, this assumption may not strictly hold, but we still expect the percolation threshold to be an approximate upper bound after which flooding, and subsequent ice disintegration, follows more rapidly than before.

4.7 Comparison with observations

We can now proceed to compare our model predictions to observations. We describe the details of these comparisons in SI section 4.S5. Polashenski et al. (2012) collected extensive field data on pond coverage and ice properties during the summer of 2009 near Barrow Alaska. Using their measurements and Eqs. 4.7 and 4.9 - 4.11, we were able to estimate all of the parameters that enter Eqs. 4.12 and 4.14. Figure 4.5a shows the measured pond coverage, along with our predictions and an estimated margin of error due to uncertainty in the physical parameters that enter the pond evolution equations, while Table 4.1 summarizes our estimates of the timescales T_{m} and T_{h}, the minimum pond coverage, p_{min}, and the percolation threshold, p_c, as well as their margin of error. Since so many physical parameters contribute to pond evolution, even modest uncertainty in measurements leads to relatively large uncertainty in pond coverage. In fact, we find that to match the pond coverage evolution to within 10% all of the physical parameters would have to be known to within about 1%. Equation 4.12 predicts that ponds drain instantly to the percolation threshold as soon as the first hole opens. The measurements, on the other hand, show a more gradual decline in pond

Table 4.1: Estimates of the timescales T_{m} and T_{h}, the minimum pond coverage, p_{min}, and the percolation threshold, p_c, found using Eqs. 4.7, 4.10, 4.11, and 4.13. The range represents the minimum and maximum estimate over an ensemble of pond coverage evolutions corresponding to the dark shaded region in Fig. 4.5a, while the best fit estimates correspond to the least-squares best-fit pond evolution curve over this ensemble shown as the black dashed line in Fig. 4.5a.

	T_{m}	T_{h}	p_{min}	p_c
Best fit	4.4 days	2.0 days	0.1	0.36
Range	(2.3, 9.2) days	(1.0,6.6) days	(0.0,0.3)	(0.2,0.5)

coverage towards the percolation threshold, likely due to the fact that real holes take time to grow and cannot drain ponds instantly. Nevertheless, we can see that observations are consistent with our predictions below the percolation threshold, and our equations capture the pattern of pond coverage variability over time. We can see that within the limited range of reasonable physical parameters, we are able to choose a combination that predicts a pond evolution that accurately matches observations below $p \approx 0.36$.

As we discussed before, our model predicts an approximate upper bound on pond coverage during stages II and III. In particular, we showed that after the beginning of stage II, ponds quickly drain to p_c, while at the end of stage III, the entire floe quickly floods when pond coverage exceeds p_c. This means that ponds likely spend little time at coverage higher than the percolation threshold. Moreover, this approximate upper bound may also be present during stage I. If during stage I there exist large flaws in the ice such as cracks, holes, or even the floe edge, that can quickly drain large volumes of water, the percolation threshold would also represent an upper limit on pond coverage during this stage. If such flaws exist, the pond coverage would in fact be bounded throughout the entire melt season. In Fig. 4.5b, we show the pond coverage distribution across the entire Arctic estimated from MODIS (Moderate Resolution Imaging Spectroradiometer) satellite data (Rösel et al., 2015b). The frequency of pond coverage observations is relatively high for $p < 0.3$ and declines rapidly for higher pond coverage values. Moreover, the pond coverage very rarely exceeds 0.4, consistent with our prediction that an upper bound on pond coverage exists. Values between 0.3 and 0.4 are also

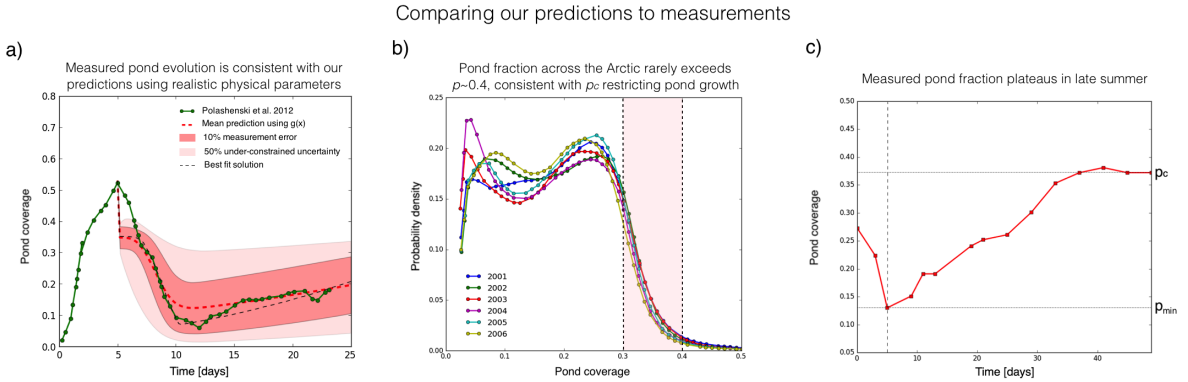

Figure 4.5: a) The green line represents time evolution of pond coverage measured by Polashenski et al. (2012) near Barrow, Alaska in the summer of 2009. The red dashed line and the dark shaded region are the mean and one-standard-deviation uncertainty of an ensemble of pond coverage evolutions found using Eqs. 4.12 and 4.14. For each pond evolution within the ensemble, every physical parameter that enters the pond evolution equations was selected randomly from a normal distribution with a mean estimated using measurements by Polashenski et al. (2012) and a standard deviation equal to 10% of the mean. The black dashed line is the least-squares best fit prediction using parameters that are within the 10% measurement error. The light shaded region is the one-standard-deviation uncertainty region assuming a 10% measurement error for all the parameters directly measured by Polashenski et al. (2012) and a 50% uncertainty for under-constrained microphysical parameters such as the shape parameter for the temperature profile, c^*, the reference temperature, θ_0, and the depth at which the freshwater plugs form, z^*. Values of 10% and 50% are not estimates of real uncertainties, but were chosen simply to demonstrate the sensitivity to model parameters. We note that the slight increase in the upper boundary of the light shaded region during stage II simply corresponds to increased uncertainty during that time, and no actual pond coverage trajectory increases during stage II. b) Distribution of pond coverage across the Arctic for different years derived from MODIS satellite data (Rösel et al., 2015a). The frequency of observations declines rapidly between $0.3 < p < 0.4$ and very few observations show $p > 0.4$, consistent with our predictions. The light shaded region shows the likely values for the percolation threshold estimated by Popović et al. (2018). c) Observations of pond coverage evolution made along a transect during the 1998 SHEBA mission. The data are taken from Perovich et al. (2003). Horizontal and vertical lines mark the estimated minimum pond coverage, $p_{\min}$, percolation threshold, p_c, and the timing of the transition between stages II and III.

consistent with Chapter 3 where we estimated p_c directly from pond photographs, and found it to be roughly between 0.3 and 0.4. We note that these values for the percolation threshold are about 0.1 lower than p_c predicted by the "snow dune" topography, developed in Chapter 5 (and described in SI section 4.S3), that accurately matches the pre-melt ice topography and predicts a p_c between 0.4 and 0.5. This decrease could be due to processes such as the formation of connecting channels between ponds during pond drainage that change the topography and increase the efficiency of drainage.

In the previous section and in Fig. 4.3b, we showed that our model predicts that the pond coverage will approach p_c in the late stages of pond evolution, after which the ice rapidly floods, presumably leading to disintegration. This late-season approach to p_c and subsequent rapid flooding may in fact account for the observations we made in Chapter 3 that late summer ponds are organized close to the percolation threshold. Furthermore, observations made during the 1998 SHEBA (Surface heat budget of the Arctic Ocean) mission, reported in Perovich et al. (2003), and shown in Fig. 4.5c, showed stage III pond evolution that strongly resembles our model prediction that pond growth slows down as it approaches p_c. There, starting from a minimum, the pond coverage increased over a period of roughly 40 days approaching a point ($p \approx 0.37$) after which it approximately stopped changing for the remainder of the field experiment (compare Figs. 4.3b and 4.5c). Again, this value of $p \approx 0.37$ is a plausible percolation threshold according to Chapter 3 and our previous discussion in this section.

4.8 Discussion

We now discuss how pond coverage in our model depends on physical parameters, how our model might be incorporated into a large-scale sea ice scheme, and the challenges of pond modeling. In the previous sections, we have related the pond evolution to parameters p_c, H, α_i, α_p, F_{sol}, S, $\Delta\theta$, θ_0, z^*, N_0, L, and l_0, all of which can be estimated by measurements, at

least in principle. However, not all of these parameters are easily estimated in a large-scale model and the qualitative dependence on some of them may not be appropriately captured in our parameterization due to the fact that we do not yet understand hole formation physics well enough.

The timescale T_{m} depends only on parameters that are available in large-scale models (H, $\Delta\alpha$, and F_{sol}). On the other hand, the hole opening timescale, T_{h}, depends on hole formation physics and is, thus, much more difficult to estimate. In our parameterization, T_{h} is both a function of parameters available in large-scale models (H, S, α_p, and F_{sol}) and those that can only be loosely constrained by field observations ($\Delta\theta$, θ_0, and z^*). In addition to this, T_{h} in our parameterization depends on salinity, S, and reference temperature, θ_0, in a qualitatively counter-intuitive way (see SI section 4.S8). Namely, in our parameterization of T_{h}, we directly related the fraction of open holes to the ice interior temperature following the suggestion of Polashenski et al. (2017). This led to T_{h} being higher at higher S and θ_0, since these conditions imply a lower ice warming rate. This is counter-intuitive because higher salinity and reference temperature also imply a higher brine volume fraction which, in reality, likely increases the hole formation rate, lowering T_{h}. For this reason, we believe that the assumption of using the ice temperature to diagnose hole opening may need to be reconsidered. Another parameter such as, for example, ice porosity, may be better suited to diagnose when holes in the ice begin to form.

The dependence of pond coverage on most of the physical parameters in our model is qualitatively robust. An exception to this is the ice thickness. We find that the effect of thickness, H, depends qualitatively on the details of hole formation physics. Increasing H has two effects - 1) it raises the freeboard, increasing T_{m}, and 2) it slows down the warming of the ice interior, increasing T_{h}. Therefore, the way in which H affects pond coverage qualitatively depends on whether the effect on T_{m} or T_{h} dominates. In SI section 4.S8, we show how a minor change in the assumptions about the hole formation physics may completely change

the effect of ice thickness. We note that Skyllingstad et al. (2015), who ran pond-resolving simulations that include pond drainage, did not find a systematic relationship between pond fraction and the initial ice thickness, consistent with our discussion here. Establishing the correct relationship between ice thickness and pond coverage may be important for estimating the strength of the ice-albedo feedback under global warming. To that end, our model could be used to test hypotheses about hole formation physics by making predictions about the relationship between pond coverage and physical parameters that can be tested against field data that exploit the natural variability in environmental conditions across the Arctic.

We believe that the dependence of pond coverage on all other physical parameters predicted by our model is qualitatively correct, even if it may be somewhat quantitatively inaccurate because of poor understanding of hole formation physics. In Fig. 4.S4 of SI section 4.S8, we specifically look at the minimum pond coverage, $p_{\min}$. There, we show that $p_{\min}$ increases with the domain size, L, percolation threshold, p_c, ice albedo, α_i, temperature range for hole opening, $\Delta\theta$, and the depth at which ice plugs tend to form, z^*. We show that it decreases with typical pond size, l_0, and pond albedo, α_p. Finally, we show that it only weakly depends on the solar flux F_{sol} and brine channel density, n_0. We note that prior to this investigation, it was not recognized that geometric parameters L, l_0, and p_c can have any effect on pond coverage.

In addition to the uncertainties we discussed above, our model predicts that accurately estimating pond coverage evolution is a fundamentally difficult problem, regardless of how well we understand the ice and pond physics. Namely, our model predicts that pond coverage is highly sensitive to physical parameters, so even small errors in measurements or natural variability can lead to large variations in predicted pond coverage. In particular, as we have noted in the previous section, to be able to predict pond coverage to within several percent in our model, all of the physical parameters need to be known to within about 1%. Moreover, even if all of the bulk parameters are perfectly known, we still cannot perfectly constrain

the pond evolution. Since the timing of the opening of the first drainage hole is intrinsically stochastic (see Eq. 4.9 and SI section 4.S9), pond coverage will fluctuate from one situation to another even if all of the bulk parameters are identical. In our simulations this stochasticity in the timing of the first hole contributed to about 5% variability in minimum pond coverage, $p_{\min}$.

Ice albedo is a critical parameter in large-scale models that controls the thermal evolution of the sea ice cover. Since melt pond coverage is a primary control on albedo, Eqs. 4.12 and 4.14 can be straightforwardly used as a physically sound and computationally inexpensive parameterization of the albedo evolution during stages II and III of pond evolution. In addition, these equations can be supplemented with a similarly inexpensive equation for stage I developed in Chapter 5. However, our discussion above clearly highlights two issues relevant for employing our model in a large-scale scheme - 1) ice microphysics that governs hole formation needs to be better understood, and 2) pond coverage possesses a built-in sensitivity to environmental conditions and stochasticity that greatly amplify any uncertainty that may exist in measurements. We emphasize that these challenges are not an artifact of our hole model - any model of melt ponds will need to address hole formation physics to accurately capture the dependence on physical parameters, and any model will likely face a similar sensitivity to physical parameters which simply stems from the fact that there are many parameters that control pond evolution. Our work here reveals that the natural way to parameterize pond coverage is through the number of drainage holes per characteristic area of the surface, η. Thus, if any model were able to track η directly rather than break it down into a multitude of environmental parameters, uncertainty in estimates of pond coverage would greatly reduce. If such a reduction is not feasible, the low computational cost of our model could be exploited to assign a distribution of pond coverage at each grid point of a large-scale model rather than to provide a single pond evolution trajectory. In addition to these issues that are likely a generic feature of melt pond physics, some of

the simplifying assumptions are specific to our model, such as, for example, neglecting the formation of connecting channels between ponds or assuming that drainage through holes is instantaneous. These assumptions may also need to be further examined to make sure our model can be used as a reliable albedo parameterization.

4.9 Conclusions

This Chapter revolves around the observation that the percolation threshold is of special significance for melt ponds. We showed that this stems from the fact that ponds typically drain through large holes, making drainage easy above the threshold and difficult below. In this way the percolation threshold represents an approximate upper bound on pond coverage throughout most of, or, in some cases, the entire summer. The fact that pond coverage often lingers around the percolation threshold leads to universality that greatly simplifies this otherwise complex problem, and allows us to write a simple formula that describes pond evolution throughout most of the melt season. It also makes it possible to connect pond evolution with measurable parameters. Observations are consistent with all of our predictions. The formula for pond coverage we provided requires very little computational power. Therefore, it holds promise as a physical, accurate, and computationally inexpensive parameterization of pond coverage in large scale models. Finally, our work connects melt ponds with the broader field of critical phenomena and our results regarding the universality of drainage may be applicable to other systems whose evolution is governed by a critical point of a phase transition.

4.10 Appendix: Table of parameters used

Table 4.2: A table of parameters used in this Chapter, their default values we used to compare our predicted pond coverage evolution to measurements, and plausible ranges where we were able to estimate them. We also give the references we used to estimate the parameter ranges. The values of parameters presented here are consistent with but not identical to those used in Chapter 2.

	Name	Unit	Default value	Plausible range	Source
t	Time	day		(0,30)	
p	Pond coverage	None		(0,1)	
p_c	Percolation threshold	None	0.35	(0.3,0.5)	(Isichenko, 1992; Popović et al., 2018), this work
$p_{\min}$	Minimum pond coverage	None		(0,p_c)	
Π	Renormalized pond coverage	None		(0,1)	
l_0	Typical pond length-scale	m	5.5	(5.2,5.8)	(Popović et al., 2019a)
L	Drainage basin size	km	1.5		(Polashenski et al., 2012)
n_0	Density of brine channels	m^{-2}	100	(60,120)	(Golden, 2001)
N_0	Number of brine channels	None	2.25×10^8		Inferred from n_0 and L
N	Number of open holes	None		(1,N_0)	
η	Renormalized number of open holes	None			this work
c	Numerical drainage constant	None	3	(3,4.1)	this work
ρ_i	Density of ice	$\mathrm{kg\ m}^{-3}$	900		
ρ_w	Density of seawater	$\mathrm{kg\ m}^{-3}$	1000		
l_m	Latent heat of melting	$\mathrm{kJ\ kg}^{-1}$	334		
γ	Constant relating heat capacity to salinity	$\mathrm{kJ\ kg}^{-1}\mathrm{ppt}^{-1}{}^{\circ}\mathrm{C}$	18		(Bitz and Lipscomb, 1999; Ono, 1967)
k	Thermal conductivity	$\mathrm{W\ m}^{-1}{}^{\circ}\mathrm{C}^{-1}$	1.8	(1.3,2.0)	(Bitz and Lipscomb, 1999; Untersteiner, 1964)
κ	Extinction coefficient	m^{-1}	1.5		(Bitz and Lipscomb, 1999; Untersteiner, 1961)
H	Ice thickness	m	1.2	(0.5,3)	
h	Post-drainage freeboard thickness	m	0.1	(0.05,0.3)	
F_{sol}	Time-averaged solar flux	$\mathrm{W\ m}^{-2}$	254	(140,350)	(Polashenski et al., 2012)
$\Delta\alpha$	Albedo difference between pond and ice	None	0.4	(0.3,0.5)	(Perovich, 1996; Polashenski et al., 2012)
α_p	Pond albedo	None	0.25	(0.2,0.3)	(Perovich, 1996)
S	Ice salinity	ppt	3		(Polashenski et al., 2012)
θ_0	Reference ice interior temperature	°C	-1.2		(Polashenski et al., 2017)
$\Delta\theta$	Temperature range for hole opening	°C	0.7		(Polashenski et al., 2017)
c^*	Temperature profile effect on heat diffusion	None	2	(1,10)	this work
z^*	Depth at which ice plugs form	m	0.6		(Polashenski et al., 2017)
t_0	Center of the hole opening distribution	day	13.4		this work
T_{m}	Memorization timescale	day	4.4		this work
T_{h}	Hole opening timescale	day	2.0		this work

4.11 Supporting Information

4.S1 Details of the hole model

We implemented our model on a grid, typically 500×500 grid points in size. For each grid point, $\mathbf{x}$, we tracked two fields - ice surface height, $h(\mathbf{x})$, and water level, $w(\mathbf{x})$. Points where $w(\mathbf{x}) > h(\mathbf{x})$ were defined as ponds. We assumed that each connected pond has the same water level, but different ponds can have different water levels. For convenience, we defined w to be equal to ice height for non-ponded grid points, $w(\mathbf{x}) = h(\mathbf{x})$. We define the sea level to be the origin of the vertical axis, so that $w(\mathbf{x}) = 0$ signifies that ponds are at sea level. We initialized the model by generating a random surface, $h(\mathbf{x})$, according to a topographic model (see section 4.S3), and setting an initial water level. Typically, we completely covered the surface with water by prescribing a water level equal to the maximum ice height. In this way, the pond coverage fraction at the beginning of a typical simulation was equal to 1. We also prescribed an initial ice thickness, H, assumed to be uniform in our model, and shifted w and h by an equal and constant amount to enforce hydrostatic balance. For a water level field as defined above, with $w(\mathbf{x}) = h(\mathbf{x})$ for non-ponded regions, the hydrostatic balance constraint is simply

$$\langle w(\mathbf{x}) \rangle = \frac{\rho_w - \rho_i}{\rho_w} H \ , \tag{4.S1}$$

where $\langle ... \rangle$ stands for the average over all grid points, and ρ_w and ρ_i are water and ice densities. Before running the model, we scaled the ice surface height field to have a standard deviation of at most 2% of ice thickness, H. This ensured that suddenly removing all the water from the ice surface would leave no depressions below sea level after hydrostatic balance is enforced.

We considered each grid point to be a potential hole, and to each one, we ascribed a "critical temperature," $\theta_c(\mathbf{x})$, above which it opens. These critical temperatures were independently drawn from a prescribed probability distribution, f_θ. As a default, we used a

normal f_θ. The mean and variance of this distribution are arbitrary, so we set the mean to 0 and variance to 1. We kept track of the "bulk ice temperature," θ. All the grid points that had a critical temperature below the current bulk ice temperature were considered open. We set the initial ice temperature to be below the critical temperature of all grid points. We note that the "critical temperature," $\theta_c(\mathbf{x})$ and the "bulk ice temperature," θ, are simply a way to diagnose where the holes open in our model and need not be related to actual ice temperature.

A model step consisted of several sub-steps:

1. First, we increase the bulk ice temperature, θ, by a fixed amount, $\mathrm{d}\theta$, and open holes at locations where the new bulk temperature exceeds the critical temperature. Multiple holes can open at each step. The amount, $\mathrm{d}\theta$, by which temperature increases within a given interval of time, $\mathrm{d}t$, depends on the pre-defined hole opening timescale, T_h. This timescale is defined such that the bulk temperature increases by one standard deviation of the prescribed critical temperature distribution, f_θ, during T_h. Since we set the standard deviation of f_θ to 1, this means that we choose $\mathrm{d}\theta = \frac{\mathrm{d}t}{T_\mathrm{h}}$.

2. Next, we drain the ponds through these newly opened holes. We simulate the drainage iteratively. We first check which holes are active, i.e., are ponded ($w(\mathbf{x}) > h(\mathbf{x})$) and are above sea level ($w(\mathbf{x}) > 0$). Next, we find the ponds connected to these active holes. Then, we decrease the water level for each of these ponds by a small amount. This changes the pond coverage slightly, and we find the new ponds as regions with $w(\mathbf{x}) > h(\mathbf{x})$, and enforce $w(\mathbf{x}) = h(\mathbf{x})$ otherwise. Again, we identify holes that are still active, find ponds connected to these holes, and repeat the drainage process until all the holes become inactive. A hole becomes inactive when either a hole's pond water level reaches the ice height at the location of the hole, $w(\mathbf{x}) = h(\mathbf{x})$, or when pond water level reaches sea level, $w(\mathbf{x}) = 0$.

3. Once drainage through all of the newly opened holes finishes, we preferentially melt

ponded ice. We do this by decreasing ice surface height, h, in ponded regions while leaving it unchanged in bare ice regions. The amount by which the ponded ice melts depends on the prescribed melt rate, $\mathrm{d}h_{\mathrm{diff}}/\mathrm{d}t$. We can neglect the melting of bare ice since it is only the relative melt that changes the topography and affects pond evolution. This is justified because we treat ice thinning independently from surface melt, by prescribing a separate parameter, $\mathrm{d}H/\mathrm{d}t$, that we can change irrespective of $\mathrm{d}h_{\mathrm{diff}}/\mathrm{d}t$, as we explain below.

4. Finally, we enforce Eq. 4.S1 to maintain hydrostatic balance. We do this by shifting the entire ice surface by some amount. Water level is also shifted by the same amount except for ponds at sea level that contain a hole and are maintained at sea level. By returning ice to hydrostatic balance, we effectively adjust the sea level relative to mean ice height.

After adjusting the hydrostatic balance a model step is complete. Then the whole process repeats until all the ponds are at sea level. In the original version of the model, we neglected ice thinning, but when studying stage III of pond evolution, we also thinned the ice using a prescribed rate, $\mathrm{d}H/\mathrm{d}t$, before enforcing hydrostatic balance. In the simulations that include ice thinning, we treat the ice thinning rate as an independent parameter from the surface melt rate, so that $\mathrm{d}h_{\mathrm{diff}}/\mathrm{d}t$ controls topography evolution while $\mathrm{d}H/\mathrm{d}t$ controls ice thickness evolution, and we do not prescribe pond and bare ice melt rates individually. We also tested versions of the model where not every grid point contains a hole, and where more than one hole can form at each grid point. These modifications did not affect our conclusions in any noticeable way.

In summary, Table 4.S1 shows variables and parameters that enter our model.

Table 4.S1: A table of variables and parameters of the hole model.

Variable	Name
$\mathbf{x}$	Coordinate
$h(\mathbf{x})$	Ice height above sea level
$w(\mathbf{x})$	Water level
θ	Bulk ice temperature
$\theta_c(\mathbf{x})$	Critical temperature of individual brine channels
f_θ	Critical temperature distribution
$\mathrm{d}h_{\mathrm{diff}}/\mathrm{d}t$	Melt rate of ponded ice relative to bare ice
T_{h}	Hole opening timescale
H	Ice thickness
$\mathrm{d}H/\mathrm{d}t$	Ice thinning rate

4.S2 Model assumptions

Our model was aimed at explaining the observation that ponds organize around the percolation threshold and exploring the implications of that observation. As such, the model contained only the sufficient elements to explain the organization around the percolation threshold, and we have made several simplifying assumptions. All of these assumptions are likely well-justified for undeformed first-year ice, and our model seems to be a good first-order representation of pond evolution after the beginning of drainage. However, in some cases the assumptions we made may not hold. We now discuss violations of our assumptions and how some of them might be accounted for in a future version of the model.

1. First, by separating pond drainage from the melting and hole opening steps, we have effectively assumed that drainage happens instantaneously. This assumption is supported by observations that find that large ponds can be drained in a matter of hours (Polashenski et al., 2012), whereas melting through the thickness of the freeboard occurs on the timescale of several days. One reason why this assumption may not hold is that it takes time for brine channels to enlarge to macroscopic sizes. Although there are no measurements of the hole enlargement process, a simple model by Polashenski

et al. (2012) suggests that this may occur on timescales of roughly a day, comparable to the timescale of melt. Another reason is that ponds are partially replenished by additional meltwater flowing into them. The rate of drainage depends primarily on the hole radius, the hydraulic head and the number of holes draining a particular pond, while the rate of replenishing scales with the ice melt rate and the area of the pond. So, large ponds replenish water more easily and it may be necessary to wait until several holes open and grow to a certain size before such ponds can actually start draining. For this reason, our assumption of quick drainage may be invalid especially at the beginning of stage II when ponds cover a large area. We tested our model including a non-negligible time to drain ponds, T_{d}. In this case we did not separate the drainage and melting steps, but rather melted the ice and adjusted the hydrostatic balance after each increment of drainage, and we assumed that each pond requires T_{d} time to drain. Our simulations included drainage timescales of up to 60% of the hole opening timescale, T_{h}, and up to 30% of the memorization timescale, T_{m}. We found that simulations with long drainage timescales deviated somewhat from the universal function, $g(\eta)$, with the post-drainage pond coverage deviating up to 10% from the instantaneous drainage predictions. Therefore, although this effect is likely not of primary importance, it may not be negligible during the initial drainage period.

2. Second, we assumed that ice is very flat at the beginning of stage II. The topography of undeformed first-year ice that underlies the snow cover at the beginning of stage I is likely very flat. However, it is questionable whether first year ice at the beginning of stage II can also be considered to be flat since different rates of melt of ponded ice, bare ice, and snow during stage I may act to amplify topography variations. Non-negligible variations in the topography will change the time it takes for different regions of ice to fall below sea level. For this reason, it may be necessary to include the effects of non-negligible initial topography variance in order to get accurate estimates of pond

evolution.

3. Third, we assumed that none of the physical parameters change with time, which may not be correct. In particular, the two timescales, T_{m}, and, T_{h}, both depend on parameters such as the solar flux or ice thickness that are not constant. Furthermore, the warming rate of the ice interior that enters the hole opening timescale depends on the temperature of the ice, and so changes as the ice warms. Short-time fluctuations, such as variation due to daily changes in solar flux, likely do not contribute significantly to pond evolution. However, longer time variation in these parameters likely affect pond evolution quantitatively, although qualitative conclusions likely remain the same. Time variability can be simply added to our model. In this case, instead of using Eqs. 4.12 and 4.14, pond coverage evolution would be found by solving a differential equation

$$\frac{\mathrm{d}\Pi}{\mathrm{d}t} = \frac{\mathrm{d}g}{\mathrm{d}\eta}\Big(\frac{\partial\eta}{\partial t} + \sum_i \frac{\partial\eta}{\partial P_i}\frac{\partial P_i}{\partial t}\Big)\ , \tag{4.S2}$$

where P_i stand for all the parameters that change with time. The term $\mathrm{d}g/\mathrm{d}\eta$ is the derivative of the universal function with respect to its argument and is approximately given by Eq. 4.4.

4. Next, we assumed that water flowing towards the holes does not change the ice topography. Faster flowing water will exchange heat with the underlying ice at a higher rate. This will then lead to the formation of channels near the drainage holes that focus water and enhance melting. These channels have been observed in the field near large holes (Landy et al., 2014; Polashenski et al., 2012). They have the potential to impact the pond evolution by allowing a single hole to drain larger portions of the ice. To assess the effect of channel formation, we added a crude channel formation scheme to our model. To allow for channel formation, we increased the melt rate along the medial line of ponds while they were draining. To include some elements of realism, we made

this increase in melt rate inversely proportional to the distance from the hole, inversely proportional to the local width of the pond in the transverse direction of the medial line, and proportional to the volume of water flowing through the hole, assuming that the water volume is equally partitioned between each hole that drains a particular pond. Such a setup led to the formation of channels between ponds with the most intense channeling occurring during initial drainage since the highest water volume is drained at that time. These assumptions are not highly realistic but we believe they are sufficient for this initial test. We ran several such simulations changing the intensity of melt along the medial line. We found that for a high enough channeling rate, a single hole may be enough to drain the entire surface. However, for any intermediate value, we found that the curve $g(\eta)$ remains approximately the same, and the effect of channel formation can be summarized by simply adjusting the values of p_c and c. In particular, the highest channeling rate we tested that did not immediately drain the whole surface reduced p_c on a "diffusion" topography from $p_c = 0.5$ to $p_c \approx 0.27$ and c from $c \approx 4.1$ to $c \approx 1.4$. This suggests that Eqs. 4.12 and 4.14 may still be used in the presence of channel formation, but the values of p_c and c may depend on channel formation physics. The fact that the effect of channel formation can be summarized by simply adjusting the values of p_c and c in our scheme is likely due to the fact that most channeling occurs after drainage through the first several holes, so the topography remains relatively unchanged as more holes open. This likely also occurs in the field, but in a scenario where the surface is modified throughout pond drainage, the values of p_c and c may need to be made time-dependent as well. Exploring this hypothesis is beyond the scope of this Chapter. We note that in Chapter 3 we estimated that the percolation threshold for late-summer ponds photographed during the 1998 SHEBA mission was around 0.3, while it was around 0.4 for ponds photographed during the 2005 HOTRAX mission. This is in contrast with the "snow dune" topography which

accurately describes the pre-melt surface conditions on first-year ice and predicts a percolation threshold of roughly between 0.4 and 0.5, with values between 0.45 and 0.5 being more likely based on the LiDAR measurements of the pre-melt snow topography (see Chapter 5). Therefore, it is possible that channel formation by water flow decreases the percolation threshold of the pre-melt snow topography by an amount on the order of 0.1 to 0.2.

5. We also assumed that at the beginning of stage II, ice is completely covered by water. This assumption is unrealistic as ice is typically incompletely covered at peak coverage. However, this assumption does not change any of the conclusions we made about pond evolution. As long as the pond coverage fraction at the beginning of the drainage stage is above the percolation threshold, pond evolution will progress identically after drainage below the percolation threshold following the opening of the first several holes. The only effect of this assumption is that non-uniform melt rates before the beginning of drainage may amplify the topography variations as already discussed in item 2 above.

6. Next, we assumed that drainage happens entirely through large holes and not through the bulk of the ice. This is in contrast with all previous melt pond models that modeled melt ponds as a balance between meltwater production and drainage through the bulk of the ice (see, e.g., Lüthje et al., 2006; Skyllingstad et al., 2015). Polashenski et al. (2012) observed that during stage II, water is almost entirely drained through large holes. Furthermore, Eicken et al. (2004) found that early in the melt season, ice permeability is negligible. However, Polashenski et al. (2017) found that very large brine channels may not close fully, and there may be some leftover bulk permeability of the ice. A significant amount of drainage through the bulk of the ice during stage II could in principle qualitatively alter the conclusions of our model. In particular, since the percolation threshold does not control bulk drainage, p_c would no longer be

a significant coverage fraction and the universal curve $g(\eta)$ would no longer control pond evolution. However, since direct observations we made in Chapter 3 show that ponds seem to be organized around the percolation threshold, bulk ice drainage likely has only a small effect.

7. We assumed that ice is a rigid plate that cannot elastically flex as the ponds drain. This implies that hydrostatic balance is a global condition that determines the height of the freeboard, rather than being determined by local mass-balance. Equation 4.5 follows from this assumption. This assumption is well-justified if the flexural wavelength of the ice is significantly larger than the typical length-scale of variability of mass-loading, which, on flat ice, is set by the snow dune length-scale. This is condition likely satisfied on flat ice as ice flexure following pond drainage has not been observed in field. The rigid-plate approximation is also employed in all current melt pond models.

8. When simulating stage III, we assumed that ponds grow entirely due to ice thinning and we have neglected lateral melting. This assumption seems justified at least on first-year ice, as observations show that freeboard sinking due to ice thinning is the dominant mode of pond evolution during stage III (Landy et al., 2014; Polashenski et al., 2012), although some models suggest lateral melting may be important (Scagliarini et al., 2018). Lateral melt would increase pond coverage during stage III, and could be included in our model by adding a lateral melt contribution as described in Chapter 2.

9. We assumed that ice represents a rigid barrier for water flowing horizontally. This is generally true, although water may be able to flow between disconnected ponds if they are only separated by a narrow strip of ice. This was demonstrated by Eicken et al. (2002) who showed that tracers released in disconnected ponds can actually get mixed. However, this likely has only a small effect on the bulk water flow. We note that while ice is mainly impermeable to horizontal flow of water, snow is not, so our "snow dune"

topography is actually meant to represent ice topography left after snow has melted away.

4.S3 Synthetic topographies

To test our model, we used several types of synthetic topographies. Each of these topographies had different statistical characteristics such as the surface height distribution and the percolation threshold which allowed us to test the generality of our results. Importantly, each of these topographies was well-described by a single characteristic length-scale, which is necessary in order for the universal function g to describe the drainage well.

Our default was the "snow dune" topography (Fig. 4.S1a). Ponds that form on this surface are shown in Fig. 4.S1d. This topography is a generalization of the void model described in Chapter 3, and ponds that form on this topography therefore reproduce the pond geometry well. In Chapter 5, we also showed that this topography reproduces the measured snow topography on undeformed ice highly accurately. We note that even though this topography was meant to describe the properties of the pre-melt snow surface, here we will consider it as a representation of impermeable ice. We generate this topography as a sum of N_{m} mounds placed randomly on an initially flat surface. These mounds have a Gaussian shape, $h(\mathbf{x}) = h_m e^{-\frac{(\mathbf{x}-\mathbf{x}_0)^2}{2r^2}}$, and a horizontal scale, r, randomly chosen from an exponential probability distribution, f_r, with a typical scale r_0 , $f_r(r) = \frac{1}{r_0} e^{-r/r_0}$, equivalent to the distribution of circle radii in the void model of Chapter 3. To prevent having unrealistically narrow and high mounds, we prescribed the height of each mound, h_m, to be proportional to its horizontal scale. Optionally, the mounds may also be elongated along a certain axis and the axes may be preferentially aligned to simulate anisotropy in the snow dunes. Including anisotropy did not change any of the conclusions of our model. The "snow dune" surface has a height distribution that is well-fit with a gamma distribution (see Chapter 5 for more details). Parameters of the surface height distribution depend on the density of mounds

placed, $\rho \equiv N_{\mathrm{m}} \frac{r_0^2}{L^2}$, where N_{m} is the number of mounds placed within the domain of size L. When few mounds are placed, such that $\rho \ll 1$, the height distribution is highly right-skewed, while when many mounds are placed, such that $\rho \gg 1$, the height distribution converges to a Gaussian. For this reason the percolation threshold also depends on the density of mounds. Specifically, when ρ is large, $p_c = 0.5$ due to the symmetric height distribution. When the height distribution significantly deviates from a Gaussian, $p_c < 0.5$. In Chapter 5, we find that the "snow dune" topography with approximately $0.2 < \rho < 0.5$ reproduces the LiDAR measurements of snow on first-year ice. Using ρ in this range, we find that the percolation threshold of a realistic "snow dune" topography lies approximately between 0.4 and 0.5.

In addition to the "snow dune" topography, we also used two other types of topographies. The first type we called the "diffusion" topography (Fig. 4.S1b). Ponds that form on this surface are shown in Fig. 4.S1e. This topography is generated by first independently assigning a height to each grid point at random, and then letting this configuration diffuse for some time. Thus, to generate this topography, we numerically solve the diffusion equation. Diffusion smooths out variability in height up to a certain length scale that depends on the time allowed for diffusion. This length scale then determines the length scale l_0. To obtain the desired l_0, we set the diffusion coefficient to 1 and tune the time for diffusion. This surface has a Gaussian height distribution. Due to this fact, the percolation threshold is $p_c = 0.5$. We note that a similar type of topography has been previously used to model melt pond geometry (Bowen et al., 2018).

We called the other type of topography we used to test our model the "Rayleigh" topography (Fig. 4.S1c). Ponds that form on this surface are shown in Fig. 4.S1f. This topography is made by generating two "diffusion" topographies, $h_1(\mathbf{x})$ and $h_2(\mathbf{x})$, with the same length-scale but initialized with a different random configuration, and then taking the square root of the sum of their squares, $h(\mathbf{x}) = \sqrt{h_1^2(\mathbf{x}) + h_2^2(\mathbf{x})}$. This surface has a non-symmetric Rayleigh height distribution (hence the name). The percolation threshold on this

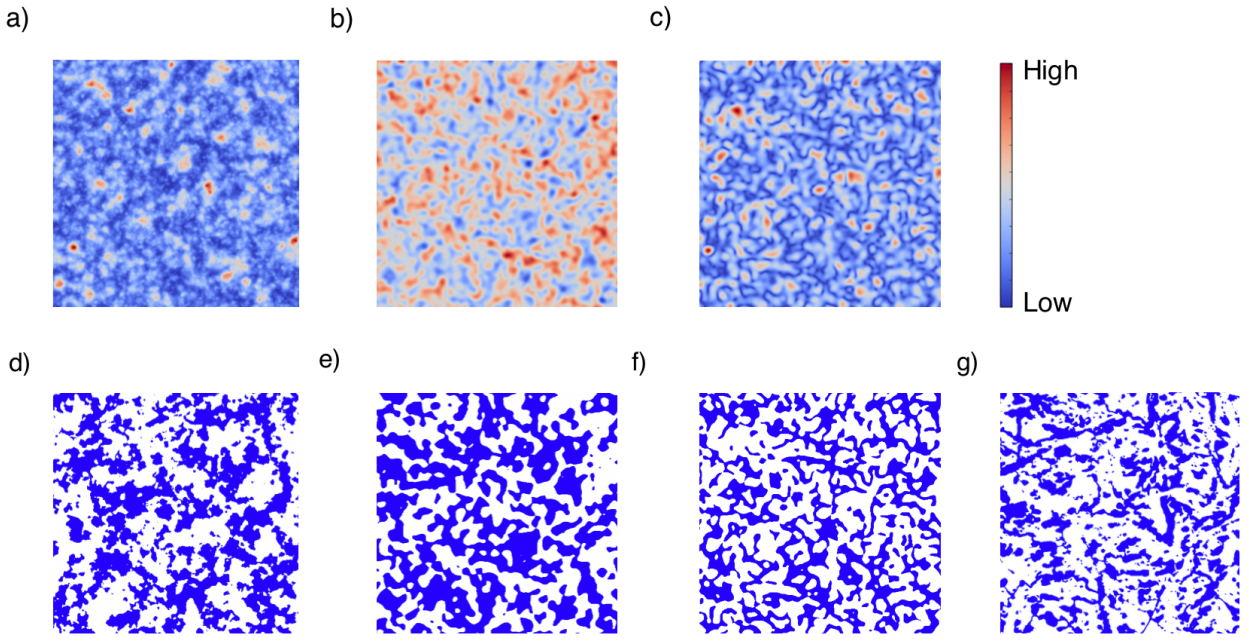

Figure 4.S1: a-c: Examples of different types of topographies we used. Red colors indicate highs of the topography, while blue colors indicate lows of the topography. a) A "snow dune" topography. b) A "diffusion" topography. c) A "Rayleigh" topography. d-f: Examples of ponds on different topographies. d) Ponds on a "snow dune" topography. e) Ponds on a "diffusion" topography. f) Ponds on a "Rayleigh" topography. g) A binarized image of a real melt pond photograph taken on August 14th during the HOTRAX mission.

surface is $p_c \approx 0.4$. A percolation threshold that deviates from 0.5 is the main reason we tested this surface. "Diffusion" and "Rayleigh" surfaces generated as above have no obvious relation to any physical feature in sea ice, but are useful in order to test the universality of drainage.

When generating each of the topographies above, for convenience, we assumed periodic boundary conditions. To estimate p_c for each synthetic topography, we cut the topography with a horizontal plane and shifted it up or down, tracking the connected clusters of the surface that lay below this plane. We found a position of the plane at which a cluster that spans the domain first appears, and estimated p_c as the fraction of the surface below the plane at this level. A constant c in the parameter $\eta = cNl_0^2/L^2$ is a property of a topography type in a similar way as p_c. In section 4.S6, we show that this constant can be related to

other properties of the surface such as the percolation threshold and the amplitude of the cluster correlation length near the percolation threshold. However, here we determined c empirically by finding a value for which curves $\Pi = g(\eta)$ on synthetic topographies best fit $g(\eta)$ estimated analytically using Eq. 4.4 according to the least-squares metric. Similar to p_c, a constant c for "snow dune" topographies could in principle depend on the density of mounds, ρ. However, we found that $c \approx 3$ for all tested densities of mounds. We found that for the "diffusion" surface $c \approx 4.1$ and $c \approx 3$ for the "Rayleigh" surface.

4.S4 Comparing the full 2d model to the estimate

In Fig. 4.3, we compared the full 2d hole model to Eqs. 4.12 to 4.14. To make this comparison, we needed to specify the hole opening distribution, F, the universal function g, and the parameters T_h, T_m, t_0, l_0, L, N_0, c and p_c in Eqs. 4.12 to 4.14. Here, we describe in detail how we related the parameters inputed in the full 2d model to parameters that enter Eqs. 4.12 to 4.14. Note that the parameters of the 2d hole model are not related to Eqs. 4.12 to 4.14 via Eqs. 4.5 to 4.11 that describe how measurable physical parameters enter the pond evolution equations since not all of these physical parameters are prescribed in the 2d model (see Table 4.S1 for the list of parameters directly prescribed in the 2d model).

1. We derived the hole opening distribution, F, as the cumulative distribution of the distribution of critical temperatures, f_θ, defined in the full 2d model. This relationship is correct because we used a constant rate of bulk ice temperature increase in the 2d model. Since, as a default, we used a normal f_θ, the default F was a cumulative normal distribution.

2. The universal function, g, is simply the solution to Eq. 4.4.

3. The hole opening timescale, T_h, was directly prescribed in the full 2d model as the time for the bulk ice temperature to increase by one standard deviation of the distribution

f_θ. Therefore, we used this timescale in Eqs. 4.12 to 4.14 as well.

4. The memorization timescale, T_m, was not prescribed directly in the 2d model, so we had to derive it in order to use it in Eqs. 4.12 to 4.14. To find T_m in simulations with $\mathrm{d}H/\mathrm{d}t = 0$, we used ice thickness, H, and the preferential ponded ice melt rate, $\mathrm{d}h_\mathrm{diff}/\mathrm{d}t$, prescribed in the full 2d model to simultaneously solve for p_min and T_m using Eqs. 4.7 and 4.13.

5. The center of the hole distribution, t_0, fluctuates slightly for each run of the 2d model. For this reason in Eqs. 4.12 to 4.14, we did not use the approximate relation for t_0 defined in Eq. 4.9. Instead, we explicitly recorded the timing of the center of the hole distribution relative to the timing of the first hole for each run of the 2d model and used that number in the corresponding estimate. Using Eq. 4.9 to find t_0 also gives relatively good results, but there are noticeable deviations between the estimate and the actual model solution.

6. For the typical pond size, l_0, we used the length at which the autocorrelation function for a configuration of ponds in the 2d model drops by a factor of e.

7. Domain size, L, is simply the number of grid points on the side of the domain in the full 2d model.

8. Potential number of holes, N_0, in simulations where each grid point represents a potential hole was equal to the total number of grid points, $N_0 = L^2$. In simulations where there can be more than one hole per grid point, N_0 is correspondingly larger.

9. Parameters c and p_c are properties of the topography type, so in the estimates, we used the parameters of the corresponding topographies we used in the full 2d simulations. As we described in section 4.S3, for each topography type, we determined c by least-squares fitting the drainage curves to Eq. 4.4, and we estimated p_c as the fraction of

the surface below a level plane that cuts through the topography such that a connected level set that spans the domain first appears.

Relating the parameters as described above, we were able to uniquely compare estimates using Eqs. 4.12 and 4.13 to the full 2d hole model for stage II in the absence of ice thinning. This comparison was shown in Fig. 4.3a. In Fig. 4.3b, we included ice thinning in the full 2d model to simulate stage III. There, we prescribed a constant ice thinning rate, $\mathrm{d}H/\mathrm{d}t$, and the initial ice thickness, H_0, such that ice thickness evolves as

$$H(t) = H_0 - \frac{\mathrm{d}H}{\mathrm{d}t} t \ . \tag{4.S3}$$

When making the estimate with ice thinning included, most of the parameters that enter Eqs. 4.12 to 4.14 can be related to the 2d model parameters in the same way as described above, with the most notable difference being the memorization timescale, T_m. Equation 4.7 defines T_m, as the time for ponded ice to melt below sea level in terms of ice thickness and pond coverage. Since T_m is the time it takes for ponded ice to melt through the thickness of *post-drainage* freeboard, the thickness and the pond coverage that enter Eq. 4.7 represent the post-drainage parameters. Therefore, to get T_m, we need to solve Eqs. 4.7 and 4.13, and Eq. 4.S3 simultaneously for post-drainage coverage, p_min, memorization timescale T_m, and post-drainage thickness, $H(T_\mathrm{m})$.

In addition to predicting the time at which pond bottoms fall below sea level, T_m estimated as above also coincides fairly accurately with the time at which the water level throughout the domain reaches sea level. This is because, if pond bottoms lay below sea level, ponds do not become disconnected as the drainage progresses, so a single hole can drain an entire pond, making the drainage highly efficient after T_m. Note that this is only true because, in our model, ice at the beginning of stage II is flat compared to the freeboard thickness, so that pond bottoms are also flat and all of ponded ice falls below sea level at

roughly the same time. If this were not the case, it could happen that drainage through a hole splits a pond into disconnected parts thereby leaving a part undrained, even if the pond bottom was initially below sea level. The fact that drainage through holes becomes efficient once pond bottoms fall below sea level means that Eq. 4.12 is approximately valid up to T_{m}, and that Eq. 4.14 is approximately valid after T_{m}. T_{m} estimated in this way is also a crossover time when $p(t)$ estimated using Eq. 4.12 becomes less than $p(t)$ estimated using Eq. 4.14. Like Eq. 4.13, Eq. 4.14 cannot be solved directly since there the pond coverage $p(t)$ depends on $T_{\mathrm{m}}(t)$, which in turn depends on $p(t)$ through Eq. 4.15. Therefore, to solve for pond coverage evolution during stage III, we have to simultaneously solve for $p(t)$ and $T_{\mathrm{m}}(t)$ using Eqs. 4.14 and 4.15 where $H(t)$ is given by Eq. 4.S3.

4.S5 Satellite and field data analysis

In section 4.7 we used field measurements and satellite data to constrain our model and to test its predictions. In this section we describe these measurements and discuss how we used them to estimate parameters that enter our model.

Estimating parameters based on field measurements

Polashenski et al. (2012) collected extensive field data aimed at understanding the formation and evolution of melt ponds. The experiment was performed on land-fast first-year ice near Barrow, Alaska and was repeated during the summers of 2008, 2009, and 2010, with the most extensive studies done during 2009. Measurements of pond coverage shown in Fig. 4.5a were made along a 200 m-long transect every few days during 2009. Additionally, they made measurements including ice thickness, temperature and salinity, ice and pond albedo, meltwater production and drainage, and ice and snow topography. Based on their measurements and data collected during other studies, we were able to estimate most of the parameters that enter the pond evolution equation. These values are reported as default

values in Table 4.2 along with a plausible range when it was possible to estimate that.

We estimated the linear size of the drainage basin, L, based on the remark of Polashenski et al. (2012) that the drainage basin where the measurements were made is 1.3 km×1.7 km in size. Therefore, we used $L \approx 1.5$ km. We estimated T_{m} using Eq. 4.7 coupled with their measurements of ice thickness ($H \approx 1.2$ m), pond and ice albedo ($\alpha_p \approx 0.25$, $\alpha_i \approx 0.6$), and measurements of solar flux from the nearby weather station ($F_{\mathrm{sol}} \approx 254$ W m^{-2} average flux during field experiment). We estimated the total number of potential holes, N_0, based on measurements of Golden (2001) who found that the density of brine channels was between 60 and 120 per m^2 in their measurements. We thus used $N_0 \approx L^2 100$ m^{-2}. We note that depending on the conditions during ice growth, the density of brine channels may vary substantially (Wakatsuchi and Saito, 1985). Nevertheless, as we show in section 4.S8, pond coverage depends only weakly on brine channel density, so even an order of magnitude difference in brine channel density leads to only several percent change in pond coverage.

Polashenski et al. (2012) did not estimate the pond size l_0. However, based on the results of Chapter 5, the pond size seems to be constant between different years with $l_0 \approx 5.5$ m. In Chapter 3, we estimated the percolation threshold for late-summer ponds for two different years and found it to be around 0.3 and 0.4 for these years. Our simulations on the "snow dune" topography predict $0.4 < p_c < 0.5$. Based on these estimates and simulations we determine that the percolation threshold likely lays somewhere between 0.3 and 0.5. The constant c had only a small effect in our simulations so we chose $c = 3$, consistent with the snow dune topography. We estimated the center of the hole distribution, t_0, based on Eq. 4.9 and we found $t_0 \approx 13.4$ days.

Finally, we estimated T_{h} using Eqs. 4.10 and 4.11. This estimate is approximate for two reasons - 1) we are uncertain about the mechanism that drives hole opening and 2) even if the mechanism is correct, some of the parameters that enter Eqs. 4.10 and 4.11 are difficult to estimate. In addition to measurements of thickness, albedo and solar flux, we

used a measurement by Polashenski et al. (2012) of ice salinity, $S = 3$ ppt. The extinction coefficient, κ, is relatively well-documented and we used $\kappa = 1.5$ m^{-1} (Untersteiner, 1961). Ice conductivity, k, can vary because ice and brine have different conductivities. Using the same conductivity parameterization as in Polashenski et al. (2012), and assuming a brine volume fraction between 0 and 0.5, we found that conductivity can vary between 1.3 and 2 W m$^{-1\circ}$C^{-1}. We used $k = 1.8$ W m$^{-1\circ}$C^{-1} which corresponds to a brine volume fraction of 0.1. Estimating parameters θ_0, $\Delta\theta$, c^*, and z^* is difficult. To estimate the reference temperature, θ_0, and the temperature range, $\Delta\theta$, we used observations made by Polashenski et al. (2017). They noted that holes tend to begin to open when ice interior temperature reaches roughly -1.6°C and open completely when ice temperature reaches around -0.9°C. Therefore, we chose the temperature range to be $\Delta\theta = 0.7$°C. Based on these observations and our solutions to the full heat equation, we chose the reference temperature to be $\theta_0 = -1.2$°C, and we used the shape parameter, $c^* = 2$ (see section 4.S7). Polashenski et al. (2017) found that freshwater plugs do not form at a single depth within the ice, but rather throughout a range of depths. Nevertheless, we used a single z^* for simplicity. Polashenski et al. (2017) took photographs that show that freshwater plugs tend not to form in the upper 0.6 m of the ice, and we estimated roughly $z^* = 0.6$ m for this reason. Future models will need to include the fact that tracking a single layer within the ice is insufficient to capture the process of hole formation.

Comparing the estimated pond coverage to Polashenski et al. (2012)

With the physical parameters estimated above, we were able to find all of the parameters that enter Eqs. 4.12 to 4.14 using Eqs. 4.7 and 4.9-4.11. We used these solutions to compare our estimate to pond coverage evolution observed by Polashenski et al. (2012) in Fig 4.5a. Parameters θ_0, $\Delta\theta$, c^*, and z^* clearly have larger uncertainty than other parameters that can be directly measured. Therefore, to find the wider error bars in Fig 4.5a (light shaded region),

we assumed a 50% error in the parameters θ_0, $\Delta\theta$, c^*, and z^*, and used a 10% measurement error for all other parameters. For narrower error bars in Fig 4.5a (dark shaded region) we used the 10% measurement error for all parameters. These measurement errors are not representative of real uncertainties, and we chose them mainly for demonstrative purposes. In fact, these errors are likely still underestimated. For this reason, our estimates of pond coverage are uncertain and all we can say is that they are at least consistent with our model.

MODIS satellite data

A dataset of pond coverage fraction estimates based on satellite measurements is available for download at https://cera-www.dkrz.de/WDCC/ui/cerasearch/. In this dataset, pond fraction is estimated using an artificial neural network that takes as input the reflectances from three channels of the visible spectrum of the MODIS instrument aboard the Earth Observation Satellite TERRA (Rösel et al., 2015b). The observations are available every 8 days, have a spatial resolution of 12.5km, and cover the entire Arctic. To make Fig. 4.5b, we collected estimated pond fractions for all grid-cells at all times during a particular year for which there were measurements available. We only considered measurements that showed a non-zero pond coverage. We then summarized these data as probability distributions for several different years. Due to the relatively coarse resolution of the measurements, the estimated maximum pond coverage is likely somewhat underestimated.

4.S6 Deriving the universal drainage curve

Here, we will motivate a form of the universal function $g(\eta)$, highlighting the origin of its universality. The goal is to estimate the change in pond coverage fraction after a hole opens at a random location on the ice surface. We are assuming that the first several holes have already driven the ponds to the percolation threshold.

We introduce the cluster correlation function, $G(l)$, as the probability that, given a

randomly chosen point on a pond, another point of distance l away will belong to the same pond. Equivalently, $G(l)$ can be viewed as the average fraction of a circle of radius l that belongs to the same pond as a point chosen randomly on any ponded location. Therefore, a quantity $G(l)2\pi l\mathrm{d}l$ is an average area of a ring of radius l and thickness $\mathrm{d}l$ connected to a hole opened randomly at some ponded location, and an integral of G over the entire 2d domain gives the average area of a pond connected to such a hole. We need to multiply this integral by the pond coverage fraction, p, to account for the fact that in our model holes can open anywhere on a surface, not just within ponds. Therefore the mean fraction of the surface connected to a randomly placed hole is

$$\Delta p = p\frac{2\pi\int_0^\infty G(l)l\mathrm{d}l}{L^2}\ . \tag{4.S4}$$

Equation 4.S4 would represent the average change in coverage fraction after opening a hole, if that hole drained the entire pond it was connected to. However, a hole can only drain a fraction of an entire pond. Let us denote that fraction as f_{drain}. The fraction of the pond drained depends on the relative size of the pond to the autocorrelation length, l_0. Namely, when a pond has a size comparable to l_0, a hole can drain a significant fraction of that pond. On the other hand, when a pond is very large compared to l_0, a small amount of drainage would quickly lead to the formation of disconnected regions, and a hole would be unable to drain a significant fraction of the pond. We can describe a typical linear size of the largest ponds using a "cluster correlation length," ξ, defined roughly as the linear extent of the largest connected pond or, equivalently, as the length beyond which $G(l)$ rapidly falls to 0. Therefore, a fraction f_{drain} can be viewed as a function of l_0/ξ such that $f_{\mathrm{drain}}(l_0/\xi) \to 0$ when $l_0/\xi \to 0$ and $f_{\mathrm{drain}}(l_0/\xi) \to 1$ when $l_0/\xi \to \infty$. The correlation length, ξ, depends on the deviation of pond coverage from the percolation threshold since connected ponds become ever larger as the pond coverage approaches p_c. Thus, close to the percolation threshold, ponds are large and $l_0/\xi \ll 1$, so, based on a general Taylor expansion and the above limiting

behavior, we have

$$f_{\text{drain}}\left(\frac{l_0}{\xi}\right) \approx a\frac{l_0}{\xi} + ... \quad \text{for} \quad \left(1 - \frac{p}{p_c}\right) \ll 1 \ , \tag{4.S5}$$

where a is some constant. We note that this expansion hides an implicit assumption that $f_{\text{drain}}(l_0/\xi)$ is analytic in the limit $l_0/\xi \to 0$ and that a is non-zero. In principle, a form $f_{\text{drain}}(l_0/\xi) \propto (l_0/\xi)^\alpha$ as $l_0/\xi \to 0$ for any $\alpha > 0$ would also be possible. So, we can justify the above expansion only a posteriori, by showing that our theoretical prediction matches the full 2d simulations well. Based on the entire discussion above we can now estimate the pond fraction drained after opening a hole as

$$\frac{\mathrm{d}p}{\mathrm{d}N} = -p\frac{2\pi\int_0^\infty G(l) l \mathrm{d}l}{L^2} f_{\text{drain}}\left(\frac{l_0}{\xi}\right) \ . \tag{4.S6}$$

Each term on the right-hand side is a function of pond coverage, so this equation defines a curve of pond coverage as a function of the number of open holes.

To close Eq. 4.S6, we need to estimate the integral $\int_0^\infty G(l) l \mathrm{d}l$ and express ξ in terms of p. General percolation theory shows that in the limit of infinite domain size, $L \to \infty$, close to the percolation threshold, $(1 - p/p_c) \ll 1$, and at distances larger than the characteristic scale, $l \gg l_0$, $G(l)$ and ξ behave as

$$G(l) = p\left(\frac{l}{l_0}\right)^{-5/24} e^{-l/\xi} \ , \tag{4.S7}$$

$$\xi = A l_0 \left(1 - \frac{p}{p_c}\right)^{-4/3} \ , \tag{4.S8}$$

for any model within the percolation universality class (Isichenko, 1992). Here, 5/24 and 4/3 are universal exponents that come from percolation theory, and A is a non-universal order one constant. At distances smaller than l_0, $G(l)$ depends on the shape of individual ponds, and, thus, on the details of the topography, but is nevertheless constrained to go to 1 as

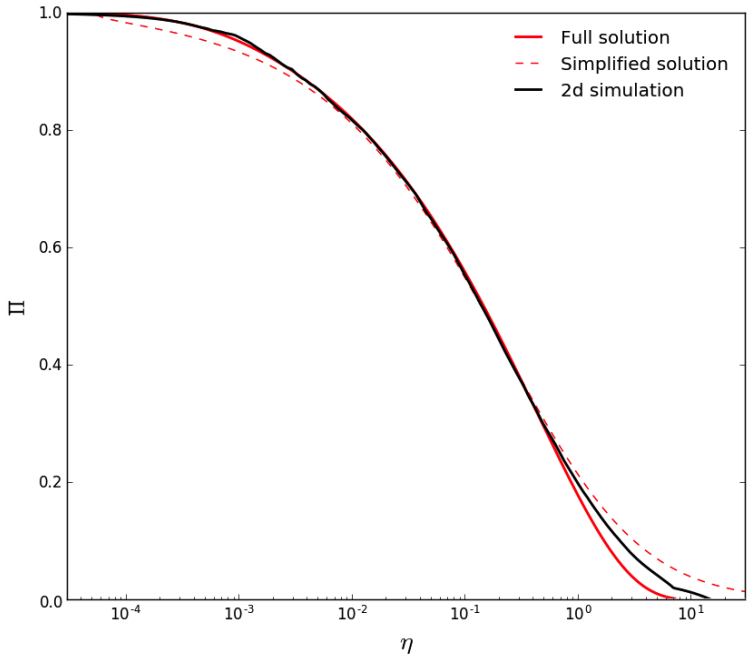

Figure 4.S2: a) Comparing $g(\eta)$ estimated by running a single 2d simulation on a synthetic "snow dune" topography with no melt (black line) with a solution of Eq. 4.S6 using the full expressions Eqs. 4.S11 to 4.S13 (solid red line) and a solution to universal Eq. 4.S10 that assumes asymptotic forms of $G(l)$ and ξ, Eqs. 4.S7 and 4.S8 (dashed red line).

$l \to 0$. The facts that 1) both the full $G(l)$ and its asymptotic form, Eq. 4.S7, have finite integrals as $l \to 0$, and 2) that $G(l)$ is significantly above 0 for $l < \xi$, mean that, if ξ is large compared to l_0, the contribution of short lengths, $l \ll l_0$, to the integral $\int_0^\infty G(l) l \mathrm{d}l$ can be ignored for both the full $G(l)$ and its asymptotic form, so we can use the asymptotic form, Eq. 4.S7, to perform the integration. If the domain size is not infinite, the size of the largest connected ponds is limited by L, and, therefore, ξ will not diverge as predicted by Eq. 4.S8, but will instead be limited by the domain size. Based on the above discussion, we can use $G(l)$ and ξ given by Eqs. 4.S7 and 4.S8 to close the pond drainage equation, Eq. 4.S6, when $l_0 \ll \xi \ll L$. Moreover, to ensure that we can use Eqs. 4.S7 and 4.S8 with Eq. 4.S6 we additionally have to assume that the hole opening process does not disrupt the geometry of the ponds, so that G and ξ have the same form as more and more holes open. Again,

the assumption of pond geometry remaining unchanged can only be justified a posteriori, by direct comparison with full 2d simulations.

We now show that pond drainage is universal in the limit $l_0 \ll \xi \ll L$, i.e., when the pond coverage is neither too close nor too far from the percolation threshold. In that case, we can use the asymptotic forms of ξ and $G(l)$ and the asymptotic expansion Eq. 4.S5 for f_{drain}. We can explicitly perform the integral of G over l to get

$$\frac{\mathrm{d}p}{\mathrm{d}N} = -C\frac{l_0^2}{L^2}p^2\left(1-\frac{p}{p_c}\right)^{-19/18} , \tag{4.S9}$$

where $C = 2\pi\Gamma(\frac{43}{24})aA^{19/24}$ is a numerical constant that depends on A, a, and constants of integration. Defining $\Pi \equiv \frac{p}{p_c}$ and $\eta \equiv c\frac{l_0^2}{L^2}N$, where $c \equiv p_c C$, we recover Eq. 4.4

$$\frac{\mathrm{d}\Pi}{\mathrm{d}\eta} = -\Pi^2(1-\Pi)^{-19/18} . \tag{4.S10}$$

The appropriate boundary condition for this equation is that ponds are at the percolation threshold when only a finite number of holes are open, $\Pi(\eta = 0) = 1$, where we used the fact that $\eta = 0$ if the domain is infinite and N is finite. We can see that Eq. 4.S10 defines a universal function $\Pi = g(\eta)$, since there are no non-universal factors that enter it. From the above derivation, we see that the universality of $g(\eta)$ comes from the universality of the percolation theory in the limit $l_0 \ll \xi \ll L$. This derivation also clarifies that the factor c that enters η depends on the type of topography because it is a combination of factors a, A, and p_c which all potentially depend on the details of the topography. A solution to Eq. 4.S10 is shown with a red dashed line in Fig. 4.S2. It agrees well with the simulations apart from at low pond coverage and at pond coverage close to the percolation threshold. Discrepancy between this solution and the simulations near p_c is due to the fact that in this region $\xi \sim L$, and the universality breaks down. We find that this region of disagreement shrinks as we increase our domain size L.

We will now show that we can closely match the simulated $g(\eta)$ also in the regime $p \to p_c$ if we use $G(l)$ that is valid for all l (including $l < l_0$) and ξ that takes into account the effect of domain size. The matching in this case, however, will not be universal.

As we have discussed above, Eqs. 4.S7 and 4.S8 are asymptotic limits only valid at large separations, l (so that $l \gg l_0$), and when the pond coverage is neither too close nor too far from p_c (so that $l_0 \ll \xi \ll L$). In the Supplementary Information of Chapter 3, we have shown that the $G(l)$ and ξ that fit the measured pond statistics at all lengths, l, and finite domain size, L, are

$$G(l) = \left(e^{-l/l_0}(1-p)+p\right)\left(1+\frac{l}{l_0}\right)^{-5/24} e^{-l/\xi} \,, \tag{4.S11}$$

$$\xi = \xi_\infty \left(1 - e^{-BL/\xi_\infty}\right) \,, \tag{4.S12}$$

$$\xi_\infty = A l_0 \left(1 - \frac{p}{p_c}\right)^{-4/3} \,, \tag{4.S13}$$

where ξ_∞ is the cluster correlation length if the domain size were infinite and has the same form as Eq. 4.S8, and B is a non-universal order one constant. These equations respect the limits for $l \gg l_0$ and $L \to \infty$, and also ensure that $G(l \to 0) \to 1$ and that $\xi \propto L$ when $\xi_\infty \to \infty$. However, the particular form of these functions is arbitrary, and we chose them due to their simplicity and the fact that they match the measured $G(l)$ and ξ highly accurately outside the scaling limit (see SI of Chapter 3). Even though these equations describe $G(l)$ and ξ well for all l and L, they only hold close to the percolation threshold, i.e., when $\xi \gg l_0$, so we still expect deviations from them when $p \ll p_c$ (i.e., when $\xi \sim l_0$).

Finally, we show the solution to Eq. 4.S6 using the full Eqs. 4.S11 to 4.S13. To be able to evaluate $\mathrm{d}p/\mathrm{d}N$ in this case, we also need to assume a concrete f_{drain} consistent with the asymptotic behavior given in Eq. 4.S5 and the fact that we require $f_{\mathrm{drain}}(l_0/\xi) \to 1$ when $l_0/\xi \to \infty$. To this end, we choose $f_{\mathrm{drain}} = 1 - e^{-l_0/\xi}$. This arbitrary choice works well because of universality in the scaling limit that we discussed above. With this form

of f_{drain}, we can use Eqs. 4.S11 to 4.S13 to solve Eq. 4.S6 and get a function $p = p(N)$. This solution in coordinates p/p_c and Nl_0^2/L^2 is shown as a solid red line in Fig. 4.S2. We can see that the agreement with the curve arising from a 2d simulation is excellent apart from a small discrepancy at small pond coverage. This discrepancy is due to the breakdown of Eqs. 4.S11 to 4.S13 far from p_c, due to our ad-hoc choice of f_{drain}, and due to the fact that opening many holes likely does not leave pond geometry completely unchanged. However, even though we were able to obtain a good match with simulations, this solution is not universal under the rescaling $p \to \Pi$ and $N \to \eta$. Namely, changing the non-universal constants A and B or f_{drain} changes the form of the solution in Π and η coordinates, so, to get a good match, we had to tune A and B specifically. This again highlights the fact that the universality occurs in the limit $l_0 \ll \xi \ll L$, i.e., when ponds are much larger then the characteristic scale of the topography (set e.g. by the size of snow dunes), and still smaller than the size of the domain (set e.g. by the ice floe size).

4.S7 The heat equation

In Eqs. 4.10 and 4.11, we noted that the order of magnitude of the hole opening timescale, T_{h}, can be estimated based on physical properties of ice if we assume that internal temperature at some depth within the ice is the relevant parameter that determines when holes start to open. In this section, following Bitz and Lipscomb (1999), we will briefly explain how we arrived at this estimate.

Energy supplied to a unit mass of salty ice partly goes into warming the ice and partly into melting the ice around brine pockets to dilute the brine and bring it into equilibrium with the surrounding ice. Ono (1967) showed that the heat capacity of a unit mass of ice of

salinity S and temperature θ in degrees Celsius can be expressed as

$$c(\theta, S) = c_0 + \frac{\gamma S}{\theta^2} \ , \tag{4.S14}$$

where $c_0 = 2.11$ kJ kg^{-1}°C^{-1} is the heat capacity of fresh ice and $\gamma = 18$ kJ kg^{-1}ppt^{-1}°C is a constant. Equation 4.S14 neglects the typically small contribution from the fact that water in brine pockets has a different heat capacity than ice. This equation shows that the heat capacity increases with temperature and diverges when the temperature approaches the melting point of fresh ice. During the summer, ice is in the process of melting, so the ice interior is only several degrees below zero. With typical salinities of 3 ppt or 4 ppt for first year ice, the salinity term in the heat capacity during summer is roughly an order of magnitude larger than c_0, so $c(\theta, S) \approx \frac{\gamma S}{\theta^2}$.

The ice interior warms because of heat diffusion and because sunlight penetrates beneath the ice surface. This can be expressed with a partial differential equation that determines the warming rate at depth z within the ice

$$\rho_i c(\theta, S) \frac{\partial \theta}{\partial t} = \frac{\partial}{\partial z} k \frac{\partial \theta}{\partial z} + \kappa F_0 e^{-\kappa z} \ , \tag{4.S15}$$

where ρ_i is the density of ice, k is the thermal conductivity of the ice, κ is the extinction coefficient from Beer's law, and F_0 is the radiative flux that penetrates the upper surface of the ice. The first term on the right hand side represents the contribution from heat diffusion while the second term is the contribution from direct solar heating at a depth z. Thermal conductivity, k, may in principle depend on depth because brine and ice have different thermal conductivities. This dependence is, however, typically weak. Equation 4.S15 should be supplied with a boundary condition that ice is at its salinity-dependent melting temperature at the top and bottom surface. Furthermore, a temperature at the initial time should also be specified. We solve this equation in Fig. 4.S3 assuming a uniform

salinity profile throughout the ice column and ice bottom temperature fixed at -1.7°C.

As we have suggested in section 4.5, our strategy is to estimate T_{h} by estimating the warming rate $\frac{\mathrm{d}\theta}{\mathrm{d}t}$ at some depth, z^*, within the ice where ice plugs tend to form. In general, the warming rate in Eq. 4.S15 cannot be simply characterized as it depends on the full vertical profiles of temperature and salinity and their history. Nevertheless, we can approximate it as

$$\frac{\mathrm{d}\theta}{\mathrm{d}t} \approx \frac{\theta_0^2}{\rho_i \gamma S}\left(c^* k \frac{\theta_0}{H^2} + (1-\alpha_p) F_{\mathrm{sol}} \kappa e^{-\kappa z^*}\right) . \tag{4.S16}$$

Here, we have assumed that the fresh ice heat capacity, c_0, is negligible, so that $c(\theta, S) \approx \frac{\gamma S}{\theta^2}$. We have also assumed that thermal conductivity, k, does not depend on brine volume fraction, and we have estimated the amount of radiation that penetrates the upper surface as $F_0 \approx (1-\alpha_p) F_{\mathrm{sol}}$, where α_p is the pond albedo and F_{sol} is the solar radiative flux. We only consider pond albedo because we are only interested in holes that open beneath ponds. A constant c^* accounts for the shape of the temperature profile, while θ_0 and z^* are the reference temperature and depth at which we are estimating the warming rate.

To be able to estimate the hole opening timescale, T_{h}, using Eq. 4.S16, we need to relate the parameters of that equation to physically meaningful quantities. We can define T_{h} as the time it takes for ice at a particular depth to warm from a temperature, θ_{min}, at which only a small fraction of the brine channels can become holes, to a temperature, θ_{max}, at which a significant fraction of the brine channels become holes (see Fig. 4.S3b). We denote the difference $\theta_{\mathrm{max}} - \theta_{\mathrm{min}}$ as $\Delta\theta$. We thus consider T_{h}, θ_{min}, θ_{max}, and $\Delta\theta$ to be measurable, physically meaningful quantities. We can approximate θ_0 in Eq. 4.S16 to be the middle of the range between θ_{max} and θ_{min}, $\theta_0 \approx \frac{\theta_{\mathrm{min}}+\theta_{\mathrm{max}}}{2}$. We consider z^* to have physical significance as the depth at which ice plugs form, and can thus be estimated using measurements. Finally, the parameter c^* takes into account the shape of the temperature profile within the ice column. As such, it depends on a multitude of factors such as the boundary conditions, the salinity profile, or the depth at which we are estimating $\frac{\mathrm{d}\theta}{\mathrm{d}t}$. To

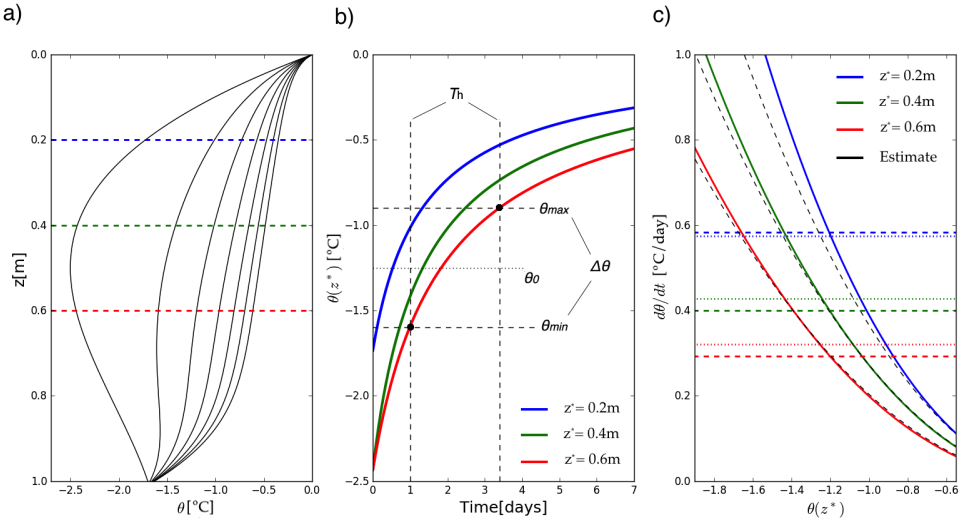

Figure 4.S3: a) Black lines represent represent the vertical temperature profiles within the ice at different times obtained by solving Eq. 4.S15. Curves to the left correspond to earlier times. Colored horizontal lines represent different choices of z^* that are shown in panels b and c. b) Time evolution of ice temperature at a fixed depth. Different colors stand for different depths, z^*, shown in panel a. Horizontal dashed lines represent the temperature at which the holes tend to start opening, $\theta_{\min}$, and the temperature at which a significant fraction of brine channels are open, $\theta_{\max}$. The temperature range, $\Delta\theta$, is also marked. Vertical dashed lines represent times at which the temperature at depth $z^* = 0.6$ m crosses $\theta_{\min}$ and $\theta_{\max}$, which defines the hole opening timescale, T_{h}. A reference temperature, θ_0, estimated as the middle of the range between $\theta_{\min}$ and $\theta_{\max}$ is also marked with a horizontal dashed line. c) Dependence of the warming rate on current ice temperature. Different colors stand for different depths, z^*, marked in panel a. Black dashed curves show estimates using Eq. 4.S16 with $c^* = 2$ and treating θ_0 as a variable. Horizontal solid colored lines show $\mathrm{d}\theta/\mathrm{d}t$ estimated as $\Delta\theta/T_{\mathrm{h}}$, where T_{h} is found numerically as in panel b. Horizontal colored dotted lines show $\mathrm{d}\theta/\mathrm{d}t$ estimated using Eq. 4.S16 with $c^* = 2$ and a reference temperature $\theta_0 = 0.5(\theta_{\max} + \theta_{\min})$.

keep matters simple, we choose $c^* = 2$, corresponding to a quadratic temperature profile with the top and bottom ice temperatures fixed at 0°C.

To determine how reliable the approximations we made above are, we solved the full heat equation, Eq. 4.S15, varying the equation parameters. In Fig. 4.S3c, we show $\frac{\mathrm{d}\theta}{\mathrm{d}t}(\theta)$ found by solving Eq. 4.S15 numerically, and compare it to $\frac{\mathrm{d}\theta}{\mathrm{d}t}(\theta_0)$ estimated using Eq. 4.S16 treating θ_0 as a variable (compare colored and dashed lines in Fig. 4.S3c). We can see that in all cases, the estimate and the numerical simulations behave qualitatively in the same way and are of similar magnitude (within around 20% of each other). In Fig. 4.S3c, we also show $\frac{\Delta\theta}{T_\mathrm{h}}$, where we estimate T_h by solving Eq. 4.S15 numerically and compare it to $\frac{\mathrm{d}\theta}{\mathrm{d}t}$ estimated using Eq. 4.S16 with $\theta_0 = \frac{\theta_\mathrm{min}+\theta_\mathrm{max}}{2}$. Again, we find that our approximations are of the same order of magnitude as the simulations (in this case within 10% of each other), which implies that T_h can be reasonably estimated using Eq. 4.S16.

For each particular numerical solution of Eq. 4.S15, we can improve the match between the simulations and estimates by tuning c^* or changing the definition of θ_0. Depending on the depth, boundary conditions, shape of the salinity profile, and the strength of direct solar heating, we find that c^* can be anything between roughly 1 and 10, while θ_0 can be modified to $\theta_0 = (1-r)\theta_\mathrm{max} + r\theta_\mathrm{min}$, with the numerical factor r anywhere between 0.4 and 0.5. Nevertheless, using $c^* = 2$ and $\theta_0 = \frac{\theta_\mathrm{min}+\theta_\mathrm{max}}{2}$, as we did above, and varying the parameters of the numerical simulation, we find that $\frac{\mathrm{d}\theta}{\mathrm{d}t}(\theta_0)$ estimated using Eq. 4.S16 and treating θ_0 as variable is always of the same order of magnitude as $\frac{\mathrm{d}\theta}{\mathrm{d}t}(\theta)$ estimated using Eq. 4.S15 for all θ_0 and θ, while $\frac{\mathrm{d}\theta}{\mathrm{d}t}$ estimated at $\theta_0 = \frac{\theta_\mathrm{min}+\theta_\mathrm{max}}{2}$ using Eq. 4.S16 is always of the same order of magnitude as $\frac{\Delta\theta}{T_\mathrm{h}}$, with T_h estimated by solving Eq. 4.S15 numerically. This means that Eq. 4.S16 with $c^* = 2$ and $r = 0.5$ is a reasonable first-order approximation to the full heat equation under any configuration, with errors in estimated $\frac{\mathrm{d}\theta}{\mathrm{d}t}$ likely being on the order of 10-20% of the full solution based on the results in Fig. 4.S3c.

Finally, using Eq. 4.S16, we can estimate the hole opening timescale, T_{h} as

$$T_{\mathrm{h}} = \frac{\Delta\theta}{\mathrm{d}\theta/\mathrm{d}t} \ , \tag{4.S17}$$

with $\frac{\mathrm{d}\theta}{\mathrm{d}t}$ estimated using Eq. 4.S16. In addition to the fact that this estimate may disagree with the full solution to the heat equation as we have discussed above, there are several additional reasons why it is uncertain - 1) it is difficult to precisely define and determine parameters $\theta_{\max}$, $\theta_{\min}$, and z^* from measurements, 2) it is unclear whether these parameters themselves depend on physical properties such as ice salinity or thickness, and, most importantly, 3) it is unclear whether the ice interior temperature is in fact a good indicator of when holes start to open. In particular, the assumption that ice interior temperature is a good indicator of hole opening leads to some counter-intuitive conclusions that we discuss in section 4.S8 and section 4.8. Namely, it predicts that holes open more slowly when ice is more saline or when it is closer to its melting point, since in these cases $\frac{\mathrm{d}\theta}{\mathrm{d}t}$ is lower due to a higher higher heat capacity stemming from a higher brine volume fraction. This is counter-intuitive because it implies that it is more difficult to create holes when ice is more porous and when more heat is expended into melting the ice pores. For these reasons, improving our understanding of hole formation physics is crucial for understanding melt pond evolution.

4.S8 Dependence of pond coverage on physical parameters

In this section, we will discuss how pond coverage depends on the measurable properties of the ice in our model. In particular, we will focus on the pond coverage minimum, $p_{\min}$, found using Eqs. 4.7, 4.9-4.11, and 4.13. In the entire discussion below, we will use the cumulative normal hole opening distribution, F, and the set of default parameters defined in Table 4.2.

As a summary of our previous results, here we recapitulate how the minimum pond

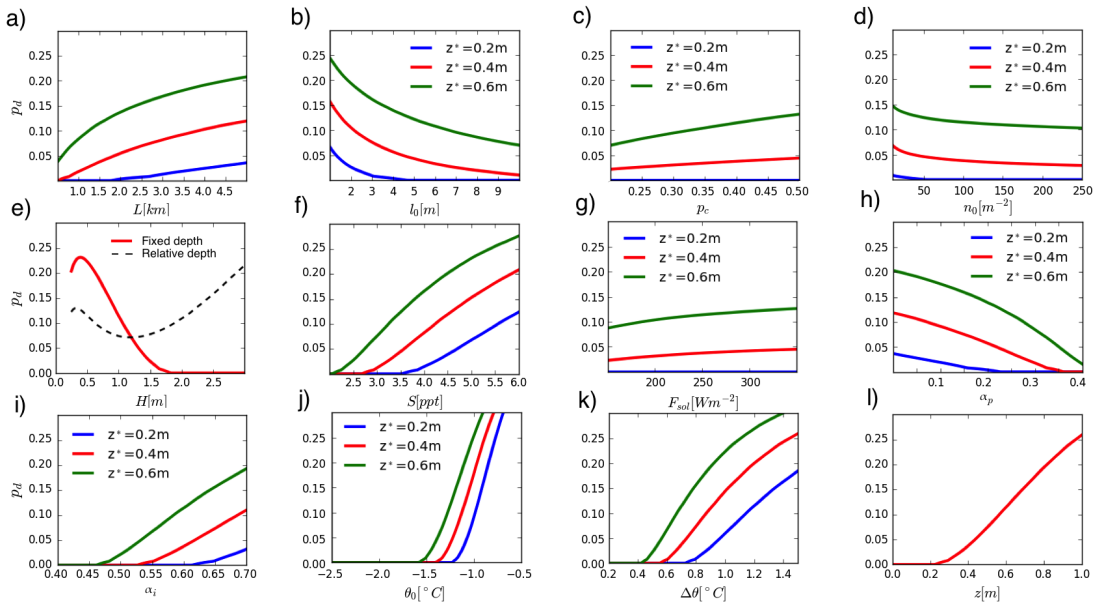

Figure 4.S4: Post-drainage pond coverage, $p_{\min}$, as a function of physical parameters using Eqs. 4.7, 4.9-4.11, and 4.13. In each panel, we are varying one parameter and assuming all other parameters are the defaults specified in Table 4.2. We are assuming a cumulative normal hole opening distribution, F. Different colors in all panels except e and l stand for different values of the depth at which ice plugs tend to form, z^*. a) Pond coverage as a function of the basin length-scale, L. Here, we are keeping the density of brine channels, $n_0 = N_0/L^2$, constant. b) Pond coverage as a function of the typical pond length-scale, l_0. c) Pond coverage as a function of the percolation threshold, p_c. d) Pond coverage as a function of the brine channel density, $n_0 = N_0/L^2$. e) Pond coverage as a function of ice thickness, H. The red curve assumes that ice plugs form at a constant depth $z^* = 0.6$ m. The black dashed curve assumes that ice plugs always form in the middle of the ice. f) Pond coverage as a function of ice salinity, S. g) Pond coverage as a function of solar flux, F_{sol}. h) Pond coverage as a function of pond albedo, α_p. i) Pond coverage as a function of bare ice albedo, α_i. j) Pond coverage as a function of the reference temperature, θ_0. k) Pond coverage as a function of the temperature range, $\Delta\theta$. l) Pond coverage as a function of the depth where ice plugs form, z^*.

coverage, $p_{\min}$, relates to physical parameters. After some manipulation of Eqs. 4.5 to 4.13, we find

$$p_{\min} = p_c g\big(\eta_0 F(\tau_{\rm m} - \tau_0)\big) \ , \tag{4.S18}$$

$$\eta_0 \equiv c n_0 l_0^2 \quad , \quad \tau_{\rm m} \equiv \frac{T_{\rm m}}{T_{\rm h}} \quad , \quad \tau_0 \equiv -F^{-1}\big(\frac{1}{n_0 L^2}\big) \tag{4.S19}$$

$$\tau_{\rm m} \approx \underbrace{\frac{l_m}{(\alpha_i - \alpha_p)F_{\rm sol}} \frac{\rho_w - \rho_i}{\rho_w} \frac{H}{1 - p_{\min}}}_{T_{\rm m}} \ \underbrace{\frac{\theta_0^2\Big(c^* k \frac{\theta_0}{H^2} + (1-\alpha_p)F_{\rm sol}\kappa e^{-\kappa z^*}\Big)}{\Delta\theta \rho_i \gamma S}}_{1/T_{\rm h}} \tag{4.S20}$$

where α_i is the ice albedo, $n_0 \equiv \frac{N_0^2}{L^2}$ is the density of brine channels, and we have introduced the non-dimensional parameters η_0, the number of brine channels per characteristic area of the surface, $\tau_{\rm m}$, the time for ponds to melt through the freeboard relative to the hole opening timescale, $T_{\rm h}$, and τ_0, the time between the first hole and the center of the hole distribution, F, relative to $T_{\rm h}$. Equation 4.S20, relates the non-dimensional timescale $\tau_{\rm m}$ to measurable parameters using Eqs. 4.5, 4.10 and 4.11. Note that $\tau_{\rm m}$ depends on $p_{\min}$ through the "memorization" timescale, $T_{\rm m}$, so Eqs. 4.S18 and 4.S20 have to be solved simultaneously for $p_{\min}$ and $\tau_{\rm m}$.

The minimum pond coverage, $p_{\min}$, is small when the differential melt is weak or when the drainage is efficient. A larger $\tau_{\rm m}$ means that ponds melt quickly relative to the timescale of hole opening, so $p_{\min}$ decreases with $\tau_{\rm m}$. In particular, in terms of $T_{\rm m}$ and $T_{\rm h}$, when $T_{\rm m}$ is large, melt is weak, so $p_{\min}$ decreases with $T_{\rm m}$, and when $T_{\rm h}$ is large, holes open slowly, so $p_{\min}$ increases with $T_{\rm h}$. More brine channels per characteristic area increase the drainage efficiency, so $p_{\min}$ decreases with η_0. A wider time separation between the initial hole and the center of the hole opening distribution means that ponds will spend more time in the tail of the distribution with few holes opening, decreasing the drainage efficiency, so $p_{\min}$ increases with τ_0. We now discuss the dependence of $p_{\min}$ on each of the physical parameters

that enter η_0, τ_m, and τ_0. We show these relationships in Fig. 4.S4, and we discuss each of the panels in the list below.

1. In Fig. 4.S4a, we show that post-drainage pond coverage increases with size of the drainage basin, L. This is because a larger basin makes it more likely for the first hole to open somewhere within the domain, initiating the drainage stage earlier, and increasing τ_0.

2. In Fig. 4.S4b, we show that minimum pond coverage decreases with the typical pond size, l_0. Physically, this is because larger ponds make it easier to drain the surface. Recall that it takes about one hole per pond of size l_0 to significantly drain the surface. Therefore, complete drainage can be achieved with fewer open holes if the individual ponds are larger.

3. Figure 4.S4c shows that minimum pond coverage increases with the percolation threshold, p_c. Pond coverage throughout its evolution from the end of the initial phase above the percolation threshold is approximately proportional to p_c. It is not exactly proportional since τ_m also depends on p_c, making the dependence of p_min on p_c slightly non-linear.

4. Figure 4.S4d shows the dependence of p_min on the brine channel density, n_0. We can see that this dependence is relatively weak - the range of n_0 measured by Golden (2001), from about 60 m^{-2} to about 120 m^{-2}, leads to only around 1% change in pond coverage. Even an order of magnitude change in n_0 would lead to less than a 10% change in pond coverage. Increasing n_0 leads to two competing effects. On the one hand, a higher n_0 increases η_0 by increasing number of potential holes, while on the other hand, it also increases τ_0 by increasing the time before a significant fraction of holes open. These two effects largely cancel each other. As we show in section 4.S9, if the hole opening distribution, F, has an exponential tail, $F(x) \propto e^{-|x|}$, the two

effects exactly cancel. Since in our case $F(x) \propto e^{-x^2}$ in the tail, some dependence on n_0 is retained, but the dependence remains weak.

5. In Fig. 4.S4e, we show the dependence of $p_{\min}$ on ice thickness, H. Ice thickness enters the non-dimensional parameter τ_{m} by increasing both the memorization and the hole opening timescale, T_{m} and T_{h}. In particular, larger H means that, on the one hand, ponds need to carve deeper depressions, thereby increasing T_{m}, while on the other hand, ice also warms more slowly, thereby increasing T_{h}. Because H affects T_{h}, the effect of ice thickness depends on hole formation physics. In Fig. 4.S4e we show two scenarios. The red line shows a case where ice plugs form at a constant depth, $z^* = 0.6$ m. We can see that in this case pond coverage peaks at an ice thickness around 0.5 m after which it decreases to 0 with increasing thickness. The black dashed line shows a case where ice plugs always form in the middle of the ice. The dependence on ice thickness in this case is qualitatively different than the fixed depth scenario. After peaking at $H \approx 0.25$ m, pond coverage drops to its minimum at $H \approx 1.5$ m, after which it keeps increasing with increasing H. The complicated manner in which pond coverage depends on H in both of these scenarios reflects two competing effects. So, depending on whether the effect on T_{m} or T_{h} is stronger, pond coverage either increases (if the effect on T_{h} dominates) or decreases (if the effect on T_{m} dominates) with H. We note that Skyllingstad et al. (2015) found that there was no clear relationship between ice thickness and post-drainage pond coverage in their detailed 3-dimensional model of ice and ponds.

6. In Fig. 4.S4f, we show that in our model $p_{\min}$ increases with ice salinity, S. In our model, this is because saltier ice warms more slowly since a large fraction of energy is deposited in melting ice around brine pockets rather than going to warming the ice. This dependence is somewhat counterintuitive since a higher salt content means a larger brine volume fraction and therefore a larger potential for hole formation. For

this reason it may be an artifact of our assumption that holes open when a certain temperature is reached. We note that Skyllingstad et al. (2015) did not find a significant relationship between salt content and minimum pond fraction in their model.

7. Figure 4.S4g shows that $p_{\min}$ depends only weakly on solar flux, F_{sol}. This weak dependence is explained by the two competing effects that nearly cancel each other. Namely, more solar radiation allows ponds to preferentially melt ice faster, decreasing T_{m}, while also warming the ice interior faster, thereby decreasing T_{h}.

8. In Fig. 4.S4h, we show how post-drainage pond coverage depends on pond albedo, α_p. More reflective ponds prevent ice beneath ponds from warming quickly, increasing T_{h}, and also lead to a smaller contrast between bare ice and ponds, $\Delta\alpha$, increasing T_{m} as well. However, the effect on T_{m} dominates and pond coverage decreases with increasing α_p.

9. In Fig. 4.S4i, we show how post-drainage pond coverage depends on ice albedo, α_i. More reflective ice leads to a larger contrast between bare ice and ponds, decreasing T_{m}, which leads to a higher pond coverage.

10. In Fig. 4.S4j, we show how $p_{\min}$ depends on the reference temperature, θ_0. This reference temperature is approximately the temperature at which holes tend to become open, and it is difficult to define more precisely without further investigation into the hole opening process. We can see that increasing θ_0 leads to a rapid increase in pond coverage in our model. As we have discussed in section 4.S7, the reference temperature affects the hole opening timescale by changing the warming rate. Namely, close to the melting point of the ice, heat capacity increases, rapidly decreasing the warming rate and increasing T_{h} (see Fig. 4.S3c). Apart from increasing heat capacity, the warming rate also decreases since heat diffusion weakens when ice is warmer. As with salinity, this may be seen as counterintuitive since warmer ice contains a high brine volume

fraction which would be expected to aid the formation of holes.

11. In Fig. 4.S4k, we show that $p_{\min}$ increases with the temperature range, $\Delta\theta$. This is due to the fact that it takes a longer time to warm a larger amount, increasing $T_{\rm h}$.

12. In Fig. 4.S4l, we show that $p_{\min}$ increases with the depth at which ice plugs form, z^*. As less sunlight can penetrate deeper within the ice, ice warms slower, increasing $T_{\rm h}$. A caveat here is that we have assumed that the rate of heat diffusion does not change with depth. As heat diffusion is likely strong near the bottom of the ice, this relation likely holds so long as the depth is not close to the ice bottom.

We believe that the assumptions we have made lead to dependencies on L, l_0, p_c, n_0, $F_{\rm sol}$, α_p, α_i, $\Delta\theta$, and z^* that are qualitatively correct. Despite this, it is difficult to make quantitative claims since some of these parameters, such as $\Delta\theta$ and z^*, are hard to constrain. In most panels of Fig. 4.S4 we showed that pond coverage varies appreciably by changing the under-constrained parameter z^*, highlighting the quantitative uncertainty. We note that prior to this investigation, it was not recognized that geometric parameters L, l_0, and p_c can have any effect on pond coverage. The dependence on parameters H, S, and θ_0 seems problematic. Namely, as we have shown, the dependence on H is highly sensitive to hole formation physics. The dependence on S and θ_0 is somewhat counter-intuitive, indicating that the assumption that temperature determines the onset of hole formation needs to be examined in more detail. The above analysis shows that, as we have already stressed several times, we need to improve our understanding of hole formation physics in order to understand how pond coverage depends on physical parameters.

Finally, we note that it is somewhat puzzling that the post-drainage coverage fraction, $p_{\min}$, is neither 0 nor p_c in a typical realistic situation. Namely, the function $g(\eta)$ behaves as $g(\eta) \to 0$ for $\eta \gg 1$ and $g(\eta) \to 1$ for $\eta \ll 1$, so there is only a limited range of η for which $p_{\min} \neq 0$ and $p_{\min} \neq p_c$. The parameter η falls within this range only when $T_{\rm m} \sim T_{\rm h}$, so a

question then arises of why the time to melt through the thickness of the ice freeboard and the time for a significant number of holes to open are comparable. Partly, it must be because both phenomena are related to ice melt, but nevertheless, the two timescales fundamentally depend on different properties of the ice. Moreover, since there are many physical parameters that determine the value of η, its value should wildly fluctuate from one set of environmental parameters to another, making the outcome $\eta \ll 1$ or $\eta \gg 1$ likely. Therefore, the fact that we typically observe $p_{\min} \neq 0$ and $p_{\min} \neq p_c$ perhaps indicates that some of the physical parameters that control pond evolution are in fact not independent as we have assumed.

4.S9 The hole opening distribution

In section 4.5, we introduced a hole opening distribution, $F(\frac{t-t_0}{T_\mathrm{h}})$, as a cumulative of some arbitrary probability density function, $f(\frac{t-t_0}{T_\mathrm{h}})$. Here, we will describe some ways that this distribution affects pond evolution.

First, we discuss how a time distribution, f, can be related to a measurable distribution of brine channel properties, f_θ. In general, we may assume that there exists some underlying probability distribution, $f_\theta(\frac{\theta-\theta_0}{\Delta\theta})$, that describes the fraction of the holes that open when the ice interior temperature (or some other bulk ice property) increases from θ to $\theta + \mathrm{d}\theta$. Such a distribution could in principle be measured in the field or modeled in some way. It is related to the time distribution, f, as

$$f\left(\frac{t-t_0}{T_\mathrm{h}}\right) = f_\theta\left(\frac{\theta-\theta_0}{\Delta\theta}\right)\frac{\mathrm{d}\theta}{\mathrm{d}t}\,. \tag{4.S21}$$

This equation is valid even when the ice warming rate is not constant and provides a basis to relate the hole opening distribution that enters Eqs. 4.12 and 4.14 to measurable sea ice properties.

Next, we discuss the variability of the distribution center, t_0. In section 4.5, we remarked

that the center of the hole opening distribution, t_0, is approximately (see Eq. 4.9)

$$t_0 \approx -T_\mathrm{h} F^{-1}\left(\frac{1}{N_0}\right) \ . \tag{4.S22}$$

We argued that, because the timing of the opening of the first hole fluctuates, the time until a given fraction of holes, $F(0)$, opens also fluctuates, and, consequently, so does t_0. Here we will discuss the probability distribution of t_0 over an ensemble of runs. Let us assume that the first hole opens at some temperature θ_i. t_0 is then the time it takes for ice to warm from θ_i to θ_0. There are N_0 holes and each one opens at a different critical temperature independently drawn from a distribution f_θ. Thus, θ_i is a minimum of a set of N_0 independent random variables drawn from a distribution f_θ. Therefore, the probability of finding some θ_i, and a corresponding t_0, is governed by extreme value statistics (see, e.g., Coles (2001) for an introduction to extreme value statistics).

In general, depending on the tail of an underlying distribution, we expect the probability of finding some minimum value from a large sample of independent random variables to fall into one of three universal distributions. In our case, we expect that f_θ has a relatively well-defined width. A distribution with a well-defined width will likely have an exponential tail, and such distributions have extreme value statistics described by a Gumbel distribution

$$f_\mathrm{Gumbel}(x) = \frac{1}{\beta} e^{-(\frac{x-\mu}{\beta} + e^{-\frac{x-\mu}{\beta}})} \ , \tag{4.S23}$$

where μ is the mode of the distribution and β is the scale. Therefore, we can expect that, for each run, t_0 is drawn from this distribution with a mode that is close to our approximation in Eq. 4.S22. Exactly how parameters μ and β depend on N_0 and T_h depends on the choice of F. Note that this distribution determines the probability of finding t_0 on an ensemble of runs, in contrast with the distributions f and f_θ that determine the probability of opening a brine channel within a single run. Because of this intrinsic variability, even runs with

identical bulk parameters can end up with different pond coverage. In our simulations this variability accounted for about 5% of the variability in the minimum pond coverage, $p_{\min}$.

Finally, we show that it is mainly the tail of the hole opening distribution, F, that controls pond evolution. We do not know F for real ice, and it can in principle have any shape as long as it is a function monotonically increasing from 0 to 1. The universal function, $g(\eta)$, behaves as $g(\eta) \to 1$ for $\eta \to 0$ and $g(\eta) \to 0$ for $\eta \to \infty$. In particular, g falls below 0.1 for $\eta \sim 10$. Therefore, when η exceeds a value of around 10, g falls to approximately zero, and further increase in η does not affect pond evolution. Recall that $\eta = \eta_0 F(\frac{t-t_0}{T_\mathrm{h}})$, where $\eta_0 \equiv c\frac{l_0^2}{L^2}N_0$. If, we assume reasonable parameter values $c \sim 3$, $l_0 \sim 5$ m (see Chapter 5), and $\frac{N_0}{L^2} \sim 100\ \mathrm{m}^{-2}$ (Golden, 2001), we get an order of magnitude estimate $\eta_0 \sim 10000$. Therefore, $\eta \sim 10$ when $F \sim 0.001$ and pond evolution only occurs in the tail of the distribution F. Thus, due to the large density of brine channels, the exact shape of F does not matter apart from determining the weight of the distribution that falls in the tail. We discuss this in more detail below.

Let us look at some particular examples of F to see exactly how it affects pond evolution. As a first example, let us assume that the probability density function, f, falls off exponentially, $f(x) \propto e^x$ for $x \ll -1$. In this case, $F(x) = Ae^x$ for $x \ll -1$ and $F^{-1}(y) = \ln y/A$ for $0 < y \ll 1$, where A is a normalizing constant that also takes into account the rest of the distribution that does not fall in the tail. If we use the approximate relationship $t_0 \approx -T_\mathrm{h} F^{-1}(1/N_0)$ (see Eq. 4.S22), we find

$$\eta(t) \approx c\frac{l_0^2}{L^2}N_0 A e^{t/T_\mathrm{h} - \ln AN_0} = c\frac{l_0^2}{L^2}e^{t/T_\mathrm{h}}\ , \tag{4.S24}$$

for $t \ll T_\mathrm{h} \ln AN_0$. Therefore, if the tail of the hole opening distribution is exponential, pond evolution is independent of the brine channel density, N_0/L^2. Pond evolution is also independent of the shape of the distribution beyond the tail as seen from the fact that the normalizing constant, A, does not appear in the equation for η. If we recall that pond

coverage during stage II is $p = p_c g(\eta(t))$ and note that g is approximately logarithmic in η within the region where pond coverage varies from p_c to 0, we see that pond coverage falls approximately linearly with time.

As a second example, we consider f consistent with a normal distribution, $f(x) \propto e^{-x^2}$, which we used in section 4.7 to compare to observations. In this case, $F(x) = Ae^{-x^2}$ for $x \ll -1$ and $F^{-1}(y) = -\sqrt{\ln A/y}$ for $0 < y \ll 1$, with A being a normalizing constant that accounts for the distribution beyond the tail. Following similar logic as above, we can derive

$$\eta(t) \approx c\frac{l_0^2}{L^2} e^{-(t/T_\mathrm{h})^2 + 2t\sqrt{\ln AN_0}/T_\mathrm{h}} \ . \tag{4.S25}$$

Here, we see that due to the term $\sqrt{\ln AN_0}$, dependence on N_0 and A is not lost. We note two facts about this dependence - 1) pond evolution depends not on the density of brine channels but explicitly on the *number* of brine channels within a drainage basin, and 2) the shape of the distribution beyond the tail only acts to modify the effective number of brine channels through AN_0. This unexpected dependence on the total number of brine channels is a consequence of the fact that stage II begins when the first hole opens rather than when a certain fraction of holes open. We discussed this in section 4.S8. We add that the dependence on N_0 and A is relatively weak - a 10-fold change in the effective number of brine channels leads to only around a 10% change in $\sqrt{\ln AN_0}$, and a correspondingly small change in the rate of change of pond coverage. As noted in Golden (2001), typical brine channel densities are between 60 m^{-2} and 120 m^{-2}, so the uncertainty in the number of channels is likely not a significant source of error so long as we can reliably estimate the size of the drainage basin, L. We also believe that the discussion above partially explains why our rather ad-hoc choice of F as a cumulative normal distribution gave good agreement with observations. Namely, even if the majority of this distribution is not normal, the prediction about pond evolution will be accurate so long as the actual hole opening distribution falls off as e^{-x^2}.

For the more general case of $F = Ae^{-|x|^a}$ in the tail, we can follow similar logic to find

that as the power a increases, the dependence on N_0 and A becomes stronger. Pond coverage depends most strongly on N_0 when the distribution F has a sharp cutoff.

CHAPTER 5

SNOW TOPOGRAPHY ON UNDEFORMED ARCTIC SEA ICE CAPTURED BY AN IDEALIZED "SNOW DUNE" MODEL[1]

5.1 Introduction

As a hallmark of climate change and a major component of the Arctic environment, Arctic sea ice retreat has garnered much scientific and media attention (Perovich and Richter-Menge, 2009; Stroeve et al., 2007). Predicting the rate of sea ice loss is a challenge. The difficulty lies in the fact that sea ice evolution is controlled by many processes that operate on scales ranging from sub-millimeter to tens of kilometers (Holland and Curry, 1999). Possibly the most notable among these processes is the interaction of ice with fluxes of energy coming from the environment mediated by detailed conditions on the ice surface. The presence of snow, water, or dirt on the ice surface can drastically change the rate of absorption of solar radiation or the rate of thermal conduction during winter growth (Perovich, 1996). Finding ways to reduce the complexity of modeling ice surface conditions is of great importance for accurately determining the ice energy balance in large-scale models and, therefore, for improving our understanding of the future of sea ice in a changing climate.

Snow insulates the ice (Sturm et al., 2002; Yen, 1981), reflects sunlight (Perovich, 1996), and provides a source of fresh water that collects into melt ponds (Polashenski et al., 2017). The net effect of each of these processes depends on the spatial distribution of the snow cover. First, ice covered with patchy snow will, on average, grow faster than if the same amount of snow were spread uniformly, since uniform cover insulates the ice more thoroughly (Sturm et al., 2002). Second, uniform snow cover also protects the underlying ice more from

1. This chapter corresponds to Popović et al. (2019a) that, at the time of writing, was under review in JGR: Oceans. It is nearly identical to the manuscript submitted to JGR: Oceans apart from minor changes made mainly to fit the formatting requirements of the thesis and to respond to the comments made by the thesis committee.

solar radiation than a patchy layer, since even a thin layer of snow can increase albedo significantly (Perovich, 1996). Finally, as snow starts to melt, melt ponds first appear in the regions where there is the least snow (Petrich et al., 2012). For this reason, patchy snow cover leads to melt ponds covering the ice surface sooner, melting more ice. In summary, patchy snow cover will lead to both more ice growth during winter as well as to more ice melt during summer.

Liston et al. (2018) modeled snow on flat ice using a simple statistical approach. They represented the snow surface by smoothing and rescaling an initially random height field to match the measured mean snow depth, its variance, and the horizontal correlation length. Their approach is likely sufficient for many practical applications where snow topography needs to be included. However, it produces some essentially unphysical predictions, such as negative snow depths in cases when snow depth standard deviation is comparable to the mean. Here, we adopt a somewhat similar approach that is physically consistent and reproduces the measurements with high accuracy.

Snow often exists in meter-scale dunes which are the most prominent features of the snow cover (Filhol and Sturm, 2015). In Chapter 3, we considered a simple geometric "void model" which represented these snow dunes as circles, and compared it to aerial photographs of melt ponds. These circles had varying size and were placed on a surface randomly and independently of each other, while melt ponds were represented as voids between these circles. Our model was able to reproduce the geometric statistics of melt ponds, such as their size distribution and the fractal dimension as a function of pond size, over the entire observational range of more than 6 orders of magnitude in pond area.

In this Chapter, we generalize the two-dimensional discontinuous "void model" to a continuous synthetic "snow dune" topography that has a vertical component. We represent snow dunes as mounds of Gaussian form that have a randomly chosen horizontal scale, a height proportional to that scale, and that are placed randomly on the surface. The surface

topography is the sum of many such mounds. Like the "void model," this topography accurately describes the horizontal melt pond features, which we take as indirect evidence that it accurately describes the horizontal snow features. We corroborate this by showing that our model fits both LiDAR scans of the pre-melt snow topography and melt pond data using the same typical horizontal mound scale. The fact that the horizontal scale is so similar is somewhat surprising since the two datasets were recoded in different years, different times of year, and different ice types.

The novel prediction of our continuous topography is a vertical snow-depth distribution. By comparing moments of our model distribution to LiDAR measurements of snow-depth, we show that our model height distribution is indistinguishable from the measurements for two occasions when the underlying ice was very flat. The one LiDAR measurement that a slightly deformed ice showed subtle deviation from our model. Thus, we conclude that our model is a highly accurate representation of snow on undeformed ice, while it becomes increasingly inaccurate on deformed ice. The close agreement between snow topography and our model is the main result of this Chapter. Since our model has only three parameters that are uniquely determined by the mean, variance, and the correlation length of snow depth, it follows that it is only necessary to measure these three quantities to completely characterize the statistics of snow cover on flat, undeformed ice.

After showing the agreement between our model and snow measurements, we consider some applications of our model. First, we consider how spatial variability in snow affects the heat conduction through the ice during winter ice growth. Sturm et al. (2002) conducted measurements of snow conductivity, k_s, on deformed multi-year ice, and found that k_s inferred from ice growth is ~ 2.4 times higher than k_s inferred from direct measurements. They found that about 40% of the increase can be explained by snow and ice geometry and that horizontal heat transport, typically neglected in large-scale models, likely contributes significantly. To understand whether these conclusions also hold for undeformed ice, we solve

a 3-dimensional heat equation within the ice assuming that the snow cover is well-described by our "snow dune" model. We develop a simple analytic equation to determine the heat flux conducted through the ice given a set of physical parameters. Contrary to Sturm et al. (2002) for deformed ice, we find that on undeformed ice horizontal heat transport is likely negligible. Moreover, we find a smaller increase in heat conduction than Sturm et al. (2002).

Next, we consider the effect of snow topography on early melt pond development. Using the fact that our model height distribution is well-fit with a gamma distribution, we write an analytic evolution equation for melt pond coverage during an early stage when ice is impermeable. This equation for melt pond evolution enables us to understand how early-stage melt pond growth depends on measurable environmental parameters. Moreover, it allows us to derive a simple condition that distinguishes whether ice will remain pond-free throughout the summer based on snow depth, variance, density and melt rate.

This Chapter is organized so that the new results are presented sections 5.2 to 5.8, while confirming previous results about melt ponds on our topography and mathematical details are left for the Supplementary Information (SI). In section 5.2, we describe our model of the "snow dune" topography. Next, in section 5.3 we describe the analytical properties of our model such as the dependence of moments and the correlation function on model parameters. Then, in section 5.4, we compare our model with the measured snow topography. In section 5.5, we apply our "snow dune" model to determine the conductive heat flux through the ice. Next, in section 5.6, we use our model to investigate melt pond evolution on flat impermeable ice. Finally, in section 5.7, we discuss the implications of our results for large-scale studies and in section and 5.8, we conclude. In SI section 5.S1, we confirm that the synthetic "snow dune" topography predicts ponds that accurately reproduce the geometric statistics of real ponds during late summer. We proove the mathematical results in the subsequent SI sections.

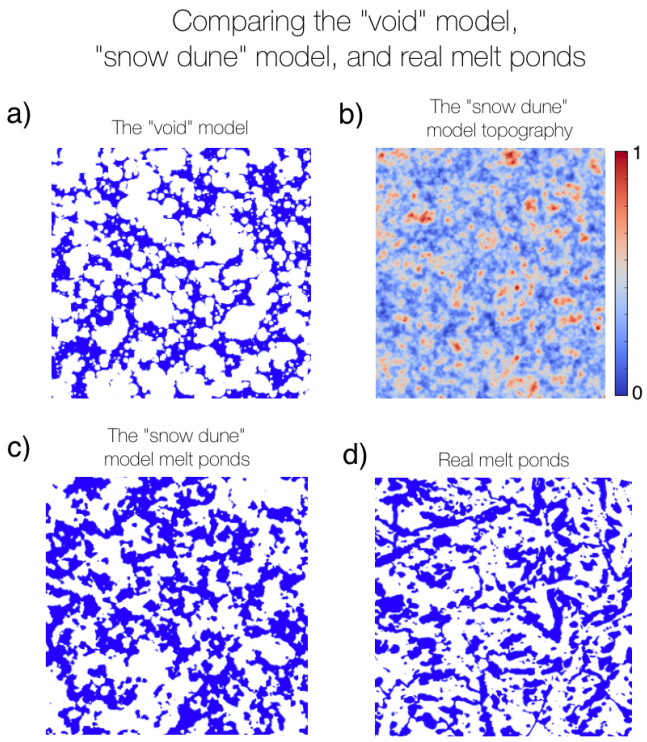

Figure 5.1: a) A realization of the "void model." Figure is taken from Chapter 3. b) Synthetic "snow dune" topography. Red colors indicate topographic highs, while blue colors indicate topographic lows. The upper bound on the scale bar, here set to 1, is arbitrary. c) Ponds on a "snow dune" topography. d) A binarized image of a real melt pond photograph taken on August 14th during the HOTRAX mission.

5.2 The synthetic "snow dune" topography

In this section we will describe our synthetic "snow dune" topography. The entire discussion later in this Chapter will hinge on this model.

In Chapter 3, we developed a simple geometric model where snow dunes were represented by overlapping circles of varying size placed randomly and independently of each other on the ice surface, while melt ponds were represented as voids between these circles. We then compared the statistical properties associated with this simple geometric model with observations of late-summer melt ponds. We found a remarkable agreement between various statistics of real and model melt ponds: by tuning only two model parameters, the model matched the measured pond area distribution, the pond fractal dimension as a function of

pond area, and two correlation functions that describe pond size and connectedness, over the entire observational range of nearly 7 orders of magnitude in pond area. A realization of this model is shown in Fig. 5.1a.

Motivated by the remarkable success of the "void model" in capturing the conditions on the ice surface, we set about to generalize it to a 3-dimensional "snow dune" topography and test the extent to which it can be used as a model of the ice surface. We will show that, in addition to reproducing melt pond features, the "snow dune" model also matches the observed snow-depth distribution.

To generalize the "void model" to a continuous topography, we replace circles with mounds that have a vertical profile. The mounds have a Gaussian shape

$$h(\mathbf{x}) = h_m e^{-(\mathbf{x}-\mathbf{x}_0)^2/2r^2} \ , \tag{5.1}$$

where $h(\mathbf{x})$ is the height of the mound at a point $\mathbf{x}$ on the surface, $\mathbf{x}_0$ is the location of the center of the mound, r is the horizontal scale, and h_m is the maximum height of the mound. Mounds are placed randomly, i.e., $\mathbf{x}_0$ can be anywhere on the surface with equal probability. The horizontal scale, r, is randomly chosen from an exponential probability distribution, f_r

$$f_r(r) = \frac{1}{r_0} e^{-r/r_0} \ , \tag{5.2}$$

where r_0 is the typical scale of the mounds. This distribution is the same as the distribution of circle radii in the "void model" of Chapter 3. To prevent having unrealistically narrow and high mounds, we prescribed the height of each mound, h_m, to be proportional to its horizontal scale, $h_m = h_{m,0} r/r_0$, where $h_{m,0}$ is the typical mound height. Optionally, the mounds also may be elongated along a certain axis and the axes may be preferentially aligned to simulate anisotropy in the snow dunes. Including anisotropy did not make any significant changes to the conclusions we make based on the model. The topography is then a sum of

N such mounds placed on an initially flat surface

$$h_{\mathrm{SD}}(\mathbf{x}) = \sum_{i=1}^{N} h_{m,0} \frac{r_i}{r_0} e^{-(\mathbf{x}-\mathbf{x}_{0_i})^2/2r_i^2} \ , \tag{5.3}$$

where $h_{\mathrm{SD}}(\mathbf{x})$ is the height of the "snow dune" topography at location $\mathbf{x}$. A realization of this topography is shown in Fig. 5.1b. Code to generate it is available at `https://github.com/PedjaPopovic/Snow-dune-topography`. Ponds that form on this surface after cutting it with a horizontal plane are shown in Fig. 5.1c. This is shown alongside a realization of the "void model" (Fig. 5.1a) and a binarized image of real melt ponds (Fig. 5.1d).

There are three parameters in this model. These are the typical horizontal mound scale, r_0, the density of mounds, ρ, placed within the domain of size L, $\rho \equiv N\frac{r_0^2}{L^2}$, and the typical mound height, $h_{m,0}$. The first two of these parameters, r_0 and ρ, also enter the "void model."

5.3 Statistics of the synthetic "snow dune" topography

Here, we describe the statistics of the "snow dune" model that we will use later. In particular, we first show how the mean, variance, and correlation length depend on model parameters. We then derive the all of the moments of the topography. Finally, we compare the height distribution of the "snow dune" topography with a gamma distribution. We derive all of the results in this section in SI section 5.S2. All of these results follow directly from the definition of the "snow dune" model we described in section 5.2.

First, we find that the mean, $\langle h_{\mathrm{SD}} \rangle$, and variance, $\sigma^2(h_{\mathrm{SD}}) = \langle (h_{\mathrm{SD}})^2 \rangle - \langle h_{\mathrm{SD}} \rangle^2$, of the topography depend on the typical mound height, $h_{m,0}$, and the density of mounds, ρ, as

$$\langle h_{\mathrm{SD}} \rangle = 12\pi h_{m,0}\rho \quad , \quad \sigma^2(h_{\mathrm{SD}}) = 24\pi h_{m,0}^2 \rho \ . \tag{5.4}$$

In fact, we can explicitly find every moment of the topography, $\left\langle (h_{\mathrm{SD}})^n \right\rangle$, by knowing the

previous moments and using the recursion formula (see SI section 5.S2 for derivation)

$$\left\langle (h_{\mathrm{SD}})^n \right\rangle = 2\pi\rho \sum_{j=1}^{n} \binom{n-1}{n-j} \frac{(j+2)!}{j} h_{m,0}^{j} \left\langle (h_{\mathrm{SD}})^{n-j} \right\rangle \ . \tag{5.5}$$

Equations 5.4 can be easily obtained using this formula.

Next, we define the height correlation function, $C_h(\mathbf{l})$, as

$$C_h(\mathbf{l}) \equiv \frac{\langle h_{\mathrm{SD}}(\mathbf{x}) h_{\mathrm{SD}}(\mathbf{x}+\mathbf{l}) \rangle - \langle h_{\mathrm{SD}} \rangle^2}{\sigma^2(h_{\mathrm{SD}})} \ , \tag{5.6}$$

where $\mathbf{l}$ is a horizontal displacement of the topography. The correlation function quantifies how much the surface height at $\mathbf{x}$ is correlated with the surface height at $\mathbf{x}+\mathbf{l}$. If the surface is isotropic, C_h only depends on the magnitude of the displacement vector, l. We can then define the correlation length, l_0, as the distance at which C_h falls by a factor of e. Beyond l_0, features on the topography can be considered approximately uncorrelated. Using these definitions, we find that C_h and l_0 depend on the horizontal mound scale, r_0, of an isotropic "snow dune" model as (see SI section 5.S2 for derivation)

$$C_h(l) = \frac{1}{24} \int_0^\infty z^4 e^{-z - l^2/(2r_0 z)^2} \mathrm{d}z \ , \tag{5.7}$$

$$l_0 = r_0 \xi_0 \ , \tag{5.8}$$

where $\xi_0 \approx 9.3689...$ is a number that can be estimated to arbitrary precision by inverting $C_h(l_0) = 1/e$ using Eq. 5.7. The mean, variance, and the correlation length are all measurable properties of real topographies. This means that computing these quantities from measurements lets us unambiguously choose the model parameters. Introducing slight changes in the model, for example adding anisotropy, would change the numerical pre-factors in these equations.

Since we can find all of the moments of the "snow dune" topography using Eq. 5.5, we

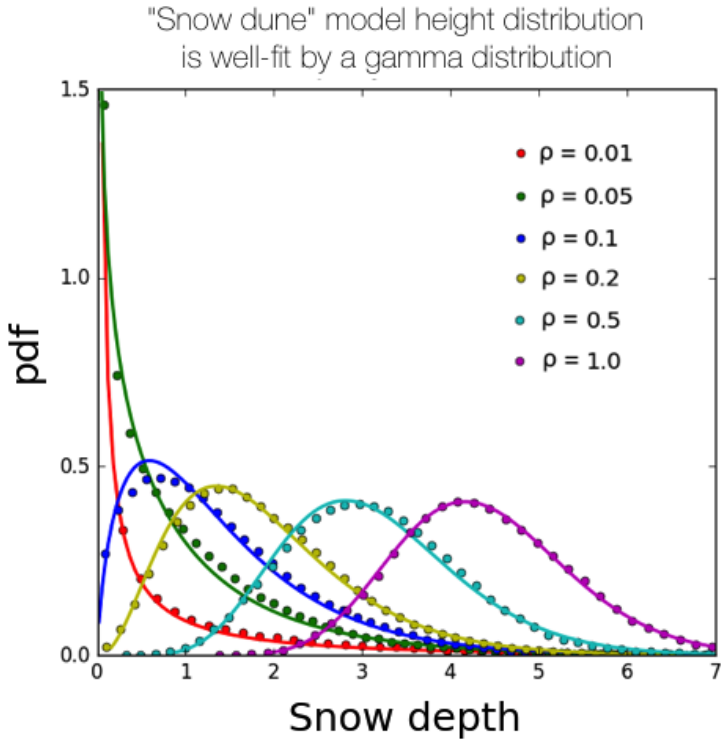

Figure 5.2: Dots represent the height distribution of the "snow dune" topography for different densities of mounds, ρ. Solid lines represent fits using a gamma distribution. Units of snow depth here are arbitrary. Note that the LiDAR measurements we consider in section 5.4 range from $\rho \approx 0.2$ to $\rho \approx 0.5$, a much smaller range than we inspected here.

can fully determine its height distribution. However, it is impractical to do this, and, for practical purposes, we now show that the height distribution of the "snow dune" topography is well-fit with a gamma distribution. The two distributions are not the same, as can be seen by comparing their moments. However, they are qualitatively very similar, and the differences between them arise from arbitrary choices in our model such as the exponential distribution of radii of the snow dunes, Eq. 5.2, and the linear relationship between the mound radius and height. We describe the relationship between the height distribution of the "snow dune" topography and the gamma distribution in detail in SI section 5.S2.

In Fig. 5.2, we show height distributions for synthetic topographies with varying spatial densities of mounds, ρ, with the variance, $\sigma^2(h_{\mathrm{SD}})$, kept fixed. We can see that varying ρ changes the shape of the distribution and that a gamma distribution can fit the height distribution well for all choices of ρ. To quantify the quality of the fit, we use the Kolmogorov-Smirnov (KS) statistic, i.e., the maximum distance between the empirical and theoretical cumulative distributions. The fit is typically considered good if this statistic is below 0.05. We find that for all choices of ρ, the maximum distance between the cumulative "snow dune" height distribution and the best-fit gamma distribution is below 0.05, and ranges between 0.03 for $\rho = 0.01$ to 0.006 for $\rho = 1$, generally decreasing for increasing ρ.

A gamma distribution has the form

$$f_\Gamma(h) = \frac{1}{\Gamma(k) h_0^k} h^{k-1} e^{-h/h_0} \ , \tag{5.9}$$

where h_0 is a scale parameter, k is a shape parameter, and $\Gamma(x)$ is a gamma function. The two parameters of the gamma distribution, h_0 and k, are related in a simple way to the mean and variance of the distribution, $\langle h \rangle$ and $\sigma^2(h)$

$$k = \frac{\langle h \rangle^2}{\sigma^2(h)} \quad , \quad h_0 = \frac{\sigma^2(h)}{\langle h \rangle} \ . \tag{5.10}$$

Both of these parameters are therefore uniquely determined by the typical height and density of mounds through Eqs. 5.4. In particular, we find that the scale parameter, h_0, scales linearly with the typical height of mounds, while the shape parameter, k, scales linearly with the density of mounds,

$$h_0 = 2h_{m,0} \quad , \quad k = 6\pi\rho \; . \tag{5.11}$$

5.4 Measured snow topography

The synthetic "snow dune" topography is meant to represent the height of snow relative to the flat underlying ice. Therefore, the height distribution of the "snow dune" topography should correspond to the pre-melt snow-depth distribution. Here, we will compare the statistics of the synthetic "snow dune" topography to detailed LiDAR measurements of pre-melt snow topography made by Polashenski et al. (2012).

During their field expedition, Polashenski et al. (2012) performed detailed LiDAR scans of the surface topography within a 100m×200m region on multiple dates in 2009 and 2010. During 2009, Polashenski et al. (2012) monitored two locations separated by about 1 km from each other, one in the north (2009N) and one in the south (2009S). In 2010 they monitored only one location. In Fig. 5.3a we show an example of such a measurement, which shows the height of snow before the start of the melt season, and compare it to a randomly generated "snow dune" topography (Fig. 5.3b). Assuming that the underlying ice is flat and the pre-melt ice is fully covered with snow, the LiDAR-estimated height in Fig. 5.3a represents the snow depth plus some reference height. Therefore, to compare with the "snow dune" topography, we estimated the snow depth from these LiDAR scans by subtracting the minimum LiDAR elevation from the rest of the scan. We show the snow-depth distribution for the three LiDAR scans in Fig. 5.3c and we show the moments of these distributions in Fig. 5.3d. We estimate the height correlation function for these three measurements in Fig. 5.4. The data from Polashenski et al. (2012) are freely available at

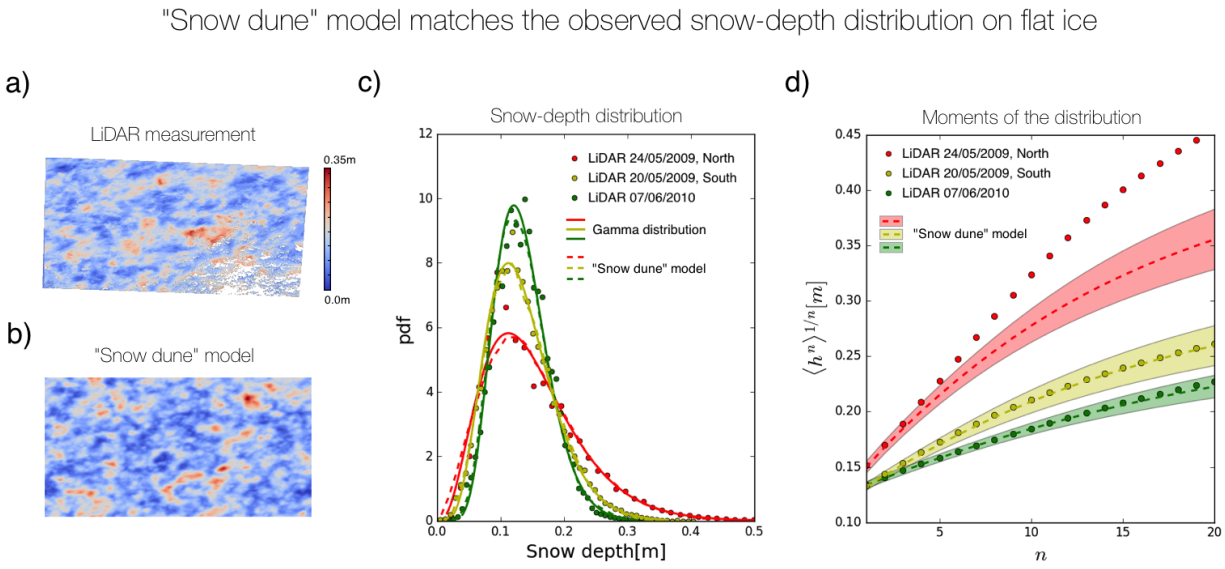

Figure 5.3: a) LiDAR measurement of the pre-melt snow topography by Polashenski et al. (2012) in early June of 2010. b) A realization of synthetic "snow dune" topography. The density of mounds was chosen such that the height distribution of the synthetic topography corresponds well to the measured snow-depth distribution. Mounds are slightly elongated to simulate anisotropy in the actual snow (we used a ratio of semi-major to semi-minor axis equal to 2). c) Dots represent snow-depth distribution estimated using LiDAR measurements for two different years. Solid lines are gamma distributions with parameters estimated based on the mean and variance of the measurements. Dashed lines are the corresponding "snow dune" topography height distributions, and are nearly indistinguishable from the solid lines. d) Moments of the height distribution. The horizontal axis is the moment order, n, while the vertical axis is the n-th root of the n-th moment. Dots represent moments of the measured snow topography. The thick dashed lines represent the mean moments across an ensemble of 50 randomly-generated "snow dune" topographies on the domain of the same size as the measurements. The colored shadings represent one standard deviation from the mean on that ensemble.

Table 5.1: Statistics of the LiDAR measurements and model parameters inferred from them. The KS statistic was calculated with respect to the gamma distribution.

	$\langle h \rangle$	$\sigma(h)$	l_0	$h_{m,0}$	ρ	r_0	h_0	k	KS
2009N	15.2 cm	7.8 cm	5.5 m	2.0 cm	0.20	0.59 m	4.0 cm	3.8	0.03
2009S	13.4 cm	5.4 cm	5.2 m	1.1 cm	0.33	0.56 m	2.2 cm	6.2	0.01
2010	13.4 cm	4.3 cm	5.8 m	0.7 cm	0.53	0.61 m	1.4 cm	9.9	0.03

`http://chrispolashenski.com/data.php`.

To see whether the snow-depth distribution of these measurements conforms to the predictions of our model and a gamma distribution, we inferred parameters $h_{m,0}$ and ρ using Eqs. 5.4 and parameters of the gamma distribution, k and h_0, using Eqs. 5.10 based only on measured mean snow depth and snow depth variance. We show the statistics of measured topographies along with model and gamma distribution parameters in Table 5.1. The solid lines in Fig. 5.3c show a gamma distribution with parameters chosen in this way, while the dashed lines show a height distribution of the synthetic "snow dune" topography. We can see that in all cases, the measured snow-depth distribution agrees well with our model and a gamma distribution, with a Kolmogorov-Smirnov (KS) statistic remaining at or below 0.03 in all cases.

We can gain a better understanding of both the measured and the synthetic snow-depth distributions by looking at their moments. Higher order moments describe a more and more detailed structure of the probability distribution. This is precisely why we can use these higher order moments to distinguish between similar, but subtly different distributions. In Fig. 5.3d, we compare moments of the measured snow topography and randomly-generated "snow dune" topographies. Higher order moments depend on the domain size, resolution, and the particular realization of the topography. For this reason, to get the moments of the simulated "snow dune" topographies, we created an ensemble of 50 randomly-generated topographies with the same resolution and domain size as the measurements. For each realization, we then found the root-moments, $\langle h^n \rangle^{1/n}$. Dashed lines in Fig. 5.3d show the mean and one standard deviation of the root-moments over this 50-member ensemble. We

used the model parameters shown in Table 5.1.

For the 2010 and 2009S measurements, all of the measured moments fall squarely within the range of values obtained with an ensemble of simulated "snow dune" topographies. In fact, we tested the first 150 moments for these two measurements, and found that this agreement holds throughout. This means that realizations of the "snow dune" topography that have *exactly* the same height distribution as the measurements are common. We can therefore conclude that the snow-depth distribution for 2010 and 2009S measurements is indistinguishable from the "snow dune" height distribution! This agreement is, however, not observed for 2009N measurements - moments of measured snow-depth distribution are consistently higher than those of the simulations and no randomly generated "snow dune" topography has high order moments that match the measurements. This difference is subtle which is why we could not observe it using the KS statistic, and for most practical uses that require only a snow-depth distribution it is likely not very important. Nevertheless, it constitutes a real observable difference between our model and the 2009N measurements, and shows that there exist features in real data that our model cannot predict. We return to explaining this difference below.

Next, we describe the height correlation function, $C_h(l)$, for measurements and the model. We find the LiDAR $C_h(\mathbf{l})$ using Eq. 5.6. Due to prevailing winds, snow on sea ice often shows a strong preferential orientation, with snow dunes elongated along the direction of the wind (Petrich et al., 2012). We observe this in the measured $C_h(\mathbf{l})$, which we find to depend on the direction of the displacement vector, $\mathbf{l}$. Such anisotropy can be included in our model by elongating the mounds along a particular axis, as we did in Fig. 5.3b for visual comparison. However, to keep our discussion as simple as possible, we chose to keep our model isotropic. Thus, to obtain a measured correlation function that depends only on the magnitude of $\mathbf{l}$, we average the measured $C_h(\mathbf{l})$ over all directions of $\mathbf{l}$. Then, we find the correlation length, l_0, the distance at which the measured $C_h(l)$ falls off by a factor of e,

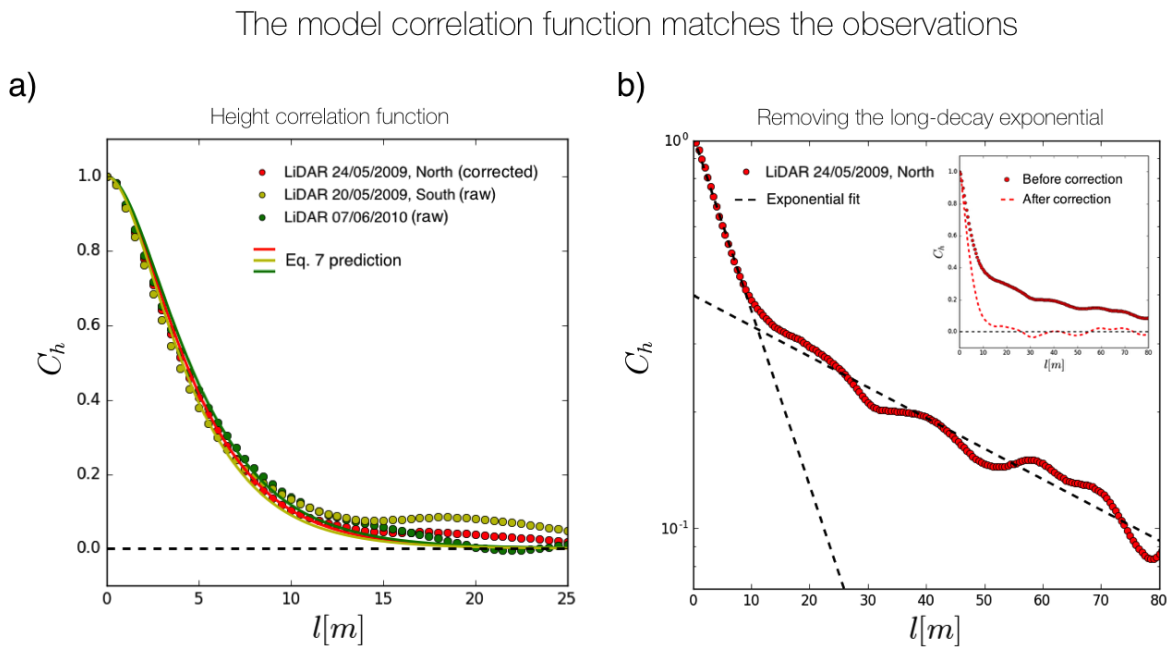

Figure 5.4: a) Height correlation functions. Dots represent measurements, and the solid lines represent predictions for the "snow dune" model using Eq. 5.7. Correlation functions for 2010 and 2009S measurements (yellow and green dots) were calculated from raw data. Correlation function for the 2009N measurement was corrected by removing a long-decay exponential. The raw 2009N data are shown in panel b. b) Correction for the 2009N correlation function. Dots represent C_h calculated with raw data on a semi-log plot. The two black dashed lines are exponential fits to the short-decay and long-decay portions of C_h. Inset shows C_h before (red dots) and after (red dashed line) removing the long-decay exponential on a linear plot.

and relate it to the model parameter r_0 according to Eq. 5.8 (see Table 5.1). We show the measured and the theoretical $C_h(l)$ calculated according to Eq. 5.7 in Fig. 5.4.

Again, we find that 2010 and 2009S measurements agree very well with model predictions (Fig. 5.4a). However, 2009N again shows a disagreement with the model. The height correlation function calculated from raw 2009N data is shown in Fig. 5.4b. It first decays quickly, and then the decay slows down, with features on the surface remaining correlated across the domain. By plotting C_h on a semi-log plot, we find that it is approximately a sum of two exponentials - one with a short decay-length and another with a long decay-length comparable to the domain size. We get good agreement with the model after removing this long decay exponential. To do this, we fit an exponential function to C_h for $l > 20$m. We then subtract this exponential from the whole C_h and rescale so that $C_h(0) = 1$. The result is a corrected correlation function, shown as the red dots in Fig. 5.4a and the dashed line in the inset of 5.4b. The result of this correction does not depend strongly on the choice of the cutoff length for the exponential fit so long as this length is large enough. The correlation length, l_0, and the model parameter r_0 reported in Table 5.1 correspond to this corrected correlation function.

In Chapter 3 and SI section 5.S1, we calculated similar correlation functions for melt pond images taken during 1998 and 2005. There, we similarly observed correlation functions with two decay lengths - one comparable to the size of melt ponds, and another comparable to the size of the images. In Chapter 3, we attributed the long-decay length to differences in ice properties between different ice floes and large-scale deformation features such as ridges. A match between the model and the data could only be achieved after removing this long-decay length by a procedure analogous to the one we described above.

Here, we again suggest that the long-decay length comes from variability in the underlying properties of the ice. In fact, we believe that all of the differences between 2009N measurements and the model can be explained by this variability in the underlying ice prop-

erties. Polashenski et al. (2012) note that 2009N site had ice that finger-rafted early in the growth season and contained some lightly rubbled ice, while the 2009S site had very flat ice. They did not comment on ice conditions during 2010 measurements. To test whether our model is consistent with variable ice properties across the domain, we created a "snow dune" topography where one half of the domain had higher $h_{m,0}$ and ρ than the other half, but together both parts had the same mean and variance as the measured 2009N topography. In this experiment, the model correlation function obtained a long decay length comparable to the domain size. Moreover, we found that we can choose the parameters in the first half of the domain such that all of the moments of the model height distribution match the moments of the 2009N data. Therefore, our model is consistent with the 2009N data if we assume that 2009N data contains regions with different underlying ice properties. We note that even though there exists an observable difference between the snow-depth distribution of 2009N and our model, it is very small and would likely not significantly change the ice evolution in a large scale model. Nevertheless, it hints that highly deformed ice may in fact significantly deviate from our model.

In SI section 5.S1, we compare melt ponds on the synthetic "snow dune" topography with melt pond data derived from images taken during 1998 and 2005. These images cover a much larger area than the LiDAR scans we considered here. Each melt pond image covers an area of roughly 1 km^2 as opposed to 0.02 km^2 covered by the LiDAR scans. As in Chapter 3, we find an agreement between the observed and model melt ponds. To match the melt pond statistics, we had to choose $r_0 \approx 0.6$ m in the model for both 1998 and 2005 ponds, in close agreement with r_0 we find here from the height correlation functions of the pre-melt height topographies (see Table 5.1). In all three measurements of the LiDAR topography, we found r_0 within at most several cm from $r_0 = 0.6$ m. We take this as evidence that melt ponds are controlled by the pre-melt snow topography and that the "snow dune" model may be meaningfully extended to at least the kilometer scale.

We will make several final notes to end this section. First, we note that since $r_0 \approx 0.6$ m in observations for four different years and multiple locations and ice types, the horizontal scale of the snow features seems to be a robust property of the snow cover. For this reason, future models that require a representation of snow may be able to keep the correlation length $l_0 \approx 5.6$m fixed, and only keep track of mean snow depth and variance in order to represent snow in a principled way. Second, we note that distributions other than a gamma distribution that have been used to model the snow-depth, such as normal (Liston et al., 2018) or lognormal (Landy et al., 2014), can also often fit the measurements well. For example, a lognormal distribution passes the KS test for all three LiDAR measurements, while a normal distribution passes the KS test for 2010 measurements. However, these distributions cannot qualitatively capture the height distribution of the synthetic "snow dune" topography for all values of the density of mounds, ρ, while a gamma distribution can. For small ρ (large ratio of standard deviation to mean), a normal distribution predicts a significant fraction of negative observations, while a lognormal distribution predicts a heavy tail at large h. Since the "snow dune" model so closely reproduces both the LiDAR and melt pond measurements, we believe that a distribution that is qualitatively consistent with the predictions of the "snow dune" model is a more justified model for a snow-depth distribution that would fit the measurements over a wider parameter range.

5.5 Heat transport through the ice

In this section we will consider the application of our model to heat conduction through the ice. Sturm et al. (2002) conducted measurements on deformed multi-year ice, and concluded that the conductivity of snow inferred from large-scale ice growth is roughly 2.4 times higher than the conductivity of snow measured on-site. They ascribed a significant portion of this difference to spatial variability of snow depth and also suggested that a significant fraction of heat is transported horizontally. Motivated by their study, here we investigate the extent

to which these conclusions also apply to undeformed ice. We consider a full 3-dimensional model of heat conduction to determine how much heat is extracted through undeformed ice with variable snow cover.

To model heat conduction, we assume that ice is a block of uniform thickness, H, that ice and snow have fixed conductivities, k_i and k_s, that the snow cover is well-described by our "snow dune" model, that the temperature at the ice-ocean interface is fixed at the freezing point of salt water, T_f, that the temperature of the snow surface is fixed at the temperature of the atmosphere, T_a, and that the temperature field within the ice and snow is in a steady state. Additionally, we assume that the temperature profile in the snow is linear (but not necessarily in the ice). This assumption is reasonable, since snow cover is typically thin compared to its horizontal correlation length. Finally, we impose periodic boundary conditions in the horizontal directions.

In SI section 5.S3, we develop relations for the mean conductive heat flux through the ice, F_c, under the assumptions above. In particular, starting from Laplace's equation for heat conduction and using the fact that our "snow dune" model is fully characterized by the mean, variance and the correlation length of the snow surface, we show that F_c must be of the form

$$F_c = F_0 \Phi\big(\eta, \Sigma, \Lambda\big) \ , \tag{5.12}$$

$$F_0 \equiv k_i \frac{T_f - T_a}{H} \quad , \quad \eta \equiv \frac{k_i}{k_s}\frac{\langle h \rangle}{H} \quad , \quad \Sigma \equiv \frac{\sigma(h)}{\langle h \rangle} \quad , \quad \Lambda \equiv \frac{l_0}{H} \ , \tag{5.13}$$

where Φ is a non-dimensional flux given a non-dimensional snow depth, η, a non-dimensional snow roughness, Σ, and a non-dimensional correlation length, Λ. The dimensional quantity F_0 is the heat flux conducted through the ice with no snow on top, so the function $\Phi \leq 1$ represents the fraction of this flux that is conducted when snow is present. After showing this, in SI section 5.S3, we show that the heat conduction problem can be explicitly solved

if $\Lambda \to \infty$ (when heat transport is purely vertical), and when $\Lambda \to 0$ (when the horizontal heat transport dominates). Knowing these two limits, we then numerically solve the heat conduction problem for various combinations of the parameters η, Σ, and Λ and show that the function Φ is approximately equal to

$$\Phi\big(\eta, \Sigma, \Lambda\big) \approx \Phi_v + \frac{\Phi_h - \Phi_v}{(1 + c\Lambda)^2} \ , \tag{5.14}$$

$$\Phi_v \equiv \int_0^\infty \frac{\tilde{f}_\Gamma(z, \Sigma)}{1 + z\eta} \mathrm{d}z \qquad \text{(purely vertical heat transport)} \ , \tag{5.15}$$

$$\Phi_h \equiv \frac{1}{1 + \eta(1 - \Sigma^2)} \qquad \text{(dominant horizontal heat transport)} \ , \tag{5.16}$$

where $c \approx 0.83$ is a numerical constant, Φ_v is the non-dimensional flux if vertical heat transport dominates, and Φ_h is the non-dimensional flux if horizontal heat transport dominates. Φ_h is an upper bound on heat flux given parameters η and Σ. The gamma distribution $\tilde{f}_\Gamma$ in Eq. 5.15 is normalized to have a mean equal to 1, and is consequently only a function of Σ with the parameters $k = \Sigma^{-2}$ and $h_0 = \Sigma^2$. Equation 5.16 is only valid for $\Sigma < 1$. If $\Sigma > 1$, we have that $\Phi_h = 1$ so that, if $\Lambda \to 0$, the heat is conducted as if there were no snow on top of the ice, $F = F_0$.

To quantify how much ice growth is due to snow-depth variability, we also consider the non-dimensional flux assuming a uniform snow cover, $\Phi_u \equiv \frac{1}{1+\eta}$. The fraction of ice growth that can be attributed to snow-depth variability can then be estimated as $\frac{\Phi - \Phi_u}{\Phi}$. We show the estimated values of all of the non-dimensional parameters discussed above for the three LiDAR measurements we considered in the previous section in Table 5.2.

From Eq. 5.14, we can see that the contribution of horizontal heat transport to total heat transport is proportional to $(1 + c\Lambda)^{-2}$. As we discussed in the previous section, the correlation length for all datasets we considered is around $l_0 \approx 5.6$ m and is likely on the same order throughout the Arctic. This means that for a realistically ice thickness of around 1 m, $\Lambda \approx 5$. This implies that horizontal heat transport contributes less than 5% of the maximum

Table 5.2: Non-dimensional parameters of the snow surface for the LiDAR measurements of Polashenski et al. (2012) assuming an ice thickness of $H = 1$ m, conductivity of fresh ice $k_i = 2.034$ $\mathrm{Wm^{-1}K^{-1}}$ (Untersteiner, 1964), snow conductivity estimated by Sturm et al. (2002), $k_s = 0.14$ $\mathrm{Wm^{-1}K^{-1}}$, and duration of stage I of pond evolution $T = 5$ days.

	η	Σ	Λ	Φ_u	Φ_v	Φ_h	Φ	$(\Phi - \Phi_u)/\Phi$	ω
2009N	2.2	0.5	5.5	0.31	0.35	0.38	0.35	0.11	1.7
2009S	1.9	0.4	5.24	0.34	0.37	0.39	0.37	0.07	1.7
2010	1.9	0.3	5.75	0.34	0.36	0.37	0.36	0.04	1.5

possible contribution, $\Phi_h - \Phi_v$. This is very small - as we can see from Table 5.2, the total non-dimensional flux, Φ, is equal to Φ_v to two significant digits for all measurements. Even for exceedingly thick ice of 2 m thickness, and snow with significant variability, as in the 2009N measurements, horizontal heat transport still contributes less than 1% of total ice growth. Therefore, horizontal heat transport can most likely be ignored on flat undeformed ice. This is in contrast with Sturm et al. (2002) who found a significant fraction of heat is transported horizontally in regions of deformed ice. For this reason, it may be necessary to include non-uniform ice thickness to appropriately capture heat transport on deformed ice.

Even though horizontal heat transport may be neglected on undeformed ice, snow variability may still noticeably contribute to conductive heat flux. In Table 5.2, we show the fraction, $(\Phi - \Phi_u)/\Phi$, of heat transport that is due to snow-depth variability. We see that snow-depth variability contributes between 4% for 2010 measurements that have the least snow-depth variability and 11% for 2009N measurements that have the most snow-depth variability, with the effect generally increasing with η and Σ. Although this is not large, it is comparable to the effect of melt ponds during summer - for example, if 15% of ice of albedo 0.6 is covered by ponds of albedo 0.25, ice will melt on average 10% faster than if there were no ponds. Therefore, the effect of snow variability on first-year ice during winter may be enough to partially compensate the effect of melt ponds during summer. Again, this effect is smaller than on deformed ice, where Sturm et al. (2002) found that about a quarter of ice growth is due to variable snow and ice geometry.

5.6 Melt pond evolution during early melt season

During the early melt season, ice is largely impermeable and ponds can quickly flood vast areas of the ice surface. This is known as stage I of pond evolution and is typically followed by stages II and III which correspond to pond drainage and subsequent slow pond growth on highly permeable ice (Landy et al., 2014; Polashenski et al., 2012). In this section, we will discuss equations for pond evolution during stage I when ice can be considered to be impermeable, which we derive in SI section 5.S4. These equations follow from the fact that the pre-melt snow distribution on flat ice is well-described by our "snow dune" topography.

5.6.1 Analytic model for pond evolution during stage I

Since water can flow relatively freely through permeable snow, during stage I of pond evolution there likely exists a common water table for the entire ice floe, and ponds are the regions where surface topography lies below it. Therefore, to model stage I of pond evolution, we will assume that snow is fully permeable and that snow below the water level is completely saturated with water, that underlying ice is impermeable and initially flat, that the pre-melt snow topography is well-described by our "snow dune" model, and that no meltwater is lost from the domain (we will reconsider this assumption in the next subsection). The ice and snow topography can change by melting, thereby creating meltwater. We will thus assume that snow, bare ice, ponded ice, and ponded snow (water-covered snow) melt at different rates but that these rates are constant in space and time and independent of factors such as snow or pond depth. Finally, we will assume that both snow and ice melt only at the surface and that ice cannot melt until snow has melted away.

In SI section 5.S4, we develop equations for the time-evolution of pond coverage, p, and water level, w, during stage I under the assumptions above. We do this by tracking the volume of water produced by melting. We use the fact that, if no water is lost from the domain, the water level can only increase, so that ponds only encounter bare snow topography

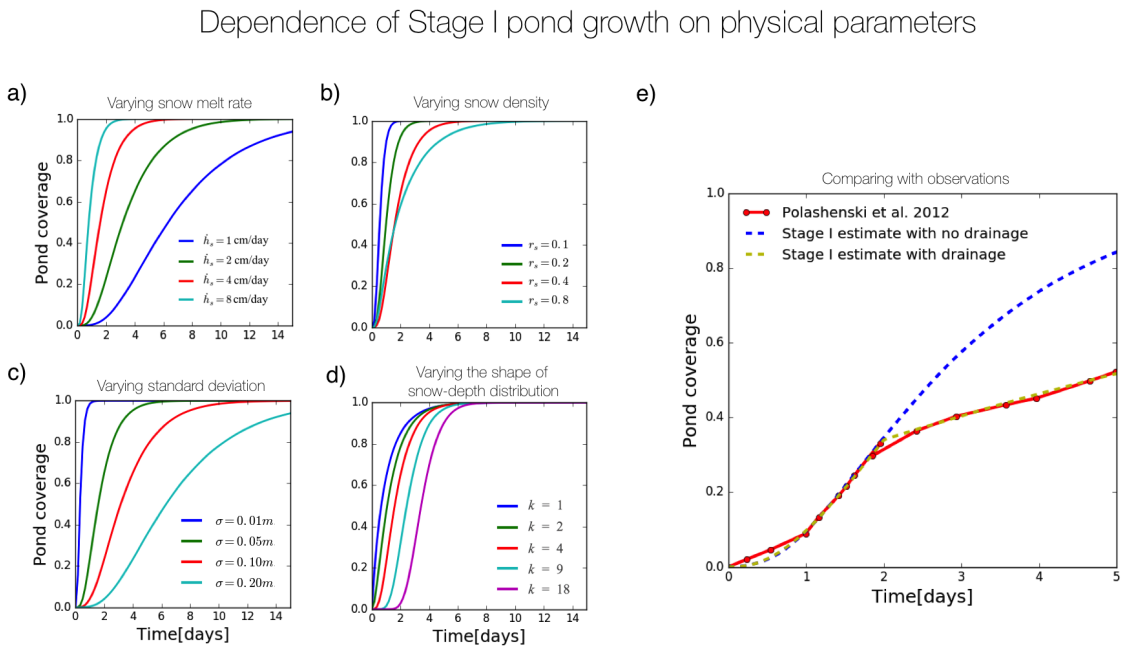

Figure 5.5: a-d: Pond coverage evolution during stage I found using Eqs. 5.17 and 5.18 for a variety of model parameters. In each panel, we change one parameter, while we keep the others fixed at default values $\dot{h}_s = 4$ cm day^{-1}, $r_s = 0.4$, $\sigma(h) = 0.05$ m, and $k = 4$. a) Pond coverage evolution for different snow melt rates, $\dot{h}_s$. b) Pond coverage evolution for different snow to ice density ratios, r_s. c) Pond coverage evolution on topographies with different snow-depth standard deviations, $\sigma(h)$. d) Pond coverage evolution on topographies with different shape parameters, k. e) Comparing pond evolution during stage I calculated using Eqs. 5.17 to 5.19 (dashed blue and yellow lines) with observations of Polashenski et al. (2012) (red line). The dashed blue line represents pond evolution estimated using Eqs. 5.17 and 5.18 that assumes no drainage during stage I. Dashed yellow line represents pond evolution estimated using Eq. 5.19, which assumes a constant drainage rate beyond the percolation threshold of $p_c = 0.35$. Topography used to calculate stage I evolution has the same mean and variance as the actual measured pre-melt snow topography obtained with LiDAR measurements.

that melts at a uniform rate and is, therefore, unaltered throughout the melt season. This means that we can use our pre-melt topography to accurately describe the ponded fraction of the surface. It also means that regions of bare ice (ice with no snow and no water on top) do not exist. We greatly simplify the problem by neglecting terms that are proportional to the density difference between water and ice, which are, in addition to being small, only relevant at very high pond coverage. Using this strategy, we show that pond coverage evolution is approximately the solution to the simple system of ordinary differential equations

$$\dot{w} \approx -\frac{r_i r_s (1-p)}{1-r_s(1-p)} \dot{h}_s \ , \tag{5.17}$$

$$\dot{p} = f_\Gamma(w - \dot{h}_s t)\Big(\dot{w} - \dot{h}_s\Big) \ , \tag{5.18}$$

where $\dot{x} \equiv \frac{\mathrm{d}x}{\mathrm{d}t}$ is a shorthand notation for the rate of change of quantity x, w is the water level, p is the pond coverage faction, $r_i \equiv \frac{\rho_i}{\rho_w}$ is the ratio of ice density to meltwater density, $r_s \equiv \frac{\rho_s}{\rho_i}$ is the ratio of snow density to pure ice density, $\dot{h}_s$ is the melt rate of bare snow, assumed to be constant in space and time, and $f_\Gamma(w - \dot{h}_s t)$ is the gamma distribution given by Eq. 5.9 and evaluated at $w - \dot{h}_s t$. The parameters of the gamma distribution are determined from the mean and variance of the pre-melt snow topography according to Eq. 5.10. The initial conditions for Eqs. 5.17 and 5.18 are no ponds at the initial time, $p(t=0) = 0$, and a water level of zero, $w(t=0) = 0$. Note that $\dot{h}_s < 0$, so $\dot{w} > 0$ and $\dot{p} > 0$. Even though Eqs. 5.17 and 5.18 are approximate, they are a very accurate approximation to the full 2d model defined by the assumptions above at low pond coverage and only deviate slightly from the full model at high pond coverage (see SI section 5.S4). In SI section 5.S4, we also derive a second-order approximation that becomes nearly indistinguishable from the full 2d model for any pond coverage.

We can see from Eqs. 5.17 and 5.18 that, since ice and water density are fixed, stage I pond coverage evolution depends mainly on the density of snow through r_s, the melt rate of bare snow, $\dot{h}_s$, and the mean and variance of the initial snow-depth distribution through f_Γ.

Note that melt rates of bare ice, ponded ice, and ponded snow do not enter this first-order approximation for pond evolution. In Figs. 5.5a-d, we change each of the parameters that enter Eqs. 5.17 and 5.18 to see how they affect stage I pond evolution. We note that in Figs. 5.5a-d, we parameterized f_Γ with its standard deviation, $\sigma(h)$, and its shape parameter, k, since $\sigma(h)$ strongly affects pond coverage evolution, while k affects it only weakly. Within a reasonable range of parameters, pond evolution during stage I is most sensitive to the rate of snow melt (Fig. 5.5a) and the standard deviation of the initial snow-depth distribution (Fig. 5.5c). In fact, as we explain in SI section 5.S4, increasing the snow melt rate by some factor leads to the same pond coverage evolution as decreasing the volume of snow by the same factor. Snow density and the shape of the initial snow-depth distribution parameterized by k and assuming that $\sigma(h)$ is fixed, do not matter as much (Figs. 5.5b and d).

5.6.2 Meltwater drainage during stage I

One important factor we have neglected is the potential for limited drainage during stage I. Even though ice is typically impermeable during this stage, outflow pathways such as cracks in the ice, seal breathing holes, or the floe edge can exist (Eicken et al., 2002; Fetterer and Untersteiner, 1998; Holt and Digby, 1985; Polashenski et al., 2012). In Chapter 4, we explain that if pond coverage is low, and the underlying surface is impermeable, such isolated flaws in the ice should not significantly affect the pond coverage. However, if pond coverage is above a special value called the percolation threshold, p_c, there can be significant pond drainage through these flaws. In fact, if the drainage rate is great enough, the pond coverage would be limited to below p_c. For example, unless ice deformation prevents water from flowing into the ocean, the floe edge will limit pond growth to below p_c. In Chapters 3 and 4, we estimate p_c to be between 0.3 and 0.4 for Arctic sea ice. Below, we show that including drainage is necessary to accurately reproduce the evolution of pond coverage throughout stage I.

Including drainage in our model leads to some inconsistencies with the assumptions

under which we derived Eqs. 5.17 and 5.18. First, drainage opens the possibility for the water level to decrease, $\dot{w} < 0$, potentially exposing bare ice and topography that was altered by different melt rates of different regions of ice. These effects were not taken into account when deriving Eqs. 5.17 and 5.18, and, therefore, we can keep these equations only if the drainage is not too great. In fact, Eqs. 5.17 and 5.18 remain valid when $\dot{w} - \dot{h}_s > 0$ (the altered topography remains submerged) and while $w > 0$ (there are no regions of bare ice). Second, the percolation threshold only affects the pond coverage in the way we discussed above if the underlying surface is impermeable. In our case, the surface is a combination of impermeable ice and permeable snow. Since the pond coverage will likely exceed the percolation threshold before all the snow melts, there likely exists a complicated transition period between a surface that is a mix of permeable snow and impermeable ice and a fully impermeable ice surface. Moreover, when drainage is great enough so that the percolation threshold limits pond growth, the water level in different ponds needs to be at least slightly different, in contrast with the assumption of a common water table we made in the previous subsection. Here, we simply ignore these complications and assume that Eqs. 5.17 and 5.18 are approximately valid even when pond drainage occurs and that drainage is only activated if pond coverage exceeds the percolation threshold. We leave a detailed analysis of pond drainage during stage I for another study.

If we assume $\dot{w} - \dot{h}_s > 0$ and $w > 0$, we can straightforwardly include drainage in pond evolution (Eqs. 5.17 and 5.18) by simply altering the water balance equation. We derive this in SI section 5.S4. For example, if ponds drain at a rate of Q cm per day, Eq. 5.18 remains the same and 5.17 is modified to

$$\dot{w} = -\frac{r_i r_s (1-p)\dot{h}_s + Q}{1 - r_s(1-p)} \ . \tag{5.19}$$

To account for the fact that we expect little drainage to occur below the percolation threshold, we can make Q a function of p. The simplest representation would be to include $Q(p) =$

$Q_0\mathcal{H}(p - p_c)$, where $\mathcal{H}$ is the Heaviside function, equal to 0 or 1 depending on whether its argument is less or greater than 0, and Q_0 is a constant that sets the maximum drainage rate. Using this function yields the yellow line in Fig. 5.5e. If $\dot{w} - \dot{h}_s < 0$, Eq. 5.18 predicts the pond coverage to decrease, $\dot{p} < 0$. So, if $\dot{w} < \dot{h}_s$, we expect the pond coverage to remain fixed at the percolation threshold, $p = p_c$.

In Fig. 5.5e we compare stage I pond evolution predicted by our model with the measurements of stage I pond coverage evolution by Polashenski et al. (2012). Since accurate measurements of pre-melt topography are available for that time and location (Fig. 5.3), we can choose the parameters of the gamma distribution highly accurately. The density of snow and the snow melt rate are uncertain. We choose the density of snow to be $\rho_s = 350$ kg m^{-3}, and the albedo of melting snow to be $\alpha_s = 0.7$, consistent with observations of Polashenski et al. (2012). We take the solar flux to be $F_{\text{sol}} = 254$ W m^{-2}, which Polashenski et al. (2012) report as the average flux of solar energy for the duration of the experiment. We treat the sum of longwave, sensible, and latent heat fluxes, F_r, as a tuning parameter. The value we choose, $F_r = -25$ W m^{-2}, is typical of the region and season, and is therefore consistent with the measurements. The blue line in Fig. 5.5e shows the stage I pond evolution predicted by Eqs. 5.17 and 5.18, while the red line represents the measurements of Polashenski et al. (2012). The two curves agree up to the point when pond coverage reaches $p \approx 0.35$, a plausible value for the percolation threshold. Thus, the measurements are consistent with drainage being activated beyond the percolation threshold. To match pond evolution beyond $p = 0.35$ we used Eq. 5.19, and tuned the drainage rate, Q_0, to 1.9 cm day^{-1} (yellow line), a rate consistent with observations of Polashenski et al. (2012). We can see that Eq. 5.19 is consistent with the observations, although this matching cannot be fully confirmed due to uncertainty in the parameters.

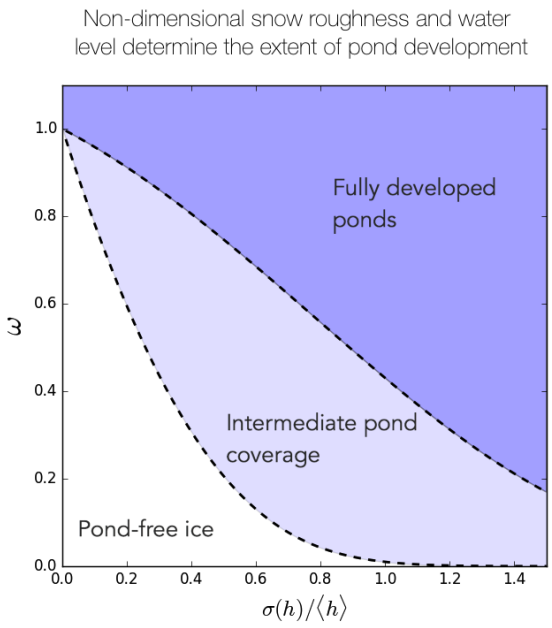

Figure 5.6: The horizontal axis shows the non-dimensional snow roughness, $\sigma(h)/\langle h \rangle$, while the vertical axis shows the non-dimensional water level, ω, described in the text. The white-colored region represents ice that remains pond-free throughout the summer, while the dark-blue region represents ice that develops pond coverage that exceeds the percolation threshold by the end of stage I. The light-blue region represents ice that has some ponds by the end of stage I, but the pond coverage does not exceed the percolation threshold.

5.6.3 A condition for pond development

Pond coverage reaches its peak by the end of stage I. Afterwards, ponds drain, and, by the end of the drainage stage, the remaining ponds correspond to regions of ice that are below sea level. Observations show that ponds that remain after drainage are a subset of ponds that exist during peak pond coverage (Landy et al., 2014; Polashenski et al., 2012). Therefore, if ponds do not develop during stage I, they will likely never develop. Since the pre-melt snow-depth distribution controls pond evolution during stage I, it, therefore, also has a disproportionate effect on later pond evolution. If the snow-depth is highly variable, ponds will develop sooner than if the snow cover is uniform. If the snow cover is relatively uniform and stage I does not last long enough, the ice may remain pond-free throughout the summer. Here, we will show how we can use the model we developed above to derive a simple criterion for whether ice will develop ponds or not.

We start with Eqs. 5.17 and 5.18. If we assume that pond coverage stays low throughout stage I, we can set $p \approx 0$ in Eq. 5.17, and integrate it directly to get the water level at time t during stage I, $w(t) \approx -\frac{r_i r_s}{1-r_s}\dot{h}_s t$. We can then non-dimensionalize Eq. 5.18 by introducing non-dimensional parameters Σ and ω to get

$$\frac{\mathrm{d}p}{\mathrm{d}\omega} = \tilde{f}_\Gamma(\omega, \Sigma) \ , \tag{5.20}$$

$$\Sigma \equiv \frac{\sigma(h)}{\langle h \rangle} \quad , \quad \omega \equiv -\frac{1 - r_s(1-r_i)}{1-r_s}\frac{\dot{h}_s t}{\langle h \rangle} \ , \tag{5.21}$$

Here, Σ is the non-dimensional roughness as in section 5.5 and ω can be interpreted as a non-dimensional water level. As in Eq. 5.15 of section 5.5, $\tilde{f}_\Gamma(\omega, \Sigma)$, is a gamma distribution with a mean equal to 1, so that it only depends on Σ, with parameters $k = \Sigma^{-2}$ and $h_0 = \Sigma^2$, and evaluated at ω. Thus, from Eq. 5.20, we get a simple relation

$$p = F_\Gamma(\omega, \Sigma) \ , \tag{5.22}$$

where $F_\Gamma(\omega, \Sigma)$ is a cumulative gamma distribution with a mean equal to 1, $F_\Gamma(\omega, \Sigma) \equiv \int_0^\omega \tilde{f}_\Gamma(z, \Sigma)\mathrm{d}z$. Therefore, if pond coverage is low, it depends only on ω and Σ and we can express it simply in terms of the cumulative gamma distribution.

Let us now assume that stage I lasts for some time, T, on the order of 5 days. If the ponds do not develop within that time, the ice will remain pond-free throughout the summer. We can set some threshold, p^*, say $p^* = 0.01$, and consider ice to be pond-free if the pond coverage is below p^*. We can then find the boundary in ω-Σ space, $\omega^*(\Sigma)$, such that if $\omega < \omega^*$, ice remains pond-free at the end of stage I. According to Eq. 5.22, this boundary is given by

$$\omega^*(\Sigma) = F_\Gamma^{-1}(p^*, \Sigma) \ , \tag{5.23}$$

where F_Γ^{-1} is an inverse of the cumulative gamma distribution (gamma percentile function) with a mean equal to 1, $k = \Sigma^{-2}$, and $h_0 = \Sigma^2$, evaluated at p^*. Equation 5.23 gives a universal criterion that ice remains pond-free. If ω, calculated given the snow melt rate, density, depth, roughness, and the duration of stage I, exceeds ω^*, ice will develop at least some ponds. The boundary, $\omega^*(\Sigma)$, is largely insensitive to the choice of the threshold coverage, p^*, so long as p^* is much smaller than 1.

In the case when ice develops some ponds, we can also ask how developed those ponds will be. In particular, we can assume that ponds are fully developed if the pond coverage exceeds the percolation threshold by the end of stage I. Beyond the percolation threshold, pond drainage likely starts to play an important role, and the post-stage I evolution of fully-developed ponds likely proceeds in a fairly typical manner. Therefore, there likely exist three typical trajectories for pond evolution during summer - pond-free, fully-developed, and intermediate. To see whether the ponds will develop fully, we can again use Eq. 5.23 but use $p^* = p_c \approx 0.35$. Using Eq. 5.23 with $p^* = 0.35$ is approximate since the pond coverage is no longer small, but it is still reasonably accurate.

In Fig. 5.6, we show the conditions for these three regimes of pond development. We can

see that when $\omega > 1$, ponds always fully develop since, in this case, the water level by the end of stage I exceeds the height of snow even when the snow cover is uniform. Otherwise, if $\omega < 1$, ponds develop more easily when the snow-depth has more variability. We can estimate ω and Σ for the measurements of Polashenski et al. (2012). We use $T = 5$ days, snow depth mean and variance estimated from the LiDAR measurements, and the same snow melt rate density as in the previous subsection. We show Σ and ω estimated in this way in Table 5.2. We can see that $\omega > 1$ in all cases so that we expect that ponds develop fully. In the study of Polashenski et al. (2012) this indeed happened. In order for ice to have remained pond-free, stage I would have had to have lasted less than 1.5 days in 2010, which had the most uniform snow, and less than 0.5 days for 2009N, which had the most variable snow. We note that persistently pond-free ice has been frequently observed in the Arctic (Perovich et al., 2002), while Antarctic sea ice only rarely develops ponds. It would be interesting to see where these pond-free ice floes fall within our pond-development diagram.

5.7 Discussion

Here, we will briefly discuss how our results can be applied to large-scale studies.

1. We believe that large-scale models should use a gamma distribution for snow depth on undeformed ice. Even though other distributions, such as normal or lognormal, may still work well enough, adopting a gamma distribution is a more principled approach that likely works over a wider range of parameters. Therefore mean and variance of snow depth are enough to characterize the whole distribution according to Eqs. 5.10. Since the correlation length appears to be stable across the Arctic, our "snow dune" model with a horizontal scale parameter $r_0 = 0.6$ m ($l_0 = 5.6$ m) may be used to study horizontal snow distribution.

2. When modeling heat conduction through undeformed ice, it is likely safe to neglect

horizontal heat transport. On deformed ice, the situation may be more complicated and further study is required.

3. To parameterize ice albedo during summer, Eqs. 5.17 and 5.18 may be used for pond evolution during stage I. Without knowing the outflow rate, Q, a reasonable approach would be to cap pond coverage to below the percolation threshold of 0.3 to 0.4. Equations 5.17 and 5.18 can be combined with similar approaches, such as the model of Popović et al. (2019b) described in Chapter 4 for stages II and III, or the model of Popović and Abbot (2017) described in Chapter 2 for stage III, to yield an analytic and accurate model of pond evolution throughout the entire melt season.

4. To estimate whether ice will remain pond-free throughout the summer, Eq. 5.23 may be used. We were not able to test this criterion against real data appropriately, as in all three cases we considered, the ponds have fully developed. So, it would be interesting to see whether this criterion can explain the observations of pond-free ice in the Arctic and the Antarctic. The non-dimensional water level, ω, in Eq. 5.23 depends on the duration of stage I. So, to be able to use this equation in large scale-studies, it will be necessary to relate the duration of stage I to parameters that are available on the large scale, such as energy fluxes, thickness, or the salinity of ice.

5.8 Conclusions

Snow cover greatly impacts sea ice evolution. It insulates the ice during the winter, reflects sunlight during the summer, and controls melt pond evolution. In this Chapter, we presented an idealized geometric model of "snow dune" topography that is capable of capturing key statistical properties of the snow cover on undeformed first-year sea ice. The main conclusion of this Chapter is that our "snow dune" model is a very accurate representation of the 3-dimensional snow distribution on flat, undeformed ice.

By comparing the moments of the height and snow-depth distributions, we showed that the height distribution of our model is statistically indistinguishable from the snow-depth distribution measured in detailed LiDAR scans on flat undeformed ice. We also compared the correlation functions for the model and the measurements to show that the horizontal statistics of snow are also well-captured by our model. In addition to this, our model captures melt pond geometry derived from helicopter images that span areas of 1 km^2 with the same model parameters as the LiDAR scans. This suggests that our model likely captures the horizontal properties of snow on such large scales. We note that in all cases we tested, the correlation length of horizontal features (either snow or melt pond), was around $l_0 \approx 5.6$ m, suggesting that this property is highly constrained in the Arctic. Since our model is fully defined by only three parameters, it follows that it is enough to know the mean snow depth, its variance, and the horizontal correlation length to fully characterize the statistics of snow on undeformed ice. On ice that was slightly deformed we showed that the measured snow-depth distribution contains subtle differences from the model and that there exist long-range correlations in the horizontal, inconsistent with our model.

After comparing our "snow dune" model to measurements, we considered its application to heat conduction through the ice and to the development of melt ponds. We solved a 3-dimensional heat conduction equation assuming the ice is flat and snow cover that is well-described by our model. We developed simple formulas that solve the conductive heat flux problem for any configuration of snow consistent with our model. Using these formulas, we showed that, in any realistic scenario, horizontal heat transport may be neglected on flat, undeformed ice (although this may not be the case for deformed ice). We then also used our model to develop a simple model for melt pond evolution during early stages of pond development when ice can be considered impermeable. We find that pond coverage evolution can be estimated using a system of two coupled ordinary differential equations that closely approximate an equivalent 2d model, but are much simpler to solve. They reveal connections

with measurable environmental parameters. For example, we show that doubling the amount of solar radiation has approximately the same effect on pond growth rate as halving the snow depth. We also show that they are consistent with observations. Using these equations, we develop a criterion in terms of non-dimensional properties of the ice surface for whether ice will develop ponds or remain pond-free during summer.

In this Chapter, we demonstrated that nearly all of the details of ice surface conditions can be summarized by only a few parameters if one is interested in bulk properties such as the total heat conducted or the mean melt pond coverage. Of the three parameters that define our model, only two can be expected to change from situation to situation, as the correlation length is likely stable, as discussed above. This means that future GCMs may need to only keep track of the total amount of snow and the snow depth variance in order to be able to represent the snow surface in a principled way. Our results, therefore, uncover an important property of sea ice snow cover that may improve the realism of sea ice models without adding to their complexity.

5.9 Supplementary Information

5.S1 Melt pond geometry

In this section we confirm that the melt pond features on the synthetic "snow dune" topography reproduce the Arctic sea ice melt pond statistics with as much accuracy as the "void model" of Chapter 3. We do this by comparing melt ponds on the synthetic "snow dune" topography to the ponds from the same dataset used by Chapter 3. Figure 5.S1 shows the comparison between the model and the data is nearly identical to that of Chapter 3 - the only difference is that the model curves now represent the synthetic "snow dune" topography instead of the "void model."

In Chapter 3, we compared the statistics of the "void model" to the statistics of real

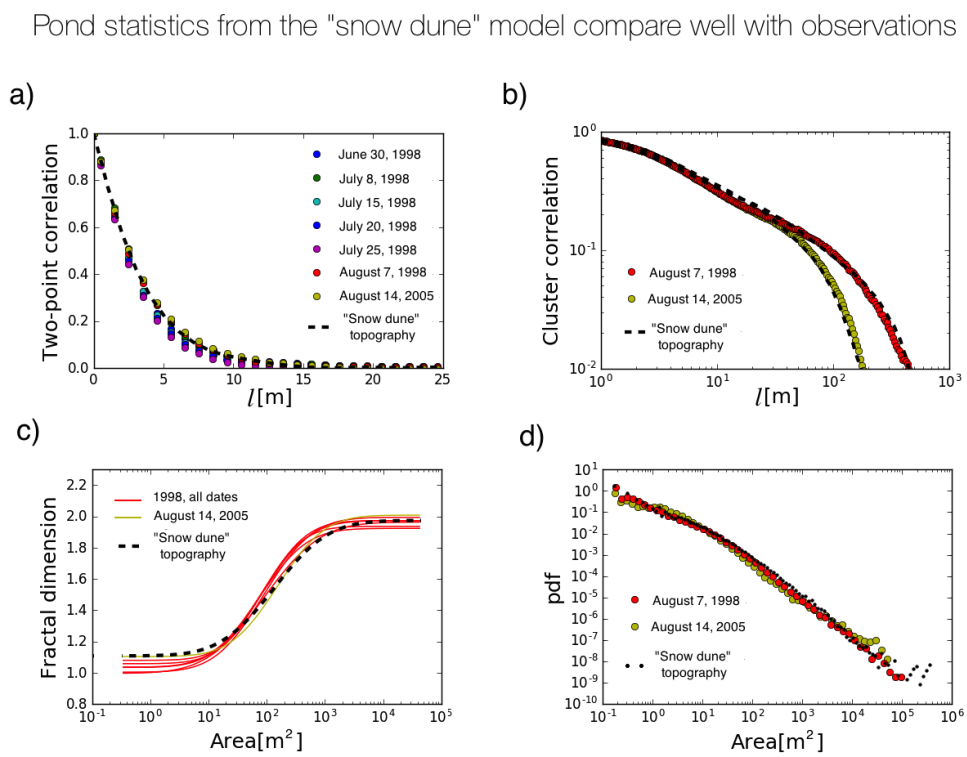

Figure 5.S1: A comparison of geometric properties of ponds photographed on different dates during the 1998 SHEBA and the 2005 HOTRAX missions with the geometry of ponds on the synthetic "snow dune" topography. The synthetic "snow dune" topography has a mean horizontal scale of mounds of $r_0 = 0.6$ m and the pond coverage fraction is set close to the percolation threshold. a) Two-point correlation function. Dots represent measurements, while the black dashed line represents synthetic topography. b) Cluster correlation function. Dots represent measurements, while the black dashed line represents synthetic topography. The two dashed black lines differ only in the domain size, with the domain sizes corresponding to the image sizes of the SHEBA and HOTRAX images. c) Fractal dimension of pond boundary as a function of pond area. Red and yellow lines are measurements, while the black dashed line represents ponds on synthetic topography. d) Pond area distribution on a log-log plot. Red and yellow dots are measurements, while the black dots represent ponds on synthetic topography

ponds derived from photographs taken during the 1998 SHEBA (Surface heat budget of the Arctic Ocean) (Uttal et al., 2002) mission and the 2005 HOTRAX (Healy-Oden Trans-Arctic Expedition) (Darby et al., 2005) missions. We compared four statistical features between the model and the data: the two-point correlation function, $C(l)$, the cluster correlation function, $G(l)$, the fractal dimension of the pond boundary, $D(A)$, as a function of pond area, A, and the pond area distribution, $f(A)$. Here we will use the same dataset and the same statistics to validate the synthetic "snow dune" topography. Below we explain each of these statistics and the method we used to obtain them only briefly, and we point the reader to Chapter 3 for details.

We form ponds on the synthetic "snow dune" topography by intersecting the surface with a flat plane (a "water table") and assuming ponds are regions of the surface below this plane. In this way, the pond coverage fraction can be changed independently of the surface parameters by simply raising and lowering the water table. This is in contrast with the "void model," where the density of circles placed controls the fraction of the surface covered by ponds, somewhat complicating the analogy between the two models. This will, however, not be a problem as pond statistics turn out to depend only on typical radius, r_0, and the deviation of pond coverage from the percolation threshold, p_c, in both the "void model" and the "snow dune" model. We explain the meaning of the percolation threshold below. Therefore, to compare the "snow dune" model with real ponds, we will use two of the statistics (e.g. $C(l)$ and $G(l)$) to calibrate r_0 and $p - p_c$ in the model, and use the other two statistics to confirm that the model reproduces the data with the same parameters.

A two-point correlation function, $C(l)$, is defined via the probability, $P(l)$, that, given a randomly chosen point on a pond, a point distance l away is also located on a pond. Precisely, the two point correlation function is given as

$$C(l) = \frac{P(l) - p}{1 - p} \ . \tag{5.S1}$$

This function is mostly sensitive to the horizontal scale of the mounds, r_0, and can be used to calibrate this parameter. The two-point correlation function for pond photographs is approximately a sum of two exponentials, similar to the height correlation function we discussed in section 5.4. The exponential with a short decay scale most likely corresponds to melt ponds, while the exponential with a long decay scale likely corresponds to large-scale features such as ridges and floe edges. To be able to compare the model to data, we have to remove the long-decay exponential in the same way as we did in section 5.4 (see also Chapter 3 for details). After removing the long-decay exponential, and choosing $r_0 = 0.6$ m, we get a good agreement for $C(l)$ between the model and the data (Fig. 5.S1a). Note that $r_0 = 0.6$ m is very close to r_0 we recovered from the LiDAR scans in section 5.4 (see Table 5.2).

A cluster correlation function, $G(l)$, is defined as the probability that, given a randomly chosen point on a non-spanning pond, a randomly chosen point a distance l away from this point is located on the *same* pond. A non-spanning pond is a pond that does not span the entire domain. This function is sensitive to the size of the largest non-spanning clusters, and therefore, to the pond coverage fraction, p. As the pond coverage fraction is increased, the largest connected cluster grows. At first it does not span the domain but after the pond coverage exceeds a special value called the percolation threshold, p_c, the largest cluster begins spanning the domain and therefore does not enter into the calculation of $G(l)$ anymore. It turns out that $G(l)$ depends on the deviation of pond coverage from the percolation threshold, $p - p_c$. For this reason, it can be used to calibrate $p - p_c$. In the void model, the percolation threshold is fixed, $p_c \approx 0.33$, while in the "snow dune" model, p_c depends on the density of mounds, ρ. So, we fix $\rho = 0.2$ and then we find p for which $G(l)$ for the model matches $G(l)$ for the data. Finding the pond coverage at which spanning ponds first appear, we find that the percolation threshold for $\rho = 0.2$ is approximately $p_c \approx 0.44$. We find that for $p - p_c \approx 0.015$, $G(l)$ for model and data agree well (Fig. 5.S1b). So, the pond coverage that

reproduces $G(l)$ for the data is close to, but slightly above the percolation threshold. The fact that ponds seem to be organized near the percolation threshold is in agreement with observations of Chapter 3 and theoretical considerations of Chapter 4.

Having calibrated r_0 and $p-p_c$, we proceed to test whether $D(A)$ and $f(A)$ agree between the model and data using the same parameters of the surface. Following Hohenegger et al. (2012) and using a method described in Chapter 3, we determined the fractal dimension of the pond boundary as the exponent, D, that relates the pond area, A, to its perimeter, P, $P \propto A^{D/2}$. We treat D as a function of pond area. In Fig. 5.S1c, we show that the fractal dimension for synthetic ponds reproduces the fractal dimension of real ponds. Finally, we look at the pond area distribution, $f(A)$. Again, using the parameters chosen by calibrating the model with the correlation functions, we find that the area distribution for real and synthetic ponds agree over the entire observational range (Fig. 5.S1d).

We also tested the model for different values of ρ and varying the anisotropy of mounds. We found that, as long as $p - p_c$ is the same, agreement between the data and the model remains. We take the accurate agreement between the "snow dune" model and the melt pond data along with the fact that the parameter r_0 is very similar for melt pond images and the LiDAR scans of the snow surface to be evidence that the horizontal characteristics of snow are well-represented in our model even on large scales. Melt pond photographs are taken at the end of summer, whereas ponds forming with a common water table on a snow-covered surface would be consistent with ponds during early summer. However, since ponded ice melts faster than bare ice and snow melts slower than bare ice, it is likely that the initial snow topography is approximately preserved throughout the melt season. Nevertheless, this difference in timing likely contributes to the fact that we estimated the percolation threshold for real ponds to be between 0.3 and 0.4 (see Chapter 3), while the "snow dune" topography predicts p_c between 0.4 and 0.5 for different values of ρ. A lower percolation threshold for real ponds could be due to the fact that ponds form channels as they drain during the later

stages (Landy et al., 2014; Polashenski et al., 2012), thereby increasing the connectivity and lowering p_c.

5.S2 Detailed statistics of the synthetic "snow dune" topography

In this section, we first prove Eqs. 5.4, 5.5, and 5.7 that we showed in section 5.3. Then we discuss the relation between the height distribution of the "snow dune" topography and the gamma distribution.

Proof of Eqs. 5.4 and 5.5

Here we derive the recursion relation, Eq. 5.5, for the moments of the synthetic "snow dune" topography. Equations 5.4 for the mean and the variance are then a corollary of this result. This proof has two steps. The first is to show where the recursion relation comes from, and the second is to find the moments of individual mounds. The first step will turn out to be universal, while the second will contain elements that depend on the details of the model. Throughout the derivation, we will use the notation $\langle \ ... \ \rangle$ for the mean of some function of topography. This mean can equally be interpreted as the mean over the domain or, since we are assuming that the domain is infinite, as the mean with respect to the probability distributions of radii, r_i, and locations, $\mathbf{x}_{0,i}$, of individual mounds. In this section, we will only take ensemble averages to derive the theoretical moments of the "snow dune" height distribution, whereas in the main text we took spatial averages to empirically find the moments of computer-generated synthetic topographies.

First, we show where the recursion relation, Eq. 5.5, comes from. The "snow dune" topography is a sum of individual mounds

$$h_{\mathrm{SD}}(\mathbf{x}) = \sum_{i=1}^{N} h_i(\mathbf{x}) \ , \tag{5.S2}$$

where $h_i(\mathbf{x})$ is the height of the i-th mound $h_i(\mathbf{x}) \equiv h_{m,0}\frac{r_i}{r_0}e^{-(\mathbf{x}-\mathbf{x}_{0,i})^2/2r_i^2}$. Therefore, the n-th power of the topography is

$$h^n_{\mathrm{SD}}(\mathbf{x}) = \sum_{i_1 \ldots i_n=1}^{N} h_{i_1}(\mathbf{x}) \ \ldots \ h_{i_n}(\mathbf{x}) \ , \tag{5.S3}$$

The n-th moment of the topography can then be found as $\langle h^n_{\mathrm{SD}} \rangle$. However, before we can find the mean of the above sum, we need to rearrange it into a different form. Since the mounds are sized and placed independently, we can use the identity $\langle h_i(\mathbf{x}) h_j(\mathbf{x}) \rangle = \langle h_i(\mathbf{x}) \rangle \langle h_j(\mathbf{x}) \rangle$ for $i \neq j$, with $\langle \ \ldots \ \rangle$ being the ensemble average over all possible locations and radii of mounds h_i and h_j. So, in the sum above (Eq. 5.S3), we need to distinguish between the terms where $i = j$ and the terms where $i \neq j$. To this end, we can first split the sum into a term where all n indexes are equal and a term where at least one of the n indexes is different from the others. We thus get

$$\sum_{i_1 \ldots i_n}^{N} h_{i_1} \ \ldots \ h_{i_n} = \sum_{i=1}^{N} h_i^n + \sum_{i; i_1 \ldots i_{n-1}}^{N\,\prime} h_i h_{i_1} \ \ldots \ h_{i_{n-1}} \ , \tag{5.S4}$$

where the prime on the second sum on the right hand side means that at least one of $i_1 \ \ldots \ i_{n-1}$ is not equal to the first index, i. It is now straightforward to take the average of the first term where all the terms are equal, but the average of the second term is still problematic. Since the second sum has at least one index different from from the first index i, we can further split it into a sum that has exactly one index different from i and a sum where there are at least two indexes different from i

$$\sum_{i, i_1 \ldots i_{n-1}}^{N\,\prime} h_i h_{i_1} \ \ldots \ h_{i_{n-1}} = (n-1) \sum_{i; j \neq i}^{N} h_i^{n-1} h_j + \sum_{i; i_1 \ldots i_{n-1}}^{N\,\prime\prime} h_i h_{i_1} \ \ldots \ h_{i_{n-1}} \ , \tag{5.S5}$$

where now $\sum''$ means that there are at least two terms among $i_1 \ \ldots \ i_{n-1}$ not equal to i.

The first sum above has exactly one term, j, not equal to i, and the factor $(n-1)$ comes from the fact that j can correspond to any of the i_1 ... i_{n-1} terms in the sum $\sum' h_i h_{i_1}$ ... $h_{i_{n-1}}$. The idea is then to continue splitting the primed sum in this way until we end up with a sum where all the indexes are different. We do this as follows. After s steps, we end up with a primed sum that has at least s terms among i_1 ... i_{n-1} not equal to i. We then split this sum to get a sum where exactly s terms are not equal to i and a sum where at least $s+1$ terms are not equal to i

$$\sum_{i,i_1 \ldots i_{n-1}}^{N(s)} h_i h_{i_1} \ldots h_{i_{n-1}} = \binom{n-1}{s} \sum_{i,j_1 \neq i, \ldots j_s \neq i}^{N} h_i^{n-s} h_{j_1} \ldots h_{j_s} + \sum_{i,i_1 \ldots i_{n-1}}^{N(s+1)} h_i h_{i_1} \ldots h_{i_{n-1}} \,. \tag{5.S6}$$

Therefore, we end up with one term where none of j_1 ... j_s are equal to i (note that there is no condition on whether or not the indexes j_1 ... j_s are equal to each other). The factor $\binom{n-1}{s}$ comes from the number of ways that we can choose s indexes j_1 ... j_s from the set i_1 ... i_{n-1}. Finally, after $n-1$ steps, we arrive at the end of this process. The final term is thus a sum where none of j_1 ... j_{n-1} are equal to the first term, i. At this step, we can proceed to take the average, $\langle h_{\mathrm{SD}}^n \rangle$. Using the fact that in each sum, the first term, i, is different than all the other terms, we get

$$\begin{aligned} \langle h_{\mathrm{SD}}^n \rangle = \sum_{i=1}^{N} \langle h_i^n \rangle + \ldots + \binom{n-1}{s} \sum_{i=1}^{N} \langle h_i^{n-s} \rangle \Big\langle \sum_{j_1 \ldots j_s \neq i}^{N} h_{j_1} \ldots h_{j_s} \Big\rangle + \\ \ldots + \sum_{i=1}^{N} \langle h_i \rangle \Big\langle \sum_{j_1 \ldots j_{n-1} \neq i}^{N} h_{j_1} \ldots h_{j_{n-1}} \Big\rangle \,. \end{aligned} \tag{5.S7}$$

First, we can note here that terms $\langle h_i^{n-s} \rangle$ are equal for all i, since all mounds are drawn from the same distribution. So, the terms $\sum_{i=1}^{N} \langle h_i^{n-s} \rangle$ can really be replaced with $N \langle h_1^{n-s} \rangle$ (where h_1 represents the first mound). Next, note that terms $\langle \sum h_{j_1} \ldots h_{j_s} \rangle$ are really just the s-th moment of h_{SD}, $\langle \sum h_{j_1} \ldots h_{j_s} \rangle = \langle h_{\mathrm{SD}}^s \rangle$. This is true even though the indexes j_1 ... j_s

are required to be different than i since, if the domain size is infinite, the number of mounds, N, also tends to infinity, and any mean of the topography is the same whether we remove one mound or not. Making a substitution $j \equiv n - s$, we finally get the recurrence relation

$$\langle h_{\mathrm{SD}}^n \rangle = N \sum_{j=1}^{n} \binom{n-1}{n-j} \langle h_1^j \rangle \langle h_{\mathrm{SD}}^{n-j} \rangle \ . \tag{5.S8}$$

To complete the proof, we only need to find the moments of individual mounds, $\langle h_1(\mathbf{x})^j \rangle$. For some quantity g that depends on radius r and position $\mathbf{x}_0$ the ensemble mean is given by

$$\langle g \rangle = \int g(r, \mathbf{x}_0) f_r(r) f_{x_0}(\mathbf{x}_0) \mathrm{d}r \mathrm{d}^2\mathbf{x}_0 \ , \tag{5.S9}$$

where $f_r(r)$ is the exponential distribution of radii given by Eq. 5.2 and $f_{x_0}(\mathbf{x}_0)$ is the uniform distribution of positions that is uniform over the domain, $f_{x_0}(\mathbf{x}_0) \equiv 1/L^2$, where L is the domain size. We have that the j-th power of an individual mound is

$$h_1(\mathbf{x})^j = h_{m,0}^j \Big(\frac{r_1}{r_0}\Big)^j e^{-j(\mathbf{x}-\mathbf{x}_{0,1})^2/2r_1^2} \ . \tag{5.S10}$$

The j-th moment of an individual mound is then

$$\langle h_1^j \rangle = \int f_r(r_1) f_{x_0}(\mathbf{x}_{0,1}) h_{m,0}^j \Big(\frac{r_1}{r_0}\Big)^j e^{-j(\mathbf{x}-\mathbf{x}_{0,1})^2/2r_1^2} \mathrm{d}r_1 \mathrm{d}^2\mathbf{x}_{0,1} \ . \tag{5.S11}$$

Assuming that $L \to \infty$, we can first evaluate the integral over $\mathbf{x}_{0,1}$

$$\int f_{x_0}(\mathbf{x}_{0,1}) e^{-j(\mathbf{x}-\mathbf{x}_{0,1})^2/2r_1^2} \mathrm{d}^2\mathbf{x}_{0,1} = \frac{1}{L^2} \frac{2\pi r_1^2}{j} \ . \tag{5.S12}$$

The term $\frac{2\pi r_1^2}{j}$ is simply the volume of a 2d Gaussian mound with a unit height and variance

r_1^2/j. Next, we can evaluate the integral over r_1. We get

$$\langle h_1^j \rangle = \frac{2\pi h_{m,0}^j}{j} \frac{1}{L^2} \int_0^\infty \frac{r_1^{j+2}}{r_0^{j+1}} e^{-r_1/r_0} \mathrm{d}r_1 = \frac{2\pi h_{m,0}^j}{j} \frac{r_0^2}{L^2} \int_0^\infty z^{2+j} e^{-z} \mathrm{d}z = \frac{2\pi h_{m,0}^j}{j} \frac{r_0^2}{L^2} \Gamma(3+j) \ , \tag{5.S13}$$

where $\Gamma(n)$ is a gamma function. Using $\Gamma(n) = (n-1)!$ for integer n, we find

$$\langle h_1^j \rangle = 2\pi h_{m,0}^j \frac{r_0^2}{L^2} \frac{(2+j)!}{j} \ . \tag{5.S14}$$

Moments of the individual mounds in Eq. 5.S8 are always multiplied by the number of mounds, N, and this product yields $N\langle h_1^j \rangle = 2\pi\rho h_{m,0}^j \frac{(2+j)!}{j}$. Finally, returning to Eq. 5.S8, we retrieve Eq. 5.5

$$\langle h_{\mathrm{SD}}^n \rangle = 2\pi\rho \sum_{j=1}^{n} \binom{n-1}{n-j} \frac{(2+j)!}{j} h_{m,0}^j \langle h_{\mathrm{SD}}^{n-j} \rangle \ . \tag{5.S15}$$

Equations 5.4 are simple consequences of the relations we derived here. In particular, the mean of the topography is

$$\langle h_{\mathrm{SD}} \rangle = N\langle h_1 \rangle = 12\pi\rho h_{m,0} \ . \tag{5.S16}$$

The variance is defined as $\sigma(h_{\mathrm{SD}})^2 \equiv \langle h_{\mathrm{SD}}^2 \rangle - \langle h_{\mathrm{SD}} \rangle^2$. Using the recursion relation to find $\langle h_{\mathrm{SD}}^2 \rangle$ and the relation for the mean we just derived, we get

$$\sigma(h_{\mathrm{SD}}^2)^2 = 24\pi\rho h_{m,0}^2 \ . \tag{5.S17}$$

Proof of Eq. 5.7

Here we derive Eq. 5.7 for the height correlation function of the synthetic "snow dune" topography. This proof follows very similar steps as the proof for the variance of the topog-

raphy shown in the previous section. For this reason, we will only outline the proof and skip some of the details.

We start with the definition of the height correlation function given by Eq. 5.6

$$C_h(\mathbf{l}) \equiv \frac{\langle h_{\mathrm{SD}}(\mathbf{x}) h_{\mathrm{SD}}(\mathbf{x}+\mathbf{l})\rangle - \langle h_{\mathrm{SD}}\rangle^2}{\sigma^2(h_{\mathrm{SD}})} \ . \tag{5.S18}$$

Using the fact that h_i and h_j are independent for $i \neq j$, we can write the term $\langle h_{\mathrm{SD}}(\mathbf{x}) h_{\mathrm{SD}}(\mathbf{x}+\mathbf{l})\rangle$ as a sum

$$\langle h_{\mathrm{SD}}(\mathbf{x}) h_{\mathrm{SD}}(\mathbf{x}+\mathbf{l})\rangle = \sum_{i,j=1}^{N} \langle h_i(\mathbf{x}) h_j(\mathbf{x}+\mathbf{l})\rangle = \sum_{i=1}^{N} \langle h_i(\mathbf{x}) h_i(\mathbf{x}+\mathbf{l})\rangle + \sum_{i\neq j}^{N} \langle h_i(\mathbf{x})\rangle \langle h_j(\mathbf{x}+\mathbf{l})\rangle \ , \tag{5.S19}$$

Then, since the averages do not depend on which mound we are considering, and since $N \gg 1$, we have

$$\langle h_{\mathrm{SD}}(\mathbf{x}) h_{\mathrm{SD}}(\mathbf{x}+\mathbf{l})\rangle = N\langle h_1(\mathbf{x}) h_1(\mathbf{x}+\mathbf{l})\rangle + N(N-1)\langle h_1\rangle^2 \approx N\langle h_1(\mathbf{x}) h_1(\mathbf{x}+\mathbf{l})\rangle + \langle h_{\mathrm{SD}}\rangle^2 \ , \tag{5.S20}$$

where we have used $N(N-1) \approx N^2$ and $N^2\langle h_1\rangle^2 = \langle h_{\mathrm{SD}}\rangle^2$ from the previous subsection. We, therefore, only need to find the term $\langle h_1(\mathbf{x}) h_1(\mathbf{x}+\mathbf{l})\rangle$. Proceeding in the same way as in the previous subsection, we have

$$\langle h_1(\mathbf{x}) h_1(\mathbf{x}+\mathbf{l})\rangle = \int f_r(r_1) f_{x_0}(\mathbf{x}_{0,1}) h_{m,0}^2 \Big(\frac{r_1}{r_0}\Big)^2 e^{-((\mathbf{x}-\mathbf{x}_{0,1})^2 + (\mathbf{x}+\mathbf{l}-\mathbf{x}_{0,1})^2)/2r_1^2} \mathrm{d}r_1 \mathrm{d}^2\mathbf{x}_{0,1} \ . \tag{5.S21}$$

Reducing this integral into a manageable form involves similar steps as in the previous subsection - first perform an integration over $\mathbf{x}_{0,1}$ and then change from integration over r_1 to integration over $z = r_1/r_0$. We skip the detailed steps and simply show the result of these

manipulations

$$\langle h_1(\mathbf{x})h_1(\mathbf{x}+\mathbf{l})\rangle = \pi h_{m,0}^2 \frac{r_0^2}{L^2}\int_0^\infty z^4 e^{-z-l^2/(2r_0 z)^2}\mathrm{d}z \ . \tag{5.S22}$$

Returning this into Eq. 5.S20 and Eq. 5.S18, and using the formula for the variance derived in the previous subsection, we retrieve Eq. 5.7 for the autocorrelation function.

Relationship between the "snow dune" topography and the gamma distribution

We will now use the results from the previous section to explore the relationship between the height distribution of the synthetic "snow dune" topography and the gamma distribution. We will show that the two distributions are not the same but are qualitatively similar.

The gamma distribution has moments

$$\left\langle h^n \right\rangle_\Gamma = h_0^n \frac{\Gamma(m+k)}{\Gamma(k)} = h_0^n k(k+1)...(k+n-1) \ , \tag{5.S23}$$

where $\langle ... \rangle_\Gamma$ is the mean with respect to the gamma distribution that has a scale parameter h_0 and a shape parameter k. We can rewrite this in a form in which we can directly compare the moments of the gamma distribution with the moments of the of the synthetic "snow dune" height distribution. In particular, we use the observation that $\langle h^n \rangle_\Gamma = h_0(k+n-1)\langle h^{n-1}\rangle_\Gamma$ to write a recursion formula for the moments of the gamma distribution

$$\left\langle h^n \right\rangle_\Gamma = k\sum_{j=1}^{n} \binom{n-1}{n-j} h_0^j \Gamma(j) \left\langle h^{n-j} \right\rangle_\Gamma \ . \tag{5.S24}$$

Comparing this equation with the recursion formula for the moments of the "snow dune" topography, Eq. 5.S8, we can see that they have exactly the same form. In particular, in both cases $\langle h^n \rangle = \sum_j a_j \binom{n-1}{n-j} \langle h^{n-j} \rangle$, for some coefficients a_j. The only difference is in

the coefficients a_j - for the "snow dune" topography, $a_j = N\langle h_1^j \rangle$, whereas for the gamma distribution $a_j = k h_0^j \Gamma(j)$. Expressing the moments of individual mounds, $\langle h_1^j \rangle$ using Eq. 5.S14, and identifying $\rho = k/(6\pi)$ and $h_{m,0} = h_0/2$ (Eqs. 5.11), we find that for the "snow dune" topography $a_j = N\langle h_1^j \rangle = k h_0^j \frac{\Gamma(3+j)}{3j2^j}$. Therefore the coefficients a_j in both distributions depend in the same way on parameters k and h_0, and are only different in the numerical constants. Moreover, "snow dune" topography and gamma distribution have the same coefficients a_1 and a_2 by construction.

The similarity between the two distributions is not unexpected - the gamma distribution is observed when the quantity of interest is a sum of k exponentially distributed, independent random variables, $\sum_{i=1}^{k} h_i$. This means that the gamma distribution will necessarily have an expansion of the form Eq. 5.S8, which was derived only under the assumption that the quantity we are interested in is a sum of independent random variables. In this recursion relation for the gamma distribution, the moments of individual terms, $\langle h_1^j \rangle$, are estimated with respect to the exponential distribution, $\langle h_1^j \rangle_{\text{Exp}} = h_0^j \Gamma(j)$. Therefore, the difference between the two distributions comes only from the fact that the height of individual mounds in the "snow dune" model is not exponentially distributed and therefore the moments $\langle h_1^j \rangle$ differ from those that enter the gamma distribution. The moments of individual mounds are, however, affected by arbitrary choices in our model such as the distribution of radii of individual mounds, and are therefore not robust.

5.S3 Ice heat conduction

In this section, we will derive Eqs. 5.12 to 5.16 for the heat flux conducted through the ice under snow cover that is well-described with our "snow dune" model. We will also consider heat conduction for arbitrary parameters η, Σ, and Λ

Non-dimensional heat equation

First, we show that the conductive heat flux must be of the form stated in Eq. 5.12, $F_c = F_0\Phi(\eta, \Sigma, \Lambda)$.

As we stated in the main text, we are assuming that ice is a block of uniform thickness, H, that ice and snow have fixed conductivities, k_i and k_s, that the snow cover is well-described with our "snow dune" model, that the temperature at the ice-ocean interface is fixed at the freezing point of salt water, T_f, that the temperature of the snow surface is fixed at the temperature of the atmosphere, T_a, and that the temperature field, T, within the ice and snow is in a steady state. Finally, we assume periodic boundary conditions in the horizontal. We define the ice-ocean interface to be the plane $z = -H$, and the snow-ice interface to be the plane $z = 0$. These assumptions are described by the following set of equations

$$\nabla^2 T = 0 \quad , \qquad T\big(z = -H\big) = T_f \quad , \tag{5.S25}$$

$$T\big(z = h_{\mathrm{SD}}(x,y)\big) = T_a \quad , \qquad k_i \frac{\partial T}{\partial z}\big(z = 0^-\big) = k_s \frac{\partial T}{\partial z}\big(z = 0^+\big) \quad , \tag{5.S26}$$

where $\nabla^2 \equiv \frac{\partial^2}{\partial x^2} + \frac{\partial^2}{\partial y^2} + \frac{\partial^2}{\partial z^2}$ is the Laplacian, x and y are the horizontal coordinates, z is the vertical coordinate, and $h_{\mathrm{SD}}(x,y)$ is the snow depth. The last equation represents the condition that the heat flux is continuous across the snow-ice interface.

At this point we make another simplifying assumption that we stated in the main text - we assume that, within snow, heat is transported purely vertically so that, at steady state, the temperature profile is linear, $T(z > 0) = T_a + \big(\frac{z}{h_{\mathrm{SD}}(x,y)} - 1\big)\big(T_a - T(z = 0)\big)$. With this simplification, we only need to solve the heat equation within the rectangular ice domain. In this case, the upper-surface boundary condition becomes $k_i \frac{\partial T}{\partial z}(z = 0) = k_s \frac{T_a - T(z=0)}{h_{\mathrm{SD}}(x,y)}$. Next, we non-dimensionalize the variables in the above equations as

$$\theta \equiv \frac{T - T_f}{T_a - T_f} \quad , \quad \tilde{x} \equiv \frac{x}{l_0} \quad , \quad \tilde{y} \equiv \frac{y}{l_0} \quad , \quad \tilde{z} \equiv \frac{z}{H} \quad , \quad \tilde{h} \equiv \frac{h_{\mathrm{SD}}}{\langle h_{\mathrm{SD}} \rangle} \; . \tag{5.S27}$$

In terms of these non-dimensional variables and non-dimensional parameters, $\eta = \frac{k_i}{k_s}\frac{\langle h \rangle}{H}$, $\Sigma = \frac{\sigma(h)}{\langle h \rangle}$, and, $\Lambda = \frac{l_0}{H}$, introduced in Eq. 5.13, we can rewrite the heat equation as

$$\frac{1}{\Lambda^2}\Big(\frac{\partial^2\theta}{\partial\tilde{x}^2} + \frac{\partial^2\theta}{\partial\tilde{y}^2}\Big) + \frac{\partial^2\theta}{\partial\tilde{z}^2} = 0 \quad , \quad \theta\big(\tilde{z} = -1\big) = 0 \quad , \quad \frac{\partial\theta}{\partial\tilde{z}}\big(\tilde{z} = 0\big) = \frac{1 - \theta(\tilde{z} = 0)}{\eta\tilde{h}} \ . \tag{5.S28}$$

Therefore, the non-dimensional temperature, θ, can only depend on η, Λ, and the parameters that determine the non-dimensional snow surface, $\tilde{h}$. If the snow surface is well-described by our "snow dune" model, the statistics of the non-dimensional snow topography, $\tilde{h}$, can only depend on Σ, since the mean is fixed to 1 and the typical dune radius, r_0, is fixed by rescaling the horizontal coordinates, x and y, by l_0. So, if our "snow dune" model applies, the spatially averaged statistics of θ can only depend on η, Λ, and Σ.

Heat flux through any surface characterized by a normal vector, $\mathbf{n}$, within the ice can be calculated as $F_{\mathbf{n}} = k_i \nabla T \cdot \mathbf{n}$. In particular, flux through the snow-ice interface is $k_i \partial T/\partial z(z = 0)$. In terms of non-dimensional temperature, the flux is then $F_0 \partial\theta/\partial\tilde{z}(\tilde{z} = 0)$, where $F_0 \equiv k_i \frac{T_f - T_a}{H}$, as in Eq. 5.13. The mean flux through the snow-ice interface is then

$$F_c = F_0 \Big\langle \frac{\partial\theta}{\partial\tilde{z}}(\tilde{z} = 0) \Big\rangle \ , \tag{5.S29}$$

where $\langle ... \rangle$ stands for averaging along the horizontal. Since $\langle \partial\theta/\partial\tilde{z}(\tilde{z} = 0) \rangle$ can only depend on η, Λ, and Σ, we have

$$F_c = F_0 \Phi\big(\eta, \Sigma, \Lambda\big) \ , \tag{5.S30}$$

and we recover Eq. 5.12.

Limiting behavior

We now solve the non-dimensional heat equation for the limits $\Sigma \to 0$, $\Lambda \to \infty$, and $\Lambda \to 0$. These limits yield non-dimensional heat flux assuming a uniform snow cover, Φ_u, a purely

vertical heat transport, Φ_v, and a dominantly horizontal heat transport, Φ_h.

1. In the limit of $\Sigma \to 0$, the snow cover is uniform and $\tilde{h} = 1$ everywhere. In this case, heat conduction is purely vertical and the temperature profile is linear, $\theta = \theta_0(\tilde{z} + 1)$, where θ_0 is the non-dimensional temperature at the snow-ice interface and we used the bottom boundary condition, $\theta(\tilde{z} = -1) = 0$. We obtain θ_0 from the top boundary condition, $\theta_0 = \frac{1-\theta_0}{\eta}$, and thus find $\theta_0 = \frac{1}{1+\eta}$. With that, the non-dimensional flux through the ice under a uniform snow cover is $\Phi_u = \frac{\mathrm{d}\theta}{\mathrm{d}\tilde{z}} = \theta_0$. We thus have

$$\Phi_u = \frac{1}{1+\eta} \ . \tag{5.S31}$$

2. In the limit $\Lambda \to \infty$, the horizontal extent of the snow features is much larger than the thickness of the ice. So, heat will again be transported vertically, but the temperature profile within the ice will be set by the local snow height. In other words, the temperature profile will be $\theta = \theta_0\big(\tilde{x}, \tilde{y}\big)(\tilde{z} + 1)$, where $\theta_0\big(\tilde{x}, \tilde{y}\big)$ is the non-dimensional temperature at the snow-ice interface at the point $\tilde{x}, \tilde{y}$. As in the previous case, we find $\theta_0\big(\tilde{x}, \tilde{y}\big)$ from the top boundary condition at $\tilde{x}, \tilde{y}$, $\theta_0\big(\tilde{x}, \tilde{y}\big) = \frac{1}{1+\eta\tilde{h}(\tilde{x},\tilde{y})}$. Since the local flux is $\frac{\mathrm{d}\theta}{\mathrm{d}\tilde{z}} = \theta_0\big(\tilde{x}, \tilde{y}\big)$, we find

$$\Phi_v = \Big\langle \frac{\mathrm{d}\theta}{\mathrm{d}\tilde{z}}(\tilde{z} = 0) \Big\rangle = \Big\langle \frac{1}{1+\eta\tilde{h}} \Big\rangle = \int_0^\infty \frac{f_\Gamma(\tilde{h})}{1+\eta\tilde{h}} \mathrm{d}\tilde{h} \ , \tag{5.S32}$$

where we used the fact that the height distribution of our "snow dune" topography is well-described with a gamma distribution. Since the non-dimensional snow topography, $\tilde{h}$, has a mean equal to 1 and a standard deviation equal to Σ, the parameters of this gamma distribution are, according to Eq. 5.10, $k = \Sigma^{-2}$ and $h_0 = \Sigma^2$. Thus, we recover Eq. 5.15 for the purely vertical heat transport.

3. In the limit $\Lambda \to 0$, the horizontal extent of the snow features is much smaller than

the thickness of the ice. In this case, temperature must be uniform in the horizontal, i.e. $\theta = \theta(\tilde{z})$. In the vertical, the temperature profile must again be linear, since the mean heat flux across any horizontal plane within the ice must be constant if the temperature is in a steady state. Thus, again, the temperature must be of the form $\theta = \theta_0(\tilde{z}+1)$. However, in this case, the snow depth is variable, and, if θ_0 is constant in the horizontal, the top boundary condition cannot be met at every point along the snow-ice interface. However, we can still determine θ_0 by requiring that the total flux conducted across the snow-ice interface remains constant. At each point along the snow-ice interface, the local non-dimensional flux through the snow is $\frac{1-\theta_0}{\eta\tilde{h}(\tilde{x},\tilde{y})}$. So, the mean non-dimensional flux through the upper boundary is $\frac{1-\theta_0}{\eta}\left\langle\frac{1}{\tilde{h}}\right\rangle$. On the other hand, using $\theta = \theta_0(\tilde{z}+1)$, this flux must be equal to $\frac{\mathrm{d}\theta}{\mathrm{d}\tilde{z}} = \theta_0$. Thus, equating the two fluxes, $\theta_0 = \frac{1-\theta_0}{\eta}\left\langle\frac{1}{\tilde{h}}\right\rangle$, we find $\theta_0 = \frac{\langle\tilde{h}^{-1}\rangle}{\langle\tilde{h}^{-1}\rangle+1}$. Thus, the non-dimensional flux in the limit $\Lambda \to 0$ is

$$\Phi_h = \frac{\left\langle\tilde{h}^{-1}\right\rangle}{\left\langle\tilde{h}^{-1}\right\rangle + 1} \ . \tag{5.S33}$$

If the snow-depth distribution is well-described with a gamma distribution with a shape parameter k, the average $\langle\tilde{h}^{-1}\rangle$ is equal to $\frac{k-1}{k}$ for $k \geq 1$. Since, in our case, $k = \Sigma^{-2}$, we have

$$\Phi_h = \frac{1}{1+\eta(1-\Sigma^2)} \ , \tag{5.S34}$$

and we recover Eq. 5.16. For $k \leq 1$, $\langle\tilde{h}^{-1}\rangle$ is infinite, and Eq. 5.S34 is no longer valid. Nevertheless, Eq. 5.S33 is still valid and implies that $\Phi_h = 1$ for $k > 1$, meaning that the heat flux is the same as if there were no snow on top of the ice. Clearly, for $\Lambda = 0$, we could not satisfy the upper boundary condition at every point along the interface. Nevertheless, for any small but non-zero Λ, a boundary layer of thickness on the order Λ develops within the ice and near the snow-ice interface. Within this boundary layer, vertical heat transport dominates, and the temperature varies along the horizontal to

match the upper boundary condition at every point.

Finite Λ

Finally, we derive Eq. 5.14 for the non-dimensional flux Φ assuming an arbitrary Λ. To understand how the heat transport changes as we increase Λ from 0 to ∞, we numerically solved the non-dimensional heat conduction problem, Eqs. 5.S28, on a 50x50x20 grid using a finite volume method. We set the typical mound radius, r_0, to be 1 grid point so that the total domain is roughly 5 correlation lengths wide. For each set of parameters η and Σ, we sweeped the parameter Λ from $\Lambda = 0.01$ to $\Lambda = 5$. Moreover, for each combination of η, Σ, and Λ we solved the heat conduction problem for 100 random realizations of the "snow dune" topography. For each of these realization, we calculated the mean heat flux across the domain and then found the mean flux across these 100 realizations. We chose to do this rather than to increase the grid size since our numerical scheme becomes increasingly inefficient for even modest increases in grid size.

The numerical scheme is especially inefficient at small Λ. This is a problem, since, for small Λ, high vertical resolution is required to resolve the boundary layer near the snow-ice interface we discussed in the previous subsection. We did not attempt to resolve this issue in a principled way, and simply carried out our low-resolution estimates. However, to ensure discrepancies at small Λ between the numerical results and the theoretical prediction given by Eq. 5.S34 are due to low resolution, we carried out one trial run at $\Lambda = 0.01$ (with $\eta = 1$ and $\Sigma = 0.75$) where we kept the snow topography fixed with a horizontal resolution of 25x25 and progressively increased the vertical resolution from 25 to 800 grid points. We found that with the vertical resolution of 25 grid points, the flux from numerical calculations was around $0.94\Phi_h$, and became closer and closer to Φ_h with increasing resolution. At a resolution of 800 vertical grid points the numerical flux was around $0.993\Phi_h$ found using Eq. 5.S33.

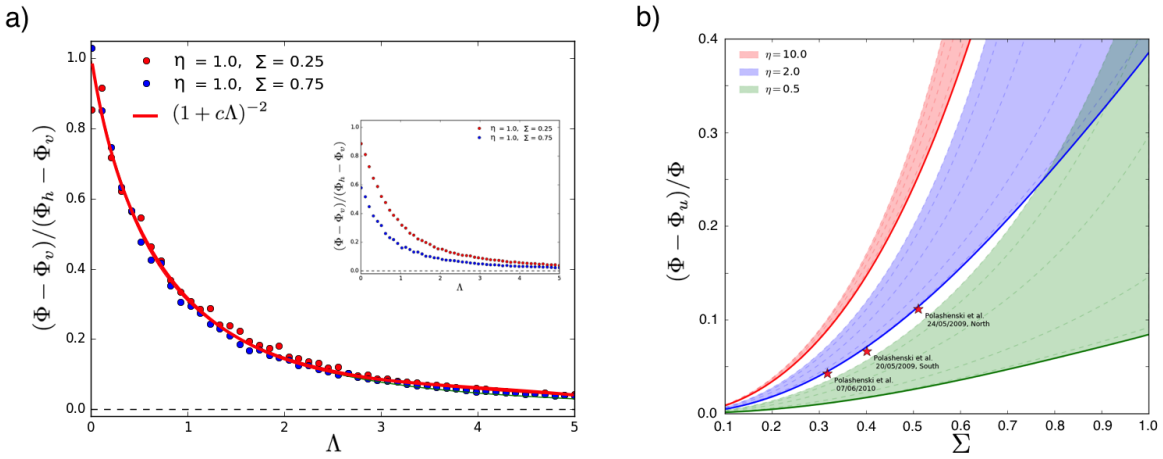

Figure 5.S2: a) The ratio $\varphi = \frac{\Phi-\Phi_v}{\Phi_h-\Phi_v}$ as a function of the non-dimensional parameter, Λ. Each dot represents the average φ across an ensemble of 100 runs with different random realizations of the "snow dune" topography and the same values of non-dimensional parameters. Since the simulated ratio φ does not tend to 1 (see the inset) as Λ tends to 0 due to low resolution of our simulations, the simulations are normalized so that $\varphi(\Lambda = 0) = 1$. The solid red curve represents the function $(1 + c\Lambda)^{-2}$ with $c \approx 0.83$. Inset shows the simulation results before normalizing to $\varphi(\Lambda = 0) = 1$. b) The fraction of the flux due to snow-depth variability, $\frac{\Phi-\Phi_u}{\Phi}$ as a function of non-dimensional snow roughness Σ. The flux Φ is calculated using Eq. 5.S35 and Φ_u is calculated using Eq. 5.S31. Different colors stand for different non-dimensional depth, η. Thick colored lines represent the heat flux with purely vertical heat transport ($\Lambda \to \infty$), while the colored shadings represent the flux attainable when the horizontal heat diffusion is included ($\Lambda < \infty$). Thin dashed lines represent the heat flux for Λ equal to 8, 2, 0.5, 0.125, and 0. The stars represent the fraction of the flux due to snow variability under the measured LiDAR topographies of Polashenski et al. (2012) with parameters given in Table 5.2.

Since we know that in the limit $\Lambda \to 0$ the non-dimensional flux must approach Φ_h and that in the limit $\Lambda \to \infty$, it must approach Φ_v, we consider the ratio $\varphi \equiv \frac{\Phi - \Phi_v}{\Phi_h - \Phi_v}$, where Φ is the numerical flux, calculated at finite Λ. This ratio must decrease from 1 at $\Lambda = 0$ to 0 for large Λ. We plot this ratio in Fig. 5.S2a. The simulated φ, however, does not reach 1 at small Λ (see inset of Fig. 5.S2a). In our single trial where we progressively increased the vertical resolution, this ratio was roughly 0.73 at a resolution of 25 vertical grid points, consistent with φ in the inset of Fig. 5.S2 we obtained in our low resolution runs. The ratio increased with increasing resolution, reaching roughly 0.97 at a resolution of 800 vertical grid points, thus consistent with Eqs. 5.S32 and 5.S34 being valid. For this reason, we believe that our ensemble runs are at odds with predictions mainly due to low resolution of our simulations. Thus, we normalized the simulation results so that $\varphi(\Lambda = 0) = 1$. This is shown in Fig. 5.S2a. We can see that in this case, the simulation results for both values of the parameters η and Σ roughly fall on the same curve that is well-fit with a function $(1 + c\Lambda)^{-2}$ where $c \approx 0.83$. With this, we get

$$\Phi\big(\eta, \Sigma, \Lambda\big) = \Phi_v + \frac{\Phi_h - \Phi_v}{(1 + c\Lambda)^2} \ , \tag{5.S35}$$

and we recover Eq. 5.14.

Exploring the parameter space

Even though the horizontal heat transport does not contribute significantly to heat conduction on flat ice, it may still be of interest to understand how it might contribute in principle. Here, we use Eq. 5.S35 to briefly explore how the heat flux behaves when changing parameters η, Σ, and Λ. We will focus our discussion on the fraction of the heat flux that is due to snow-depth variability, $\frac{\Phi - \Phi_u}{\Phi}$, where we find Φ using Eq. 5.S35 and we find Φ_u using Eq. 5.S31.

Our main results here are summarized in Fig. 5.S2b. We find that the amount of flux that can be attributed to snow-depth variability strongly increases with the snow roughness, Σ, and also increases with the non-dimensional snow depth, η. We find that it is roughly proportional to Σ^2, although this dependence is highly approximate. The sensitivity to other parameters also increases with Σ. The effect of horizontal heat transport may be be large in principle: e.g. decreasing Λ from ~ 10 to 0.1 would roughly double the effect of snow variability on ice with the same η and Σ as 2009N LiDAR measurements. This is even more pronounced at larger Σ and smaller η. As we have discussed in the previously, for $\Sigma \geq 1$, there exists a possibility that snow is not registered at all if Λ is small enough. This occurs because, if $\Sigma \geq 1$ a certain fraction of the ice is snow-free, so that if horizontal heat transport is efficient enough, all of the heat is exported through these regions.

5.S4 Deriving stage I pond evolution

In this section, we derive Eqs. 5.17 to 5.19 for pond evolution during stage I. We also develop a higher order approximation for pond coverage evolution and we test these approximations against a 2d model of pond evolution. We use the notation $\dot{x} \equiv \frac{\mathrm{d}x}{\mathrm{d}t}$ for the rate of change of a quantity x, as in section 5.6.

Proof of Eqs. 5.17 and 5.18

As we stated in section 5.6, we are assuming that snow is fully permeable, that there exists a common water table below which the snow is completely saturated with water, that underlying ice is impermeable and initially flat, that the initial snow topography is well-described by our "snow dune" topography, that no meltwater is lost from the domain, that snow, bare ice, ponded ice, and ponded snow (water-covered snow) melt at different rates that are constant in space and time, and that both snow and ice melt only at the surface.

We denote the ice and snow topography as $h(\mathbf{x})$, which represents the vertical coordinate

of snow, or ice if there is no snow on top. Because we have assumed that snow is permeable, there exists a common water level, w, such that all points with $h(\mathbf{x}) < w$ are ponded. Since we have assumed that the underlying ice is initially flat, there also exists an initial common ice level, which we can define as $h = 0$, such that all points with $h(\mathbf{x}) < 0$ have no snow on top of ice. Because of this assumption, the depth of snow in snow-covered regions, $h(\mathbf{x}) > 0$, is given by $h(\mathbf{x})$. Since we have assumed that meltwater cannot be lost during stage I, pond coverage can only grow during this stage. We can see from the assumptions above that there can be no regions of bare ice (ice that is snow-free and pond-free). Therefore, it is enough to consider the melt of bare snow, ponded snow, and ponded ice.

Since we have defined snow-free ice regions to be $h(\mathbf{x}) < 0$ and pond regions to be $h(\mathbf{x}) < w$, where w is the height of the water table, we have

$$p_i = \int_{-\infty}^{0} f(h,t)\mathrm{d}h \ , \tag{5.S36}$$

$$p = \int_{-\infty}^{w} f(h,t)\mathrm{d}h \ , \tag{5.S37}$$

where p_i is the ice fraction, p is the pond fraction, and $f(h,t)$ is the surface height distribution that, due to different regions melting at different rates, depends on time, t. Since, under our assumptions, there are no regions of bare ice, bare snow fraction can be found as $1 - p$ and ponded snow fraction as $p - p_i$.

By knowing the melt rates of different regions of the ice, we can find the rate of change of the distribution f. Let us, for the moment, assume that the ice melt rate $\dot{h}$ is an arbitrary function of height, $\dot{h} = \dot{h}(h)$. We are interested in finding the the quantity $f(h, t+\mathrm{d}t)\mathrm{d}h$, i.e., the fraction of the ice surface with a height between h and $h + \mathrm{d}h$ at a time $t + \mathrm{d}t$. To first order in $\mathrm{d}t$, the surface with a height h at time $t+\mathrm{d}t$ used to be at a height $h-\dot{h}(h)\mathrm{d}t$, while the surface at with a height $h+\mathrm{d}h$ at time $t+\mathrm{d}t$ used to be at a height $h+\mathrm{d}h-\dot{h}(h+\mathrm{d}h)\mathrm{d}t$,

where we are assuming a sign convention $\dot{h} < 0$. So, we have

$$f(h, t + \mathrm{d}t)\mathrm{d}h = f(h - \dot{h}\mathrm{d}t, t)\mathrm{d}h_2 \ , \tag{5.S38}$$

for some height range $\mathrm{d}h_2$ that may be different than the range $\mathrm{d}h$ because the melt rate $\dot{h}(h)$ may be different than the melt rate $\dot{h}(h + \mathrm{d}h)$. In particular, $\mathrm{d}h_2$ is the difference between the heights $h + \mathrm{d}h - \dot{h}(h + \mathrm{d}h)\mathrm{d}t$ and $h - \dot{h}(h)\mathrm{d}t$, so to first order in $\mathrm{d}t$, we have

$$\mathrm{d}h_2 = \mathrm{d}h(1 - \mathrm{d}t\frac{\mathrm{d}\dot{h}}{\mathrm{d}h}) \ . \tag{5.S39}$$

Combining Eqs. 5.S38 and 5.S39, we find

$$f(h, t + \mathrm{d}t) = f(h - \dot{h}\mathrm{d}t, t)(1 - \mathrm{d}t\frac{\mathrm{d}\dot{h}}{\mathrm{d}h}) \ . \tag{5.S40}$$

Expanding this equation to first order in $\mathrm{d}t$, we find the conservation law for the height probability distribution

$$\frac{\partial f}{\partial t} = -\frac{\partial(f\dot{h})}{\partial h} \ . \tag{5.S41}$$

Note that, because ice is melting ($\dot{h} < 0$), it is the melt rate slightly above h that enters the conservation law, Eq. 5.S41. This distinction will be important when considering the rates of change of coverage fractions due to the discontinuous change in melt rates when the surface type changes.

We can now express the rate of change of the pond coverage fraction as

$$\dot{p} = \frac{\mathrm{d}}{\mathrm{d}t}\int_{-\infty}^{w} f(h, t)\mathrm{d}h = f(w, t)\Big(\dot{w} - \dot{h}_s\Big) \ , \tag{5.S42}$$

where we have used Eqs. 5.S37 and 5.S41 and the fact that, since $w > 0$, the melt rate slightly above the water level, w, is the snow melt rate, $\dot{h}(w + \mathrm{d}h) = \dot{h}_s$. Since, under our

assumptions, all non-ponded regions melt at the same constant rate, the height distribution for $h > w$ does not change shape and is simply shifted downwards as the time progresses, and we can express $f(w,t) = f(w - \dot{h}_s t)$. At time $t = 0$, this distribution is well-described by the gamma distribution, so we find

$$\dot{p} = f_\Gamma(w - \dot{h}_s t)\Big(\dot{w} - \dot{h}_s\Big) \ . \tag{5.S43}$$

Therefore, to close this equation, we only need to express $\dot{w}$.

The water level can be expressed in terms of the water volume, V_{w}. Because snow is porous, some fraction of the water is stored in the saturated snow. We consider all snow below w to be saturated and all of the pores to be filled with water. For this reason, 1 m^3 of saturated snow will contain $1 - r_s$ meters cubed of water, where $r_s = \frac{\rho_s}{\rho_i}$. The volume of water can then be expressed as

$$V_{\mathrm{w}} = V_{\mathrm{pi}} + V_{\mathrm{ps}} + V_{\mathrm{bs}} \ , \tag{5.S44}$$

where V_{pi}, V_{ps}, and V_{bs} are the volumes of water contained in regions of ponded ice, ponded snow, and bare snow. A small element of area, ΔA, of each of these categories then contains the following amounts of water

$$\Delta V_{\mathrm{pi}} = (w - h(\mathbf{x}))\Delta A \ , \tag{5.S45}$$

$$\Delta V_{\mathrm{ps}} = \Big((w - h(\mathbf{x})) + h(\mathbf{x})(1 - r_s)\Big)\Delta A = (w - r_s h(\mathbf{x}))\Delta A \ , \tag{5.S46}$$

$$\Delta V_{\mathrm{bs}} = w(1 - r_s)\Delta A \ . \tag{5.S47}$$

We can then find the total volumes of water in these regions as

$$V_{\mathrm{pi}} = A_{\mathrm{pi}} w - A \int_{-\infty}^{0} f(h,t) h \mathrm{d}h \ , \tag{5.S48}$$

$$V_{\mathrm{ps}} = A_{\mathrm{ps}} w - A r_s \int_{0}^{w} f(h,t) h \mathrm{d}h \ , \tag{5.S49}$$

$$V_{\mathrm{bs}} = A_{\mathrm{bs}} w (1 - r_s) \ , \tag{5.S50}$$

where A is the total area of the domain, and A_{pi}, A_{ps}, and A_{bs} are areas of ponded ice, ponded snow, and bare snow. After some rearrangement, this finally yields the volume of water as

$$\frac{V_{\mathrm{w}}}{A} = w(1 - r_s(1-p)) - \bar{h}(-\infty, 0) - r_s \bar{h}(0, w) \ , \tag{5.S51}$$

where we have introduced a shorthand notation, $\bar{h}(a,b) \equiv \int_a^b f(h,t) h \mathrm{d}h$. To find the rate of change of w, we need to find the rates of change of $\bar{h}$. In general, we have

$$\dot{\bar{h}}(a,b) = b\dot{b} f(b,t) - a\dot{a} f(a,t) + \int_a^b \dot{f}(h,t) h \mathrm{d}h \ . \tag{5.S52}$$

Applying this rule along with Eq. 5.S41, applying partial integration once, and using Eqs. 5.S36, 5.S37, and 5.S42, we get

$$\dot{\bar{h}}(-\infty, 0) = \dot{h}_{\mathrm{pi}} p_i \ , \tag{5.S53}$$

$$\dot{\bar{h}}(0, w) = w\dot{p} + \dot{h}_{\mathrm{ps}}(p - p_i) \ , \tag{5.S54}$$

where $\dot{h}_{\mathrm{pi}}$ and $\dot{h}_{\mathrm{ps}}$ are melt rates of ponded ice and ponded snow. Therefore, we find the rate of change of water volume expressed in terms of the rate of change of water level, coverage fractions and melt rates of different regions of the ice as

$$\frac{\dot{V}_{\mathrm{w}}}{A} = \dot{w}(1 - r_s(1-p)) - \dot{h}_{\mathrm{pi}} p_i - r_s \dot{h}_{\mathrm{ps}}(p - p_i) \ . \tag{5.S55}$$

On the other hand, we can express the meltwater production rate using the rates of melt of different regions of the ice

$$\frac{\dot{V}_{\mathrm{w}}}{A} = -\frac{1}{\rho_w}\Big(\rho_s \dot{h}_s(1-p) + \rho_s \dot{h}_{\mathrm{ps}}(p-p_i) + \rho_i p_i \dot{h}_{\mathrm{pi}}\Big) \ . \tag{5.S56}$$

Finally, using Eqs. 5.S55 and 5.S56, we can express the rate of change of the water level as

$$\dot{w} = -\frac{r_i r_s(1-p)\dot{h}_s - (1-r_i)\big[r_s p \dot{h}_{\mathrm{ps}} + p_i(\dot{h}_{\mathrm{pi}} - r_s \dot{h}_{\mathrm{ps}})\big]}{1 - r_s(1-p)} \ . \tag{5.S57}$$

This, together with Eq. 5.S43, represents a solution to pond coverage evolution that makes no approximations under the assumptions stated at the beginning of this section. However, this system of equations is not closed since it still depends on the fraction of ponded ice, p_i. So to have a complete solution, Eqs. 5.S43 and 5.S57 would have to be supplemented with an equation for the evolution of p_i, which could be achieved by evolving the distribution $f(h,t)$ according to Eq. 5.S41. This would, however, complicate matters significantly, and we will now show how this can be avoided with an approximation which detracts very little from the accuracy of the solution.

Firstly, note that, since ice and water have similar densities, $r_i = 0.9 \approx 1$, making the second term in Eq. 5.S57, proportional to $(1-r_i)$, small compared to the first term. Secondly, the first term is proportional to $(1-p)$ while the second term is proportional to p which means that during initial pond growth, the significance of the second term is additionally diminished. Therefore, the second term only becomes important when $p \sim 1$, which is rarely observed in real ponds. By simply neglecting the second term, we get Eqs. 5.17 and 5.18 discussed in section 5.6

$$\dot{w} \approx -\frac{r_i r_s(1-p)}{1-r_s(1-p)}\dot{h}_s \ , \tag{5.S58}$$

$$\dot{p} = f_\Gamma(w - \dot{h}_s t)\Big(\dot{w} - \dot{h}_s\Big) \ , \tag{5.S59}$$

We show in section 5.S4 that this approximation is very good at the beginning of the melt season and shows a slight deviation when the pond coverage becomes high enough (Fig. 5.S3).

Including pond drainage

We now note how to include limited drainage during stage I to get Eq. 5.19. If drainage of Q cm per day occurs, this will modify the water balance equation, Eq. 5.S56. Simply adding a term $-Q$ to $\frac{\dot{V}_\mathrm{w}}{A}$ in Eq. 5.S56 and following through the same steps as before yields the correct equation. In this case, the water level equation after neglecting the term proportional to p_i becomes

$$\dot{w} = -\frac{r_i r_s (1-p)\dot{h}_s + Q}{1 - r_s(1-p)} \ , \tag{5.S60}$$

as discussed in section 5.6. Q can be made a function of pond coverage, such that ponds only drain above the percolation threshold. As was also discussed in section 5.6, drainage makes it possible for the water level to decrease. This can lead to exposing regions of bare ice and topography that was altered by differential melting, which makes it impossible to use the height distribution f_Γ. To avoid this, it is sufficient that $\dot{w} - \dot{h}_s > 0$ and that $w > 0$.

Invariants of Eqs. 5.17 and 5.18

Finally, we will explain the remark we made in section 5.6 that the pond evolution is unchanged by increasing the snow melt rate and the volume of snow by the same factor. That is to say, Eqs. 5.17 and 5.18 are invariant under $\dot{h}_s \to a\dot{h}_s$ and $h(\mathbf{x}) \to ah(\mathbf{x})$. First, we note that the rate of change of water level, $\dot{w}$, is proportional to the snow melt rate, $\dot{h}_s$, so that $\dot{w} \to a\dot{w}$ when $\dot{h}_s \to a\dot{h}_s$, assuming that the pond coverage does not change. From here and using Eq. 5.S43, it follows that $\dot{p} \to a f_\Gamma\big(a(w - \dot{h}_s t)\big)\left(\dot{w} - \dot{h}_s\right)$ when $\dot{h}_s \to a\dot{h}_s$. Second, from the definition of the Gamma distribution (Eq. 5.9), we can see that when the scale, h_0,

transforms as $h_0 \to a h_0$, the gamma distribution transforms as $f_\Gamma(x) \to \frac{1}{a} f_\Gamma(x/a)$. Equation 5.10 relates h_0 to the mean and the variance of the surface height as $h_0 = \sigma^2(h)/\langle h \rangle$, from which it follows that changing the surface height as $h(\mathbf{x}) \to a h(\mathbf{x})$ leads to $h_0 \to a h_0$. Combining the transformation properties of the gamma distribution under $h(\mathbf{x}) \to a h(\mathbf{x})$ and the transformation properties of the water level under $\dot{h}_s \to a\dot{h}_s$, we find that the pond coverage evolution described by $\dot{p}$ is unchanged.

Second-order approximation

The approximation we made to get Eq. 5.S58 can be improved by noting that the term proportional to p_i in Eq. 5.S57 is a difference between melt rates of different types of ponded surface, $\dot{h}_{\rm pi} - r_s \dot{h}_{\rm ps}$. Expressing this difference in terms of heat fluxes, we can see it is equal to $(\alpha_{\rm ps} - \alpha_{\rm pi}) \frac{F_{\rm sol}}{l_m \rho_i}$, where $\alpha_{\rm ps}$ and $\alpha_{\rm pi}$ are the albedos of ponded snow and ponded ice. Therefore, if ponded snow and ponded ice have similar albedos, this difference is small. For this reason, it is justified to neglect the term proportional to p_i in Eq. 5.S57. Under this approximation, we get a closed system of equations

$$\dot{w} = -\frac{r_i r_s (1-p)\dot{h}_s - (1-r_i) r_s p \dot{h}_{\rm ps}}{1 - r_s(1-p)} \ , \tag{5.S61}$$

$$\dot{p} = f_\Gamma(w - \dot{h}_s t)\Big(\dot{w} - \dot{h}_s\Big) \ . \tag{5.S62}$$

In the next subsection, we show that these equations are nearly indistinguishable from the full 2d model. Equations 5.S61 and 5.S62 are as simple to solve as Eqs. 5.S58 and 5.S59, but we chose to focus on Eqs. 5.S58 and 5.S59 in section 5.6 since they highlight the dominant role of snow melt rate. We can add drainage in this apporximation in the same way as in the previous subsection

$$\dot{w} = -\frac{r_i r_s (1-p)\dot{h}_s - (1-r_i) r_s p \dot{h}_{\rm ps} + Q}{1 - r_s(1-p)} \ , \tag{5.S63}$$

Including additional details is also possible within this framework. For example, if melt rates change with time all of the derived evolution equations can still be used, except that the term $\dot{h}_s t$ entering f_Γ in Eq. 5.S43 should be replaced with $\langle \dot{h}_s \rangle t$, where $\langle \dot{h}_s \rangle$ means mean snow melt rate up to time t.

Testing the analytic model

The assumptions stated at the beginning define a model that can be solved numerically on the full 2d topography with all of the details of the topography included. In this case, we initiate the model by generating a "snow dune" topography with a desired mean and variance. Then, at each time step, we find the water level, use it to find regions of ponded ice and ponded snow, update the topography by melting different regions of the surface at their prescribed rates, find the volume of water generated, and, finally, update the water level again. We show the results of these simulations as colored lines in Fig. 5.S3.

In Figs. 5.S3, we compare the simple estimate, Eqs. 5.S58 and 5.S59 (red dashed lines), and the second order estimate, Eqs 5.S61 and 5.S62 (red dotted lines), with the solutions to the full 2d model (colored lines). We can see that the simple estimate is a good approximation to the full 2d model in the beginning and shows slight discrepancy at large p, as expected. We can also see that the second-order approximation is nearly indistinguishable from the full 2d solutions.

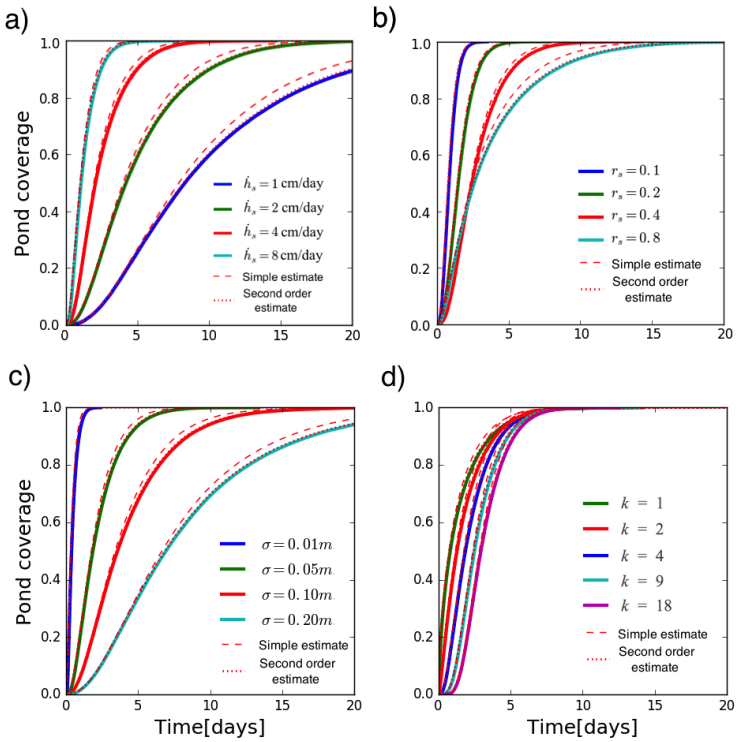

Figure 5.S3: Pond coverage evolution during stage I for a variety of model parameters. The solid lines are solutions to the full stage I 2d model on a "snow dune" topography for different model parameters, the red dashed lines are solutions to Eqs. 5.S58 and 5.S59, while the red dotted lines are solutions to Eqs. 5.S61 and 5.S62. As in Fig. 5.5, in each panel, we change one parameter, while we keep the others fixed at default values $\dot{h}_s = 4$ cm day^{-1}, $r_s = 0.4$, $\sigma(h) = 0.05$ m, and $k = 4$ a) Pond coverage evolution for different snow melt rates, $\dot{h}_s$. b) Pond coverage evolution for different snow to ice density ratios, r_s. c) Pond coverage evolution on topographies with different snow-depth standard deviations, $\sigma(h)$. d) Pond coverage evolution on topographies with different shape parameters, k.

CHAPTER 6

CONCLUSIONS

In this thesis, we studied Arctic sea ice melt ponds using idealized models with the goals of providing a deeper understanding into melt pond evolution, providing accurate and computationally inexpensive methods for making estimates about melt pond coverage, and making robust predictions under varying environmental conditions. We showed that pond coverage evolution as well as pond geometry throughout the majority of the melt season can be understood using these simple models without sacrificing the accuracy or realism of significantly more complicated higher-dimensional models. However, more work is still needed in order to provide a fully unified picture of melt pond evolution. For example, understanding the hole formation physics, the formation of connecting channels between ponds during stage II, and lateral and enhanced melt during stage III is necessary to fully connect different pond evolution stages and accurately relate pond evolution to physical parameters. Under global warming many parameters that control pond evolution, such as ice thickness or radiative fluxes, will likely change. Thus, it is important to correctly understand the relationship between ponds and these parameters in order to correctly capture the ice albedo feedback under a warming scenario. It may be possible to exploit the natural spatial and temporal variability in these parameters across the Arctic to validate and improve the predictions of our models.

Chapters of this thesis correspond to papers published over a period of more than five years. As such, the assumptions and parameter values used in different chapters are slightly different. Nevertheless, the conclusions of all the chapters are consistent with each other. In particular, the results of Chapters 4 and 5 follow directly from the findings of Chapter 3. Chapter 2 explores stage III of pond evolution which is revisited in Chapter 4. Nevertheless, the conclusions of these two chapters do not overlap much since Chapter 2 addresses the effects of enhanced and lateral melt, whereas Chapter 4 addresses the processes that determine

the ice topography which controls pond evolution during stage III and its relation to stage II of pond evolution. Below, we summarize the main conclusions of each of the chapters.

In Chapter 2, we studied the late-summer pond coverage evolution, assuming that ice is fully permeable. Our findings include:

- Pond coverage evolution can be estimated by solving two uncoupled ODEs that are controlled by the initial hypsographic curve and four parameters that govern the rates of melt of ponded ice, bare ice, ice bottom, and enhanced melting near the pond edge.
- Under a global warming scenario, ice loss due to pond feedback is likely comparable to ice loss due to direct forcing.
- Pond growth is more sensitive to changes in bare ice albedo than to pond albedo.
- If freeboard sinking is suppressed by topography, as is likely the case on multi-year ice, enhanced melting near the pond edge becomes the dominant mode of pond growth. In this case, pond evolution likely depends strongly on the dependence of ice albedo on height above sea level.
- The complicated physics of lateral melting can be summarized by a single non-dimensional constant that relates the lateral melt flux to the flux used for melting the pond bottoms.

In Chapter 3, we studied melt pond geometry. By analyzing hundreds of thousands of ponds derived from aerial photographs of sea ice taken during the SHEBA and HOTRAX missions, we found that:

- Pond geometry can be captured with a simple model that represents ponds as voids that surround randomly sized and placed circles that represent snow dunes. Pond size distribution, fractal dimension as a function of pond size, the two-point correlation function, and the cluster correlation function can all be accurately reproduced over the

entire observational range of more than 6 orders of magnitude by tuning only the two parameters of this model: the typical circle radius and the pond coverage fraction.

- Late summer ponds are organized close to the critical threshold of the percolation transition.
- For both study years, pond length-scale as measured by the two-point correlation function is remarkably constant.

In Chapter 4, we explained the observation made in Chapter 3 that late-summer ponds are organized close to the percolation threshold. Using a model where holes open at random locations and drain ponds that exist on a randomly generated ice topography, we show that:

- The percolation threshold of 0.3-0.5 is an upper bound on pond coverage following pond drainage.
- Pond drainage is universal in that it does not depend on the details of the underlying topography, but rather only on several aggregate parameters. A universal curve, that can be analytically calculated, determines the pond fraction when a certain number of holes is open on the surface.
- The universal curve determines pond evolution with time during stage II when ice melt is included. All of the parameters of the equation can be related to measurable ice properties.
- Assuming that ponds are approximately level during stage II, that pond coverage only decreases during stage II and only increases during stage III, and that lateral or enhanced melt does not occur, the same universal curve governs pond evolution during stage III.
- Pond coverage is highly sensitive to physical properties of ice - even a 1% measurement error in physical parameters may lead to a 10% error in pond coverage. The most

uncertain parameter that enters the formula for pond evolution is the timescale of hole opening. Therefore, to gain a better understanding of pond evolution, the the hole formation physics must be better understood.

In Chapter 5, we generalized the void model of Chapter 3. We created a continuous "snow dune" topography by representing snow dunes as Gaussian mounds. We found that:

- The pre-melt snow depth distribution on undeformed ice as measured by detailed LiDAR scans is nearly indistinguishable from the synthetic "snow dune" topography height distribution that is well-fit with a Gamma distribution. Horizontal statistics of the snow topography on undeformed ice is also well-captured by the synthetic "snow dune" topography. This agreement becomes worse when ice is deformed.

- This synthetic surface is fully characterized by 3 parameters - mean snow depth, snow roughness, and the the horizontal correlation length. Therefore, knowing these three parameters is enough to fully characterize the snow surface on undeformed ice.

- The synthetic "snow dune" model allows the conductive heat flux through the ice under a realistic snow cover to be approximated analytically.

- The fact that the snow-depth distribution is well-fit with a Gamma distribution allows pond coverage evolution during stage I to be analytically calculated. This analytic model yields a simple criterion for whether ponds will develop in the summer or not.

This work shows that Arctic sea ice melt ponds can be described accurately and analytically. This will allow melt ponds to be examined more rigorously and understood more deeply. In this way, better parameterizations of sea ice albedo in large-scale climate models may be developed which, in turn, may lead to improving sea ice predictions. Finally, our model developed in Chapter 4 represents a novel mechanism for organization towards the percolation threshold, that, due to its universality, may have application to a broader range of natural phenomena.

REFERENCES

Abbot, D. S., Silber, M., and Pierrehumbert, R. T. (2011). Bifurcations leading to summer arctic sea ice loss. *Journal of Geophysical Research: Atmospheres*, 116(D19).

Aharony, A. and Stauffer, D. (2003). *Introduction to percolation theory*. Taylor & Francis.

Arntsen, A. E., Song, A. J., Perovich, D. K., and Richter-Menge, J. A. (2015). Observations of the summer breakup of an arctic sea ice cover. *Geophysical Research Letters*, 42(19):8057–8063.

Bitz, C. M. and Lipscomb, W. H. (1999). An energy-conserving thermodynamic model of sea ice. *Journal of Geophysical Research: Oceans*, 104(C7):15669–15677.

Bowen, B., Strong, C., and Golden, K. M. (2018). Modeling the fractal geometry of arctic melt ponds using the level sets of random surfaces. *Journal of Fractal Geometry*, 5(2):121–142.

Bowen, B., Strong, C., and Golden, K. M. (in press, 2017). Modeling the fractal geometry of arctic melt ponds using the level sets of random surfaces. *Journal of Fractal Geometry*, page 21.

Cole, D. and Shapiro, L. (1998). Observations of brine drainage networks and microstructure of first-year sea ice. *Journal of Geophysical Research: Oceans*, 103(C10):21739–21750.

Coles, S. (2001). *An introduction to statistical modeling of extreme values*, volume 208. Springer.

Darby, D. A., Jakobsson, M., and Polyak, L. (2005). Icebreaker expedition collects key arctic seafloor and ice data. *Eos, Transactions American Geophysical Union*, 86(52):549–552.

Delfino, G., Viti, J., and Cardy, J. (2010). Universal amplitude ratios of two-dimensional percolation from field theory. *Journal of Physics A: Mathematical and Theoretical*, 43(15):152001.

Eicken, H., Grenfell, T., Perovich, D., Richter-Menge, J., and Frey, K. (2004). Hydraulic controls of summer arctic pack ice albedo. *Journal of Geophysical Research: Oceans*, 109(C8).

Eicken, H., Krouse, H., Kadko, D., and Perovich, D. (2002). Tracer studies of pathways and rates of meltwater transport through arctic summer sea ice. *Journal of Geophysical Research: Oceans*, 107(C10):SHE–22.

Eisenman, I. and Wettlaufer, J. (2009). Nonlinear threshold behavior during the loss of arctic sea ice. *Proceedings of the National Academy of Sciences*, 106(1):28–32.

Essam, J. W. (1980). Percolation theory. *Reports on Progress in Physics*, 43(7):833.

Fetterer, F. and Untersteiner, N. (1998). Observations of melt ponds on arctic sea ice. *Journal of Geophysical Research: Oceans*, 103(C11):24821–24835.

Filhol, S. and Sturm, M. (2015). Snow bedforms: A review, new data, and a formation model. *Journal of Geophysical Research: Earth Surface*, 120(9):1645–1669.

Flocco, D. and Feltham, D. L. (2007). A continuum model of melt pond evolution on arctic sea ice. *Journal of Geophysical Research: Oceans*, 112(C8). C08016.

Flocco, D., Feltham, D. L., and Turner, A. K. (2010). Incorporation of a physically based melt pond scheme into the sea ice component of a climate model. *Journal of Geophysical Research: Oceans*, 115(C8).

Frey, K. E., Perovich, D. K., and Light, B. (2011). The spatial distribution of solar radiation under a melting arctic sea ice cover. *Geophysical Research Letters*, 38(22). L22501.

Golden, K. (2001). Brine percolation and the transport properties of sea ice. *Annals of glaciology*, 33:28–36.

Golden, K. M., Eicken, H., Heaton, A., Miner, J., Pringle, D., and Zhu, J. (2007). Thermal evolution of permeability and microstructure in sea ice. *Geophysical Research Letters*, 34(16).

Goldenfeld, N. (1992). *Lectures on phase transitions and the renormalization group*. Addison-Wesley, Advanced Book Program, Reading.

Grebmeier, J. M., Smith, W. O., and Conover, R. J. (1995). Biological processes on arctic continental shelves: Ice-ocean-biotic interactions. *Arctic Oceanography: Marginal Ice Zones and Continental Shelves*, pages 231–261.

Halperin, B. I., Feng, S., and Sen, P. N. (1985). Differences between lattice and continuum percolation transport exponents. *Physical review letters*, 54(22):2391.

Hanesiak, J., Barber, D., De Abreu, R., and Yackel, J. (2001). Local and regional albedo observations of arctic first-year sea ice during melt ponding. *Journal of Geophysical Research: Oceans*, 106(C1):1005–1016.

Hohenegger, C., Alali, B., Steffen, K., Perovich, D., and Golden, K. (2012). Transition in the fractal geometry of arctic melt ponds. *The Cryosphere*, 6(5):1157–1162.

Holland, M. M., Bailey, D. A., Briegleb, B. P., Light, B., and Hunke, E. (2012). Improved sea ice shortwave radiation physics in ccsm4: The impact of melt ponds and aerosols on arctic sea ice. *Journal of Climate*, 25(5):1413–1430.

Holland, M. M. and Bitz, C. M. (2003). Polar amplification of climate change in coupled models. *Climate Dynamics*, 21(3-4):221–232.

Holland, M. M., Bitz, C. M., and Tremblay, B. (2006). Future abrupt reductions in the summer arctic sea ice. *Geophysical research letters*, 33(23).

Holland, M. M. and Curry, J. A. (1999). The role of physical processes in determining the interdecadal variability of central arctic sea ice. *Journal of climate*, 12(11):3319–3330.

Holt, B. and Digby, S. A. (1985). Processes and imagery of first-year fast sea ice during the melt season. *Journal of Geophysical Research: Oceans*, 90(C3):5045–5062.

Isichenko, M. B. (1992). Percolation, statistical topography, and transport in random media. *Reviews of modern physics*, 64(4):961.

Kerstein, A. R. (1983). Equivalence of the void percolation problem for overlapping spheres and a network problem. *Journal of Physics A: Mathematical and General*, 16(13):3071.

Lake, R. and Lewis, E. (1970). Salt rejection by sea ice during growth. *Journal of Geophysical Research*, 75(3):583–597.

Landy, J., Ehn, J., Shields, M., and Barber, D. (2014). Surface and melt pond evolution on landfast first-year sea ice in the canadian arctic archipelago. *Journal of Geophysical Research: Oceans*, 119(5):3054–3075.

Liston, G. E., Polashenski, C., Rösel, A., Itkin, P., King, J., Merkouriadi, I., and Haapala, J. (2018). A distributed snow-evolution model for sea-ice applications (snowmodel). *Journal of Geophysical Research: Oceans*, 123(5):3786–3810.

Lüthje, M., Feltham, D., Taylor, P., and Worster, M. (2006). Modeling the summertime evolution of sea-ice melt ponds. *Journal of Geophysical Research: Oceans*, 111(C2). C02001.

Ma, Y.-P., Sudakov, I., and Golden, K. M. (2014). Ising model for melt ponds on arctic sea ice. *arXiv preprint arXiv:1408.2487*.

Mandelbrot, B. (1967). How long is the coast of Britain? Statistical self-similarity and fractional dimension. *Science*, 156(3775):636–638.

Morassutti, M. and LeDrew, E. (1996). Albedo and depth of melt ponds on sea-ice. *International journal of climatology*, 16(7):817–838.

Nishimori, H. and Ortiz, G. (2010). *Elements of phase transitions and critical phenomena*. OUP Oxford.

North, G. R. (1984). The small ice cap instability in diffusive climate models. *Journal of the atmospheric sciences*, 41(23):3390–3395.

Ono, N. (1967). Specific heat and heat of fusion of sea ice. *Physics of Snow and Ice*, 1(1):599–610.

Pedersen, C. A., Roeckner, E., Lüthje, M., and Winther, J.-G. (2009). A new sea ice albedo scheme including melt ponds for echam5 general circulation model. *Journal of Geophysical Research: Atmospheres*, 114(D8).

Perovich, D., Tucker, W., and Ligett, K. (2002). Aerial observations of the evolution of ice surface conditions during summer. *Journal of Geophysical Research: Oceans*, 107(C10).

Perovich, D. K. (1996). The optical properties of sea ice. Technical report, Cold Regions Research and Engineering Lab Hanover NH.

Perovich, D. K. and Gow, A. J. (1996). A quantitative description of sea ice inclusions. *Journal of Geophysical Research: Oceans*, 101(C8):18327–18343.

Perovich, D. K., Grenfell, T. C., Richter-Menge, J. A., Light, B., Tucker, W. B., and Eicken, H. (2003). Thin and thinner: Sea ice mass balance measurements during sheba. *Journal of Geophysical Research: Oceans*, 108(C3).

Perovich, D. K., Light, B., Eicken, H., Jones, K. F., Runciman, K., and Nghiem, S. V. (2007). Increasing solar heating of the arctic ocean and adjacent seas, 1979–2005: Attribution and role in the ice-albedo feedback. *Geophysical Research Letters*, 34(19).

Perovich, D. K. and Polashenski, C. (2012). Albedo evolution of seasonal arctic sea ice. *Geophysical Research Letters*, 39(8).

Perovich, D. K. and Richter-Menge, J. A. (2009). Loss of sea ice in the arctic. *Annual Review of Marine Science*, 1:417–441.

Perovich, D. K., Roesler, C. S., and Pegau, W. S. (1998). Variability in arctic sea ice optical properties. *Journal of Geophysical Research: Oceans*, 103(C1):1193–1208.

Petrich, C., Eicken, H., Polashenski, C. M., Sturm, M., Harbeck, J. P., Perovich, D. K., and Finnegan, D. C. (2012). Snow dunes: A controlling factor of melt pond distribution on arctic sea ice. *Journal of Geophysical Research: Oceans*, 117(C9).

Polashenski, C., Golden, K. M., Perovich, D. K., Skyllingstad, E., Arnsten, A., Stwertka, C., and Wright, N. (2017). Percolation blockage: A process that enables melt pond formation on first year arctic sea ice. *Journal of Geophysical Research: Oceans*, 122(1):413–440.

Polashenski, C., Perovich, D., and Courville, Z. (2012). The mechanisms of sea ice melt pond formation and evolution. *Journal of Geophysical Research: Oceans*, 117(C1).

Popović, P. and Abbot, D. (2017). A simple model for the evolution of melt pond coverage on permeable arctic sea ice. *The Cryosphere*, 11(3):1149–1172.

Popović, P., Cael, B., Silber, M., and Abbot, D. S. (2018). Simple rules govern the patterns of arctic sea ice melt ponds. *Physical review letters*, 120(14):148701.

Popović, P., Finkel, J., Silber, M., and Abbot, D. (2019a). Arctic sea ice snow topographic statistics accurately captured by an idealized model. submitted to JGR: Oceans.

Popović, P., Silber, M., and Abbot, D. (2019b). Critical percolation threshold restricts late-summer arctic sea ice melt pond coverage. submitted to JGR: Oceans.

Rösel, A., Kaleschke, L., and Kern, S. (2015a). Gridded melt pond cover fraction on arctic sea ice derived from terra-modis 8-day composite reflectance data bias corrected version 02.

Rösel, A., Kaleschke, L., and Kern, S. (2015b). Gridded melt pond cover fraction on arctic sea ice derived from terra-modis 8-day composite reflectance data bias corrected version 02.

Scagliarini, A., Calzavarini, E., Mansutti, D., and Toschi, F. (2018). Modelling sea ice and melt ponds evolution: sensitivity to microscale heat transfer mechanisms. *arXiv preprint arXiv:1809.06924*.

Schröder, D., Feltham, D. L., Flocco, D., and Tsamados, M. (2014). September arctic sea-ice minimum predicted by spring melt-pond fraction. *Nature Climate Change*, 4(5):353.

Scott, F. and Feltham, D. (2010). A model of the three-dimensional evolution of arctic melt ponds on first-year and multiyear sea ice. *Journal of Geophysical Research: Oceans*, 115(C12).

Screen, J. A. and Simmonds, I. (2010). The central role of diminishing sea ice in recent arctic temperature amplification. *Nature*, 464(7293):1334–1337.

Serreze, M. C., Holland, M. M., and Stroeve, J. (2007). Perspectives on the arctic's shrinking sea-ice cover. *science*, 315(5818):1533–1536.

Serreze, M. C. and Stroeve, J. (2015). Arctic sea ice trends, variability and implications for seasonal ice forecasting. *Philosophical Transactions of the Royal Society A: Mathematical, Physical and Engineering Sciences*, 373(2045):20140159.

Sicilia, A., Arenzon, J. J., Bray, A. J., and Cugliandolo, L. F. (2007). Domain growth morphology in curvature-driven two-dimensional coarsening. *Physical Review E*, 76(6):061116.

Skyllingstad, E. D. and Paulson, C. A. (2007). A numerical study of melt ponds. *Journal of Geophysical Research: Oceans*, 112(C8).

Skyllingstad, E. D., Paulson, C. A., and Perovich, D. K. (2009). Simulation of melt pond evolution on level ice. *Journal of Geophysical Research: Oceans*, 114(C12).

Skyllingstad, E. D., Shell, K. M., Collins, L., and Polashenski, C. (2015). Simulation of the melt season using a resolved sea ice model with snow cover and melt ponds. *Journal of Geophysical Research: Oceans*, 120(7):5194–5215.

Stroeve, J., Holland, M. M., Meier, W., Scambos, T., and Serreze, M. (2007). Arctic sea ice decline: Faster than forecast. *Geophysical research letters*, 34(9).

Sturm, M., Perovich, D. K., and Holmgren, J. (2002). Thermal conductivity and heat transfer through the snow on the ice of the beaufort sea. *Journal of Geophysical Research: Oceans*, 107(C10):SHE–19.

Taylor, P. and Feltham, D. (2004). A model of melt pond evolution on sea ice. *Journal of Geophysical Research: Oceans*, 109(C12).

Timco, G. and Frederking, R. (1996). A review of sea ice density. *Cold regions science and technology*, 24(1):1–6.

Untersteiner, N. (1961). On the mass and heat budget of arctic sea ice. *Archiv für Meteorologie, Geophysik und Bioklimatologie, Serie A*, 12(2):151–182.

Untersteiner, N. (1964). Calculations of temperature regime and heat budget of sea ice in the central arctic. *Journal of Geophysical Research*, 69(22):4755–4766.

Uttal, T., Curry, J. A., McPhee, M. G., Perovich, D. K., Moritz, R. E., Maslanik, J. A., Guest, P. S., Stern, H. L., Moore, J. A., Turenne, R., et al. (2002). Surface heat budget of the arctic ocean. *Bulletin of the American Meteorological Society*, 83(2):255–276.

Wakatsuchi, M. and Saito, T. (1985). On brine drainage channels of young sea ice. *Annals of glaciology*, 6:200–202.

Wang, M. and Overland, J. E. (2009). A sea ice free summer arctic within 30 years? *Geophysical research letters*, 36(7).

Webster, M. A., Rigor, I. G., Perovich, D. K., Richter-Menge, J. A., Polashenski, C. M., and Light, B. (2015). Seasonal evolution of melt ponds on arctic sea ice. *Journal of Geophysical Research: Oceans*, 120(9):5968–5982.

Weinrib, A. (1982). Percolation threshold of a two-dimensional continuum system. *Physical Review B*, 26(3):1352.

Yackel, J., Barber, D., and Hanesiak, J. (2000). Melt ponds on sea ice in the canadian archipelago: 1. variability in morphological and radiative properties. *Journal of Geophysical Research: Oceans*, 105(C9):22049–22060.

Yen, Y.-C. (1981). Review of thermal properties of snow, ice and sea ice. Technical report, Cold Regions Research and Engineering Lab Hanover NH.

Zallen, R. and Scher, H. (1971). Percolation on a continuum and the localization-delocalization transition in amorphous semiconductors. *Physical Review B*, 4(12):4471.

Zhang, J., Lindsay, R., Steele, M., and Schweiger, A. (2008). What drove the dramatic retreat of arctic sea ice during summer 2007? *Geophysical Research Letters*, 35(11).